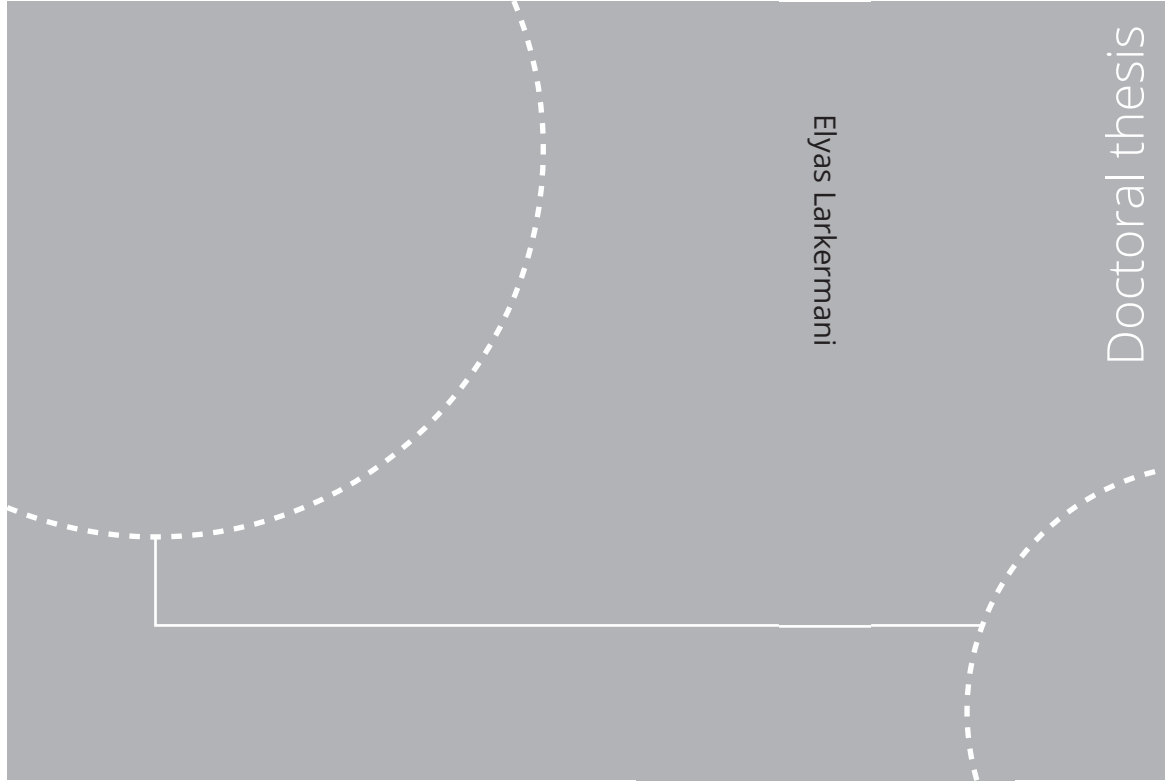


ISBN 978-82-326-8262-1 (printed ver.)
ISBN 978-82-326-8261-4 (electronic ver.)
ISSN 1503-8181 (printed ver.)
ISSN 2703-8084 (electronic ver.)



Doctoral theses at NTNU, 2024:335

Elyas Larkermanni

Development of a Numerical Framework using Orthogonal Grids and Immersed Boundary Methods for Large Eddy Simulation of Indoor Airflows

 **NTNU**
Norwegian University of
Science and Technology

Doctoral theses at NTNU, 2024:335

 NTNU

NTNU
Norwegian University of
Science and Technology
Thesis for the degree of
Philosophiae Doctor
Faculty of Engineering
Department of Energy and Process Engineering

 **NTNU**
Norwegian University of
Science and Technology

Elyas Larkermani

Development of a Numerical Framework using Orthogonal Grids and Immersed Boundary Methods for Large Eddy Simulation of Indoor Airflows

Thesis for the degree of Philosophiae Doctor

Trondheim, September 2024

Norwegian University of Science and Technology
Faculty of Engineering
Department of Energy and Process Engineering



Norwegian University of
Science and Technology

NTNU

Norwegian University of Science and Technology

Thesis for the degree of Philosophiae Doctor

Faculty of Engineering

Department of Energy and Process Engineering

© Elyas Larkermani

ISBN 978-82-326-8262-1 (printed ver.)

ISBN 978-82-326-8261-4 (electronic ver.)

ISSN 1503-8181 (printed ver.)

ISSN 2703-8084 (electronic ver.)

Doctoral theses at NTNU, 2024:335



Printed by Skipnes Kommunikasjon AS

Preface

This thesis is submitted to the Norwegian University of Science and Technology (Norges teknisk-naturvitenskapelige universitet) in partial fulfillment of the requirements for the degree of Doctor of Philosophy (PhD).

The work presented in this thesis was carried out at the Department of Energy and Process Engineering, Faculty of Engineering, Norwegian University of Science and Technology (NTNU), Norway. The doctoral work was conducted under the main supervision of Professor Laurent Georges at the Department of Energy and Process Engineering of NTNU, with co-supervision by Professor Bernhard Müller at the Department of Energy and Process Engineering of NTNU, Professor Hans Bihs at the Department of Civil and Environmental Engineering of NTNU and Professor Grégoire Winckelmans at the Institute of Mechanics, Materials, and Civil Engineering (iMMC) of Université Catholique de Louvain (UCLouvain).

Abstract

Energy efficiency is regarded as a key measure to reduce greenhouse gas emissions and minimize the dependency on energy imports. In the European Union, building energy consumption, particularly in heating, represents a significant share of energy usage. Innovative strategies and measures are required to promote energy conservation. Ventilation systems play a crucial role in this scenario, constituting a significant fraction of building energy use. This includes both the electricity consumed by the fans and the heat losses associated with ventilation through the building envelope. Although ventilation consumes energy, its primary purpose is to ensure excellent Indoor Air Quality (IAQ) while directly contributing to the indoor thermal environment and overall comfort within buildings. The significance of IAQ is particularly pronounced in environments such as hospitals or clean rooms, where the effective dispersion of pollutants and prevention of airborne diseases are critical. The advent of the COVID-19 pandemic has increased the importance of understanding airborne diseases, emphasizing the dominant role of indoor spaces in disease transmission.

This Ph.D. thesis aims to facilitate high-resolution Large Eddy Simulation (LES) for indoor airflow. A numerical framework is implemented and tested by adapting an existing flow solver initially developed for hydrodynamic simulations, namely REEF3D. REEF3D is an incompressible flow solver based on staggered orthogonal grids. It can simulate the fluid-solid interaction of rigid moving structures within a viscous fluid using Immersed Boundary Method (IBM). To adapt REEF3D, a new low-dispersion central scheme for the convective term is required to perform explicit LES on staggered grids. This scheme is developed, implemented and validated in this thesis. The new finite difference scheme (HCDS6) conserves the discrete mass and momentum with limited production or dissipation of discrete kinetic energy. The performance of the numerical approach

is evaluated on viscous and inviscid flow simulations conducted on both uniform and non-uniform grids. First, a set of benchmark test cases without IBM is selected, such as the convection of an isentropic vortex, 3D Taylor-Green vortex flow and simulation of turbulent channel flow. The results indicate that the proposed scheme is more accurate than the standard second-order scheme. Moreover, it has a numerical stencil that is more compact compared to existing fourth-order kinetic energy-conserving schemes, which makes its implementation and the treatment of boundary conditions easier.

In the second validation, two additional benchmark test cases are introduced to assess the capabilities of the numerical approach in scenarios where the IBM is employed. These cases include two generic benchmark test cases: the flow past a wall-attached cube and steady non-axisymmetric flow past a sphere. The findings indicate that the IBM can accurately capture the detached flow around an object, whether it has a smooth slope (such as a sphere) or sharp edges (like a wall-mounted cube).

Finally, the potential of the framework is investigated for contaminant breach in isolation rooms with a sliding door. This containment failure due to airflows induced by sliding door movement is a critical concern, particularly in healthcare facilities. Traditional hinged doors exacerbate this issue, making sliding doors an attractive alternative. The study employs Computational Fluid Dynamics (CFD) simulations using the LES approach to predict detailed airflow patterns during sliding door operations. An improved version of a continuous, direct forcing Immersed Boundary Method is used for modeling a rigid sliding door. It is based on an implicit representation of the body on a stationary grid using a level set function. This test case demonstrates that IBM can simulate moving objects for airflow inside buildings. The findings can provide practical knowledge for healthcare facility design and overall occupant safety.

An inherent challenge of IBM is to accurately represent high Reynolds number flows. Therefore, for further work, wall functions should be implemented in REEF3D, with a thorough investigation into their impact on the solution.

Acknowledgment

As I approach the completion of my Ph.D. journey, I want to express my deep gratitude for the invaluable support and guidance that have brought me to this significant milestone.

First and foremost, I want to express my deepest gratitude to my main supervisor, Professor Laurent Georges, for giving me an interesting research topic and enabling me to explore many possibilities in this field. Despite his demanding schedule, he consistently made time for meetings, offering valuable advice and encouraging feedback on my work progress. His expertise and mentorship have been invaluable in shaping the trajectory of my work.

I extend my sincere appreciation to my co-supervisors – Professor Grégoire Winckelmans, Professor Hans Bihs, and Professor Bernhard Müller. I gratefully acknowledge their support, contributions, and boundless patience throughout this extensive research journey. Their collective expertise and commitment to my growth as a researcher have been a continuous source of inspiration. I am truly grateful for the collaborative effort of this exceptional team, which has significantly contributed to the successful completion of this research endeavor.

To my friends both here in Trondheim and back home—especially Iman Bayat, Milan Malhotra, Masab Khalid Annaqeeb, Mohammad Liravi, Tomáš Fečer, Yang Bi, Yiyu Ding, Jakub Wladyslaw Dziejczak, Sadjed Alboghobeish and Milad Naeimaei Aali, I am grateful for the tolerant attitudes, support and kindness you provided during my four-year research. Your presence has made Trondheim feel like a second home, adding a lot of joy and enrichment to my journey.

I would like to thank my office mates, Xingji Yu and Vegard Heide, for their support, discussion, and wonderful moments during our time together. Our cozy

"brain center" was the hub for moments where we shared wisdom and humor and occasionally pondered the mysteries of the universe—one cup of coffee at a time.

The foundation of this Ph.D. project would not have been possible without the exceptional resources and collaborative environment provided by NTNU. The access to cutting-edge technology, the support of fellow researchers, and the vibrant intellectual atmosphere have all played a crucial role in shaping the course of my research.

The global COVID-19 pandemic, which emerged just six months into this journey, brought unexpected challenges and uncertainties. In the face of this adversity, the collective resilience of the academic community and the support of my supervisors were crucial in maintaining momentum and focus.

Finally, across the vast distance of thousands of kilometers, my parents and dear brother have been my sources of support and love. Despite the pixelated screen of video calls connecting us, I longed for the warmth of their hugs and the reassuring strength of their presence. Their encouragement and belief in my journey have been the cornerstone of my resilience.

This Ph.D. project has been a result of years of dedication, and collaborative effort. With a heart full of gratitude, I extend my deepest appreciation to everyone who has been a part of this remarkable journey and with whom I have had the pleasure of collaborating.



Elyas

List of publications

List of international journal and conference articles appended in this thesis:

- Paper I.** Elyas Larkermani, Guangyu Cao and Laurent Georges. “Characterization of the density-driven counter-flow through a doorway using Large Eddy Simulation”. In: *Building and Environment* 221 (2022), p. 109319.
- Paper II.** Elyas Larkermani, Hans Bihs, Grégoire Winckelmans, Matthieu Duponcheel, Tobias Martin, Bernhard Müller and Laurent Georges. “Development of an accurate central finite-difference scheme with a compact stencil for the simulation of unsteady incompressible flows on staggered orthogonal grids”. In: *Computer Methods in Applied Mechanics and Engineering* 428 (2024), p. 117117.
- Paper III.** Elyas Larkermani, Hans Bihs, Grégoire Winckelmans, Bernhard Müller, Laurent Georges. “High-fidelity explicit Large Eddy Simulations of airflows inside buildings using the immersed boundary method and orthogonal grids”. In: *Journal of Building Engineering*. Submitted.
- Paper IV.** Elyas Larkermani and Laurent Georges. “Analysis of the interfacial mixing in the gravity-driven counterflow through a large vertical opening using Large Eddy Simulation”. In: *International Conference Organised by IBPSA-Nordic, 13th–14th October 2020, OsloMet. BuildSIM-Nordic 2020. Selected papers*. SINTEF Academic Press. 2020.
- Paper V.** Elyas Larkermani, Vegard Mikkelsen Bjerke and Laurent Georges. “Comparing the performance of RANS turbulence models between different cavity flow benchmarks”. In: *Proceedings ROOMVENT*

CONFERENCE. 16TH 2022. (ROOMVENT 2022)(2 PARTS) Item#: 065443 Held 16-19 September 2022, Xi'an, China. EDP Sciences. 2022

Paper VI. Simon Bjuri, Elyas Larkermani and Laurent Georges. “Influence of the Inlet Boundary Conditions on the LES Performance for the Cavity Flow Benchmark”. In: *Proceedings ROOMVENT CONFERENCE. Stockholm, Sweden. Apr. 2024*

Declaration of Authorship

In the three international journal articles and the conference articles appended to this thesis, the thesis author was the main contributor and responsible for developing the numerical method, validations, simulation setups, analyses and paper writing. The co-authors contributed by supervising and critically reviewing the corresponding parts of the work.

Contents

Abstract	iv
Acknowledgment	vi
List of Publications	viii
List of Figures	xiii
List of Tables	xvii
1 Introduction	1
1.1 Background and Motivation	1
1.1.1 Indoor Air Quality and Health Concerns	2
1.2 Research Objectives and Scope	2
1.3 Research Goal and Thesis Outline	5
2 Literature Review	9
2.1 Indoor Airflow Simulation	9
2.1.1 Indoor Airflow Simulation Using RANS	11
2.1.2 Indoor Airflow Simulation Using LES	13
3 Potential of LES for Indoor Airflow Simulations	15
3.1 Simulation of Cavity Flow Benchmarks using RANS and LES	16
3.1.1 Description of the Cavity Flow Benchmarks	16
3.1.2 Governing Equations and Numerical Setup	18
3.1.3 Results and Discussion	20
3.2 Density-driven Bidirectional Flow through a Large Vertical Doorway	25
3.2.1 A Counter-flow Passing Through an Opening	26
3.2.2 Methodology	27
3.2.3 Results and Discussion	30
3.3 Key Takeaways	35

4	High Fidelity LES on Orthogonal Grids	37
4.1	High-Fidelity LES for Indoor Airflow Simulations	37
4.2	Higher-order Numerical Schemes on Orthogonal Grids	39
4.3	Why Orthogonal Grids?	41
5	Development of a Numerical Framework tailored for Explicit LES on Staggered Orthogonal Grids	45
5.1	Adapted Incompressible Flow Solver for Cartesian Nonuniform Meshes	45
5.2	Numerical Method	47
5.2.1	Governing Equations	48
5.2.2	Spatial Discretization	48
5.2.3	Temporal Integration	58
5.2.4	SGS Turbulence Model	61
6	Validation and Verification	63
6.1	Benchmark Test Cases without IBM	64
6.1.1	Convection of an Isentropic Vortex	64
6.1.2	3D Taylor-Green Vortex Flow	67
6.1.3	Simulation of Turbulent Channel Flows	72
6.2	Benchmark Test Cases with IBM	83
6.2.1	Flow Past a Wall-attached Cube	84
6.2.2	Steady Non-axisymmetric Flow Past a Sphere	86
7	LES of the Contaminant Breach in Isolation Rooms with a Sliding Door	89
7.1	Isolation Rooms with a Sliding Door	89
7.1.1	Vortical Structures	91
7.1.2	Air Volume Migration	94
7.1.3	Passive Scalar Concentration	95
8	Conclusions and Outlook	99
8.1	Main Achievements	99
8.2	Future Work and Perspectives	101
	Bibliography	105
A	Appendix	119
A.1	Paper I	119
A.2	Paper II	137
A.3	Paper III	159

A.4 Paper IV	188
A.5 Paper V	199
A.6 Paper VI	206

List of Figures

1.1	Interlinked Research Papers Mapping the Trajectory Towards Thesis Objectives.	7
3.1	IEA Annex 20 test room [34]. The measurement lines in benchmarks 1 and 2 are two vertical lines and two horizontal lines in red.	17
3.2	Normalized velocity and temperature profiles for benchmark 1 (left column), benchmark 2 (middle column) and benchmark 3 (right column).	20
3.3	Normalized velocity profiles for benchmark 4 at a Reynolds number of 1000.	21
3.4	Velocity profiles of RANS using the standard $k - \varepsilon$ model, DES and LES with a turbulence intensity of 50% at the CFD inlet for the fully turbulent benchmark.	24
3.5	Velocity profiles of RANS using the standard $k - \omega$ model, DES and LES for the transitional benchmark at a Reynolds number of 1000.	25
3.6	Velocity profiles of RANS using the BSL $k - \omega$ model, DES and LES for the transitional benchmark at a Reynolds number of 2500.	26
3.7	Streamwise velocity profiles (left) and re-entrainment by cross-stream interfacial mixing (right) for the bidirectional flow in a doorway.	27
3.8	Three-dimensional multizone enclosure configuration ($H \times W \times D = 8 \times 16 \times 8 m^3$).	29
3.9	Instantaneous velocity magnitude in the doorway $y - z$ plane (left) and on an $x - z$ plane at the middle of the door (right).	32
3.10	Time-averaged temperature (a,b) and streamwise velocity (c,d) profiles along a vertical line in the middle of the doorway. The thick blue and red lines in the thermally stratified case (b) indicate the vertical profiles of measured air temperature in the cold and warm zones, respectively.	33

3.11	Mean temperature with streamlines on the vertical plane ($y = 0$). A dashed black box highlights a region where the re-entrainment of warm airstream occurs.	35
5.1	Staggered arrangement of variables in two dimensions.	49
5.2	Comparison of the numerical stencil for HCDS6 (a) and CDS4 (b) for $i = 1$ and $j = 2$	52
5.3	Non-dimensional modified wavenumber (a), phase velocity (b), and group velocity (c) for $a = 1$ with CDS2, CDS4, and HCDS6.	58
6.1	Convection of strong isentropic vortex on a uniform grid: grid dependence of the Root-Mean-Square value of difference with the analytical solution at the time $u_\infty t/L = 37.5$. (a): velocity component u , (b): velocity component v	65
6.2	y velocity component along the midline at $y = 0$. Left: coarse grid ($\Delta x = L/2$), Right: fine grid ($\Delta x = L/4$).	66
6.3	Temporal evolution of the volume-averaged kinetic energy.	69
6.4	Temporal evolution of the dissipation rate based on kinetic energy.	70
6.5	Instantaneous vorticity norm from the pseudo-spectral scheme on the periodic plane ($y = 0$) at $t/t_c \approx 9$	70
6.6	Iso-contours of the vorticity norm on the periodic plane ($y = 0$) at $t/t_c \approx 9$. The spectral solution is in black and the finite difference is in red.	72
6.7	Mean streamwise velocity normalized by the DNS shear velocity (a), non-dimensional mean total Reynolds shear stress (b), mean normalized square root of the second-order velocity moments (c) (u_{rms} (top), v_{rms} (middle), w_{rms} (bottom)) for the DNS of turbulent channel flow at $Re_\tau = 180$	75
6.8	Mean streamwise velocity normalized by the DNS shear velocity for the TNS of turbulent channel flow at $Re_\tau = 180, 640, 950$ and 2000	77
6.9	Non-dimensional mean total Reynolds shear stress for the TNS of turbulent channel flow at $Re_\tau = 180, 640, 950$ and 2000	78
6.10	Velocity fluctuations in streamwise (u_{rms} , top), wall-normal (v_{rms} , middle) and spanwise (w_{rms} , bottom) direction as a function of the distance to the wall (y^+) for the TNS of turbulent channel flow at $Re_\tau = 180, 640, 950$ and 2000	79
6.11	Mean cell Reynolds number based on vorticity ($Re_\Delta - \omega$) and strain term ($Re_\Delta - S$) as a function of the distance to the wall (y^+) for the TNS of turbulent channel flow at $Re_\tau = 180, 640, 950$ and 2000	81

6.12	Mean streamwise velocity normalized by the DNS shear velocity (a), non-dimensional mean total Reynolds shear stress (b), mean normalized square root of the second-order velocity moments (c) (u_{rms} (top), v_{rms} (middle), w_{rms} (bottom)) for the LES of turbulent channel flow at $Re_\tau = 640$	83
6.13	Time-averaged streamwise velocity contours with mean flow streamline around a wall-attached cube at $Re_H = 500$. Left: $x - y$ plane, right: $x - z$ plane. The color scale for \bar{u} spans from $-0.1U_\infty$ in dark blue to $1.1U_\infty$ in dark red for the left column and $0.2U_\infty$ in dark red for the right column.	86
6.14	Streamlines of projected streamwise velocity for a flow past a sphere at $Re_D = 250$	88
7.1	The geometry of the isolation room and anteroom connected via a sliding door.	90
7.2	Contours of the vertical component of vorticity $(\nabla \times u)_z$ at the end of door opening stage.	93
7.3	Time evolution of the AVM during the sliding door operation cycle.	94
7.4	Contours of the passive scalar concentration at six different door opening stages using CDS2 (left) and HCDS6 (right).	97

List of Tables

3.1	Cavity flow benchmark description.	18
3.2	Grid size based on grid sensitivity analysis.	19
5.1	Coefficients for semi-implicit Runge-Kutta method.	60
6.1	Comparison of the execution time of the CDS2 and HCDS6 for the convection of an isentropic vortex.	67
6.2	Channel flow mesh resolution at $Re_\tau = 180$	74
6.3	Computational domain size and mesh densities for TNS of channel flow at $Re_\tau = 180, 640, 950$ and 2000	76
6.4	Computational domain size and mesh densities for LES of channel flow at $Re_\tau = 640$	82
6.5	Computational domain size and mesh resolution for DNS of the wall-attached cube.	84
6.6	Positions of stagnation points for the mean flow around the wall-attached cube immersed in a laminar boundary layer.	86
6.7	Drag and lift coefficients for a flow past a sphere at $Re_D = 250$	87

Acronyms

AVM Air Volume Migration. xv, 94, 95

BPS Building Performance Simulation. 9

CFD Computational Fluid Dynamics. iv, xiii, 2, 4, 9–12, 22, 24, 27–29, 45, 63, 90, 100

CFL Courant–Friedrichs–Lewy. 91, 101

DES Detached Eddy Simulation. xiii, 14, 23–26

DHIT Decaying Homogeneous Isotropic Turbulence. 80, 81

DNS Direct Numerical Simulation. xiv, xvii, 10, 14, 39, 47, 51, 68, 69, 73–80, 82–85, 100

FFD Fast Fluid Dynamics. 10

FTT Flow-Through Time. 74

HIT Homogeneous Isotropic Turbulence. 80

HPC High-Performance Computing. 12, 29, 63

IAQ Indoor Air Quality. iii, 2, 5

IBM Immersed Boundary Method. iii, iv, 4–6, 38, 41–47, 64, 83–88, 95, 99–102

LDA Laser Doppler Anemometry. 11, 16

- LES** Large Eddy Simulation. iii, iv, xiii, xv, xvii, 2–6, 13–16, 23–27, 29–39, 42, 43, 47, 59, 68, 75, 80–83, 90, 91, 95, 99, 100, 102
- MPI** Message Passing Interface. 29, 46
- MWNA** Modified Wave Number Analysis. 55
- NP** Neutral Plane. 27, 28, 30, 31, 33, 34
- NS** Navier–Stokes. 10, 23, 48, 50, 61, 84
- RANS** Reynolds-Averaged Navier-Stokes. xiii, 2–5, 11–16, 18, 22–27, 29, 32–36, 43, 99, 102
- RK** Runge-Kutta. 5, 46, 47, 59, 74
- RMS** Root-Mean-Square. xiv, 64, 65, 100
- RNG** Re-Normalisation Group. 4, 12, 16, 19–22, 29
- RSM** Reynolds Stress Model. 11
- SGS** SubGrid-Scale. 3, 4, 13, 15, 23, 29, 38, 39, 42, 47, 61, 62, 80–83, 90
- SHC** Solar Heating and Cooling. 9
- SIMPLE** Semi-Implicit Method for Pressure Linked Equations. 19, 29
- SST** Shear-Stress Transport. 4, 12, 16, 19, 20, 22, 23
- TNS** Truncated Navier-Stokes. xiv, xvii, 75–82
- TVD** Total Variation Diminishing. 46, 47
- UDF** User Defined Function. 30
- URANS** Unsteady Reynolds-Averaged Navier-Stokes. 30, 90
- WALE** Wall-Adapting Local Eddy-viscosity. 3, 29, 42, 61, 62, 82, 90
- WENO** Weighted Essentially Non-Oscillatory. 46, 47

List of Symbols

Scalar quantities are typically represented by normal symbols, while vector and tensor quantities are denoted by boldface symbols.

Dimensionless Groups

Pr Prandtl number

Pr_{SGS} SubGrid-Scale Prandtl number

Re Reynolds number

$Re_{\Delta} - \omega$ Cell Reynolds number based on the vorticity norm

$Re_{\Delta} - S$ Cell Reynolds number based on the norm of strain rate tensor

Re_{τ} Frictional Reynolds number

Re_{θ} Reynolds numbers based on the momentum thickness

Re_{δ^*} Reynolds numbers based on the displacement thickness

Sc_t Turbulent Schmidt number

Greek Symbols

α Thermal diffusivity

α_t Turbulent thermal diffusivity

α_{SGS} SubGrid-Scale thermal diffusivity

β	Thermal expansion coefficient
Δ	Grid spacing
δ^*	Displacement thickness
ϵ	Kinetic energy dissipation
γ	Stretching factor
ν	Kinematic viscosity
ν_t	Turbulent kinematic viscosity
ν_{SGS}	SubGrid-Scale kinematic viscosity
ω	Vorticity
ϕ	Generic discrete quantity
ρ	Density
ζ	General spatial coordinate in a computational domain
θ	Momentum thickness

Roman Symbols

S	Resolved scale strain rate tensor
u	Velocity field
x	General spatial coordinate in a physical space
<i>a</i>	Constant advection velocity
<i>C</i>	Tracer mass concentration
C_D	Drag coefficient
C_L	Lift coefficient
C_s	Smagorinsky constant
C_w	WALE coefficient
<i>E</i>	Total kinetic energy
<i>g</i>	Gravitational acceleration

J	Jacobian determinant of the coordinate transformation
k	Wave number
L	Characteristic length
N	Total number
p	Static pressure
T	Temperature
t	time
U	Characteristic velocity
u, v, w	Cartesian velocity components
u^*	Intermediate velocity
U^+	Normalized mean streamwise velocity
u_τ	Shear velocity
V	Volume
x, y, z	Cartesian coordinates
y^+	Dimensionless distance to the wall

Introduction

1.1 Background and Motivation

The building industry has emerged as a focal point for the implementation of energy-saving strategies, given its significant contribution to overall energy consumption. Ventilation is important for maintaining a healthy and safe indoor environment in buildings. However, the operation of ventilation systems demands energy input. To enhance energy efficiency, ventilation systems can be designed based on both natural and mechanical forces. In this respect, natural ventilation methods present a valuable alternative. Understanding the complexities of natural ventilation within multizone enclosures has attracted significant attention due to its direct influence on crucial aspects of indoor environments. This includes the distribution of indoor air contaminants, room air circulation patterns, and thermal comfort within buildings.

The dynamic nature of natural ventilation flow presents a multifaceted challenge. Unlike mechanical ventilation, which is externally driven by fans, natural ventilation arises from density differences, wind forces, occupant movements, or even the motion of doors. When the flow is primarily driven by thermal buoyancy, it is often termed "density-driven", "temperature-driven" or "gravity-driven". It is this complex interplay of physical forces that highlights the importance of comprehensive studies in natural ventilation strategies, ultimately paving the way for sustainable and energy-efficient building design.

1.1.1 Indoor Air Quality and Health Concerns

Ensuring Indoor Air Quality (IAQ) is a critical imperative, with a growing emphasis on the continuous improvement of advanced ventilation strategies. Nowhere is this more crucial than in environments such as hospitals, clean rooms, and public transportation, where the dispersion of contaminants and pollutants must be carefully controlled. The advent of the COVID-19 pandemic has intensified the interest in understanding and mitigating the airborne transmission of viruses and contaminants. This has highlighted the need for robust IAQ measures to safeguard public health.

Indoor airflow modeling has become a key tool in building design and engineering. Designers now have the capacity to simulate and analyze the complexities of air circulation within indoor spaces, allowing for a detailed evaluation of proposed ventilation strategies. This proactive approach not only helps meet established thermal comfort standards but also ensures that IAQ criteria are met from the outset of the design process. By using indoor airflow modeling, designers can make informed decisions about ventilation system designs, placements, and configurations. This sets the stage for environments that optimize both comfort and health.

One key aspect linked to ventilation efficiency is the distribution of air and the dispersion of contaminants within a room. In this respect, Computational Fluid Dynamics (CFD) serves as a dominant simulation tool, employing a numerical approach to solve the governing flow equations. Turbulence, a complex flow phenomenon, is challenging to model. The popularity of CFD has been gained by significant developments in numerical methods, turbulence modeling techniques and the remarkable enhancement of computational capabilities in terms of both speed and capacity [1]. Moreover, reliable results require a balance between accuracy and cost-effectiveness. Achieving sufficiently detailed results should not come at the expense of excessive financial and labor costs. Hence, different turbulence modeling approaches, such as the Reynolds-Averaged Navier-Stokes (RANS) and Large Eddy Simulation (LES), have been devised. Despite the superiority of LES in terms of accuracy, its computational demands are substantially higher, keeping RANS as the prevailing method for indoor airflow prediction.

1.2 Research Objectives and Scope

In this section, we outline the specific objectives that guide our investigation and provide a comprehensive overview of the scope of our research. The primary aim of this study is to advance the understanding and application of a solver optimized

for orthogonal non-conformal grids for indoor airflow simulations. It is important to emphasize that the developed method is specifically designed for indoor airflows. As outlined by Blocken [2], a clear distinction should be made between indoor and outdoor airflows. The significance of accurately capturing boundary layers becomes more pronounced in outdoor airflows, potentially making body-conformal grids more suitable for such scenarios. The objective of this study is not to assert the superiority of the current approach over widely-used general-purpose flow solvers such as ANSYS Fluent or OpenFOAM across all indoor airflow applications. These tools should be considered as alternatives, each with its own merits and limitations. Nevertheless, the study clearly highlights the benefits of the proposed framework, particularly in the context of high-resolution LES, transitional flows, and scenarios involving moving objects. The research objectives can be summarized as follows:

1. Gain better knowledge of the Potential of LES for indoor airflow simulations:
 - Evaluate the potential of LES to provide a more accurate representation of indoor airflow dynamics with turbulence models that are less dependent on the specific application and flow regime (i.e., more universal). The focus is on two airflow scenarios of key importance for ventilation applications: the cavity flow and the density-driven flow through a doorway.
 - Compare the prevalent two-equation RANS turbulence models to Dynamic Smagorinsky or WALE SubGrid-Scale (SGS) models to understand the performance of LES in capturing complex airflow phenomena.
 - Gain better knowledge of the requirements of the simulation setup for high-resolution LES, including spatial discretization and mesh considerations.
2. Adaptation of an existing flow solver to perform Large Eddy Simulation of indoor airflows on orthogonal grids:
 - Develop an adaptation of the REEF3D solver [3], originally designed for hydrodynamics applications, to suit the specific requirements of accurate LES for indoor airflow.
 - Explore the flexibility of the adapted solver and identify key parameters that contribute to its optimization.
3. Advantages of orthogonal grids and spatial discretization:

- Investigate and clarify the advantages offered by orthogonal grids in the context of spatial discretization.
 - Assess the accuracy and performance gains achieved through optimized spatial discretization on orthogonal grids, particularly in comparison to conventional central schemes.
4. Transitional flows and validation of Immersed Boundary Method (IBM):
- Evaluate the capability of the proposed framework to accurately capture transitional flows in indoor environments.
 - Validate the performance of the IBM strategy through the simulations of detached flows around objects with varying geometries, including both smooth slopes and sharp edges.
5. Simulation of moving objects and practical applicability:
- Explore the simulation capabilities of moving objects, demonstrated through the sliding door test case, to assess the practical applicability of the framework.
 - Investigate the method's ability to handle moving objects without resorting to complex re-meshing techniques, with a focus on real-world applications and varying airflow dynamics.

To achieve these objectives, the following research questions are formulated:

- Research Question 1: What are the specific requirements and considerations in terms of simulation setup, including grid structure and inlet boundary conditions, to conduct high-resolution LES for the cavity flow benchmark and the density-driven bidirectional airflow through a doorway, and how do these requirements differ from those of RANS simulations in the same scenarios?
- Research Question 2: How do different RANS turbulence models, including standard $k - \varepsilon$, RNG $k - \varepsilon$, and SST $k - \omega$, perform in accurately simulating indoor airflow characteristics under various flow regimes, and what are the limitations of these models in capturing inherently unsteady flow phenomena within building science?
- Research Question 3: To what extent is the performance of SGS models in LES influenced by the different flow regimes, compared to various RANS turbulence models, considering factors such as inlet boundary conditions and other parameters influencing CFD solutions?

- Research Question 4: How does the adapted REEF3D solver perform in the context of indoor airflow simulations, and what are the key parameters influencing its optimization?
- Research Question 5: What specific advantages do orthogonal grids offer in terms of spatial discretization accuracy, and how do they compare to conventional schemes with non-orthogonal grids?
- Research Question 6: Can the proposed framework accurately capture transitional flows in indoor environments, and how does it perform under coarser mesh resolutions?
- Research Question 7: To what extent does the IBM contribute to the simulation of detached flows around objects with different geometries, and how effectively does it handle moving objects, such as the sliding door test case?

1.3 Research Goal and Thesis Outline

This thesis is organized into eight main chapters, each contributing to a better understanding of the performance and requirement of LES for airflow inside buildings and to introduce an adapted solver optimized for orthogonal non-conformal grids in the context of indoor airflow simulations. The thesis is built on six main papers, including three conference papers and three journal papers. Figure 1.1 represents how the six papers are linked toward achieving the research goal.

In chapter 1, the background and motivation for the study are discussed. Emphasis is placed on the critical importance of IAQ and the associated health concerns. A comprehensive review of the existing approaches for indoor airflow simulation is presented in chapter 2. The advantages and limitations of both RANS and LES approaches are discussed. Chapter 3 focuses on the potential of LES in indoor airflow simulations. The chapter begins with an analysis of cavity flow benchmarks, comparing simulations using both RANS and LES (Papers V and VI). Moreover, the density-driven bidirectional flow through a large vertical doorway is examined (Papers IV and I). The significance behind using orthogonal grids, along with the higher-order numerical schemes to perform high-fidelity LES is discussed in chapter 4. Chapter 5 presents a detailed account of the development of a numerical framework tailored for explicit LES on staggered orthogonal grids. The REEF3D flow solver is adapted based on the proposed numerical framework by implementing an improved spatial discretization scheme and a low-dissipative semi-implicit Runge-Kutta scheme. Chapter 6 is dedicated

to the validation and verification of the proposed framework. Benchmark test cases, both with and without the IBM, are extensively examined. The focus is on assessing the accuracy and reliability of the numerical framework across various scenarios (Papers II and III). The application of LES to simulate the contaminant breach in isolation rooms with a sliding door is investigated in chapter 7. The vortical structures, air volume migration, and passive scalar concentration shed light on the practical application of the developed framework (Papers III). The final chapter 8 provides an overview of the main achievements, recognizes the limitations of the scope, and outlines potential directions for future research and development in the field.

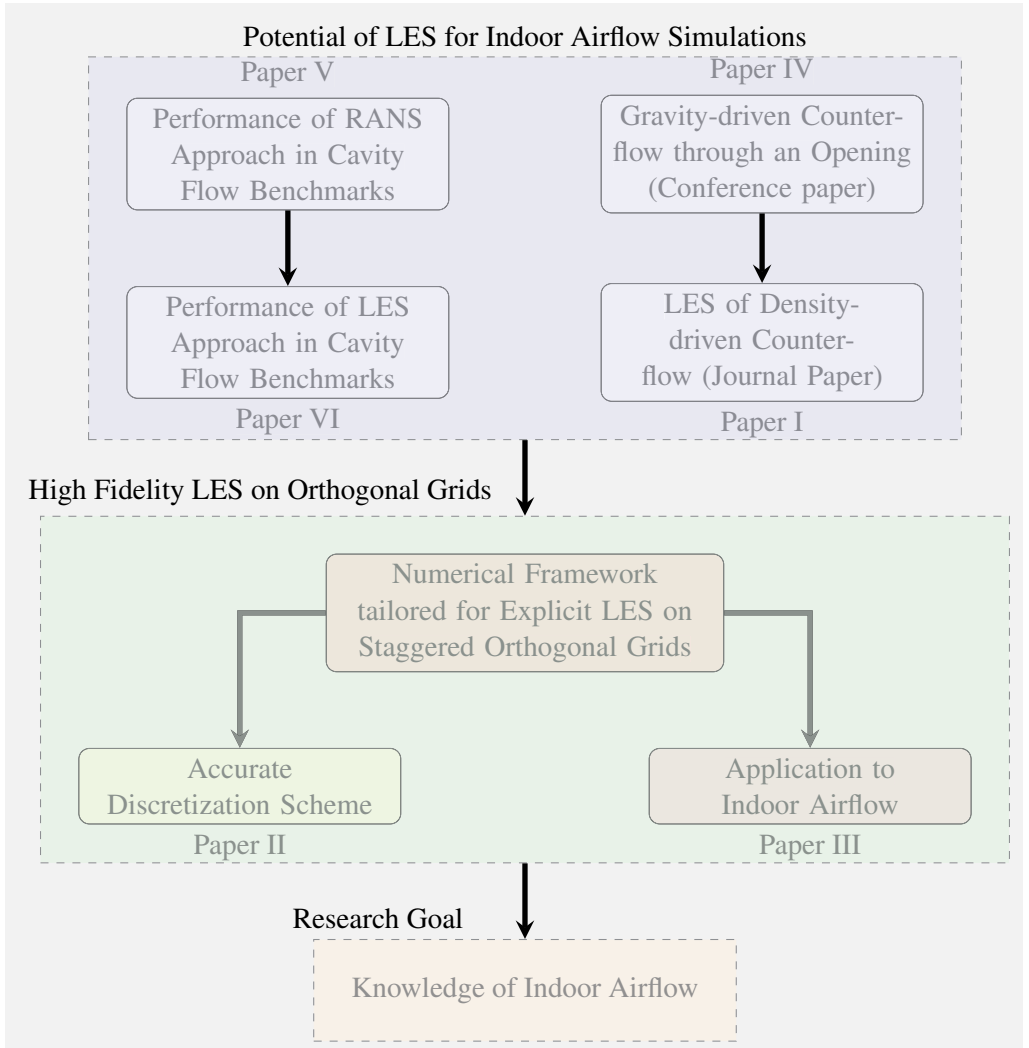


Figure 1.1: Interlinked Research Papers Mapping the Trajectory Towards Thesis Objectives.

Literature Review

2.1 Indoor Airflow Simulation

Diverse modeling and simulation techniques have been extensively employed to delve into the complexities of airflow dynamics within buildings. Moreover, they can facilitate the design of effective ventilation and Solar Heating and Cooling (SHC) strategies [4]. However, it is important to note that there exists a wide variety of modeling methodologies, each with its own set of assumptions and capabilities. In Building Performance Simulation (BPS) tools, which encompass widely used software packages like IDA-ICE, EnergyPlus and TRNSYS, conventional room models typically do not account for airflows inside the room. In these room models, air velocity is not computed, and temperature as well as pollutant concentrations are assumed to remain uniform within each room. Instead, the focus is on computing airflows between rooms or towards the outdoor environment, achieved through the ventilation network approach [5]. While these approaches may seem simplistic, they have proven effective in addressing many specific flow-related challenges, particularly in supporting the design of natural ventilation systems.

To further refine our understanding of airflow patterns within buildings, two alternative approaches have gained prominence: zonal models and Computational Fluid Dynamics. Zonal models involve a trade-off between the simplicity of conventional room models in BPS and the computational rigor of CFD [6, 7]. They involve subdividing a room into a limited number of control volumes, where semi-empirical principles enable the computation of fluxes between these volumes. As an alternative, zonal models can also leverage simplified CFD

techniques, such as coarse grid CFD or Fast Fluid Dynamics (FFD) [8]. While these zonal models are not computationally expensive, it is important to note that they are not universally applicable. Their effectiveness relies on careful validation for specific applications and may exhibit limitations when applied beyond their validated scope. Consequently, for a comprehensive and versatile analysis of airflows within buildings, CFD stands out as the preeminent simulation tool.

CFD modeling has emerged as a popular method for analyzing fluid flow phenomena, owing to its ability to provide instructive results and its cost-effectiveness. At the heart of CFD lies the mathematical representation of a fluid flow problem through a system of coupled nonlinear partial differential equations, inherently based on the Navier–Stokes (NS) equations [9]. These equations encapsulate the governing principles of fluid dynamics, including the conservation of mass, momentum, and energy. However, while they can be solved analytically for relatively simple and straightforward geometries, more complex conditions necessitate a numerical approach.

To accurately simulate indoor airflow using the Navier–Stokes equations, Direct Numerical Simulation (DNS) necessitates the explicit resolution of the full range of turbulence scales. DNS achieves this by precisely solving for all spatial and temporal variations, providing a comprehensive snapshot of the flow field. This level of detail not only serves as an invaluable reference solution but also affords an in-depth understanding of the underlying flow physics, making it an essential tool in fundamental research. While DNS offers unparalleled precision in representing flow fields by resolving the entire spectrum of spatial and temporal scales, its computational demands are extremely high. The computational cost associated with DNS is a critical consideration. The total computational cost increases dramatically with the Reynolds number raised to the third power (Re^3). This exponential growth renders DNS impractical for flows characterized by high Reynolds numbers, a limitation particularly pronounced in aeronautical applications. In building airflow, where Reynolds numbers may vary widely depending on the specific conditions, DNS has traditionally been viewed as a method reserved for fundamental research rather than practical applications.

With the steady advancement of computational power, there is a compelling argument to reassess the applicability of DNS in certain building airflow scenarios. In cases involving generic airflows like jets, bidirectional airflows through large vertical openings or plumes [10], as well as a fraction of the room space with specific functionalities, so-called micro-environments, DNS is no longer as prohibitive as it once was. The typical smallest eddies in such scenarios, ranging from 1 to 10 millimeters, necessitate a substantial number of computational points. In practice, DNS may now be feasible with a billion points,

representing a significant leap forward for research applications in building airflow analysis.

2.1.1 Indoor Airflow Simulation Using RANS

The Reynolds-Averaged Navier-Stokes (RANS) approach stands as a cornerstone in CFD, particularly in the context of turbulence modeling. By time-averaging the governing equations of fluid motion, the well-known Reynolds stress tensor emerges as a pivotal component [2]. To establish a closed system of equations, a large array of turbulence models has been developed. In RANS turbulence modeling, a clear distinction is made between the time-averaged flow field computed on the mesh and the modeled turbulent fluctuations. This approach has found widespread use across various applications, including the complex airflow dynamics within buildings.

In the early 1970s, pioneering efforts were initiated to predict airflow within buildings using computational techniques. Nielsen, a trailblazer in this field, established the groundwork for simulating indoor airflow using CFD [11, 12]. Faced with the computational limitations of the time, Nielsen initiated his work with a 2D simulation of room airflow. He compared the computed velocity profiles with experimental hot-wire measurements obtained from various locations within the room. As the field advanced, Nielsen further refined his approach. By the end of 1978, he used the standard $k - \varepsilon$ turbulence model to solve the 2D Reynolds-Averaged Navier-Stokes equations, conducting comparative studies with Laser Doppler Anemometry [13]. Later, Nielsen considered the energy equation in his simulations to account for buoyancy effects in room ventilation flow [14]. Based on this initial groundwork, Nielsen and his colleagues extended their calculation methodology to include 3D isothermal ventilation simulations [15].

Parallel efforts in the early days of CFD saw Murakami and Kato conducting a 3D RANS simulation, employing the standard $k - \varepsilon$ model to explore various room configurations [16]. Likewise, Awbi utilized a similar turbulence model to simulate a wall jet interacting with obstacles within a room [17]. The contributions of researchers like Jones and Whittle solidified the potential of CFD in building environment design [18]. They emphasized the need for careful application of CFD to obtain optimal results. They noted that the standard $k - \varepsilon$ model is a suitable candidate for simulating indoor airflow and highlighted situations where more advanced models, like the full Reynolds Stress Model (RSM), might be needed. Specifically, RSM could be considered in cases of non-isotropic turbulence, where the $k - \varepsilon$ model cannot provide sufficient resolution of airflow at higher expenses and computational time.

The impact of the different turbulence modeling on airflow predictions within buildings using the RANS approach was evaluated by Barbason[19]. Through a series of evaluations, employing models like the Re-Normalisation Group (RNG) $k - \varepsilon$ model, the Shear-Stress Transport (SST) $k - \omega$ model, and the Spalart-Allmaras turbulence model, it was revealed that these models often yield similar results, with no significant differences observed at the design stage.

One of the notable advantages of the RANS approach lies in its computational efficiency. Airflows within confined indoor spaces can be accurately computed using RANS models with meshes comprising millions of computational points or even fewer. This makes the process feasible on standard personal computers or compact workstations, eliminating the need for specialized High-Performance Computing (HPC) resources. Among the prevalent turbulence models employed for modeling airflows in buildings, the two-equations turbulence models, such as the $k - \varepsilon$ model, have gained significant popularity. These models, which account for both turbulence kinetic energy (k) and its dissipation rate (ε), find a balance between computational accuracy and computational cost.

However, it is essential to accept the inherent limitations of the RANS approach. Although proficient in representing the time-averaged behavior of turbulent flows, this approach inevitably encounters challenges in accurately simulating some complex unsteady flow phenomena. This discrepancy arises from the need to rely on turbulence models to represent the unsteady and chaotic nature of turbulence. For example, in building airflow simulations, selecting the most appropriate turbulence model becomes a critical consideration. The RNG $k - \varepsilon$ model, known for its robust performance, is frequently preferred for accurately simulating building airflows. In contrast, the Realizable $k - \varepsilon$ model may be more suitable when modeling plumes, as specific flow characteristics in such scenarios demand a tailored turbulence model [20]. Therefore, the accuracy of RANS simulations in building applications is widely recognized to be contingent on the expertise of the user [20, 21]. This expertise spans from the ability to generate an appropriate mesh to the wise selection of the suitable RANS turbulence model tailored to the specific application. A RANS model aligns with a given application once its performance has been rigorously validated against reference solutions or benchmarks within the same category of airflows. As such, it serves as a powerful predictive tool for applied research and industrial applications. However, RANS turbulence models are not universal. Some unsteady flow phenomena pose significant challenges or may even be captured properly using the RANS modeling approach [2]. This recognition stresses the value of high-fidelity CFD, where a more limited portion of the flow physics is modeled, particularly within building science.

2.1.2 Indoor Airflow Simulation Using LES

Large Eddy Simulation (LES) is a powerful computational technique that offers a distinct advantage in capturing the complex dynamics of turbulent flows. Unlike RANS simulations, which rely on modeling the entire range of turbulent eddies, LES takes a different approach. It distinguishes the larger turbulent eddies that exceed the grid size and explicitly resolves them while simultaneously employing models to represent the smaller eddies that fall below the mesh resolution. This dual approach makes LES inherently unsteady, as it accurately resolves the eddies that contain the majority of the kinetic energy within the flow. Notably, the behavior of large eddies in turbulent flows is influenced by geometric features, while the smaller scales exhibit a more universal behavior. This distinction enables LES models, referred to as SubGrid-Scale (SGS) models, to be more flexible and applicable across a wide range of flow scenarios compared to RANS turbulence models.

One of the key strengths of LES is its ability to capture phenomena like detached flows and situations where turbulence-induced mixing has a dominant influence. Additionally, LES provides a direct prediction of turbulent intensity, enabling it to be employed in scenarios where the flow exhibits transitional characteristics [22] or has not fully developed [23]. This flexibility positions LES as a valuable tool for simulating airflow within complex environments, especially in cases where unsteady or transitional behavior plays a critical role.

The pioneering work of Sakamoto and Matsuo in 1980 marked a significant milestone in the application of LES to simulate airflow within buildings [24]. Their innovative study demonstrated a strong agreement between LES results and empirical measurements, providing a robust validation for this computational approach in a controlled model room setting. Based on this initial progress, researchers in the mid-1980s, including Hibi [25] and Murakami [26], performed three-dimensional simulations for recirculating flow. Their detailed comparisons between simulation results and experimental data provided a valuable benchmark for understanding the capabilities and limitations of LES in capturing complex indoor airflow patterns.

Nielsen conducted a thorough comparison of turbulence modeling approaches [27]. He emphasized that LES has the potential to yield highly detailed information about airflow. Additionally, he noted that the $k - \varepsilon$ turbulence model finds its strength in modeling stratified flows and scenarios with low Reynolds numbers, particularly in applications related to near-surface treatment. While the potential of LES was evident, challenges persisted. In 2001, Chen et al. identified a lack of comprehensive LES applications in indoor environment modeling,

primarily attributing it to the computational power requirements [28]. Nonetheless, they held a positive perspective, expecting rapid advancements in computer processing speed coupled with the introduction of advanced numerical methods. These advancements, they believed, would position LES as a powerful tool for solving the complexities of indoor airflow.

Sørensen and Nielsen have emphasized that LES demonstrates better agreement with experimental data, particularly in cases of non-fully developed turbulent flow [29]. Their assessment of LES as a valuable tool highlights its potential in the near future, again with the increasing availability of computational resources and enhanced processing speeds. Furthermore, Zhai et al. conducted a comprehensive review of turbulence modeling approaches, including RANS, LES, and Detached Eddy Simulation (DES), for predicting airflow patterns within enclosed environments [20]. Their findings concluded that there is no universally preferred turbulence model for indoor airflow simulation. The selection of an appropriate modeling approach depends on computation time and desired accuracy. They also advocated for LES as a more precise and detailed model than the RANS approach. However, they recognized its current status primarily as a research tool due to high computational demands and dependency on user knowledge.

It is worth noting that previous investigations into LES application were conducted with relatively limited computational grid points, raising a valid question about the validity of comparisons between RANS and LES approaches [30]. In a study by Van Hooff et al., focused on indoor airflows, LES exhibits superior performance compared to RANS in assessing cross ventilation [31]. However, it should be noted that the grid resolution required near the walls is comparable to that of DNS. This specific type of LES, known as wall-resolved LES, demands mesh resolutions based on inner viscous wall scaling, leading to a substantial increase in computational effort as the Reynolds number rises [32]. Therefore, it presents a significant constraint, rendering it impractical for numerous applications, including design purposes.

Potential of LES for Indoor Airflow Simulations

To unlock the full potential of LES as a practical tool in understanding and optimizing indoor environments, its potential is extensively assessed in this chapter. This forms a basis to justify the legitimacy of LES using orthogonal non-conformal grids. This investigation is initiated with a comprehensive evaluation of the performance of RANS turbulence models in different cavity flow benchmarks representative of mixing ventilation. It is shown that RANS turbulence models, despite their widespread use, exhibit limitations in uniformly performing well across all benchmarks in different flow regimes. Overall, the dependence on the flow regime can make the use of RANS approach less reliable during the ventilation design phase.

The study is further extended by comparing the performance of LES and RANS on two isothermal cavity flow benchmarks in transitional and fully turbulent flow regimes. Through a comprehensive analysis, LES using the Dynamic Smagorinsky SGS model behaves as a universal tool to predict the ventilation performance of mixing ventilation in buildings. It reproduces the velocity field for both flow regimes, but the results are strongly dependent on the turbulence level at the airflow inlet. The outcomes of these simulations highlight the need for more knowledge of the turbulence intensity at the air inlets, which may not be a straightforward task during design.

After identifying the limitations of RANS models, the focus is shifted toward LES, recognizing its potential as a more robust candidate for accurate indoor

airflow predictions. The shift towards LES is motivated by its capability to resolve finer turbulent structures and its application to a broader range of flow regimes. To validate this transition, high-resolution LES of density-driven counter-flow through a doorway is performed—a scenario with direct implications for ventilation and heat distribution between rooms in buildings. The results show that unsteady RANS is a good alternative to the resource-intensive LES if the analysis of turbulent jets is not of interest.

In summary, this chapter not only highlights the limitations of RANS models but also reveals the potential offered by LES for indoor airflow simulations. The insights gained from these simulations serve as a basis for the subsequent focus on high-fidelity LES on orthogonal non-conformal grids.

3.1 Simulation of Cavity Flow Benchmarks using RANS and LES

In the first paper [33], the performance of RANS two-equation eddy viscosity models in four different cavity flow benchmarks representative for mixing ventilation at both transitional and fully turbulent regimes is evaluated.

3.1.1 Description of the Cavity Flow Benchmarks

A cavity flow represents an airflow in an empty ventilated space where an attached wall jet is discharged into the room along the ceiling (Figure 3.1). With a sufficiently high inlet velocity, the jet impinges the opposing wall and deflects into the cavity zone. The separation of the boundary layer close to the top corner of the room generates a recirculation region in the enclosure. The four cavity flows differ by the geometry aspect ratio, the airflow regime and thermal effects (i.e., isothermal and non-isothermal cases). The first benchmark, called the IEA Annex 20 test room, is isothermal. The experimental measurements were carried out by Nielsen et al. [34] using Laser Doppler Anemometry (LDA). The slot Reynolds number is 5000, indicating a fully turbulent room airflow. Since its creation, multiple attempts [35–39] have been made to reproduce the airflow pattern and velocity profile of this cavity flow using the prevailing turbulence models for indoor airflows such as $k - \varepsilon$, RNG $k - \varepsilon$, $k - \omega$ and $k - \omega$ SST. The dimension of the computational domain is defined in Table 3.1.

Benchmark 2 has a same geometry as benchmark 1 but with a different aspect ratio (Table 3.1). The experimental data are reported by Nielsen [12] in his Ph.D. thesis for both isothermal and non-isothermal conditions. The isothermal flow was measured with hot wire anemometry, and measurements were done only at a vertical line $x = 2H$. The benchmark is simulated here for a Reynolds number of

7100 in isothermal mode.

In benchmark 3, a slightly different geometrical configuration compared to benchmarks 1 and 2 is adopted as the width is considerably smaller than the length and height (Table 3.1). So, inlet and outlet openings have a smaller area than the previous ones. The flow is non-isothermal. In the experiments done by Blay et al. [40], the setup has two guard cavities to make the side walls adiabatic. The walls were made of aluminum and kept at a constant temperature using temperature-controlled water (with a precision of $0.25\text{ }^{\circ}\text{C}$). The floor is kept at a constant temperature of $35.5\text{ }^{\circ}\text{C}$, while the remaining three walls have a temperature equal to the inlet temperature of $15\text{ }^{\circ}\text{C}$. A uniform velocity profile of 0.57 m/s is imposed at the inlet, leading to a Reynolds number of 684 based on the inlet height. Velocity measurements were done using Laser Doppler Velocimetry (LDV) and temperature measurements with Cr-Al thermocouples.

Benchmark 4 is a cubical cavity without buoyancy effects (Table 3.1). The experiment was done by van Hooff et al. [41] at two different Reynolds numbers, 1000 and 2500, representing a transitional flow. The working fluid was water, and the velocity field was measured with a 2D PIV system.

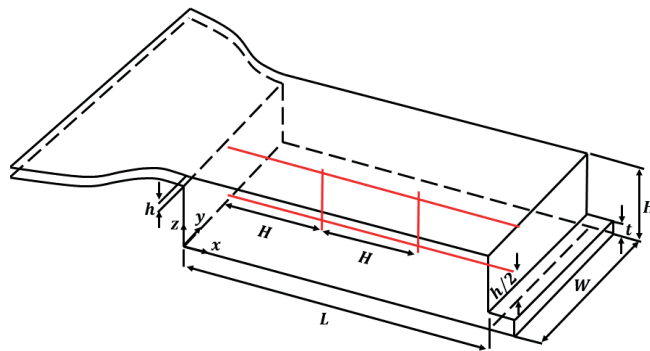


Figure 3.1: IEA Annex 20 test room [34]. The measurement lines in benchmarks 1 and 2 are two vertical lines and two horizontal lines in red.

Benchmark	1	2	3	4
Re at inlet	5000	7100	684	1000/2500
Flow regime	Fully Turbulent	Fully Turbulent	Unknown	Transitional
Thermal effects	Isothermal	Isothermal	Non-Isothermal	Isothermal
L/H	3	3	1	1
W/H	1	4.7	0.288	1
h/H	0.056	0.056	0.0173	0.1
t/H	0.16	0.16	0.0231	0.0167
H [m]	0.0893	0.127	1.04	0.3

Table 3.1: Cavity flow benchmark description.

3.1.2 Governing Equations and Numerical Setup

The airflow field in a cavity is computed using the Reynolds-Averaged Navier-Stokes equations for the mass, momentum and energy conservations where the Reynolds stresses have been modeled using an eddy viscosity:

$$\frac{\partial \bar{u}_j}{\partial x_j} = 0 \quad (3.1)$$

$$\frac{\partial \bar{u}_i}{\partial t} + \frac{\partial \bar{u}_i \bar{u}_j}{\partial x_j} = -\frac{1}{\rho_{\text{ref}}} \frac{\partial \bar{p}}{\partial x_i} + \frac{\partial}{\partial x_j} \left[(\nu + \nu_t) \frac{\partial \bar{u}_i}{\partial x_j} \right] + \beta g_i (\bar{T} - T_{\text{ref}}) \quad (3.2)$$

$$\frac{\partial \bar{T}}{\partial t} + \frac{\partial \bar{u}_j \bar{T}}{\partial x_j} = \frac{\partial}{\partial x_j} \left[(\alpha + \alpha_t) \frac{\partial \bar{T}}{\partial x_j} \right] \quad (3.3)$$

where the bar represents the time averaging, x_i denotes the i^{th} spatial coordinate direction, \bar{u}_i represents the time-averaged velocity field in the x_i direction, t the time, \bar{p} the time-averaged static pressure, and \bar{T} the time-averaged temperature. The effect of buoyancy forces is taken into account using the Boussinesq approximation where $\beta = 1/T_{\text{ref}}$ is the thermal expansion coefficient of the air modeled as an ideal gas and g_i the gravitational acceleration. The parameters ν and α are the kinematic viscosity and thermal diffusivity, respectively. Turbulent kinematic viscosity and thermal diffusivity are defined with the subscript t .

After conducting a grid sensitivity analysis for each benchmark, a structured orthogonal mesh is selected based on a trade-off between accuracy and computational cost. An overview of the grid size adopted for each benchmark is provided in Table 3.2. All meshes have been constructed to have y^+ less than five on the walls to resolve the boundary layers. The turbulence model that showed good convergence in previous studies is selected for grid analysis. The inlet turbulent intensity is set to match the experimental value.

Benchmark	1	2	3	4
Geometry	3D	3D	3D	3D
Number of cells	342000	1771000	189000	1214000
Inlet turbulent intensity	4%	5%	6%	6%
Turbulence model	Standard $k - \varepsilon$	Standard $k - \varepsilon$	RNG $k - \varepsilon$	SST $k - \omega$

Table 3.2: Grid size based on grid sensitivity analysis.

The nonlinear governing equations are discretized using a second-order cell-centered finite volume method implemented in the ANSYS Fluent commercial CFD package. The Semi-Implicit Method for Pressure Linked Equations (SIMPLE) algorithm is employed for pressure-velocity coupling. The time derivatives are advanced in time using the “Second Order Implicit” scheme. The “Second Order Upwind” scheme is adopted for the treatment of the convective terms of the governing equations. The pressure interpolation is provided by the “Second Order” scheme. “Enhanced wall treatment” has been used as the default wall modeling option. The no-slip boundary condition is applied to all walls.

All benchmarks are run in steady-state mode. However, the averaging technique introduced by Blocken [42] is applied when fluctuations of the residuals and other physical quantities (such as the drag coefficients on the floor or ceiling) are detected. In this technique, the solution is averaged over many iterations to get a statistically independent solution. The number of iterations required is case-dependent and must be investigated for each benchmark. The convergence criteria for all simulations are fulfilled when the absolute residuals drop down to 10^{-6} , and the drag coefficient on the ceiling and floor walls reaches stable values.

3.1.3 Results and Discussion

The performance of six turbulence models, the standard $k - \varepsilon$, RNG $k - \varepsilon$, realizable $k - \varepsilon$, AKN low-Re $k - \varepsilon$, standard $k - \omega$ and the $k - \omega$ SST, is shown for the four benchmarks in Figures 3.2 and 3.3.

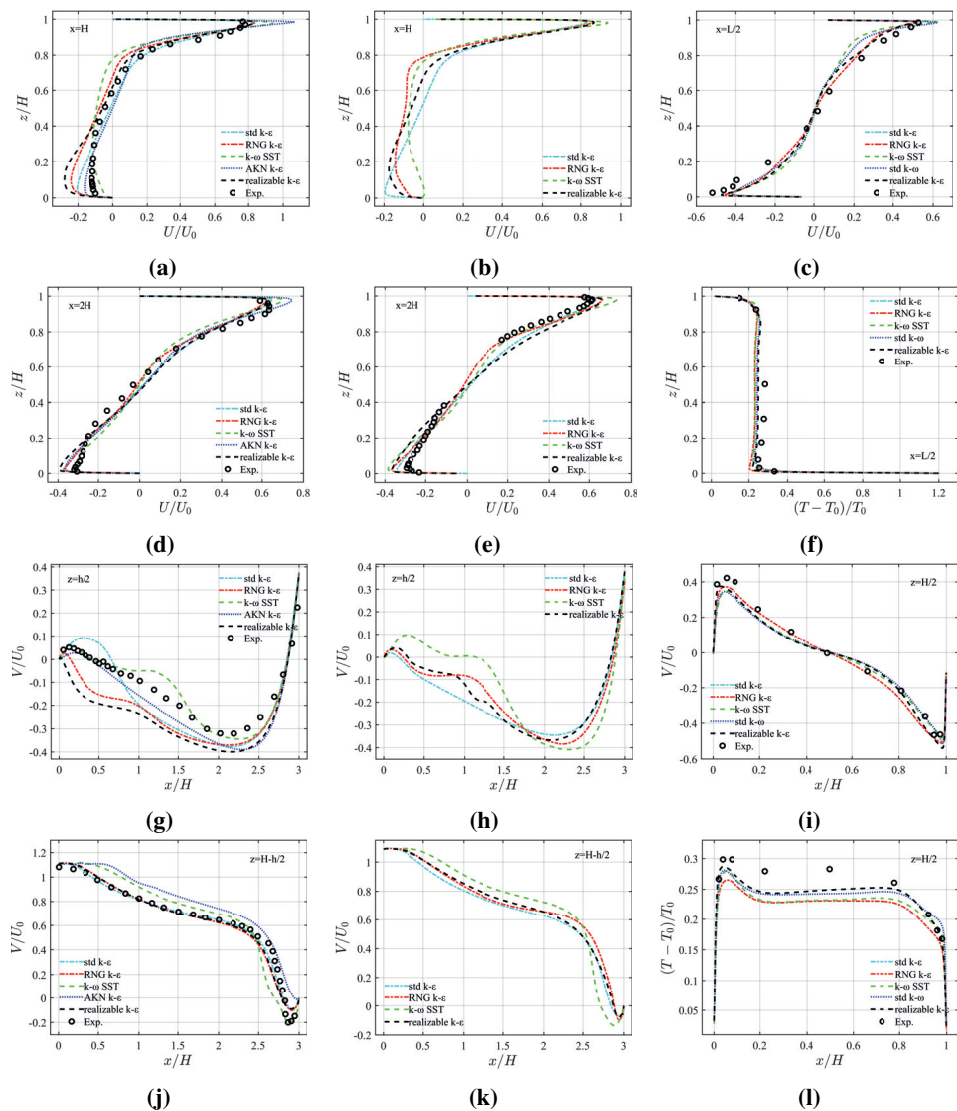


Figure 3.2: Normalized velocity and temperature profiles for benchmark 1 (left column), benchmark 2 (middle column) and benchmark 3 (right column).

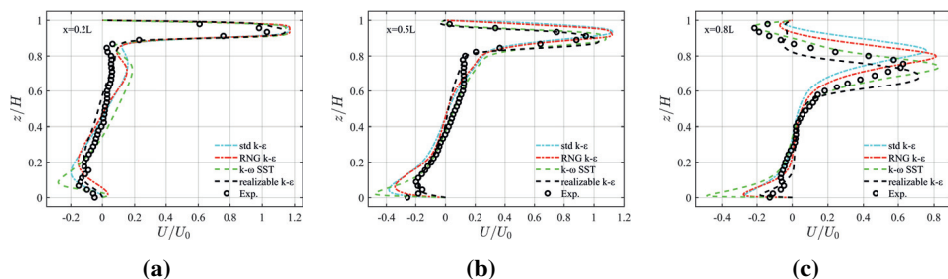


Figure 3.3: Normalized velocity profiles for benchmark 4 at a Reynolds number of 1000.

Benchmarks 1 and 2

The distribution of the normalized streamwise velocity component along the cavity height at two vertical lines ($x = H$, $x = 2H$) is plotted in Figures 3.2(a), 3.2(d), 3.2(b) and 3.2(e). The negative velocities in the lower part of the cavity are evidence of a substantial air recirculation region inside the cavity. Figures 3.2(g), 3.2(j), 3.2(h) and 3.2(k) show normalized vertical velocity distribution along two horizontal lines ($z = h/2$, $z = H - h/2$) in the mid-plane. None of the turbulence models achieves a perfect fit of the experimental data. In particular, in Figure 3.2(g), simulation results differ remarkably from experiments. From this figure, the RNG and realizable $k - \epsilon$ turbulence models cannot correctly predict the flow direction on the cavity's left part. In other words, solutions from these models have a different flow pattern than experiments in this part of the cavity. The most apparent differences between the turbulence models can also be found in the lower-left corner of the cavity, i.e., the left part of Figures 3.2(g) and 3.2(h). Turbulence models struggle to model the flow in this part of the cavity because the flow may be dominated by the transitional regime and have anisotropic behavior. Figures 3.2(a) and 3.2(d) also reveal a noticeable deviation between the turbulence models regarding the jet velocity along the floor and ceiling.

Benchmarks 3

Profiles of normalized velocity and temperature along a vertical centerline ($x = L/2$) are depicted in Figures 3.2(c) and 3.2(f) as well as along a horizontal centerline ($x = H/2$) in Figures 3.2(i) and 3.2(l). Since simulations gave oscillatory residuals, the results were averaged over 2000 iterations for each model. According to Figures 3.2(c), 3.2(f), 3.2(i) and 3.2(l), all turbulence models predict fairly accurately the flow pattern. However, the maximum velocity for the jet along the ceiling is overestimated by two $k - \omega$ models. Moreover, all models underestimate the jet velocity along the floor and left wall under the inlet. Although the air temperature along the cavity walls is in good agreement with

measurement data, it is underpredicted by all models inside the recirculation zone due to insufficient air mixing (Figures 3.2(f) and 3.2(l)). The realizable $k - \varepsilon$ model reproduces experimental data better than other turbulence models, whereas the $k - \omega$ SST model is relatively less successful.

Benchmark 4

Normalized velocity profiles from standard $k - \varepsilon$, RNG $k - \varepsilon$, realizable $k - \varepsilon$, and $k - \omega$ SST turbulence models at three vertical lines ($x = 0.2L, 0.5L, 0.8L$) are compared with the experimental results at a Reynolds number of 1000 in Figures 3.3(a) to 3.3(c). Using the $k - \omega$ SST model, the location of the detachment of the jet can be predicted quite well (Figure 3.3(c)). The other models predict detachment further away from the inlet. Right above the floor, a large discrepancy with measurement data can be observed in the velocity profile at all three lines. However, no conclusion can be drawn due to reflections from the glass floor leading to inaccurate measurements. For all three lines, each model appears to overpredict the maximum jet velocity. The $k - \omega$ SST shows the best performance, while the standard $k - \varepsilon$ has the largest deviation from experiments.

Cross Comparison

It can be concluded that none of the turbulence models perform equally well for all benchmarks, so none of the models seem universal. This highlights the importance of selecting a suitable turbulence model based on specific case requirements, e.g., according to the flow regime. The key findings are as follows:

- Generally, a good agreement is found between CFD results and measurements that validate the use of CFD for the prediction of airflows in buildings.
- The standard $k - \varepsilon$ model is the most accurate for benchmarks 1 and 2. In addition, the results obtained using the standard $k - \varepsilon$ model are consistent with the literature. The standard $k - \varepsilon$ model is thus a good choice when simulating indoor airflows with fully turbulent characteristics without large pressure gradients.
- The deviation from the experimental measurements in the area below the inlet in benchmarks 1 and 2 may be attributed to the anisotropy of the transitional flow present in that region because RANS eddy-viscosity models cannot be taken into account the flow anisotropy.
- All three $k - \varepsilon$ models provided the best agreement with experiments in benchmark 3, whereas the $k - \omega$ SST model was clearly superior to the

$k - \varepsilon$ models for benchmark 4. Benchmark 4 has larger pressure gradients along the wall jet. The poor results of $k - \varepsilon$ models are primarily caused by an incorrect determination of the location of jet detachment, so they should be used with caution for transitional flows. The standard $k - \varepsilon$ model gave the worst results. The $k - \omega$ SST model performs better in the transitional flow regime with pressure gradients and jet impingement.

LES vs RANS for Benchmarks 1 and 4

Taghinia et al. [43] and Zasimova et al. [44] also investigated LES approaches on benchmark 1. Taghinia et al. employed a custom-made SGS model on a mesh with 4 million cells and obtained good results. Zasimova et al. used wall-modeled LES (WMLES) with up to 48 million cells and got relatively good results except for the backflow region. In both cases, the meshes were refined near the walls and at the junction of the inlet jet with the air in the cavity. Both research groups conducted a separate LES of a periodic channel flow to recreate turbulence at the inlet of the cavity before performing the LES of the cavity itself. Van Hooff et al. [45] tested out LES on benchmark 4 with a Reynolds number of 2500, using the dynamic Smagorinsky model on a mesh similar to their previous study [46]. The findings indicated that LES outperformed the RANS model for this specific case.

In the second paper [47], the performance of LES and DES approaches are compared with RANS turbulence models on the cavity flow benchmarks, covering both fully turbulent and transitional flow regimes as documented by Nielsen [34] and Van Hooff et al. [41], respectively. The objective is to assess whether a single turbulence model can accurately predict both test cases and whether it could consistently be applied to solve other cavity flows without prior knowledge of the flow regime, making the model more universal. Special care is given to the inlet boundary conditions for LES and DES.

The governing equations for LES are the filtered incompressible Navier–Stokes equations, as extensively detailed in Section 5.2.4. A common SGS model, the Dynamic Smagorinsky model, is used. Furthermore, the performance of DES is also investigated and compared using both the Spalart-Allmaras and realizable $k - \varepsilon$ models. The DES is a method that combines LES and RANS. In the region near the wall, where a high cell count would be required to perform LES, DES employs RANS. On the other hand, in the far-field region where fewer cells are required for LES, DES switches to LES.

For LES and DES, a mesh consisting of 6.8 and 7.3 million cells was utilized for benchmark 1 and 4, respectively. This resolution is sufficient to resolve over 80% of the turbulent kinetic energy, meeting the accuracy requirements for the LES

approach [48]. A time sensitivity analysis determined the optimal time step as 0.1 seconds for benchmark 1. For benchmark 4 with Reynolds numbers of 1000 and 2500, two distinct time steps of 0.025 and 0.01 were adopted, respectively. The airflow in both cases was averaged over a minimum of six flow-through times (FTTs), which was sufficient to obtain converged first-order flow statistics. At the CFD inlet, the turbulence intensity (TI) was equal to 6% and 18%, respectively, for the cases with Reynolds numbers of 1000 and 2500. The numerical settings applied for LES and DES are identical to the RANS simulations, except for the momentum discretization, which is performed using Bounded Central Differencing.

The velocity profiles of the overall best-performing RANS model in a fully turbulent regime, the standard $k - \varepsilon$, are compared with those of the DES realizable $k - \varepsilon$ model and the LES model with a TI of 50% in Figure 3.4. All models provide relatively good predictions of the velocity field when compared to experimental data. LES and DES show superior performance at the line near the floor ($y = 2.919 m$), while the standard $k - \varepsilon$ model yields the best results at the line near the ceiling ($y = 0.084 m$).

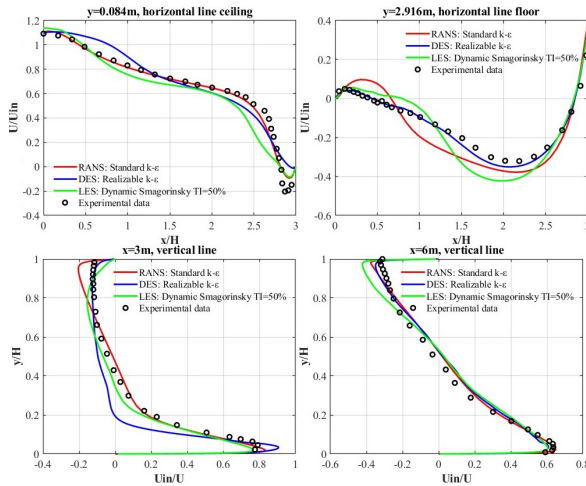


Figure 3.4: Velocity profiles of RANS using the standard $k - \varepsilon$ model, DES and LES with a turbulence intensity of 50% at the CFD inlet for the fully turbulent benchmark.

For the transitional regime at a Reynolds number of 1000, the best-performing RANS model is the standard $k - \omega$, which is compared with DES Spalart-Allmaras and LES, as illustrated in Figure 3.5. The DES model anticipates an early detachment, while the RANS model and LES produce comparable profiles, with the standard $k - \omega$ model slightly outperforming the

LES.

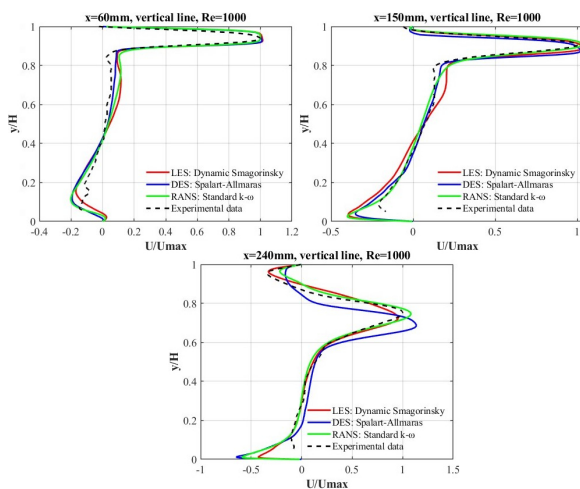


Figure 3.5: Velocity profiles of RANS using the standard $k - \omega$ model, DES and LES for the transitional benchmark at a Reynolds number of 1000.

In the concluding comparison, Figure 3.6 displays the velocity profiles of the top-performing RANS model (BSL $k - \omega$), DES realizable $k - \varepsilon$, and LES. The BSL $k - \omega$ model shows the best performance, whereas DES gives the worst results. For DES, the detachment point is predicted prematurely, leading to an inaccurate velocity profile. The main challenge with DES in transitional cases lies in its difficulty in generating adequate turbulent structures in the flow. This problem may stem from the transition from LES to RANS, which dampens the turbulence structures in the flow, causing an early detachment of the jet from the ceiling. This issue is also evident in the scenario with a Reynolds number of 1000.

The RANS approach suffers from the lack of a universal model that performs well across different turbulent regimes and geometric configurations in cavity flows. For the transitional cases, the $k - \omega$ models outperform the $k - \varepsilon$ models, while the opposite is the case for the fully turbulent benchmark. Therefore, LES emerges as a more versatile approach, enabling the application of the same LES model across diverse cavity flow scenarios with relatively good precision.

3.2 Density-driven Bidirectional Flow through a Large Vertical Doorway

In the third paper [49], the airflow passing through an open doorway is simulated using both high-resolution LES and RANS approaches.

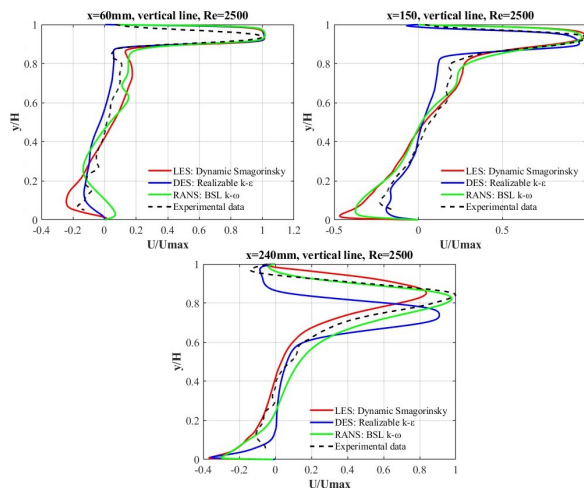


Figure 3.6: Velocity profiles of RANS using the BSL $k - \omega$ model, DES and LES for the transitional benchmark at a Reynolds number of 2500.

3.2.1 A Counter-flow Passing Through an Opening

Airflow through large vertical openings between two enclosures could significantly contribute to the thermal behavior of buildings and the air circulation patterns in a room [50]. The influence of airflow is also determinant in transmitting airborne diseases, such as COVID-19. Hence, correct estimation of doorway flow rates and flow patterns is essential from the airborne contaminant control point of view. Several mechanisms, such as pressure and density differences, occupant movement, and door motion, may drive the airflow through a large vertical opening [51]. In the bulk flow regime, the room air temperature is assumed to be in thermal equilibrium with the wall temperature. The air temperature difference between interconnected rooms leads to different air densities and, consequently, different hydrostatic pressure fields that drive the flow through the door opening. A previous study by Allard et al., IEA EBC Annex 20 [52], demonstrated that the bulk flow regime is dominant in buildings.

The standard theoretical model assumes a bulk flow to compute airflow rates through large vertical openings in airflow networks. It considers two isothermal reservoirs at different temperatures and a one-dimensional inviscid steady-state flow. These assumptions lead to a simple model based on the Bernoulli equation. The resulting maximum theoretical flow is then corrected using the discharge coefficient (C_d) to match the actual airflow in the doorway.

Assuming an inviscid bulk flow through a doorway, the velocity profile shows a

sharp gradient at the level of the Neutral Plane (NP) shown in Figure 3.7(a). With viscous flow, the two airstreams going in opposite directions create a shear layer. In addition, as reported by [53], interfacial mixing between the two airstreams in opposite directions causes a fraction of the warm airflow initially flowing toward the opening to be brought back into the warm zone, entrained by the cold airstream. This re-entrainment effect also takes place for the cold airflow and leads to an exchange of momentum between the two counter-flowing streams passing through a large vertical opening (Figure 3.7(b)). According to these authors, the resulting velocity and temperature profiles are smoother at the level of the NP compared to the inviscid flow.

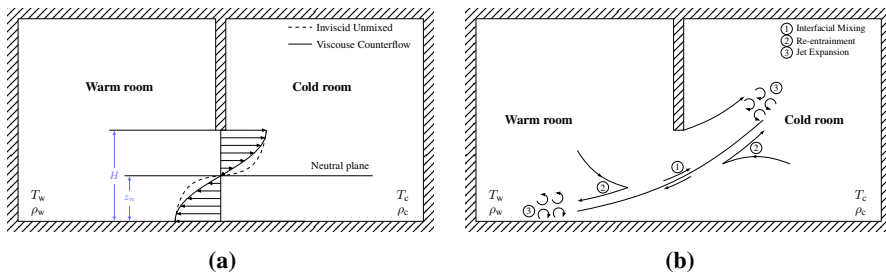


Figure 3.7: Streamwise velocity profiles (left) and re-entrainment by cross-stream interfacial mixing (right) for the bidirectional flow in a doorway.

Several studies have investigated the bulk flow through large vertical openings using CFD. However, these studies did not aim to capture complex unsteady flow phenomena within the doorway as well as the evolution of non-isothermal jets in the adjoining rooms. These studies mainly used unsteady RANS turbulence modeling, and it has not been verified whether the RANS approach is suitable for capturing the instabilities of shear flows in this specific case. Hence, to capture the flow instabilities and characterize flow separation at the opening edge, interfacial mixing between counter-flowing streams and turbulent flow development, a high-resolution LES of the bulk flow passing through the doorway in a pseudo steady-state regime is performed. Moreover, the ability of the RANS method to capture the bulk flow can be investigated by comparing it to the reference LES solution.

3.2.2 Methodology

Experimental Setup

The air temperature difference (ΔT) between warm and cold zones in an interconnected multizone enclosure and the aperture geometry are the only physical parameters needed to define the bulk flow regime. Due to the conservation of mass, hydrostatic pressure fields on both sides of the opening are

equal at the NP located near the middle of the doorway (Figure 3.7(a)). The difference in hydrostatic pressure above and below the NP generates two counter-flowing streams of warm and cold air.

The experiment has been conducted by Paul Minard [54] in a full-scale climate chamber. The environmental chamber consists of two rooms connected by an open doorway with a height of 1.9 m and a width of 0.83 m, located in the middle of the vertical partition wall. The dimensions of the warm and cold rooms are $2.65 \times 2.3 \times 3.8 \text{ m}^3$ and $3.9 \times 7.8 \times 6.9 \text{ m}^3$ ($H \times W \times D$), respectively. The partition wall has a thickness of 0.1 m. Both rooms are equipped with a mechanical ventilation system that is turned off during the experiment. Two electric panel heaters were installed in the warm room far away from the door while the cold room remained unheated. Measurements were taken using ten omnidirectional anemometers (TSI 8475) with an accuracy of $\pm 3\% \pm 0.005 \text{ m/s}$ for air velocity and PT-100 sensors with an accuracy of $\pm 0.1 \text{ }^\circ\text{C}$ for temperature. These sensors were mounted on a vertical bar at the center of the doorway. The sensors were uniformly distributed along the vertical axis (z) from the floor to the top of the door. To minimize the impact of thermal radiation, the surfaces of all PT-100 sensors were coated with aluminum. Temperature stratification within the warm and cold rooms was assessed using five PT-100 sensors mounted on a vertical pole located 2 meters away from the opening. When radiators were turned on, it took several hours to achieve steady-state conditions. Then, data were recorded every 20 seconds over a period of 10-minute. More details regarding the procedure and probe locations can be found in References [54, 55].

Numerical Method

Measurements showed significant temperature stratification in both rooms, especially in the heated room. It is challenging to reproduce the same stratification in CFD. It would require detailed measurements of the surface temperature for both rooms and the heat emitters. Fortunately, measurements revealed that the airflow was in the bulk flow regime. Consequently, the computational domain was defined to enforce this bulk flow regime rather than precisely replicate the laboratory's geometry. In this respect, the rooms were defined considerably larger than the doorway size (Figure 3.8). In addition, the measured temperature stratification is imposed as initial conditions within both reservoirs. At the start of the simulation, when both reservoirs come into contact, a transient flow is established through the doorway until it reaches a pseudo steady-state. The same procedure was followed in the experimental setup of Lefauve et al. [56]. As both rooms are large, the convective heat transfer through the doorway lacks sufficient time to significantly influence the temperature of both reservoirs during the period of physical time computed by the CFD. The

partition wall has the same thickness as the laboratory experiments.

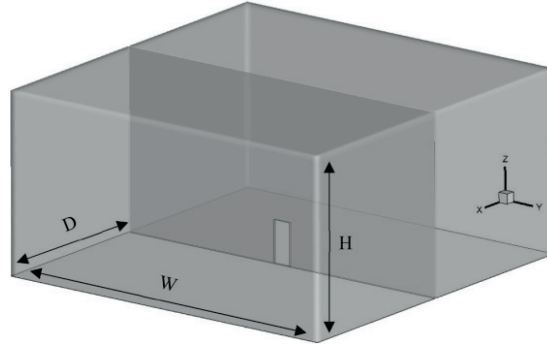


Figure 3.8: Three-dimensional multizone enclosure configuration ($H \times W \times D = 8 \times 16 \times 8 \text{ m}^3$).

The Wall-Adapting Local Eddy-viscosity (WALE) SubGrid-Scale model is used to close the system of equations in the LES approach. The RANS approach is also used here to investigate the influence of turbulence modeling. The widely used RNG $k - \varepsilon$ model for ventilation flow prediction is adopted. The governing equations for this approach are the Reynolds-Averaged Navier-Stokes equations. The nonlinear governing equations are discretized using the second-order cell-centered finite volume method (FVM) implemented in the ANSYS Fluent commercial CFD package. The SIMPLE algorithm is employed for pressure-velocity coupling. The time derivatives are advanced in time using the Second Order Implicit scheme. In the LES, a constant time step of $\Delta t = 0.01 \text{ s}$ is applied to keep the Courant number below 1.0 to achieve high temporal accuracy. For the LES, the Central Differencing scheme is adopted for the treatment of the convective terms of the governing equations, while a Second Order Upwind scheme is used for the RANS and Euler simulations. The pressure interpolation is provided by the Body Force Weighted scheme, recommended by the ANSYS Fluent User's Guide.

ANSYS Fluent is capable of running on distributed processors and uses the public domain Open MPI implementation of the standard Message Passing Interface (MPI) to conduct inter-processor communication. The present LES simulations were performed on the resources provided by Sigma2, the National Infrastructure for High-Performance Computing and Data Storage in Norway. The simulations are performed on a 15-node cluster equipped with multiple 32-core Intel Xeon processors leading to a total of 480 cores and a minimum of 160 GB of RAM.

A structured grid with 127,316,480 hexahedral cells is generated for the interconnected rooms. A refined uniform grid is defined in the vicinity of the

doorway, with the finest elements having a dimension of 0.6 cm to adequately resolve interfacial mixing, re-entrainment, and other unsteady flow phenomena. The aperture area on the $y - z$ plane is covered by 44,800 cells and extruded in the x -direction by 20 cells. A smooth transition between cells of different sizes is performed. The maximum growth ratio of 1.03 is adopted for top corners far enough from the doorway, and 1.008 is used inside a domain of 1.5 m around the doorway.

To keep a constant temperature inside the reservoirs throughout the simulations, all walls, including the partition wall, are assumed to be adiabatic. Slip boundary conditions are applied to each wall. This choice eliminates the need for near-wall grid refinement, as no boundary layer is generated. The bidirectional airflow through the aperture is simulated for the stratified interconnected rooms (baseline case) and isothermal rooms at different temperatures. In the baseline case, the initial temperature is derived from the temperature stratification measured in Paul Minard's experiments [54]. This one-dimensional vertical air temperature profile is applied to the computational domain using a User Defined Function (UDF) hooked into ANSYS Fluent. In the isothermal reservoirs, the initial temperature is derived from the averaged air temperature along the vertical direction (z) in the stratified case. This results in a temperature difference of $1.68\text{ }^{\circ}\text{C}$ ($\Delta T = 1.68\text{ }^{\circ}\text{C}$). The reference temperature (T_{ref}) is determined as the arithmetic average of room air temperatures at the level of the Neutral Plane in the middle of the warm and cold zones. Despite preliminary tests suggesting that initializing the simulation with URANS before switching to LES could partly reduce the initialization time, both enclosures are initialized with zero velocity for simplicity and to ensure that the initialization procedure does not impact the final results. Consequently, each room acts as a large reservoir, and the flow through the door is only driven by differences in hydrostatic pressure between the two reservoirs.

In the initial phase of the simulation, the bidirectional airflow through the doorway is strongly transient. After approximately 60 seconds of physical time, a pseudo-stationary regime is attained. Subsequently, the airflow becomes fully established throughout the enclosure, and the transition to turbulent flow is finalized. During this pseudo-steady state regime ($t > 60\text{ s}$), data are gathered over 40 seconds to achieve fully converged time-averaged statistics. Throughout this period, the volume-averaged air temperature in both reservoirs remains nearly constant.

3.2.3 Results and Discussion

The analysis of results starts with a general description of the flow. Figure 3.9 illustrates the instantaneous velocity magnitude field on the opening plane and

midplane, as computed using LES. As expected, a bidirectional flow is observed. Warm air moves from the warm room (on the left) to the cold room (on the right) in the upper part of the doorway, while cold air flows in the opposite direction in the lower part of the doorway. The bidirectional flow generates a shear layer, inclined by 39° upwards in the middle of the doorway compared to the horizontal plane.

This observation clearly contradicts the assumption of horizontal airflow made by the standard theory. Additionally, both airstreams experience a contraction when expanding into the opposite room, a phenomenon known as the vena contracta effect. This contraction reduces the mass flow through the doorway compared to the standard theory, partly justifying the introduction of a discharge coefficient. The warm airstream develops into a warm jet that expands upwards in the cold zone, while the cold airstream forms an attached cold jet along the floor in the warm zone. Near the middle of the doorway, at the location of the NP, the velocity magnitude is zero.

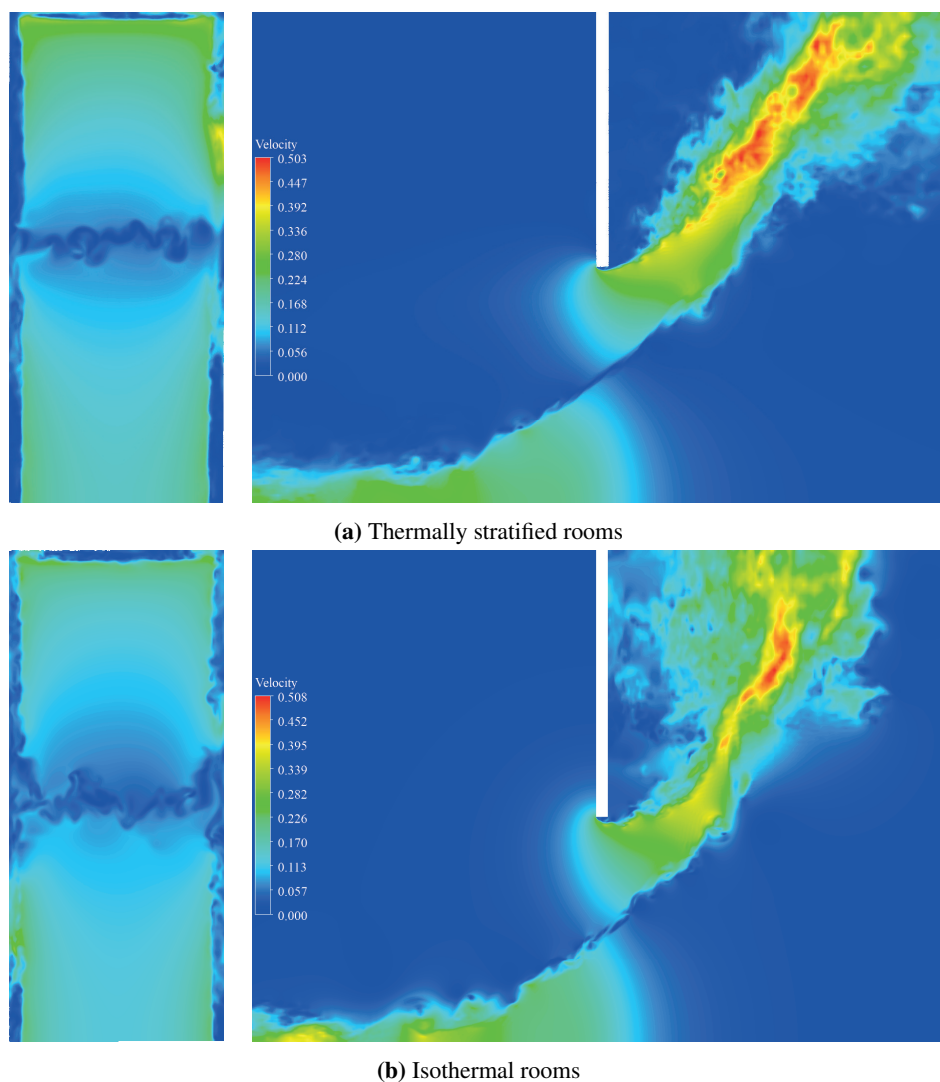


Figure 3.9: Instantaneous velocity magnitude in the doorway $y - z$ plane (left) and on an $x - z$ plane at the middle of the door (right).

Re-entrainment and Shear Layer Mixing

The time-averaged streamwise velocity and air temperature along a vertical line in the middle of the doorway are illustrated in Figure 3.10. The time-averaged streamwise velocity in Figure 3.10(d) computed using LES, RANS, and Euler shows excellent agreement with laboratory measurements, with an average deviation of less than 10%. However, the measured temperature in Figure 3.10(b)

is only qualitatively similar to the LES, RANS, and Euler results. This implies that the time-averaged temperature above the NP progressively moves from the temperature of the cold zone to the temperature of the warm zone over the same distance (from the NP at about $0.9\text{ m} - 1.6\text{ m}$ above the floor).

The transition between the temperature of the warm airstream and the cold airstream provides an indication of the shear layer thickness. Additionally, the shear layer thickness can be evaluated by examining the time-averaged temperature field on the midplane in Figure 3.11.

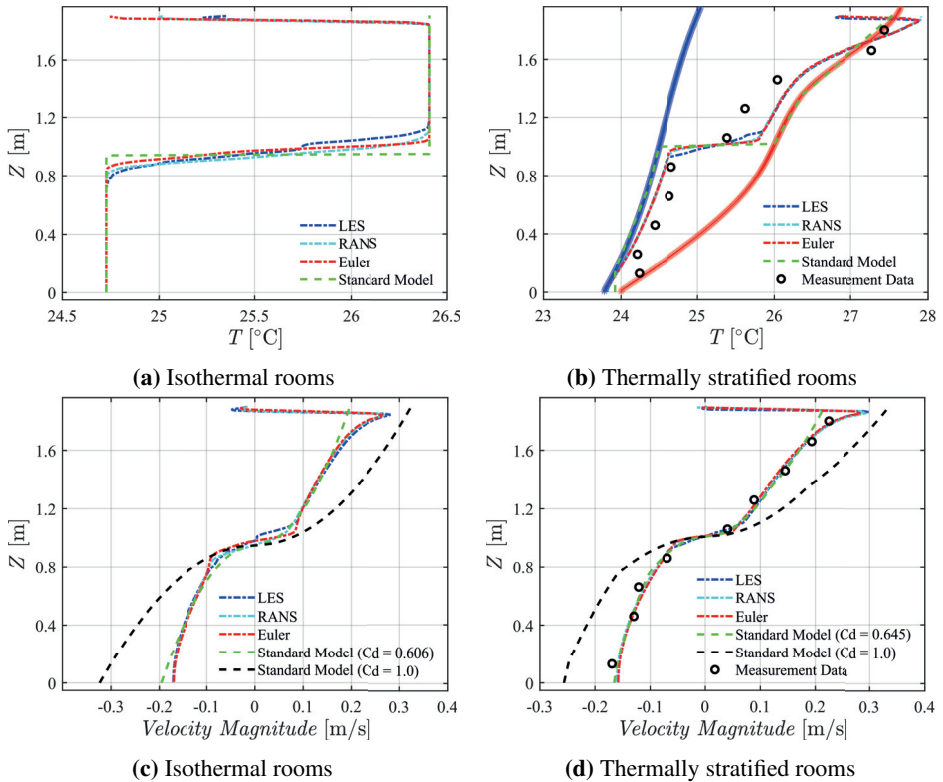


Figure 3.10: Time-averaged temperature (a,b) and streamwise velocity (c,d) profiles along a vertical line in the middle of the doorway. The thick blue and red lines in the thermally stratified case (b) indicate the vertical profiles of measured air temperature in the cold and warm zones, respectively.

Re-entrainment results from interfacial mixing between counter-flowing streams, with a focus on air streams developing into turbulent jets in opposite rooms. The turbulent jets induce entrainment, and the amount of air in the opposite air stream diverted from the doorway by this phenomenon needs to be determined.

Streamlines in Figure 3.11 illustrate that the warm rising jet modifies the airflow direction of the cold air approaching the doorway. This effect is less pronounced for the cold jet expanding in the warm zone. Compared to RANS and Euler, re-entrainment computed by the LES deviates the airflow over a more extensive zone, especially for thermally stratified rooms (highlighted by a dashed rectangle in Figure 3.11). This highlights the significance of re-entrainment in LES and suggests potential underestimation when using RANS.

Analyzing the flow near the NP in Figures 3.10 and 3.11 reveals limited differences between the LES, RANS, and Euler solutions for the baseline case with thermally stratified interconnected rooms, indicating that the shear layer does not induce intense interfacial mixing. In the isothermal interconnected rooms, the Euler and RANS solutions are nearly identical. However, the shear layer generated by the LES for this case is slightly thicker, attributed to the mixing generated by the unsteady flow structures depicted in Figure 3.9. In conclusion, unsteady flow structures do not consistently develop in the middle of the doorway, and if they do, their impact on mixing remains confined to the vicinity of the NP.

A well-resolved LES can accurately capture unsteady flow structures and turbulent mixing. These structures may emerge when turbulent expansion occurs in the cold and warm rooms, particularly when the warm and cold jets become turbulent. Additionally, the LES reveals that the detached flows at the edges of the doorway, originating from both the horizontal head jamb and the vertical side jambs, are unsteady, especially in isothermal rooms. The instantaneous velocity field in Figure 3.9 illustrates the development of various unsteady flow structures, a level of detail that could not be achieved with unsteady RANS simulations.

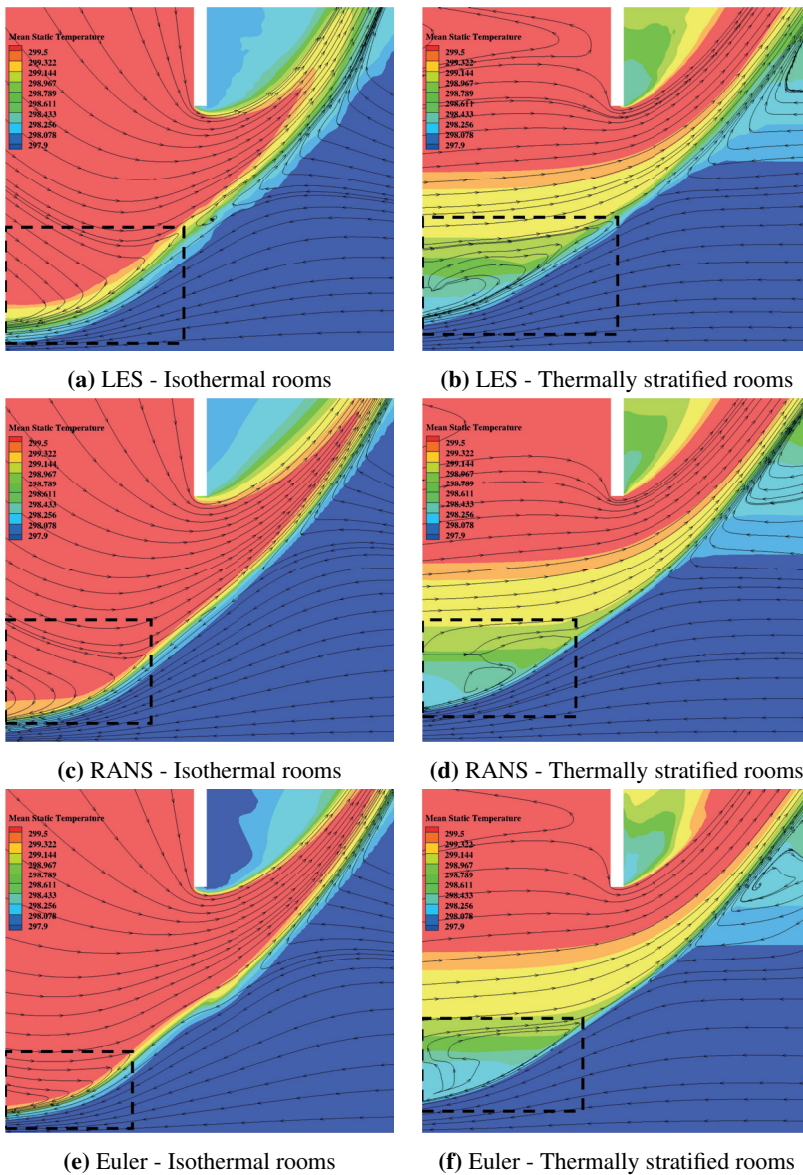


Figure 3.11: Mean temperature with streamlines on the vertical plane ($y = 0$). A dashed black box highlights a region where the re-entrainment of warm airstream occurs.

3.3 Key Takeaways

The performance of RANS and LES approaches were compared using two flow benchmarks relevant for indoor environments in buildings: the cavity flow and

density-driven flow through a doorway.

In the case of cavity flow, it was demonstrated that RANS turbulence models yield reliable results for both fully turbulent and transitional flow regimes. However, none of the RANS turbulence models could achieve optimal performance simultaneously for both regimes. In contrast, a same LES model showed consistent performance across both flow regimes, making it more universal. In design, this implies that no prior knowledge of the flow regime would be necessary. However, LES was found to be influenced by the amount of resolved turbulence at the domain inlet. While determining this quantity precisely in design may be challenging, the results indicated that a rough estimate might be sufficient.

In the case of density-driven flow through a doorway, RANS can capture the primary features of the time-averaged flow, similar to LES. However, it fails to capture unsteady flow phenomena such as re-entrainment or the development of cold and warm airstreams originating from the door. Finally, the benchmarks highlighted the need for a very regular mesh to guarantee both accuracy and numerical stability in simulations. This observation aligns closely with the main research question of the thesis, which investigates the potential of orthogonal grids to perform high-resolution LES for indoor airflow simulations.

High Fidelity LES on Orthogonal Grids

4.1 High-Fidelity LES for Indoor Airflow Simulations

As computational resources continue to grow, wall-resolved LES of moderately high Reynolds number turbulent flows is gradually becoming feasible. However, the accuracy of such LES is highly sensitive to the numerical algorithm employed. Previous studies [57–62] have demonstrated the significant influence of numerical errors on the predictive accuracy of LES, highlighting the critical role of the numerical algorithm in ensuring accurate simulations. The combination of increased computational power and improved numerical techniques would enable researchers to apply LES to a wide variety of problems, such as aerodynamics, combustion, heat transfer, and fluid-structure interactions, among others.

Significant energy at high wavenumbers in the LES approach requires a numerical scheme that performs well in this range. While spectral methods are known for their uniform accuracy at all wavenumbers, they do have inherent limitations concerning geometry and boundary conditions, making them less applicable in practical cases involving irregular or complex geometries [63]. Furthermore, aliasing errors can be a significant challenge that arise due to the high-resolution requirements at high wavenumbers. These errors can lead to a degradation of the solution and negatively impact the accuracy of the simulation unless explicitly removed using filtering techniques [64].

In LES, aliasing errors should be kept small, and the numerical method used should be robust and not overly sensitive to these errors. Finite difference and finite element methods are alternatives with lower aliasing errors due to damping at high wavenumbers [64]. Eliminating these high-frequency components reduces aliasing errors, and the solution is better preserved at the resolved scales. While finite difference schemes may not provide the same level of accuracy at high wavenumbers as spectral methods, they are often preferred in practical LES applications due to their computational efficiency and flexibility for boundary conditions [65]. In addition, the focus in LES is typically on capturing the dominant large-scale structures and turbulence characteristics rather than resolving every single small-scale detail accurately.

LES using finite difference schemes can be categorized based on different criteria. Two primary aspects are highlighted in this context:

- A significant distinction arises from the interaction between the spatial discretization error and the SGS model. In LES, it is crucial to accurately reproduce the energy cascade between the various flow length scales. The discretization scheme adopted for the convective term can introduce artificial dissipation, interacting with the energy cascade by removing kinetic energy. In explicit LES, the SGS model is solely responsible for the dissipation related to the subgrid scales. This necessitates that artificial dissipation from the discretization of convective terms be minimized or eliminated, typically using a central scheme. To ensure the stability of a pure central scheme, the discrete kinetic energy must be conserved. In contrast, implicit LES tailors the artificial dissipation of the discretization scheme to act as a consistent SGS model [66].
- Another notable distinction depends on the use of body-conformal and nonbody-conformal orthogonal grids. Body-conformal meshes precisely follow the surface geometry of objects, potentially resulting in either complex structured grids or unstructured grids for complex geometries. On the contrary, nonbody-conformal orthogonal grids do not need to strictly follow surface geometry. This flexibility allows the use of more regular grids, such as orthogonal or Cartesian grids. The treatment of walls is addressed in a specialized manner by applying Immersed Boundary Method (IBM) [67]. The combination of orthogonal grids with IBM simplifies the generation of meshes for complex geometries.

Most applications of LES in modeling airflow inside buildings resort to explicit LES on body-conformal grids, whether structured or unstructured [22, 31]. In this

context, it becomes essential to limit artificial dissipation, which is a main reason behind using almost structured grids characterized by good orthogonality and skewness. This leads to specific criteria regarding grid quality that should be followed when conducting LES using general-purpose flow solvers like Fluent or OpenFoam [2]. However, it is worth noting that, as will be discussed, airflow patterns within buildings exhibit distinctive characteristics that make non-body conformal orthogonal grids a compelling alternative to general-purpose flow solvers.

4.2 Higher-order Numerical Schemes on Orthogonal Grids

According to Ghosal, "the reliability of numerical simulations of turbulence depends on our ability to quantify and control discretization errors" [59]. The second-order finite difference scheme developed by Harlow and Welch [68] on a staggered mesh is a remarkable example within the domain of numerical methods well suited to the DNS or LES of turbulent incompressible flow [69–72]. This scheme conserves not only mass and momentum by convection but also kinetic energy in a discrete sense on a uniform mesh in the absence of pressure work and viscous dissipation, which contributes to its robustness and accuracy in LES. On a non-uniform mesh, the numerical stencil coefficients are not adapted as a function of the local grid spacings to preserve the symmetries of the uniform mesh case (or skew-symmetric operator) and ensure the discrete conservation of kinetic energy. While the second-order central scheme is widely used for its simplicity and computational efficiency, it has limitations. Rivas demonstrated that the second-order finite difference scheme to approximate the first derivative has a first-order truncation error on a non-uniform grid while achieving second-order accuracy on a continuously stretched grid [73]. These errors can potentially influence the fidelity of resolved scales and interfere with the modeling of the SGS dynamics [58, 59, 61]. For a comparable magnitude of truncation errors to the modeled terms in LES, distinguishing between sources of errors becomes challenging. This ambiguity makes it difficult to assess whether errors originate from the numerical scheme or the SGS modeling. Lastly, Ghosal noted that the precision of a second-order finite difference scheme is limited, and dense meshes are needed to attain satisfactory results [59].

Higher-order numerical schemes alleviate the impact of truncation errors, leading to more accurate approximations and an enhanced fidelity of resolved scales [74]. Under their improved resolution at high wavenumbers and reduced sensitivity to aliasing errors, the conservation properties of high-order numerical schemes on staggered grids play a key role in enhancing the accuracy and reliability of LES results [75].

A study conducted by Morinishi et al. delves into the analysis of various finite difference schemes, with a specific emphasis on their conservation properties [76]. These schemes are formulated in divergence, advective, and skew-symmetric forms. They successfully derived the general family of discrete conservative higher-order accurate finite difference schemes tailored for both regular and staggered grid approaches on uniform meshes. To generalize the scheme in non-uniform grids, the scheme weights in the difference operators were adapted as a function of local grid stretching while preserving the order of local truncation error. However, the resulting scheme no longer preserves the symmetries of the uniform mesh case. Hence, they concluded it can be tailored to prioritize strict conservation of kinetic energy or to achieve strict fourth-order accuracy. According to Verstappen and Veldman [77], the scheme must preserve the symmetries of the underlying operator on non-uniform meshes in order to be fully conservative in a discrete sense. In other words, the approximation of the convective derivative should be achieved through a skew-symmetric operator.

Vasilyev extended the second and fourth-order methods proposed by Morinishi et al. [76], combining fourth-order accuracy with the discrete conservation of either momentum or kinetic energy on non-uniform grids [78]. It was determined that the commutation error between discrete differencing and averaging operators was a key factor contributing to non-conservation on non-uniform meshes while preserving the symmetries of the uniform mesh case in computational space.

The approach proposed by Verstappen and Veldman additionally introduces a skew-symmetric discrete operator to approximate convective terms [79, 80]. Based on finite volume principles, this method inherently adopts a divergence form while preserving the skew-symmetry of the discretization operator. Moreover, the method is based on the Richardson extrapolation of the symmetry-preserving second-order scheme of Harlow and Welch [68], allowing for the preservation of both fourth-order accuracy and full conservation on non-uniform Cartesian grids. It is important to note that the stencil coefficients (scheme weights) in Verstappen and Veldman's method remain unchanged with respect to local grid stretching when applied to non-uniform grids. This assumption relies on a smooth mapping between the computational and physical spaces. While modifying the coefficients of these schemes on non-uniform grids in physical space can effectively minimize local truncation errors, a potential trade-off emerges in the form of compromised conservation of kinetic energy, which could negatively impact the global discretization error [81, 82].

However, one of the primary challenges associated with these high-order schemes is the non-compact nature of the numerical stencil. This characteristic arises from the use of high-order interpolations in all three spatial directions. From second to

fourth-order accuracy, these numerical stencils are not only expanded from three to seven points along lines for the three spatial directions but also enlarged from two to four points in the perpendicular directions to each line. As a result, these schemes tend to be more complex to implement and can introduce challenges in treating boundary conditions, especially in scenarios involving complex geometries and the application of Immersed Boundary Method in practical engineering problems.

4.3 Why Orthogonal Grids?

Airflows within buildings exhibit distinct characteristics that set them apart from other flow environments. The airflow can appear in different states: laminar, transitional, and turbulent, often simultaneously within different areas of the same room. Notably, these flows are characterized by relatively lower Reynolds numbers compared to applications in aerospace and are treated as incompressible. In buildings, the influence of specific geometric details on airflow tends to be less pronounced than in aerospace applications. Additionally, the internal flow dynamics within buildings, including buoyancy effects, are equally significant as those observed in environmental flows. Employing orthogonal grids in building airflow simulations has several advantages and challenges. These factors play a crucial role in shaping effective simulation methods:

- a. **Grid configurations:** The numerical stencil for the standard second-order central finite volume method (with a linear reconstruction of flow variables to the cell faces) in usual flow solvers typically employs five points in each spatial direction on a structured mesh. A solver tailored specifically for orthogonal grids can provide the opportunity to extend the numerical stencil to incorporate additional points. This extension can improve numerical accuracy by reducing truncation errors, thereby contributing to more precise simulations. In transitional flows, the minimized dispersion error is crucial to achieve a high level of accuracy in capturing the advection of flow structures. Furthermore, using orthogonal grids facilitate the application of line-iterative techniques and geometrical multigrid solvers.
- b. **Non-conformal grids:** Considering the anisotropic nature of velocity fields in boundary layers, body-fitted grids offer the advantage of potentially lower grid point density compared to non-conformal meshes, especially in situations involving high Reynolds number flows. However, several factors may counterbalance this effect. Firstly, in building airflows, the lower Reynolds numbers imply that this effect may be less critical compared to

aeronautical applications. Secondly, in many building scenarios, geometric complexity is localized, often concentrated around occupants and air supply terminals. This allows for grid refinement using a non-uniform orthogonal mesh along walls, while the rest of the room can be represented using a coarser grid. A similar approach was followed in a high-resolution LES of density-driven bidirectional flow through an open doorway conducted by Larkermanni et al. [49]. They faced challenges related to grid arrangements in the vicinity of the doorway. The authors chose a structured non-uniform grid to keep numerical stability, given that preliminary analyses using an unstructured mesh indicated a susceptibility to numerical errors, particularly when the non-dissipative central scheme is necessary for LES. Typically, the shape of a room can be approximated by a combination of boxes, permitting a combination of body-conformal and nonbody-conformal meshes. Lastly, in wall-resolved LES, grid resolution near the wall can pose a significant computational demand. Nevertheless, advancements in wall functions for wall-modeled LES have been made, leading to significant reductions in required grid resolution near the wall. Recent developments, such as improved wall functions that account for buoyancy effects, represent a noteworthy step forward in this regard [83].

- c. SubGrid-Scale model: In explicit LES, the choice of SGS models significantly influences the accuracy and performance of the simulation. Common SGS models, such as the Smagorinsky and WALE models [84], can exhibit excessive dissipative behavior, particularly on the larger resolved scales of the flow. Even when applied with dynamic procedures, these models may not fully capture the finer details of the flow. Multiscale SGS models offer a promising alternative by applying a spatial filtering procedure that discriminates between large and small resolved scales. This approach ensures that SGS dissipation is primarily applied to the smallest resolved scales, leaving the larger scales relatively untouched [85]. As a result, the SGS model remains inactive in the laminar and transitional regions of the flow, leading to more accurate representations of flow behavior. The application of discrete spatial filters, a fundamental component of multiscale SGS models, is feasible with both unstructured and structured meshes. However, the performance of these filters can be more effectively assessed and characterized on orthogonal grids [86].
- d. Immersed Boundary Method (IBM): IBM presents clear advantages over traditional body-fitted meshes. One advantage is its ability to accommodate moving objects without the need for re-meshing at each time step [67]. This is in contrast to body-fitted meshes, where the analysis of moving objects

can be computationally demanding and time-consuming. By using IBM, researchers can easily simulate dynamic elements commonly encountered in building applications, including the movement of individuals, transient operations of doors and windows, and other dynamic scenarios.

- e. Staggered arrangement: A staggered arrangement of incompressible flow variables is accessible by using an orthogonal mesh [87]. This approach leads to a robust coupling between the pressure and velocity fields, effectively avoiding the checkerboard problem, also known as odd-even decoupling. Unlike non-staggered grids, which may require specific numerical treatments to address this issue, staggered grids naturally eliminate the need for such interventions. This characteristic enhances simulation stability and reduces the potential introduction of numerical dissipation associated with defining an interpolation scheme for the pressure [88]. Moreover, implementing a staggered grid allows for defining a convective scheme that precisely conserves discrete kinetic energy, which is crucial for explicit LES [78, 79].

Some previous studies have already applied some of these advantages of orthogonal grids to perform LES of airflows inside buildings. However, these studies lack an extended discussion of the pros and cons of orthogonal grids, covering the five points discussed earlier.

Kempe et al. [89] introduced a numerical scheme for LES of indoor airflows using orthogonal staggered grids and IBM for stationary objects. However, their spatial discretization scheme is a standard second-order central scheme. Therefore, they do not exploit the capacity to improve spatial discretization, as discussed in point a.. On the contrary, Morozova et al. [90] resort on a fourth-order symmetry preserving finite volume method on an orthogonal staggered mesh to perform LES of airflows inside buildings. However, the treatment of complex geometries is not discussed in their work, addressing points b. and d.. It is worth mentioning that these two studies introduced their methods to perform high-fidelity LES at moderate computational efforts.

IBM on orthogonal grids has been previously used to simulate contaminant transport in buildings. Mao and Celik [91] used orthogonal staggered grids along with a standard second-order method for the spatial discretization to perform (U)RANS simulations. Choi and Edwards investigated contaminant transport by human movement using LES [92, 93]. They resort to a second-order low-diffusion scheme for spatial discretization on collocated orthogonal grids. It is worth noting that the IBM has also been used in unstructured flow solvers to study body movement and pollutant dispersion in buildings, as seen in works like

Löhner et al. [94] and Saarinen et al. [95] using ANSYS CFX. To avoid confusion, it is important to note that orthogonal grids are not the prerequisite for implementing IBM; rather, it is IBM that facilitates the use of orthogonal grids, especially with complex geometries.

Hence, it is evident that integrating higher-order numerical methods on orthogonal grids with IBM holds promise for further investigation of indoor airflow simulations. Employing IBM in this framework facilitates the treatment of complex geometries and dynamic elements, making this approach more applicable in realistic indoor environments.

Development of a Numerical Framework tailored for Explicit LES on Staggered Orthogonal Grids

5.1 Adapted Incompressible Flow Solver for Cartesian Nonuniform Meshes

REEF3D is an open-source CFD software package focusing on CFD in hydrodynamics, environmental and marine engineering [3]. It is a powerful high-order flow solver and offers many advantages compared to academic and commercial CFD packages. On top of all these, the usage of REEF3D is free in an open-source environment. This allows for a deeper understanding of how the numerical model works and provides an opportunity to build valuable competence and experience in this field. In REEF3D, physical models, numerical methods and solvers are implemented as a collection of C++ classes and objects. The object-oriented design of REEF3D allows for modularity, extensibility and easy customization of the code. Users can modify existing solvers or create new ones by subclassing and extending the existing classes. REEF3D uses a ghost cell Immersed Boundary Method to deal with complex geometry on an orthogonal grid [96]. Besides, REEF3D also takes advantage of parallel processing within the implemented domain decomposition framework. Smaller domains created by

dividing the primary domain communicate with their neighbors through ghost cells. The Parallel Message Passing Interface (Parallel MPI) is used for inter-processor communication via the ghost cell method [3].

The structure of REEF3D positions it as a suitable candidate within the framework outlined in section 4.3. The grid configuration is orthogonal, characterized by one-dimensional grid stretching in each spatial direction. Flow variables are staggered across the grid. Additionally, the fundamental numerical stencil for the convective term involves seven points in each spatial direction, enabling the development of high-resolution schemes. The baseline scheme within REEF3D is a Weighted Essentially Non-Oscillatory (WENO) scheme, a fifth-order accurate scheme in linear advection problems. This formulation, however, is hybrid in nature, as it combines the WENO scheme with second-order central finite differences for discretizing mass conservation, pressure gradients, and diffusion terms. While formally second order, REEF3D can minimize dispersion errors by employing a seven-point numerical stencil for the discretization of convective terms. For the viscous terms and the pressure term, the second-order central differential scheme is adopted. By default, the governing equations are advanced in time using a fully explicit third-order Total Variation Diminishing (TVD) Runge-Kutta (RK) scheme [97]. At each Runge-Kutta stage, the advancement of the velocity field satisfies the continuity equation and is divergence-free. The Poisson equation is solved at each substep (i.e., three times per time step) to obtain the pressure term at the new time level [98]. Moreover, the fractional step method is employed to enforce the discrete continuity equation [99]. With the second-order discretization of the velocity divergence outlined in Equation (5.1) and the pressure gradient in Equation (5.2), this involves solving a second-order discretization of the Poisson equation. The Poisson equation is solved using an efficient geometric multigrid linear solver sourced from the HYPRE library [100]. Finally, to account for complex geometries, the IBM is integrated into the process.

The ghost cell approach employed belongs to the general category of IBM, which can potentially treat arbitrary immersed bodies on orthogonal meshes [101]. Moreover, the immersed and rigid boundaries of solid objects can be precisely represented, especially beneficial at high Reynolds numbers [67]. To address sharp corners accurately, the local directional ghost cell approach introduced by Berthelsen and Faltinsen [96] has been implemented. While sharp-interface methods like cut cells and ghost cells effectively maintain boundary sharpness, they encounter a primary challenge related to boundary motion. The movement of a solid body may cause a cell to transition into the fluid domain, introducing spatial discontinuity. This spatial discontinuity near the sharp immersed boundary

can, in turn, lead to temporal discontinuity for cells near the boundary. Consequently, a direct temporal discretization of momentum on these cells becomes impractical, given that flow variables lack a valid time history in these regions [67]. Hence, an IBM approach that directly integrates a continuous forcing term into the momentum equation is implemented. This integration of a forcing term follows the methodology proposed by Yang [102], offering a robust solution for treating dynamic boundaries. The core concept involves applying the forcing term strategically to a select number of grid cells positioned on both sides of the solid boundary such that a smooth transition between the fluid and solid phases is provided and temporal discontinuity for cells emerging into the fluid is eliminated [67].

To effectively conduct explicit LES, the flow solver should be adapted accordingly. As the WENO scheme is too dissipative to perform LES, a new central scheme had to be developed, the hybrid second-order central finite difference scheme (HCDS6). To achieve this objective, the non-dissipative spatial discretization (HCDS6) is implemented into REEF3D, as detailed in Section 5.2. The default temporal discretization scheme is the third-order explicit TVD Runge-Kutta method with a projection step at each stage. However, a prevalent strategy in LES and DNS is to employ explicit time integration for convective terms and implicit integration for diffusion terms. The main reason for treating diffusive terms implicitly is the severe time step constraints necessary for numerical stability, particularly in regions characterized by substantial grid refinement, often observed along walls. Since velocity tends to be small near the wall, the time step requirements for explicit convective terms are comparatively less strict. As a result, REEF3D has been customized by implementing a low-dissipative semi-implicit RK scheme, detailed in Section 5.2.3. Furthermore, SubGrid-Scale models with or without spatial filters [85] are implemented within the solver, providing the flexibility to choose between a multiscale SGS model and a standard one.

5.2 Numerical Method

To alleviate the complexity in terms of implementation and boundary condition treatment, a new scheme with enhanced numerical properties on staggered grids is introduced. This scheme involves seven points in each spatial direction. However, unlike existing fourth-order schemes on staggered grids, the numerical stencil remains compact, thereby simplifying its implementation and treatment of boundary conditions. Despite its formal second-order accuracy, the scheme demonstrates sixth-order accuracy for linear advection problems, resulting in relatively lower dispersion errors than the conventional second-order schemes of

Vasilyev [78] and Verstappen et al. [79]. To enable this improvement, the strict conservation of discrete kinetic energy has to be sacrificed. Nonetheless, the numerical tests presented in Chapter 6 demonstrate that this compromise has a limited impact on the simulation results.

5.2.1 Governing Equations

In indoor airflow applications, the Boussinesq approximation provides a simplified yet effective means of accounting for the influence of temperature on flow behavior in modeling the buoyancy-driven flow of fluids with temperature variations. The incompressible Navier–Stokes equations express the principles of mass, momentum and energy equations conservation mathematically through Equations (5.1)-(5.3).

$$\frac{\partial u_j}{\partial x_j} = 0 \quad (5.1)$$

$$\frac{\partial u_i}{\partial t} + \frac{\partial}{\partial x_j} (u_i u_j) = -\frac{1}{\rho} \frac{\partial p}{\partial x_i} + \frac{\partial}{\partial x_j} \left[\nu \left(\frac{\partial u_i}{\partial x_j} + \frac{\partial u_j}{\partial x_i} \right) \right] + g_i [1 - \beta (T - T_{\text{ref}})] \quad (5.2)$$

$$\frac{\partial T}{\partial t} + \frac{\partial u_j T}{\partial x_j} = \frac{\partial}{\partial x_j} \left[\alpha \frac{\partial T}{\partial x_j} \right] \quad (5.3)$$

where x_i denotes the i^{th} Cartesian coordinate. u_i represents the velocity field in the x_i direction, t the time, p the pressure, and T the temperature. The last term in Equation (5.2) is the buoyancy term where $\beta = 1/T_{\text{ref}}$ is the thermal expansion coefficient of the air modeled as an ideal gas and g_i the gravitational acceleration. Here, parameters ν and α are the kinematic viscosity and the thermal diffusivity, respectively. They are assumed constant (i.e., independent of the air temperature) and taken for the air at T_{ref} . The system of equations is solved numerically using finite differences on orthogonal grids.

5.2.2 Spatial Discretization

A fully staggered grid arrangement is employed for the strong coupling of velocity and pressure fields, avoiding spurious oscillations. This is achieved by assigning the velocity components to the center of the corresponding cell faces while the pressure and other scalar quantities are stored in the cell centers. A schematic representation of a uniform two-dimensional fully staggered grid arrangement [103] is illustrated in Figure 5.1 as a reference. Here i and j are mesh indices in the x_i and x_j directions, respectively.

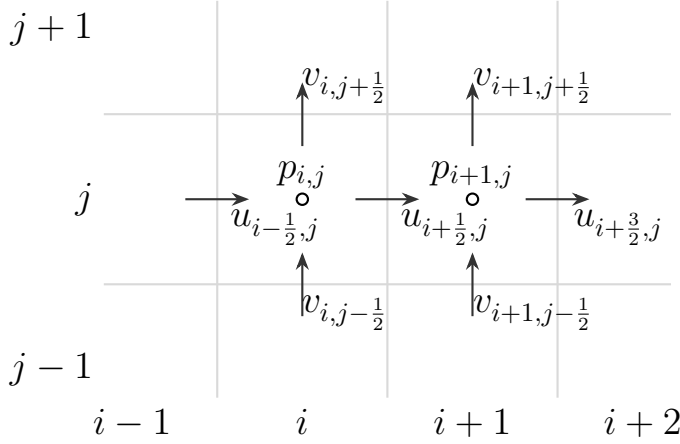


Figure 5.1: Staggered arrangement of variables in two dimensions.

To generalize the high-order schemes of Morinishi et al. [76] to non-uniform meshes, the discretization operation should be performed in computational space to preserve symmetries of the underlying operator [77, 78]. The derivatives in physical space are calculated using the local Jacobian, which can be determined numerically using the same stencil and corresponding weights as the finite differencing operator in the computational space. In a one-dimensional case:

$$\frac{\delta\phi}{\delta x} = \frac{1}{J} \frac{\delta\phi}{\delta\zeta} = \frac{1}{J} \frac{\phi_{i+1} - \phi_{i-1}}{2\Delta} \quad (5.4)$$

In the above definition, ζ denotes the spatial coordinate in the computational domain, and ϕ represents a discrete variable in three spacial coordinate directions. J is the Jacobian determinant of the transformation $x \rightarrow \zeta$ that can be defined numerically as:

$$J = \frac{\delta x}{\delta\zeta} = \frac{x_{i+1} - x_{i-1}}{2\Delta} \quad (5.5)$$

where Δ is the uniform grid spacing in the computational domain.

Using the notation of Vasilyev [78], the finite difference ($\delta_n/\delta_n\zeta_i$) and the interpolation ($\bar{\phi}^{n\zeta_i}$) operators in computational space with stencil n acting on ϕ are defined respectively as:

$$\left. \frac{\delta_n\phi}{\delta_n\zeta_i} \right|_{\zeta_i, \zeta_j, \zeta_k} = \frac{\phi(\zeta_i + n\Delta_i/2, \zeta_j, \zeta_k) - \phi(\zeta_i - n\Delta_i/2, \zeta_j, \zeta_k)}{n\Delta_i} \quad (5.6)$$

$$\bar{\phi}^{n\zeta_i} \Big|_{\zeta_i, \zeta_j, \zeta_k} = \frac{\phi(\zeta_i + n\Delta_i/2, \zeta_j, \zeta_k) + \phi(\zeta_i - n\Delta_i/2, \zeta_j, \zeta_k)}{2} \quad (5.7)$$

Following these operators, the standard second-order scheme of Vasilyev (CDS2) for the non-linear convective terms in Equations (5.2) and (5.3) on the non-uniform staggered grid are defined as:

$$(Div.)_i = \frac{\delta(u_j u_i)}{\delta x_j} \Big|_{x_i, x_j, x_k} = \left[\frac{\delta_1}{\delta_1 x_j} \left\{ \bar{u}_j^{1x_i} \bar{u}_i^{1x_j} \right\} \right]_{x_i, x_j, x_k} \quad (5.8)$$

$$(Adv.)_i = u_j \frac{\delta(u_i)}{\delta x_j} \Big|_{x_i, x_j, x_k} = \frac{1}{J_j} \left[\overline{u_j^{1\zeta_i} \frac{\delta_1 u_i}{\delta_1 \zeta_j}} \right]_{\zeta_i, \zeta_j, \zeta_k} \quad (5.9)$$

$$(Skew.)_i = \left[\frac{1}{2}(Div.)_i + \frac{1}{2}(Adv.)_i \right]_{x_i, x_j, x_k} \quad (5.10)$$

Note that the convective terms are evaluated at the respective velocity points. Morinishi et al. highlighted the various forms of convective terms present in the Navier–Stokes equations [76]. These include the divergence, advective, skew-symmetric, and rotational forms, each offering unique approaches to representing flow behavior. However, among these alternatives, the divergence form for the convective terms has proven to be the most straightforward and computationally efficient approach because of its simplicity. Vreman et al.[104] emphasized that the skew-symmetric form introduces a substantial truncation error compared to the divergence form.

The divergence form of the convective terms in the Navier–Stokes equations preserves the conservation of continuity and momentum at the discrete level using exact time integration in the absence of viscous dissipation. However, kinetic energy conservation by convection may not be guaranteed using the divergence form on a non-uniform staggered grid due to the commutation error term [78]. On the other hand, the skew-symmetric form of the convective term conserves the discrete kinetic energy while solely enforcing the discrete continuity equation is insufficient to reach the discrete momentum conservation. Again, it arises from the inherent presence of a commutation error term, a factor that is non-zero for non-uniform meshes.

Morinishi et al. have pointed out that the second-order finite difference method in Equation (5.8) in divergence form does not strictly conserve kinetic energy [76]. However, the error generated by the discretization scheme for convective terms

could be negligible (by a factor of three to four orders of magnitude) compared to the dissipation introduced by viscosity in Direct Numerical Simulations [104], making it a robust option for scale-resolving simulations [105].

The new scheme, denoted as HCDS6, addresses the discretization of the convective term by employing a symmetric seven-point stencil in divergence form. In HCDS6, a second-order accurate interpolation operator is used for the convection velocity, while the convective fluxes are discretized using a high-order central interpolation scheme:

$$\frac{\delta(u_j u_i)}{\delta x_j} \Big|_{x_i, x_j, x_k} = \left[\frac{\delta_1}{\delta_1 x_j} \left\{ \bar{u}_j^{1x_i} (\alpha_1 \bar{u}_i^{1x_j} + \alpha_3 \bar{u}_i^{3x_j} + \alpha_5 \bar{u}_i^{5x_j}) \right\} \right]_{x_i, x_j, x_k} \quad (5.11)$$

The scheme employs constant coefficients α_1 , α_3 , and α_5 , which are independent of the local grid stretching. These coefficients, chosen as $\alpha_1 = 37/30$, $\alpha_3 = -8/30$, and $\alpha_5 = 1/30$, are selected to ensure that Equation (5.11) aligns with the standard sixth-order central difference approximation for a constant convection velocity. When $\alpha_1 = 1$, $\alpha_3 = 0$, and $\alpha_5 = 0$, the method is degraded to the standard second-order central differential scheme initially proposed by Harlow and Welch. The HCDS6 is thus tailored to reduce dispersion errors compared to the CDS2. However, the conservation of the discrete kinetic energy by convection had to be sacrificed for this purpose. While the HCDS6 conserves the discrete momentum on non-uniform grids, it does not conserve the discrete kinetic energy, even in the case of uniform grids. Nonetheless, the results will demonstrate that this effect is limited, as the stencil weights are not adapted according to the local grid-stretching.

Both the new HCDS6 and the CDS2 schemes exhibit a more compact (condensed) formulation compared to the fourth-order finite-difference schemes as presented by Vasilyev [78], such as the one in divergence form (CDS4):

$$\frac{\delta(u_j u_i)}{\delta x_j} \Big|_{x_i, x_j, x_k} = \left[\frac{9}{8} \frac{\delta_1}{\delta_1 x_j} \left\{ \left(\frac{9}{8} \bar{u}_j^{1x_i} - \frac{1}{8} \bar{u}_j^{3x_i} \right) \bar{u}_i^{1x_j} \right\} - \frac{1}{8} \frac{\delta_3}{\delta_3 x_j} \left\{ \left(\frac{9}{8} \bar{u}_j^{1x_i} - \frac{1}{8} \bar{u}_j^{3x_i} \right) \bar{u}_i^{3x_j} \right\} \right]_{x_i, x_j, x_k} \quad (5.12)$$

The term "compact stencil" should not be confused with compact finite difference schemes [106]. In this context, a compact stencil means that the spatial extension of the points involved in the numerical stencil remains localized in a limited volume. Like the HCDS6, the CDS4 has a seven-point stencil in each spatial direction. However, in contrast to the HCDS6, the CDS4 computes the convection velocity using a fourth-order interpolation. Consequently, CDS4 has a stencil that involves four points in the directions perpendicular to each spatial direction, making the stencil non-compact, as shown in Figure 5.2.

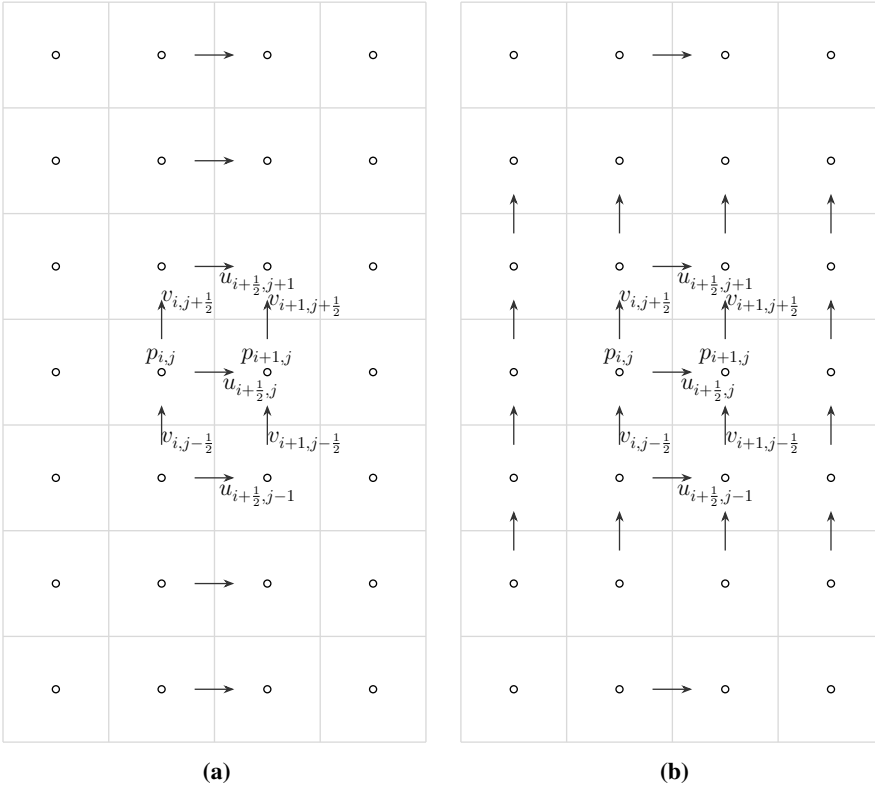


Figure 5.2: Comparison of the numerical stencil for HCDS6 (a) and CDS4 (b) for $i = 1$ and $j = 2$.

Using the definitions of finite difference and interpolation operators as outlined in Equations (5.6) and (5.7), and with mesh indices i , j , and k , the new central differential scheme for convective terms on staggered grids can be rewritten. To avoid any potential confusion with Cartesian tensor notation, u_i and u_j are simplified here to u and v , respectively:

$$\begin{aligned}
& \frac{\delta(uu)}{\delta x} \Big|_{x_{i+\frac{1}{2}}, y_j, z_k} = \\
& \frac{u_{i+\frac{1}{2}, j, k} + u_{i+\frac{3}{2}, j, k}}{2} \times \\
& \frac{x_{i+1} - x_i}{\left(\alpha_1 \frac{u_{i+\frac{1}{2}, j, k} + u_{i+\frac{3}{2}, j, k}}{2} + \alpha_3 \frac{u_{i-\frac{1}{2}, j, k} + u_{i+\frac{5}{2}, j, k}}{2} + \alpha_5 \frac{u_{i-\frac{3}{2}, j, k} + u_{i+\frac{7}{2}, j, k}}{2} \right)} \\
& - \frac{u_{i-\frac{1}{2}, j, k} + u_{i+\frac{1}{2}, j, k}}{2} \times \\
& \frac{x_{i+1} - x_i}{\left(\alpha_1 \frac{u_{i-\frac{1}{2}, j, k} + u_{i+\frac{1}{2}, j, k}}{2} + \alpha_3 \frac{u_{i-\frac{3}{2}, j, k} + u_{i+\frac{3}{2}, j, k}}{2} + \alpha_5 \frac{u_{i-\frac{5}{2}, j, k} + u_{i+\frac{5}{2}, j, k}}{2} \right)}
\end{aligned} \tag{5.13}$$

$$\begin{aligned}
& \frac{\delta(vu)}{\delta y} \Big|_{x_{i+\frac{1}{2}}, y_j, z_k} = \\
& \frac{v_{i, j+\frac{1}{2}, k} + v_{i+1, j+\frac{1}{2}, k}}{2} \times \\
& \frac{y_{j+\frac{1}{2}} - y_{j-\frac{1}{2}}}{\left(\alpha_1 \frac{u_{i+\frac{1}{2}, j, k} + u_{i+\frac{1}{2}, j+1, k}}{2} + \alpha_3 \frac{u_{i+\frac{1}{2}, j-1, k} + u_{i+\frac{1}{2}, j+2, k}}{2} + \alpha_5 \frac{u_{i+\frac{1}{2}, j-2, k} + u_{i+\frac{1}{2}, j+3, k}}{2} \right)} \\
& - \frac{v_{i, j-\frac{1}{2}, k} + v_{i+1, j-\frac{1}{2}, k}}{2} \times \\
& \frac{y_{j+\frac{1}{2}} - y_{j-\frac{1}{2}}}{\left(\alpha_1 \frac{u_{i+\frac{1}{2}, j-1, k} + u_{i+\frac{1}{2}, j, k}}{2} + \alpha_3 \frac{u_{i+\frac{1}{2}, j-2, k} + u_{i+\frac{1}{2}, j+1, k}}{2} + \alpha_5 \frac{u_{i+\frac{1}{2}, j-3, k} + u_{i+\frac{1}{2}, j+2, k}}{2} \right)}
\end{aligned} \tag{5.14}$$

Assuming a constant convection velocity (a) and uniformly spaced grids ($x_{i+1} - x_i = y_{j+1/2} - y_{j-1/2} = \Delta x = \Delta y$), the method is simplified to:

$$\begin{aligned}
 a \frac{\delta(u)}{\delta x} \Big|_{x_{i+\frac{1}{2}}, y_j, z_k} &= \\
 \frac{a}{\Delta x} \times & \\
 \left(\alpha_1 \frac{u_{i+\frac{1}{2}, j, k} + u_{i+\frac{3}{2}, j, k}}{2} + \alpha_3 \frac{u_{i-\frac{1}{2}, j, k} + u_{i+\frac{5}{2}, j, k}}{2} + \alpha_5 \frac{u_{i-\frac{3}{2}, j, k} + u_{i+\frac{7}{2}, j, k}}{2} \right. & \\
 \left. - \alpha_1 \frac{u_{i-\frac{1}{2}, j, k} + u_{i+\frac{1}{2}, j, k}}{2} - \alpha_3 \frac{u_{i-\frac{3}{2}, j, k} + u_{i+\frac{3}{2}, j, k}}{2} - \alpha_5 \frac{u_{i-\frac{5}{2}, j, k} + u_{i+\frac{5}{2}, j, k}}{2} \right) & \quad (5.15)
 \end{aligned}$$

$$\begin{aligned}
 a \frac{\delta(u)}{\delta y} \Big|_{x_{i+\frac{1}{2}}, y_j, z_k} &= \\
 \frac{a}{\Delta y} \times & \\
 \left(\alpha_1 \frac{u_{i+\frac{1}{2}, j, k} + u_{i+\frac{1}{2}, j+1, k}}{2} + \alpha_3 \frac{u_{i+\frac{1}{2}, j-1, k} + u_{i+\frac{1}{2}, j+2, k}}{2} + \alpha_5 \frac{u_{i+\frac{1}{2}, j-2, k} + u_{i+\frac{1}{2}, j+3, k}}{2} \right. & \\
 \left. - \alpha_1 \frac{u_{i+\frac{1}{2}, j-1, k} + u_{i+\frac{1}{2}, j, k}}{2} - \alpha_3 \frac{u_{i+\frac{1}{2}, j-2, k} + u_{i+\frac{1}{2}, j+1, k}}{2} - \alpha_5 \frac{u_{i+\frac{1}{2}, j-3, k} + u_{i+\frac{1}{2}, j+2, k}}{2} \right) & \quad (5.16)
 \end{aligned}$$

Unlike CDS2, HCDS6 employs a numerical stencil with seven points in each spatial direction. This requires the creation of three layers of ghost points to address Dirichlet and Neumann boundary conditions. Additionally, in parallel computation, three layers of points need to be exchanged between partitions in a multiblock domain decomposition. This leads to an increased data exchange between processors compared to the CDS2, which only requires the communication of one layer of points. Moreover, it is worth noting that while HCDS6 may require additional computational resources near boundaries, it does not significantly increase the computational time for evaluating the momentum equation in the inner part of the computational domain.

The continuity equation is discretized in the same way for the CDS2 and HCDS6 schemes. This means that the computational time required to solve the continuity equation remains consistent for both methods. For instance, the computational effort is comparable for both schemes when employing a projection method that involves solving the Poisson equation. This consistency in computational

demands for the continuity equation emphasizes the practical applicability of the HCDS6 scheme, as it provides enhanced accuracy in representing convective terms without significantly affecting the computational load associated with solving the continuity equation. This characteristic further highlights the potential benefits of adopting the HCDS6 scheme in simulations of indoor airflow behavior.

Modified Wave Number Analysis

The Modified Wave Number Analysis (MWNA) [106] represents a variant of the classical Fourier analysis, a technique traditionally employed in Von Neumann analysis. This analytical approach serves as a powerful tool for analyzing the stability and accuracy of numerical methods designed to solve partial differential equations (PDEs). To delve into its application, consider the 1D linear advection equation of the form:

$$\frac{\partial \bar{u}}{\partial t} + a \frac{\partial u}{\partial x} = 0 \quad (5.17)$$

where a is the constant advection velocity on the spatial domain $x \in [0, 2\pi]$ with periodic boundary conditions. For an initial condition $u(x, 0) = e^{ikx}$, the exact solution of the form:

$$u(x, t) = e^{ik(x-at)} \quad (5.18)$$

is admitted. Here k is the wavenumber.

Using the new central difference scheme (HCDS6) defined in Equation (5.11) to discretize the convective term on a uniform mesh ($\Delta x = h$), the semi-discretized one dimensional linear advection equation is obtained:

$$\frac{\partial u_i}{\partial t} + \left[a \frac{\delta_1}{\delta_1 x_i} \left(\frac{37}{30} \bar{u}_i^{1x_i} - \frac{8}{30} \bar{u}_i^{3x_i} + \frac{1}{30} \bar{u}_i^{5x_i} \right) \right]_{x_i, y_j, z_k} = 0 \quad (5.19)$$

$$\frac{\partial u_i}{\partial t} + \frac{a}{2h} \left(\frac{1}{30} u_{i+3} - \frac{3}{10} u_{i+2} + \frac{3}{2} u_{i+1} - \frac{3}{2} u_{i-1} + \frac{3}{10} u_{i-2} - \frac{1}{30} u_{i-3} \right) = 0 \quad (5.20)$$

The numerical solution can be expressed in terms of its Fourier series:

$$u_i(t) = \sum_k u_k(t) e^{ikx_i} \quad (5.21)$$

where u_k is the amplitude of the k^{th} Fourier mode.

The Fourier transform of the semi-discretized Equation (5.20) is obtained by substituting $u_i(t)$ from Equation (5.21):

$$\frac{\partial u_k(t)}{\partial t} e^{ikx_i} = -\frac{au_k(t)}{2h} \left(\frac{1}{30} e^{3ikh} - \frac{3}{10} e^{2ikh} + \frac{3}{2} e^{ikh} - \frac{3}{2} e^{-ikh} + \frac{3}{10} e^{-2ikh} - \frac{1}{30} e^{-3ikh} \right) e^{ikx_i} \quad (5.22)$$

and is simplified using the Euler's formula ($e^{\pm ikh} = \cos(kh) \pm i \sin(kh)$):

$$\frac{\partial u_k(t)}{\partial t} = -\frac{ai}{h} \left(\frac{1}{30} \sin(3kh) - \frac{3}{10} \sin(2kh) + \frac{3}{2} \sin(kh) \right) u_k(t) \quad (5.23)$$

The solution of Equation (5.23) in Fourier space can be written as:

$$u_k(t) = e^{-\frac{ai}{h} \left(\frac{1}{30} \sin(3kh) - \frac{3}{10} \sin(2kh) + \frac{3}{2} \sin(kh) \right) t} \quad (5.24)$$

Substituting this expression into Equation (5.21), the numerical solution can be obtained in physical space:

$$u_i(t) = \sum_k e^{i(kx_i - \frac{at}{h} \left(\frac{1}{30} \sin(3kh) - \frac{3}{10} \sin(2kh) + \frac{3}{2} \sin(kh) \right))} \quad (5.25)$$

Comparing the exact and numerical solutions of the 1D linear advection equation (Equations (5.18) and (5.25)), the non-dimensional modified wavenumber ($\tilde{k}_{mod} = k_{mod}h$) reads as a function of the non-dimensional wavenumber ($\xi = kh$):

$$\tilde{k}_{mod} = \frac{1}{30} \sin(3\xi) - \frac{3}{10} \sin(2\xi) + \frac{3}{2} \sin(\xi) \quad (5.26)$$

The dispersion relation ($\omega = k_{mod}a$), the phase velocity (ω/k) and the group velocity ($d\omega/dk$) become:

$$\omega = \frac{a}{h} \left(\frac{1}{30} \sin(3\xi) - \frac{3}{10} \sin(2\xi) + \frac{3}{2} \sin(\xi) \right) \quad (5.27)$$

$$\frac{\omega}{k} = \frac{a}{\xi} \left(\frac{1}{30} \sin(3\xi) - \frac{3}{10} \sin(2\xi) + \frac{3}{2} \sin(\xi) \right) \quad (5.28)$$

$$\frac{d\omega}{dk} = a \left(\frac{1}{10} \cos(3\xi) - \frac{3}{5} \cos(2\xi) + \frac{3}{2} \cos(\xi) \right) \quad (5.29)$$

Figure 5.3(a) shows that the non-dimensional modified wavenumbers ($k_{mod}h$) of the CDS2 and HCDS6 schemes almost follow the exact wavenumber up to about $\xi = kh = 0.4$ and 1.2 , respectively. The non-dimensional modified wavenumber

for CDS2 decreases from the maximum at $\xi = \pi/2$ to zero at $\xi = \pi$, while the $k_{mod}h$ for HCDS6 stays near the exact solution even at $\xi = \pi/2$, where $k_{mod}h = 1.47$.

Figure 5.3(b) shows that the phase velocity for CDS2 and HCDS6 is close to the exact value a up to $\xi \approx 0.25$ and $\xi \approx 1.1$, respectively. Beyond $\xi \approx 0.25$ and $\xi \approx 1.1$, respectively, the waves computed with CDS2 and HCDS6 lag behind the exact waves, leading to large dispersion errors, particularly for CDS2. At $\xi = \pi$, the computed waves for both CDS2 and HCDS6 are stationary.

The group velocity ($d\omega/dk$) is the velocity with which groups of waves and also energy are transported. Figure 5.3(c) indicates that HCDS6 computes the group velocity more correctly than CDS2. For $\xi \geq \pi/2$, groups of waves and energy are transported in the wrong direction with CDS2, while they are transported in the right direction with HCDS6 for $\xi \leq 1.936$. For very high non-dimensional wavenumbers ($\xi \geq 2.191$), the absolute error of HCDS6 is larger than the absolute error of CDS2. For $\xi = \pi$, $d\omega/dk = -a$ and $d\omega/dk = -2.2a$ for CDS2 and HCDS6, respectively. Remember that the exact group velocity is a .

As HCDS6 better represents the phase velocity and group velocity at higher wavenumbers than CDS2, fewer points per wavelength are required for HCDS6 than for CDS2. In three dimensions, this can result in a significant reduction in the number of grid points to reach the same accuracy. It is worth noting that, for a linear advection problem, the performance of HCDS6 is superior to the fourth-order accurate scheme of Vasilyev (CDS4) [78].

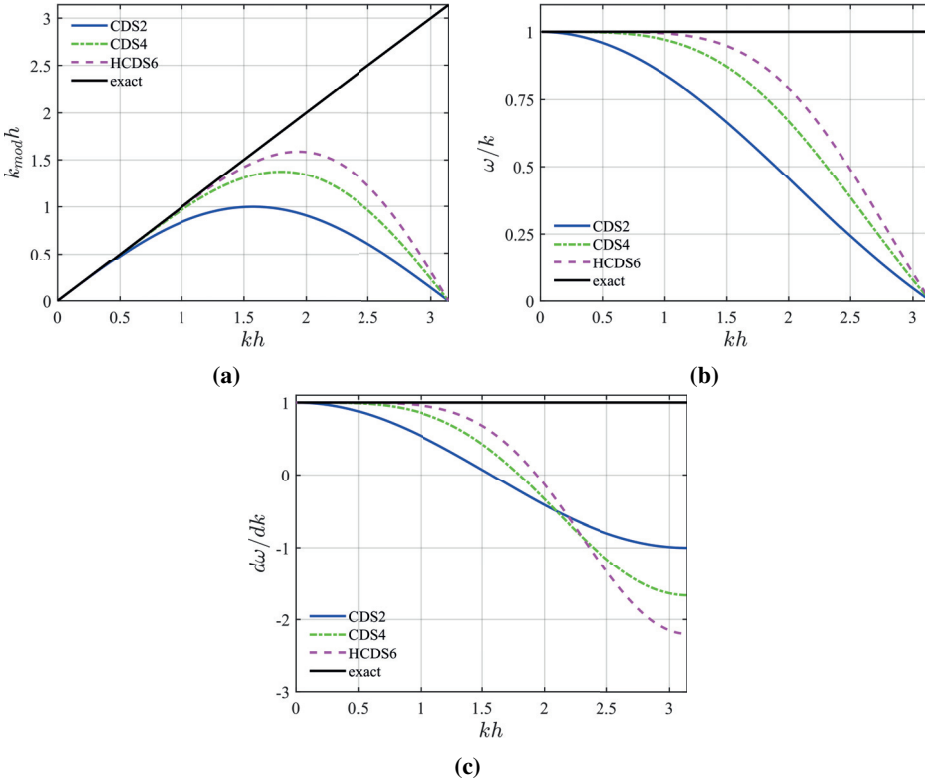


Figure 5.3: Non-dimensional modified wavenumber (a), phase velocity (b), and group velocity (c) for $a = 1$ with CDS2, CDS4, and HCDS6.

5.2.3 Temporal Integration

Explicit Time Integration

The projection method proposed by Chorin [107] is adopted for the pressure-velocity coupling in incompressible flows. This method is a time marching procedure based on a fractional-step technique, wherein each time step is decomposed into three steps. Here, viscous diffusion and incompressibility effects are decoupled using a predictor-corrector strategy. During the first step, the incompressibility constraint is temporarily neglected to compute an intermediate velocity field (u^*) using Equation (5.30).

$$\frac{u_i^* - u_i^n}{\Delta t} + \frac{\delta(u_i^n u_j^n)}{\delta x_j} = -\frac{1}{\rho} \frac{\delta p^n}{\delta x_i} + \frac{\delta}{\delta x_j} \left[\nu \left(\frac{\delta u_i^n}{\delta x_j} + \frac{\delta u_j^n}{\delta x_i} \right) \right] + g_i [1 - \beta (T^n - T_{ref}^n)] \quad (5.30)$$

where u_i^n is the velocity at the n^{th} time step. Note that the resulting intermediate velocity (u_i^*) does not satisfy the continuity equation (Equation (5.1)). To enforce continuity, the intermediate velocity is projected onto the space of incompressible divergence-free vector fields to obtain u_i^{n+1} :

$$\frac{u_i^{n+1} - u_i^*}{\Delta t} = -\frac{1}{\rho} \frac{\delta(p^{n+1} - p^n)}{\delta x_i} \quad (5.31)$$

This is done by solving a Poisson equation for the pressure field using the divergence of the intermediate velocity field and enforcing $\delta u_i^{n+1}/\delta x_i = 0$. The fully parallelized Bi-Conjugate Gradients Stabilized (BiCGStab) algorithm [108] solves the resulting Poisson pressure equation using geometric multigrid preconditioning provided by the high-performance solver library, HYPRE [109].

$$\frac{\delta}{\delta x_i} \left(\frac{1}{\rho} \frac{\delta(p^{n+1} - p^n)}{\delta x_i} \right) = \frac{1}{\Delta t} \frac{\delta u_i^*}{\delta x_i} \quad (5.32)$$

The result is a pressure field that enforces the incompressibility constraint on the velocity field. Finally, the new velocity field u_i^{n+1} at time step $n + 1$ is obtained by subtracting the gradient of the pressure correction field ($p^{n+1} - p^n$) scaled by $\Delta t/\rho$ from intermediate velocity (Equation (5.31)). This results in a velocity field that satisfies both the momentum and the continuity equations.

A similar procedure as Equation (5.30) is utilized for the time advancement of the energy equation:

$$\frac{T^{n+1} - T^n}{\Delta t} + \frac{\delta(u_j^n T^n)}{\delta x_j} = \frac{\delta}{\delta x_j} \left[\alpha \frac{\delta T^n}{\delta x_j} \right] \quad (5.33)$$

Semi-implicit Time Integration

An accurate and low-dissipation semi-implicit integration scheme might be needed when the grid is well-refined near the walls to perform wall-resolved LES. As a solution, the popular semi-implicit Runge-Kutta method by Le and Moin [110] can be chosen. In this temporal approach, every time step is advanced in three sub-steps, each of which uses the second-order-implicit Crank-Nicholson method to integrate the diagonal contribution of the diffusive term (Laplacian term), while the other terms are explicitly integrated using a second-order Adams-Bashforth method. The predictor-corrector technique and the Poisson equation for the three steps are formulated as follows:

$$\begin{aligned}
 & \frac{\hat{u}_i^m - u_i^{m-1}}{\chi_m \Delta t} + \gamma_m \frac{\delta(u_i^{m-1} u_j^{m-1})}{\delta x_j} + \kappa_m \frac{\delta(u_i^{m-2} u_j^{m-2})}{\delta x_j} \\
 &= -\frac{1}{\rho} \frac{\delta p^{m-1}}{\delta x_i} + \frac{\delta}{\delta x_j} \left[\nu \left(\gamma_m \frac{\delta u_j^{m-1}}{\delta x_i} + \kappa_m \frac{\delta u_j^{m-2}}{\delta x_i} \right) \right]_{i \neq j} \\
 &+ \theta \left(\frac{1}{2} \frac{\delta}{\delta x_j} \left[\nu \frac{\delta \hat{u}_i^m}{\delta x_j} \right] + \frac{1}{2} \frac{\delta}{\delta x_j} \left[\nu \frac{\delta u_i^{m-1}}{\delta x_j} \right] \right) + g_i [1 - \beta (T^{m-1} - T_{\text{ref}}^{m-1})]
 \end{aligned} \tag{5.34}$$

Here, the superscript m represents the sub-step number, taking values from 1 to 3. For the initial sub-step ($m = 1$), the term corresponding to $m - 2$ is disregarded. The u_i^0 and u_i^3 denote the velocities at time steps n and $n + 1$, respectively. The coefficients γ_m , κ_m and χ_m at each sub-step m are constants provided in Table 5.1. The coefficient θ equals 2 for $i = j$, and 1 otherwise. The second term on the right-hand side includes the non-diagonal components of the diffusive term, while the third term incorporates the diagonal components integrated using the Crank-Nicholson method.

m	χ_m	γ_m	κ_m
1	$\frac{8}{15}$	1	0
2	$\frac{2}{15}$	$\frac{25}{8}$	$-\frac{17}{8}$
3	$\frac{1}{15}$	$\frac{9}{4}$	$-\frac{1}{4}$

Table 5.1: Coefficients for semi-implicit Runge-Kutta method.

To obtain the new velocity u_i^3 , a similar procedure as explicit time integration is followed to project the resulting intermediate velocity onto the space of incompressible divergence-free vector field and solve a Poisson equation for the pressure field (Equations (5.35)-(5.36))

$$\frac{u_i^m - \hat{u}_i^m}{\chi_m \Delta t} = -\frac{1}{\rho} \frac{\delta (p^m - p^{m-1})}{\delta x_i} \tag{5.35}$$

$$\frac{\delta}{\delta x_i} \left(\frac{1}{\rho} \frac{\delta (p^m - p^{m-1})}{\delta x_i} \right) = \frac{1}{\chi_m \Delta t} \frac{\delta \hat{u}_i^m}{\delta x_i} \tag{5.36}$$

The time integration of the energy equation is done using:

$$\frac{T^m - T^{m-1}}{\Delta t} + \gamma_m \frac{\delta(u_j^{m-1} T^{m-1})}{\delta x_j} + \kappa_m \frac{\delta(u_j^{m-2} T^{m-2})}{\delta x_j} = \frac{1}{2} \left(\frac{\delta}{\delta x_j} \left[\alpha \frac{\delta T^{m-1}}{\delta x_j} \right] + \frac{\delta}{\delta x_j} \left[\alpha \frac{\delta T^m}{\delta x_j} \right] \right) \quad (5.37)$$

A similar approach is applied for the advection of a passive scalar, such as the concentration of a gaseous pollutant.

5.2.4 SGS Turbulence Model

Applying an implicit filtering operator to Equations (5.1)-(5.3), the filtered incompressible Navier–Stokes equations can be expressed as:

$$\frac{\partial \bar{u}_j}{\partial x_j} = 0 \quad (5.38)$$

$$\frac{\partial \bar{u}_i}{\partial t} + \frac{\partial \bar{u}_i \bar{u}_j}{\partial x_j} = -\frac{1}{\rho} \frac{\partial \bar{p}}{\partial x_i} + \frac{\partial}{\partial x_j} \left[\nu \left(\frac{\partial \bar{u}_i}{\partial x_j} + \frac{\partial \bar{u}_j}{\partial x_i} \right) \right] - \frac{\partial \tau_{ij}}{\partial x_j} + g_i [1 - \beta (\bar{T} - T_{\text{ref}})] \quad (5.39)$$

$$\frac{\partial \bar{T}}{\partial t} + \frac{\partial \bar{u}_j \bar{T}}{\partial x_j} = \frac{\partial}{\partial x_j} \left[\alpha \frac{\partial \bar{T}}{\partial x_j} \right] - \frac{\partial \tau_{jT}}{\partial x_j} \quad (5.40)$$

where the bar represents the implicit grid filtering. The SubGrid-Scale (SGS) stress tensor and the scalar SGS thermal flux vector are included, respectively, in the momentum and energy equations above via the unresolved terms $\tau_{ij} = \overline{u_i u_j} - \bar{u}_i \bar{u}_j$ and $\tau_{jT} = \overline{u_j T} - \bar{u}_j \bar{T}$.

The closure of the Navier–Stokes equations can be achieved through the application of the WALE turbulence model, which calculates the SGS kinematic viscosity, ν_{SGS} , based on the invariants of the velocity gradient tensor:

$$\tau_{ij} = \overline{u_i u_j} - \bar{u}_i \bar{u}_j = -2\nu_{\text{SGS}} \bar{S}_{ij} + \frac{2}{3} k_{\text{SGS}} \delta_{ij} \quad (5.41)$$

$$\nu_{\text{SGS}} = \bar{\Delta}^2 C_w^2 \frac{(\bar{S}_{ij}^* \bar{S}_{ij}^*)^{3/2}}{(\bar{S}_{ij} \bar{S}_{ij})^{5/2} + (\bar{S}_{ij}^* \bar{S}_{ij}^*)^{5/4}} \quad (5.42)$$

$$\bar{S}_{ij}^* = \frac{1}{2} (\bar{g}_{ij}^2 + \bar{g}_{ji}^2) - \frac{1}{3} \bar{g}_{kk}^2 \delta_{ij} \quad (5.43)$$

$$\bar{g}_{ij}^2 = \bar{g}_{ik} \bar{g}_{kj} = \frac{\partial \bar{u}_i}{\partial x_k} \frac{\partial \bar{u}_k}{\partial x_j} \quad (5.44)$$

where C_w is the model coefficient, here taken at a constant value of 0.325 [84], and the effective filter width ($\bar{\Delta}$) is computed using the local cell volume (V_k), $\bar{\Delta} = \sqrt[3]{V_k}$. k_{SGS} and \bar{S}_{ij} are the SGS kinetic energy and resolved scale strain rate tensor:

$$k_{\text{SGS}} = \frac{1}{2} (\overline{u_k^2} - \bar{u}_k^2) \quad (5.45)$$

$$\bar{S}_{ij} = \frac{1}{2} \left(\frac{\partial \bar{u}_i}{\partial x_j} + \frac{\partial \bar{u}_j}{\partial x_i} \right) \quad (5.46)$$

By analogy to the SGS stress tensor modeling, the scalar SGS thermal flux vector, τ_{jT} , can be approximated by the following expression [111]:

$$\tau_{jT} = \overline{u_j T} - \bar{u}_j \bar{T} = - \frac{\nu_{\text{SGS}}}{Pr_{\text{SGS}}} \frac{\partial \bar{T}}{\partial x_j} \quad (5.47)$$

$$Pr_{\text{SGS}} = \frac{\nu_{\text{SGS}}}{\alpha_{\text{SGS}}} \quad (5.48)$$

where Pr_{SGS} denotes the SGS Prandtl number.

The selection of the WALE SGS model is motivated by several factors. Notably, the WALE turbulence model accurately reproduces the near-wall behavior without the need for a wall-damping function, in contrast to the Smagorinsky SGS model. This characteristic ensures the WALE eddy viscosity model recovers the correct y^3 near-wall scaling for turbulent eddy viscosity [112]. Additionally, the WALE model generates zero turbulent viscosity in cases of pure shear, enabling it to effectively capture the transition from laminar to turbulent flow [112, 113]. Furthermore, the formulation of the WALE SGS model considers both the strain and rotation rate of small turbulent structures, enhancing its reliability compared to the dynamic Smagorinsky model, especially in accurately predicting the interfacial mixing layer [112, 114, 115].

Chapter 6

Validation and Verification

A diverse set of test cases enables a comprehensive evaluation of the numerical approach under different flow conditions, geometries, and resolution levels. The accuracy, reliability, and trustworthiness of CFD for indoor environment studies strongly depend on validation studies using experimental data. The challenge of addressing uncertainties arising from model assumptions, numerical approximations, and experimental constraints in CFD predictions must be comprehensively investigated despite their potential impact on simulation outcomes and, consequently, the quality and reliability of results. Therefore, it is necessary to establish robust procedures for both verifying and validating CFD simulations. In this context, verification involves assessing how accurately the equations have been solved, while validation aims to confirm that the correct equations have been solved [116, 117].

The current simulations were performed on the FRAM machine provided by Sigma2, the National Infrastructure for High-Performance Computing and Data Storage in Norway. FRAM named after the Norwegian arctic expedition ship Fram, the new Linux cluster hosted at UiT Arctic University of Norway, is a shared resource for research computing capable of 1.1 PFLOP/s theoretical peak performance. Fram is a distributed memory system that consists of 1,004 dual socket and two quad socket nodes, interconnected with a high-bandwidth, low-latency Infiniband network. The interconnect network is organized in an island topology, with 9,216 cores in each island. Each standard compute node has two 16-core Intel Broadwell chips (2.1 GHz) and 64 GiB memory. In addition, eight larger memory nodes with 512 GiB RAM are available, catering to computational tasks that demand substantial memory resources for more complex

simulations and data-intensive processing. The total number of compute cores is 32,256.

6.1 Benchmark Test Cases without IBM

In this section, three benchmark test cases are conducted using the adapted flow solver. These tests serve to showcase the capabilities and effectiveness of the current numerical approach when no Immersed Boundary Method is adopted. These cases include three generic scenarios: the convection of an isentropic vortex, the three-dimensional Taylor-Green vortex flow, and turbulent channel flow simulations.

6.1.1 Convection of an Isentropic Vortex

In order to test the performance of the HCDS6 finite difference scheme concerning its dissipation and dispersion properties, the convection of a two-dimensional isentropic vortex in a uniform flow is considered using incompressible Euler equations. The vortex is convected by a uniform flow in the positive x direction. The initial solution is represented by the velocity components in the streamwise and spanwise directions:

$$\begin{pmatrix} u \\ v \end{pmatrix} = \begin{pmatrix} u_\infty \\ 0 \end{pmatrix} + u_A e^{(1-(r/b)^2)/2} \begin{pmatrix} (y - y_0)/b \\ -(x - x_0)/b \end{pmatrix} \quad (6.1)$$

with $r^2 = (x - x_0)^2 + (y - y_0)^2$ being the distance from the vortex center (x_0, y_0) . The circumferential velocity induced by the vortex reaches its maximum value (u_A) at $r = b$. The vortex is translated with a mean-flow velocity in the x direction within a two-dimensional periodic domain. To minimize the impact of the boundary conditions and geometry on the results, a large computational domain with a dimension of $x \in [-25L, 25L]^2$ is considered. Here $L = \sqrt{\ln 2}b$ is a representative length scale of the vortex where $e^{-(r/b)^2} = 1/2$ at $r = L$.

A strong vortex with $u_A/u_\infty = 0.8$ is convected from the initial location at $(x_0, y_0) = (-18.75L, 0)$ to the final position $(x, y) = (18.75L, 0)$ for a time period of $u_\infty t/L = 37.5$ on a uniform cartesian grid. The Courant number is selected to be extremely small ($CFL = 1.152 \times 10^{-3}$) on the finest grid so that the effect of time discretization error is negligible.

Verification and Consistency

The Root-Mean-Square (RMS) error between the numerical and analytical solutions as a function of the grid resolution for the CDS2 and HCDS6 schemes is shown in Figure 6.1.

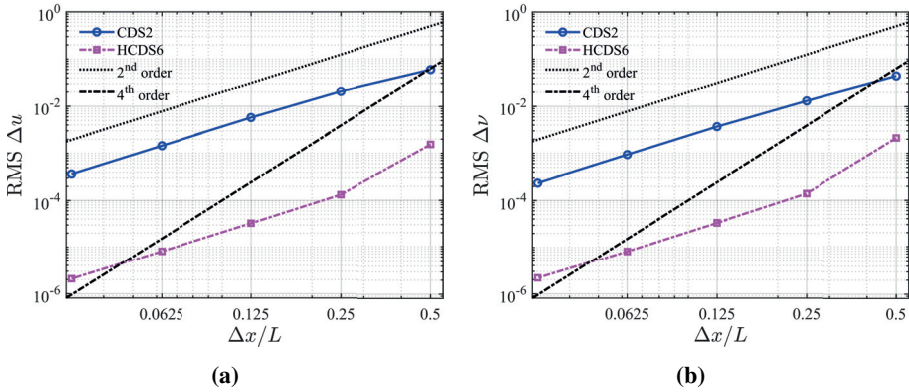


Figure 6.1: Convection of strong isentropic vortex on a uniform grid: grid dependence of the Root-Mean-Square value of difference with the analytical solution at the time $u_\infty t/L = 37.5$. (a): velocity component u , (b): velocity component v .

Figure 6.1 shows that the HCDS6 scheme is indeed second-order accurate, while the convergence is faster on a uniform mesh for the first and second refinement steps. For cell sizes smaller than $L/4$, the discretization error of second-order starts to dominate the global error. However, the error is reduced by approximately two orders of magnitude for the HCDS6, compared to the standard CDS2.

Shape and Position of the Vortex

The local resolution of the vortex on two different grid sizes ($\Delta x = L/2, L/4$) is shown in Figure 6.2. Here, the y velocity component along the midline at $y = 0$ is compared with the analytical solution. For CDS2, the vortex has clearly lost its shape on a coarse grid ($\Delta x = L/2$), while it is better preserved by the lower dispersion error of the HCDS6. Hence, a close agreement with the analytical curve is achieved. As the mesh is further refined, the vortex shape is improved significantly by the CDS2 scheme, while the improvement for HCDS6 is minor as the solution was already accurate on the coarser mesh. The vortex center drifted upward using the CDS2 scheme due to the dispersion error, as indicated by a smaller difference between the numerical and analytical solution for the positive peak than for the negative one. In other words, the vortex consists of a collection of waves with different wavelengths that are propagated at different velocities. Using the CDS2 scheme, the waves with low wavenumbers are propagated at the correct speed, whilst those with higher wavenumbers travel at the wrong speed. Consequently, those that are not propagated correctly are lagging and oscillating as a result of the dispersion error. In addition, the amplitude of low wavenumbers is carried correctly. In contrast, the amplitude carried by the higher wavenumbers

appears as oscillation and reduces the vortex peak amplitude. The HCDS6 outperforms the CDS2 in maintaining the shape and position of the vortex.

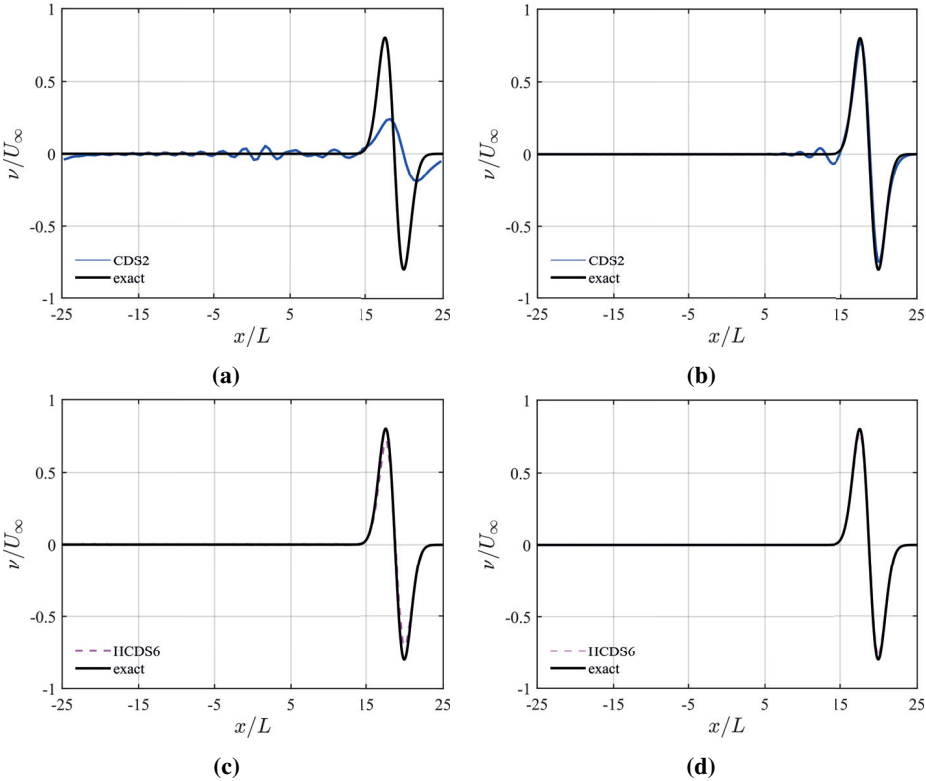


Figure 6.2: y velocity component along the midline at $y = 0$. Left: coarse grid ($\Delta x = L/2$), Right: fine grid ($\Delta x = L/4$).

The computational time of both numerical schemes ($t_{\text{CDS2}}, t_{\text{HCDS6}}$) is shown in Table 6.1. The required wall-clock time to convect the vortex from the initial position to the final position with a time step of $\Delta t = 2e-5s$ is almost identical for both CDS2 and HCDS6 ($t_{\text{HCDS6}}/t_{\text{CDS2}} \approx 1$). It should be noted that the additional computational time to evaluate this test case using the HCDS6 scheme compared to the CDS2 scheme is small. A main reason is related to the resolution of the Poisson equation for the pressure. It takes most of the CPU time per time step, while the spatial discretization of this equation is similar for both the CDS2 and HCDS6 schemes. The ratio of the wall-clock time of each numerical scheme to the time required by the same scheme on the next coarser grid is defined by r when the grid is refined consecutively. This ratio is almost similar for both CDS2 and HCDS6, and about 6% higher for HCDS6 on the finest grid. This ratio shows a significant reduction when the grid is refined from $\Delta x = L/8$ to $\Delta x = L/16$ due

to an increase in the number of processors.

Δx	n_t	$t_{\text{CDS2}}[s]$	r_{CDS2}	$t_{\text{HCDS6}}[s]$	r_{HCDS6}	$t_{\text{HCDS6}}/t_{\text{CDS2}}$
$L/2$	$1.875e6$	$2.983e4$	-	$2.964e4$	-	0.9936
$L/4$	$1.875e6$	$7.188e4$	2.4096	$7.355e4$	2.4814	1.0232
$L/8$	$1.875e6$	$2.01e5$	2.7963	$2.081e5$	2.8294	1.0353
$L/16$	$1.875e6$	$2.734e5$	1.36	$2.784e5$	1.3378	1.0183
$L/32$	$1.875e6$	$8.069e5$	2.9513	$8.717e5$	3.1311	1.0803

Table 6.1: Comparison of the execution time of the CDS2 and HCDS6 for the convection of an isentropic vortex.

6.1.2 3D Taylor-Green Vortex Flow

The Taylor-Green vortex flow is a well-defined, transient, three-dimensional flow that is generated by the interaction of two counter-rotating vortices in a periodic cubic domain. This classic benchmark problem is typically used to validate numerical methods for scale-resolving simulations [118] and evaluate high-fidelity flow solvers [119, 120]. Interactions between different scales of motion in the fluid, driven by the non-linear advection term in the Navier-Stokes equations, lead to the formation of smaller-scale vortices through vortex stretching, filamentation, and reconnection. These features are responsible for transferring energy from large-scale motion to smaller scales through the energy cascade. The counter-rotating vortices are initialized in a checkerboard arrangement from an analytical periodic vortex field where a sinusoidal velocity field with a uniform vorticity distribution in the $x - y$ plane is specified:

$$\begin{aligned}
 \frac{u}{U} &= \sin\left(\frac{x}{L}\right) \cos\left(\frac{y}{L}\right) \cos\left(\frac{z}{L}\right) \\
 \frac{v}{U} &= -\cos\left(\frac{x}{L}\right) \sin\left(\frac{y}{L}\right) \cos\left(\frac{z}{L}\right) \\
 \frac{w}{U} &= 0
 \end{aligned} \tag{6.2}$$

where L and U are the characteristic length and velocity scales of the problem, respectively. The Reynolds number of the flow is defined as $Re = UL/\nu$ and is equal to 1,600. A periodic cubic domain with a periodicity length of $L_x = L_y = L_z = 2\pi L$ is considered. A uniform grid is adopted with a same resolution in all three directions as $h = 2\pi L/N$, where N is the number of grid cells in one direction. The baseline and refined grid resolutions are 256^3 and 512^3 , respectively. The characteristic convective time $t_c = L/U$ is defined as the

time required for a fluid particle to traverse the characteristic length scale of the flow (L) at the characteristic velocity scale (U). A non-dimensional physical time step of $\Delta t^* = \Delta t/t_c = 0.001$ is adopted for the baseline grid to capture the temporal scales adequately. The physical time step size is halved for each subsequent grid refinement. The Courant number is set such that $CFL \leq 0.1$ for each grid resolution to minimize the temporal error. The simulations are performed for a time period of $t/t_c = 10$.

Different diagnostics are introduced to evaluate the performance of the HCDS6 for the Taylor-Green vortex flow simulation. A common and important one is the temporal evolution of the total kinetic energy per unit mass of the flow averaged over the control volume (V) defined as:

$$E_k = \frac{1}{V} \int_V \frac{u_i u_i}{2} dV \quad (6.3)$$

As the kinetic energy is not expected to vary much between the different scenarios investigated here, the time derivative of the total kinetic energy, defined as kinetic energy dissipation (ϵ), is a more sensitive characteristic than the total kinetic energy to assess the numerical method's performance.:

$$\epsilon = -\frac{dE_k}{dt} \quad (6.4)$$

A numerical scheme with significant artificial dissipation would fail to reproduce the time evolution of kinetic energy dissipation, making the scheme inappropriate for DNS or explicit LES.

Verification and Consistency

The evolution of the total volume-averaged kinetic energy is plotted in Figure 6.3 for two different grid resolutions with 256^3 and 512^3 cells, respectively. This is compared with the reference solution from a Direct Numerical Simulation computed using a pseudo-spectral code [119]. Even at the coarsest resolution, the solution from both the CDS2 and the HCDS6 are in good agreement with the reference pseudo-spectral solution. As the variations are negligible, the temporal evolution of the kinetic energy is not sufficiently sensitive to discriminate between the performance of the two central schemes. Therefore, the temporal development of the total kinetic energy dissipation rate is considered to highlight differences.

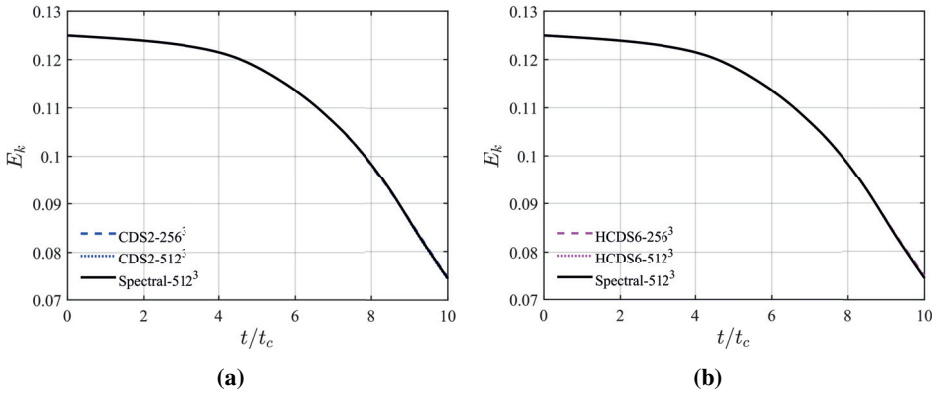


Figure 6.3: Temporal evolution of the volume-averaged kinetic energy.

Evolution of the Dissipation

Figure 6.4 depicts the evolution of the kinetic energy-based dissipation rate using two grid resolutions compared to the reference DNS solution [119]. This is characterized by an initial rapid increase in dissipation rate associated with the formation and stretching of the initial vortices, followed by a gradual decay to a steady-state value. As these vortices interact and break down, they transfer energy to smaller scales, thereby increasing the dissipation rate. However, as the flow evolves and the vortices continue to break down, the dissipation rate eventually reaches a steady-state value, which indicates that the energy injection and dissipation are balanced.

To assess the performance of the numerical scheme, a comparison between second-order CDS2 and HCDS6 on a low-resolution grid 256^3 and a refined grid 512^3 is carried out. At around $t/t_c \approx 4$, the dissipation rate increases rapidly when the transition from simple initial vortices to small-scale anisotropic turbulence occurs. This increase reaches the dissipation peak at around $t/t_c \approx 9$. For the highest under-resolution computation with 256^3 grid cells, the HCDS6 scheme deviates from the pseudo-spectral results around $t/t_c \approx 8.6$ and underpredicts the dissipation peak up to $t/t_c \approx 10$. The standard CDS2 scheme overestimates the dissipation rate too early at around $t/t_c \approx 7.9$ up to $t/t_c \approx 8.35$ when a significant deviation from the reference data is predicted. From $t/t_c \approx 9$, the dissipation rate gradually decreases until it intersects the pseudo-spectral line at around $t/t_c \approx 9.4$. From now on, the dissipation rate is slightly overestimated up to around $t/t_c \approx 10$. As the grid is refined, the numerical dissipation rate converges to the reference solution.

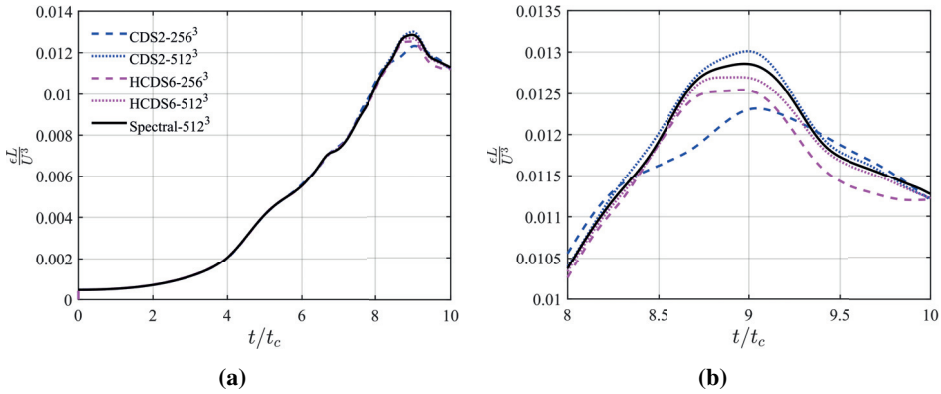


Figure 6.4: Temporal evolution of the dissipation rate based on kinetic energy.

Vortical Structures

Regular counter-rotating vortices stretch and twist as the flow evolves, generating smaller and more complex vortical structures. These structures continue to interact with each other, which leads to the formation of the most intricate vortices close to the dissipation peak at $t/t_c \approx 9$. A comparison of the instantaneous vorticity field is therefore performed to analyze the accuracy and reliability of the numerical scheme to transport complex vortical structures. It is sufficient to visualize vortical structures on only a limited portion ($1/16$) of the periodic plane, as the remaining portions will be identical due to different symmetries of the flow [118], as illustrated in Figure 6.5.

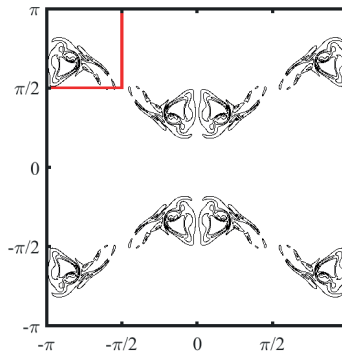


Figure 6.5: Instantaneous vorticity norm from the pseudo-spectral scheme on the periodic plane ($y = 0$) at $t/t_c \approx 9$.

The vorticity iso-contours for $\omega \in [1, 5, 10, 20, 30]$ on a subset of the periodic plane ($y = 0$) at $t/t_c \approx 9$ obtained by CDS2, CDS4, and HCDS6 schemes are

superposed with those from the pseudo-spectral scheme as a reference solution [119] in Figure 6.6. Exceptionally, the performance of the fourth-order discrete kinetic energy conserving scheme (CDS4) proposed by Vasilyev [78] and provided by M. Duponcheel [119] is also evaluated for this diagnostic. The results are presented for two different grid resolutions of 256^3 and 512^3 in the left and right columns, respectively. On the coarse grid, the position of the large vortical structures is somewhat captured by the CDS2 and CDS4 schemes, while the smaller vortices are diffused and contaminated by numerical noise. The HCDS6 scheme can capture the vortical structures better, although small details of the solution are smeared. The shape of the vortex structure improves and overlaps with the reference spectral solution as the grid is refined using all three schemes. However, the CDS2 scheme still struggles to predict the correct position of vortical structures even on the fine grid.

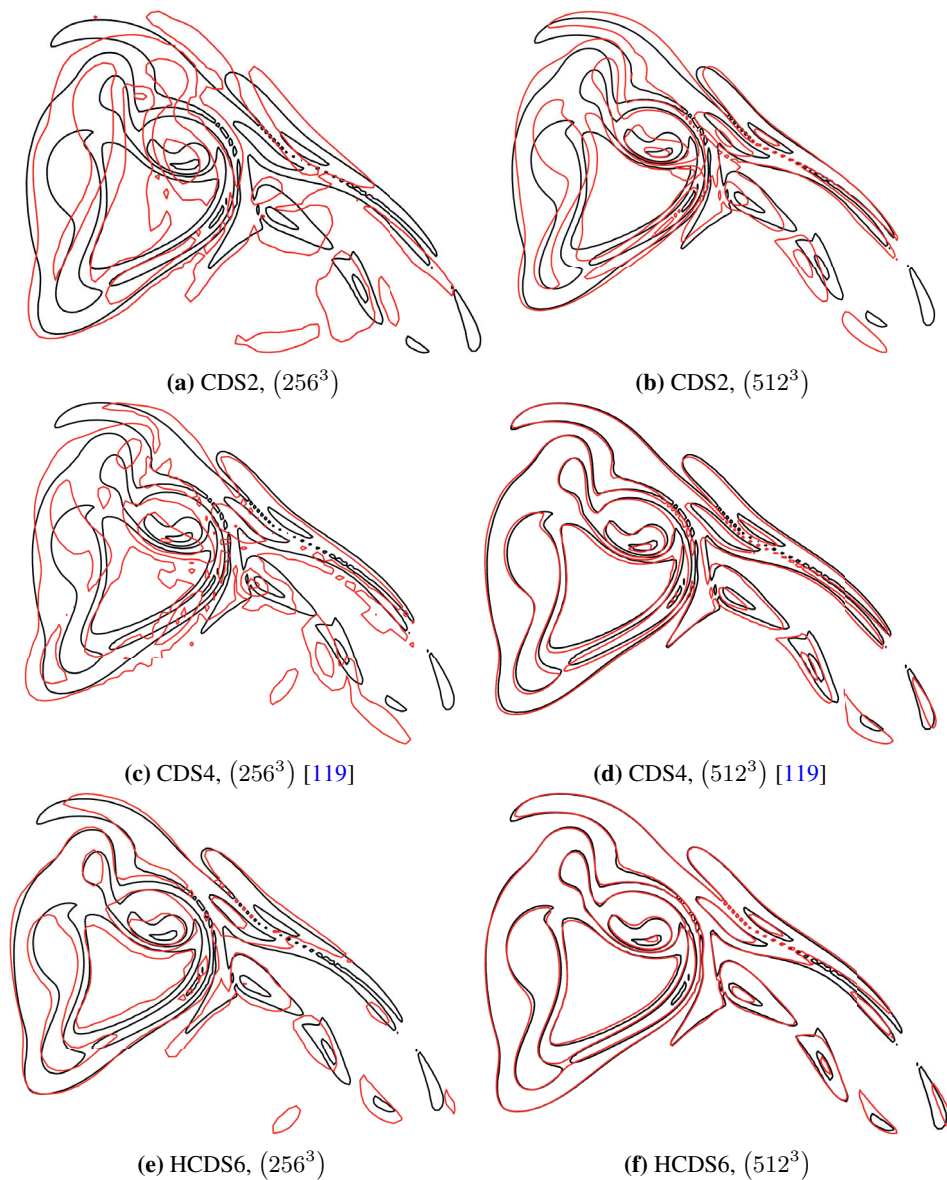


Figure 6.6: Iso-contours of the vorticity norm on the periodic plane ($y = 0$) at $t/t_c \approx 9$. The spectral solution is in black and the finite difference is in red.

6.1.3 Simulation of Turbulent Channel Flows

Numerical simulations of turbulent channel flow are performed to assess the performance of the new HCDS6 scheme. This is an insightful flow benchmark

where the flow is bounded with a no-slip boundary condition, which generates turbulence. The previous test cases were performed on a uniform mesh while, for the channel flow, a grid-stretching is applied in the wall-normal direction. The under-resolved channel flow is very sensitive to spurious production and dissipation of the discrete kinetic energy. Uncontrolled numerical dissipation strongly impacts the flow statistics, and significant spurious discrete kinetic energy production can lead to numerical instability.

In this benchmark, a fully developed turbulent flow is driven between two infinite parallel plates separated by a distance 2δ . A constant adverse pressure gradient is applied to the flow in the streamwise direction to drive the flow through the channel. The no-slip boundary condition is set for the top and bottom walls. Periodic boundary conditions are applied in the streamwise and spanwise directions to approximate infinite homogenous directions. The dimensions of the periodic domain are selected to ensure that the two-point correlations in the streamwise and spanwise directions would be essentially zero at maximum separation, which corresponds to half the domain size. In other words, these boundaries should be placed far enough from each other that the largest vortical structures would not intersect the computational domain. A uniform grid is adopted in the periodic directions, whilst the grid is stretched in the direction normal to the wall in order to resolve the boundary layers properly. This grid-stretching is based on a hyperbolic tangent function:

$$y_j = -\frac{\tanh\left(\gamma\left(1 - \frac{2j}{N_y}\right)\right)}{\tanh\gamma} \quad j = 0, 1, \dots, N_y \quad (6.5)$$

where N_y is the number of grid points in the wall-normal direction, and γ is the stretching factor. A small time step is selected to capture temporal scales precisely and keeps the Courant number below one, guaranteeing numerical stability.

Verification and Consistency

In this section, the DNS of a turbulent channel flow at the frictional Reynolds number of $Re_\tau = 180$ is carried out to verify the consistency of the HCDS6 scheme, and demonstrate whether the numerical solution converges to the exact solution as the grid resolution is refined. These results are compared to DNS data obtained using a spectral code [121, 122]. A same computational domain as that of Moser et al. [122] with $L_x = 4\pi\delta$, $L_y = 2\delta$, $L_z = 4\pi\delta/3$ is used. The grid resolution is $N_x = 256$, $N_y = 256$, $N_z = 256$, where N_x , N_y , and N_z are the number of cells in x , y and z directions, respectively. The stretching factor is equal to 1.6. The corresponding non-dimensional grid spacings in wall units are reported

in Table 6.2.

Re_τ	Δx^+	Δz^+	Δy^+
180	8.836	2.945	$\in [0.372 - 2.441]$

Table 6.2: Channel flow mesh resolution at $Re_\tau = 180$.

The computational domain is initialized with a random solenoidal velocity field. The default explicit time integration scheme is not used for this specific test case. The semi-implicit time marching algorithm is rather applied with the implicit Crank Nicholson for the diffusion term and an explicit third-order Runge-Kutta method for the other terms [110]. The bulk time scale ($t^* = L_x/U_b$) is equivalent to a Flow-Through Time (FTT) of the domain, which corresponds to how long it takes for the fluid to traverse the entire computational domain at a constant mean bulk velocity (U_b). Once the flow has reached a statistical steady state condition, the flow statistics are averaged in the streamwise and spanwise homogeneous directions across the entire channel over a time interval of $50\delta/u_\tau$ approximately equivalent to 37FTT , thereby ensuring fully converged statistics.

The mean streamwise velocity profile U^+ , the total Reynolds shear stress T_{xy} , and the square root of the second-order velocity moments normalized by the friction velocity are shown in Figure 6.7 as a function of the dimensionless distance to the wall.

The HCDS6 solution is in excellent agreement with the reference DNS results. The mean total Reynolds shear stress compares relatively well with the DNS data shown in the top-right graph in Figure 6.7. Investigating turbulence intensities involves analyzing the individual components of the total stress tensor illustrated at the bottom of Figure 6.7. The predictions for the spanwise (w_{rms}) and wall-normal (v_{rms}) turbulence-intensity components overlap with the reference DNS of Moser et al. [122]. The streamwise component (u_{rms}) exhibits only a slight deviation for y^+ above 80. All the predictions confirm the consistency of the HCDS6 scheme on non-uniform meshes.

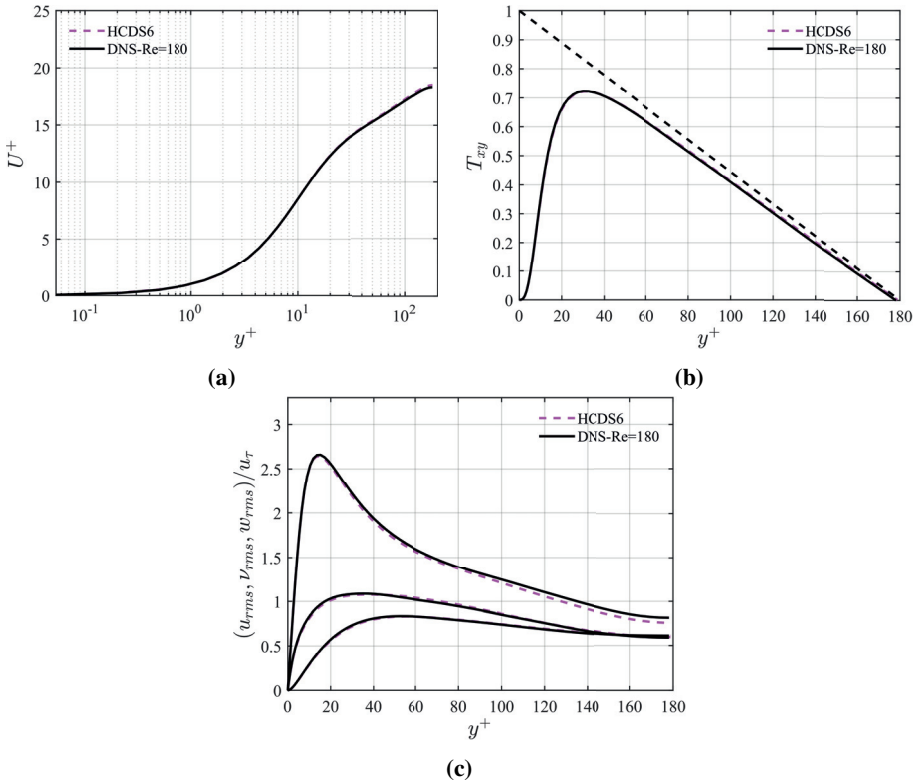


Figure 6.7: Mean streamwise velocity normalized by the DNS shear velocity (a), non-dimensional mean total Reynolds shear stress (b), mean normalized square root of the second-order velocity moments (c) (u_{rms} (top), v_{rms} (middle), w_{rms} (bottom)) for the DNS of turbulent channel flow at $Re_\tau = 180$.

TNS of the Channel Flow at $Re_\tau = 180, 640, 950$ and 2000

In contrast to DNS, which resolves all the turbulent scales, the performance of the HCDS6 in marginally resolved simulations termed Truncated Navier-Stokes (TNS) Simulations is also investigated. In TNS approach, turbulence modeling is not applied. In cases where a scheme fails to conserve discrete kinetic energy, there is a risk of spurious injection or dissipation of kinetic energy, and this phenomenon intensifies as the simulation becomes more under-resolved. TNS thus enables us to explore whether the lack of discrete kinetic energy conservation impacts the performance of HCDS6. The same setup as DNS of turbulent channel flow is carried out at four frictional Reynolds numbers of $Re_\tau = 180, 640, 950$ and 2000, but on a coarser mesh. In addition, the grid-stretching is increased compared to the DNS and tailored to be representative of LES applications. The computational

domain size, grid resolution, and corresponding non-dimensional grid spacings for each frictional Reynolds number are provided in Table 6.3.

Re_τ	L_x	L_y	L_z	N_x	N_y	N_z	Δx^+	Δz^+	Δy^+	γ	FTT
180	$2\pi\delta$	2δ	$\pi\delta$	128	128	128	8.96	4.48	$\in [0.12 - 14.4]$	2.8	42
640	$2\pi\delta$	2δ	$\pi\delta$	128	128	128	31.2	15.6	$\in [0.43 - 29.7]$	2.8	175
950	$2\pi\delta$	2δ	$\pi\delta$	128	128	128	45.7	22.9	$\in [0.63 - 37.1]$	2.8	266
2000	$2\pi\delta$	2δ	$\pi\delta$	128	128	128	99.4	49.7	$\in [1.37 - 58.9]$	2.8	167

Table 6.3: Computational domain size and mesh densities for TNS of channel flow at $Re_\tau = 180, 640, 950$ and 2000 .

As the grid is non-uniform with significant grid stretching, the CDS2 does not conserve the discrete kinetic energy. To establish a reference solution, the skew-symmetric form of the second-order scheme of Vasilyev [78] (given in Equation (5.10)) is also simulated since it strictly conserves the discrete kinetic energy on a non-uniform mesh. However, the simulation showed identical results for the divergence and skew-symmetric forms. This aligns with the findings in the channel flow tests conducted by Morinishi et al. [76]. Given that both the divergence and skew-symmetric forms yield the same results, they will not be distinguished and will be simply referred to as CDS2 in this section. It is noteworthy that adjusting the weights of the HCDS6 stencil to accommodate local grid stretching would result in unstable simulations, even at $Re_\tau = 180$.

The mean normalized streamwise velocity profiles for four frictional Reynolds numbers of $Re_\tau = 180, 640, 950$ and 2000 along the channel height are shown in Figure 6.8. The two discretization schemes agree well with the DNS data at $Re_\tau = 180$. For higher frictional Reynolds numbers, HCDS6 and DNS profiles almost collapse within the viscous sublayer and buffer layer with a slight underprediction in the logarithmic inertial layer. However, the buffer layer, the log layer, and the outer region are strongly affected using the CDS2 scheme, where it starts to deviate from the reference in the buffer layer at $y^+ \approx 10$. At $Re_\tau = 2000$, the grid resolution is insufficient to accurately capture the viscous sublayer, buffer layer and log layer. While HCDS6 tends to overestimate the velocity profile, it manages to capture the accurate shape across the channel height. Conversely, CDS2 struggles to predict the correct velocity profile behavior, and the deviation from DNS data notably increases, particularly in the log layer.

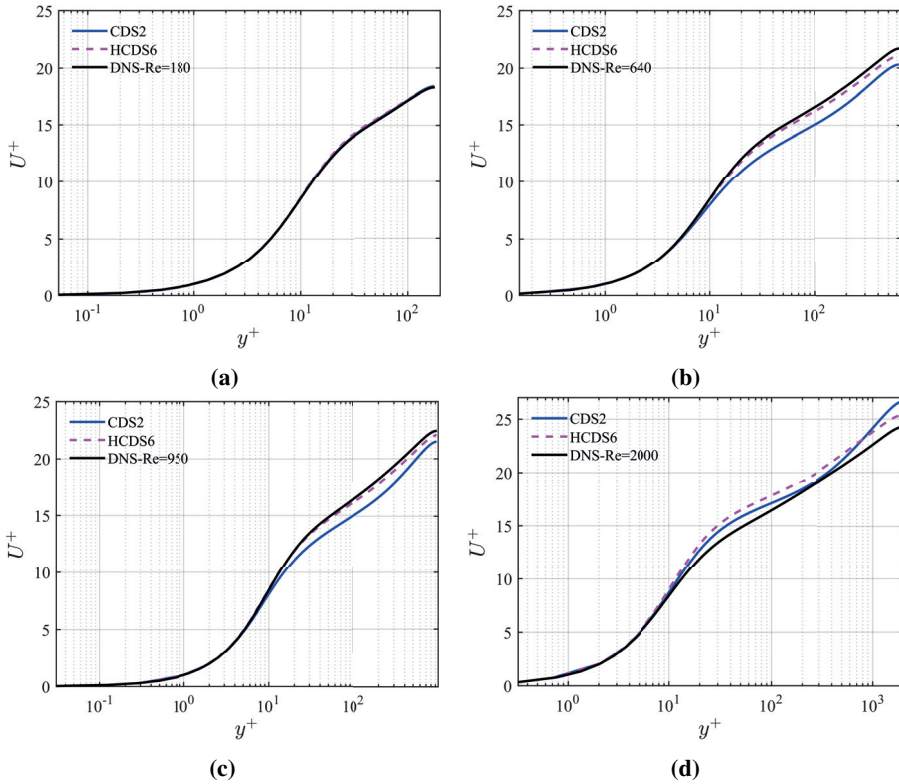


Figure 6.8: Mean streamwise velocity normalized by the DNS shear velocity for the TNS of turbulent channel flow at $Re_\tau = 180, 640, 950$ and 2000 .

The non-dimensional profiles of mean total Reynolds shear stress at four frictional Reynolds numbers are depicted as a function of the distance from the wall to the center of the channel in Figure 6.9. In a fully developed channel flow, the shear stresses and velocity gradients are more significant near the wall, which is indicated by a peak that decreases gradually to the channel centerline as the interaction between the mean velocity profile and the turbulent fluctuations is dampened. For all four frictional Reynolds numbers, CDS2 and HCDS6 can properly reproduce the total Reynolds shear stress of DNS. As the Reynolds number increases in a fully developed channel flow, the peak values of the non-dimensional Reynolds stress near the channel walls become more pronounced due to higher turbulence intensity. Moreover, stronger velocity gradients near the walls contribute to a steeper slope of the Reynolds stress profile in this region and promote more efficient mixing and transport of momentum across the flow cross-section. With higher Reynolds numbers, the peak location is shifted toward the wall due to the altered balance between turbulent production

and dissipation.

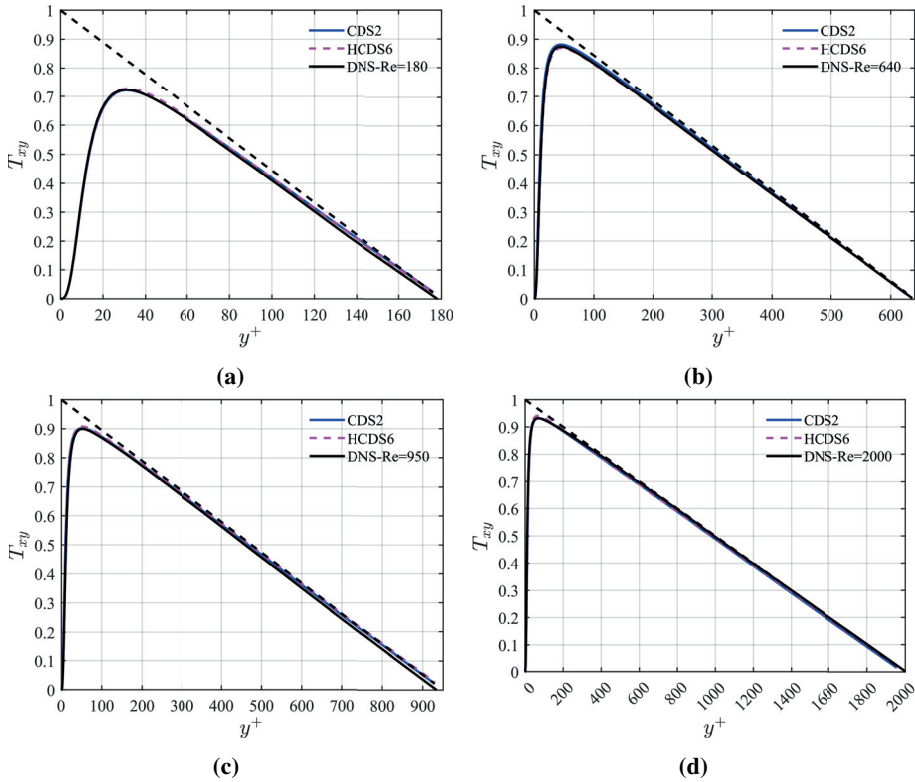


Figure 6.9: Non-dimensional mean total Reynolds shear stress for the TNS of turbulent channel flow at $Re_\tau = 180, 640, 950$ and 2000 .

The mean normalized velocity fluctuations of the TNS are compared to DNS data in Figure 6.10. For turbulent channel flow at a low Reynolds number of $Re_\tau = 180$, CDS2 performs an excellent job of representing all three components of the total stress tensor in the near wall and core section of the flow. However, the results from HCDS6 predict a slight overprediction, particularly for u_{rms} shear stress distribution when y^+ exceeds 10. By increasing the frictional Reynolds number to $Re_\tau = 640$, all the predictions of HCDS6 for the three velocity fluctuations remain accurate across the channel height, whilst significant deviations from the DNS data are observed for the CDS2 with reduced values of u_{rms} in the buffer and log layers. Both the spanwise and wall-normal components, w_{rms} and v_{rms} , are underpredicted with the CDS2 scheme for the buffer layer and outer region in the core of the flow. The agreement of the turbulent intensity components with DNS at a higher Reynolds number of

$Re_\tau = 950$ clearly shows the superiority of the HCDS6 scheme compared to the CDS2. The exception is streamwise stress, u_{rms} , that fails to capture the peak intensity in the vicinity of the wall. The deviation is more pronounced for CDS2, where the elevated prediction of the peak is followed by an underprediction away from the wall. Similarly to $Re_\tau = 640$, wall-normal velocity fluctuation shows an underprediction for wall units of approximately 20 to 210, and it is more pronounced in the outer region for y^+ above 800. Again, HCDS6 successfully reproduces the DNS profile of w_{rms} and v_{rms} . In a highly under-resolved simulation at $Re_\tau = 2000$, streamwise velocity fluctuation swings up and down around the DNS profile using the CDS2 scheme. This indicated that the CDS2 is less reliable as the under-resolution increases. The HCDS6 scheme tends to overpredict the streamwise stress across the channel. Despite this, the overall behavior remains consistent when compared to the DNS solution, particularly for the other two components of velocity fluctuations.

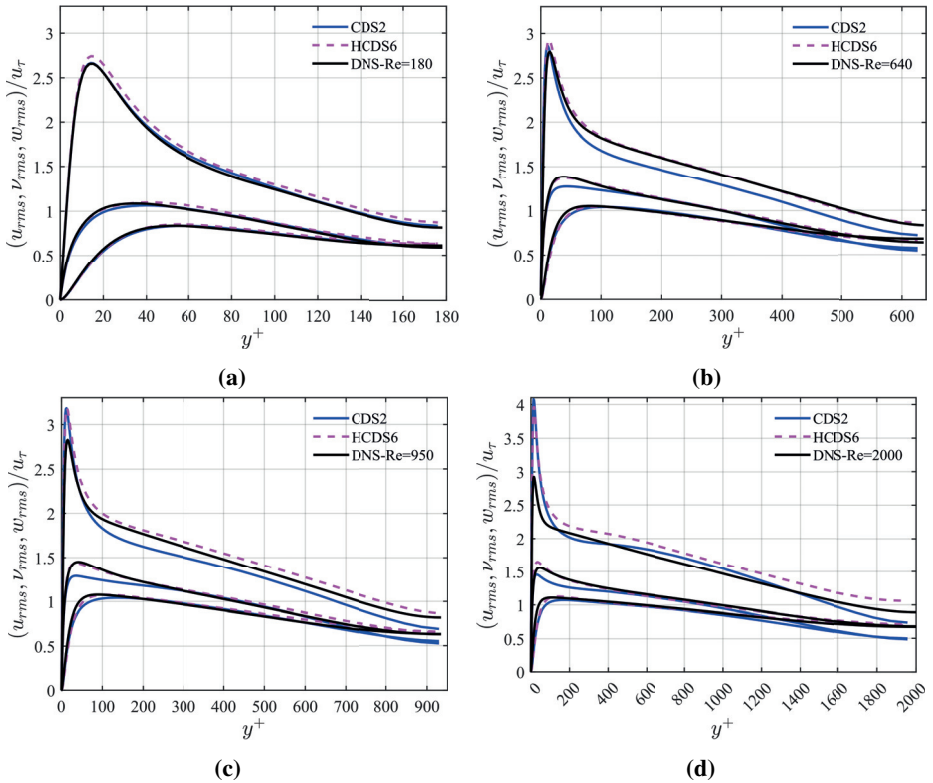


Figure 6.10: Velocity fluctuations in streamwise (u_{rms} , top), wall-normal (v_{rms} , middle) and spanwise (w_{rms} , bottom) direction as a function of the distance to the wall (y^+) for the TNS of turbulent channel flow at $Re_\tau = 180, 640, 950$ and 2000 .

Two dimensionless gradient-based cell Reynolds numbers evaluated using the norm of vorticity and the strain rate tensor are defined to assess the resolution level of each TNS. The cell Reynolds number based on the vorticity norm ($Re_{\Delta} - \omega$) and the norm of strain rate tensor ($Re_{\Delta} - S$) are defined as:

$$\begin{aligned} Re_{\Delta} - \omega &= \left(\frac{\sqrt[3]{\Delta x \Delta y \Delta z} * u_{\tau}}{\nu} \right)^2 = \frac{\langle \omega \rangle (\sqrt[3]{\Delta x \Delta y \Delta z})^2}{\nu} \\ Re_{\Delta} - S &= \left(\frac{\sqrt[3]{\Delta x \Delta y \Delta z} * u_{\tau}}{\nu} \right)^2 = \frac{\langle S \rangle (\sqrt[3]{\Delta x \Delta y \Delta z})^2}{\nu} \end{aligned} \quad (6.6)$$

where $\langle \omega \rangle$ represents the vorticity magnitude and $\langle S \rangle$ denotes the strain rate magnitude averaged along homogeneous directions. $\sqrt[3]{\Delta x \Delta y \Delta z}$ is the characteristic cell size based on the cell volume. Δx , Δy , and Δz are the cell dimensions in x , y , and z directions, respectively. The profiles of the mean cell Reynolds numbers across the channel height using the HCDS6 scheme are shown in Figure 6.11.

As expected, the cell Reynolds numbers increase with the Re_{τ} . They reach a maximum value in the laminar sublayer and then decrease to a relatively flat profile towards the center of the channel. The following argument demonstrates that the TNS is well under-resolved for $Re_{\tau} = 2000$:

- At the wall, the vorticity is equal to the gradient of the streamwise velocity component with respect to y , leading to $Re_{\Delta} - \omega = (\Delta y^+)^2$. In a wall-resolved DNS or LES, the typical recommended near-wall resolution is $\Delta y^+ \approx 1$. This value is lower or close to 1 in the four TNS, as shown in Table 6.3. However, the cell Reynolds number exhibits a peak value in the vicinity of the wall. This peak increases by a factor of 50 from the TNS at $Re_{\tau} = 180$ to $Re_{\tau} = 2000$.
- In the center of the channel, the flow exhibits characteristics similar to Homogeneous Isotropic Turbulence (HIT). Therefore, the cell Reynolds number of an LES applied to HIT serves as a pertinent reference for TNS simulations provided here. In an LES of Decaying Homogeneous Isotropic Turbulence (DHIT) at high Reynolds numbers, employing the Smagorinsky SubGrid-Scale model entails a theoretical expectation that the model constant (denoted as C_s) should be set to 0.027. This corresponds to a $Re_{\Delta} - S$ approximately equal to 37 when evaluated on the SubGrid-Scale eddy viscosity. In a research study by Thiry et al. [123], a LES of the DHIT was carried out using the dynamic Smagorinsky model. The study involved

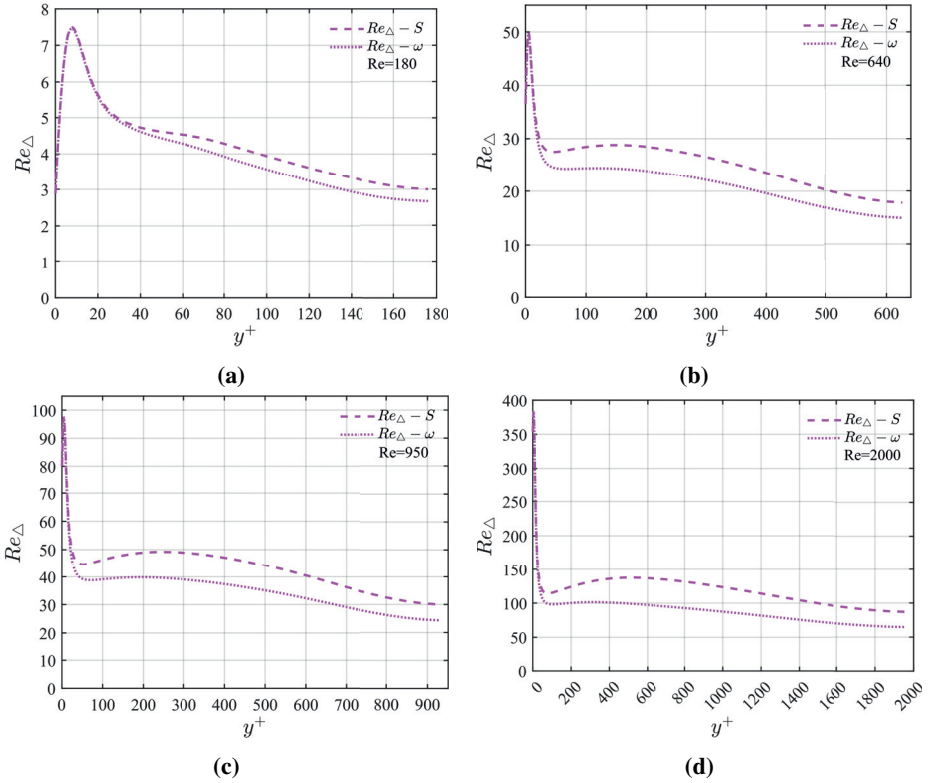


Figure 6.11: Mean cell Reynolds number based on vorticity ($Re_{\Delta} - \omega$) and strain term ($Re_{\Delta} - S$) as a function of the distance to the wall (y^+) for the TNS of turbulent channel flow at $Re_{\tau} = 180, 640, 950$ and 2000 .

setting a significantly large Taylor micro-scale Reynolds number (i.e., ν_{SGS}/ν converges to infinity), and the DHIT was computed on a 512^3 mesh using a pseudo-spectral method. Despite the theoretical constant suggesting a C_s value of 0.027, the dynamically determined C_s in this study was 0.0115, considerably lower. This discrepancy resulted in a $Re_{\Delta} - S$ of approximately 87 based on the SubGrid-Scale eddy viscosity. For a TNS at $Re_{\tau} = 2000$ and adopting HCDS6, the $Re_{\Delta} - S$ reached about 100 in the channel center. This observation indicates that the level of under-resolution achieved by TNS at $Re_{\tau} = 2000$ is representative of a LES at an extremely high Reynolds number in the center of the channel flow.

In conclusion, when a scheme fails to conserve the discrete kinetic energy, the resulting spurious production or dissipation of discrete kinetic energy increases with the level of under-resolution. Even though the TNS at $Re_{\tau} = 2000$ is

under-resolved near the wall and has a resolution comparable to LES at high Reynolds numbers in the center of the channel, the HCDS6 scheme remains unaffected by the non-conservation of the discrete kinetic energy. As demonstrated earlier, the flow statistics predicted by the HCDS6 are similar to those obtained with the standard second-order scheme of Vasilyev in the skew-symmetric form that strictly conserves the discrete kinetic energy. Additionally, it is important to note that a significant spurious injection of discrete kinetic energy could potentially render a simulation unstable. This is not the case for the TNS simulations when the HCDS6 scheme is adopted.

LES of the Channel Flow at $Re_\tau = 640$

The performance of the flow solver has been previously conducted through benchmarks involving DNS and under-resolved TNS simulations without turbulence modeling. In this section, the focus shifts to examining the interaction between the numerical method and the SGS model by employing the wall-resolved turbulent channel flow benchmark. Additionally, a key objective is to showcase that the newly proposed numerical scheme maintains accuracy and stability even when applied to a non-uniform mesh. The LES of a turbulent channel flow is conducted at a frictional Reynolds number of $Re_\tau = 640$. The WALE SGS model is employed, where the SGS kinematic viscosity is determined based on the invariants of the velocity gradient tensor [84]. Notably, the model coefficient, denoted as C_w , has been calibrated within the range of $0.55 \leq C_w \leq 0.6$ by Nicoud et al. [84]. However, this value is not universally applicable and may vary depending on the specific numerical method and Reynolds number. For the current investigation, the model coefficient is specifically calibrated to be $C_w = 0.46$. The same setup employed for the TNS simulation of turbulent channel flow at $Re_\tau = 640$ is replicated. The computational domain size, grid resolution, and corresponding non-dimensional grid spacings in wall units are given in Table 6.4.

Re_τ	L_x	L_y	L_z	N_x	N_y	N_z	Δx^+	Δz^+	Δy^+	γ	FTT
640	$2\pi\delta$	2δ	$\pi\delta$	128	128	128	31.6	15.8	$\in [0.43 - 29.7]$	2.8	175

Table 6.4: Computational domain size and mesh densities for LES of channel flow at $Re_\tau = 640$.

The mean streamwise velocity profile (U^+), the total Reynolds shear stress (T_{xy}), and the square root of the second-order velocity moments normalized by the friction velocity are shown in Figure 6.12 as a function of the dimensionless distance to the wall (y^+). The HCDS6 solution is in excellent agreement with the reference DNS results of Abe et al. [124]. The mean total Reynolds shear stress

using both central schemes compares relatively well with the DNS data shown in the top-right graph in Figure 6.12. Moreover, the predictions for the spanwise (w_{rms}) and wall-normal (v_{rms}) turbulence-intensity components overlap with the reference DNS [124]. However, the streamwise component (u_{rms}) exhibits a slight deviation for y^+ above 60 when CDS2 is employed. In conclusion, these predictions confirm the consistency of the explicit LES approach, where no artificial numerical dissipation competes with the dissipation of the SGS model.

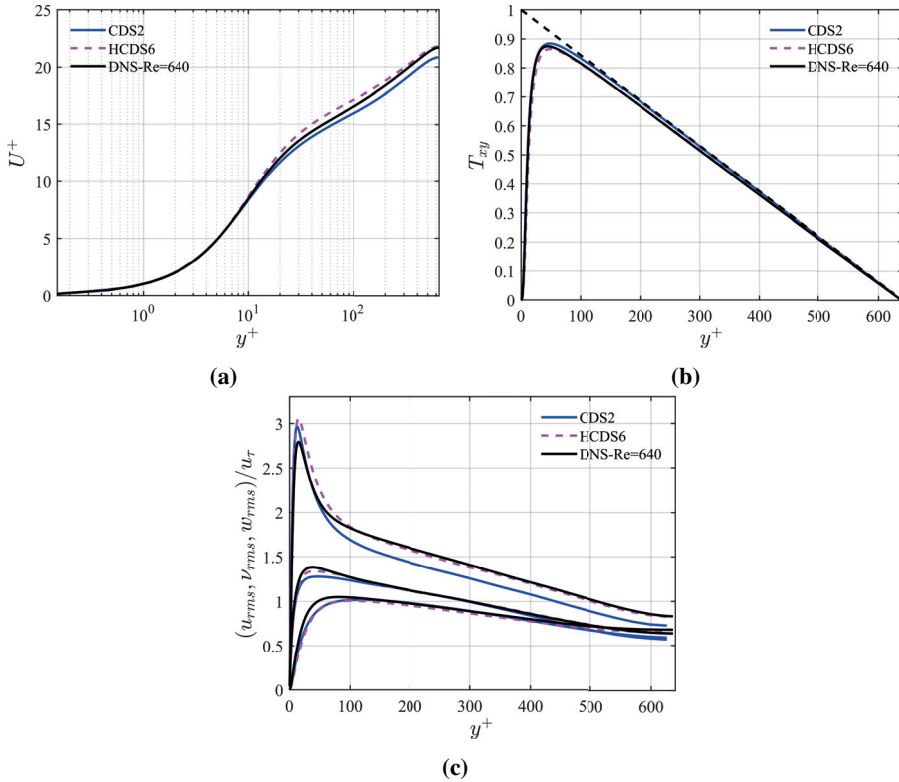


Figure 6.12: Mean streamwise velocity normalized by the DNS shear velocity (a), non-dimensional mean total Reynolds shear stress (b), mean normalized square root of the second-order velocity moments (c) (u_{rms} (top), v_{rms} (middle), w_{rms} (bottom)) for the LES of turbulent channel flow at $Re_\tau = 640$.

6.2 Benchmark Test Cases with IBM

In this section, two benchmark test cases are simulated using the adapted flow solver. These tests aim to demonstrate and assess the capabilities and effectiveness of the current numerical approach, particularly in scenarios where the Immersed

Boundary Method is utilized. These cases include two generic scenarios: the flow past a wall-attached cube, and steady non-axisymmetric flow past a sphere.

6.2.1 Flow Past a Wall-attached Cube

The flow around a wall-attached solid cube is a simple geometry that offers valuable insights into the interaction between a boundary layer and complex bodies immersed within it. While the primary focus of this study revolves around indoor airflows, it is noteworthy to include simulations of the flow around square cylinders with varying aspect ratios. This serves as a valuable test case in the context of environmental applications, enabling a simulation of airflow dynamics around simplified architectural structures [125, 126]. The sharp corners of the cube challenge the performance of the IBM using the ghost cell approach. In REEF3D, the local directional ghost cell approach [96] was introduced to solve this challenge. Another approach called an enhanced direct forcing IBM implemented in the REEF3D is also adopted where the effect of solid boundaries in the Navier–Stokes equations is incorporated by introducing additional terms or forcing functions.

The wall-attached cube is a geometric solid positioned in a zero-pressure gradient boundary layer. The computational setup is identical to those used by Diaz-Daniel et al. [127] for the DNS of a wall-attached cube immersed in laminar and turbulent boundary layers. For the sake of simplicity, only the laminar case at $Re_H = 500$ is investigated here, where the inlet boundary condition is defined by the Blasius laminar boundary layer profile. The cube is located at a distance $9H$ from the inlet, where H is the cube height. The coordinate system is aligned with the front plane of the cube where the origin is located at $x = 0$. A no-slip boundary condition is applied at the bottom wall, while a homogeneous Neumann condition is imposed at the top boundary. In the spanwise direction, the periodic boundary condition is adopted to simulate an infinite array of cubes. The computational domain size and grid resolution are summarized in Table 6.5.

Re_H	Re_θ	Re_{δ^*}	$\frac{L_x}{H} \times \frac{L_y}{H} \times \frac{L_z}{H}$	$N_x \times N_y \times N_z$	$\frac{\Delta y_{\text{wall}}}{H}$	$\frac{\Delta y_{\text{top}}}{H}$	$\frac{\Delta t U_\infty}{H}$	$\frac{TU_\infty}{H}$
500	68	175	$35 \times 15 \times 8$	$336 \times 144 \times 186$	0.02	0.68	$1.516e - 3$	10000

Table 6.5: Computational domain size and mesh resolution for DNS of the wall-attached cube.

Re_θ and Re_{δ^*} are Reynolds numbers based on the momentum thickness (θ) and the displacement thickness (δ^*), respectively, for the freestream velocity (U_∞).

A uniform grid with a cell size of $0.02H$ is created in a rectangular refinement area measuring $[2H \times 2H \times 2H]$ around the cube. The cells are elongated with

a growth ratio of 1.2 in the wall-normal direction from the refined zone to the top boundary of the domain, ensuring that the largest cell size does not exceed $0.68H$. A smaller growth ratio of 1.05 is set in streamwise and spanwise directions from the focus zone up to the lateral boundaries of the domain, where the maximum cell size is $0.2H$ and $0.5H$ in x and z directions, respectively. The flow statistics are time-averaged over a period T following a long initial transient period until the flow is statistically steady-state.

Mean Flow Statistics

The time-averaged streamwise velocity contours with mean flow streamlines around the wall-attached cube are illustrated in Figure 6.13. A deceleration region is created as the flow encounters the cube front plane. The flow accelerates gradually along the cube's leading face, with a well-behaved velocity gradient near the wall. A mild separation occurs at the leading edge, followed by a thin boundary layer along the cube top face. In the wake region behind the cube, vortices and disturbances are less pronounced than higher Reynolds numbers, resulting in a more organized flow structure. The mean-flow streamlines show a closed recirculation region in front of the cube (Figure 6.13, left) surrounded by a horseshoe vortex system upstream and around the wall-attached cube (Figure 6.13, right). The contours of time-averaged streamwise velocity show that the flow structures align remarkably well with benchmark DNS data, thereby underlining the robustness and reliability of the Immersed Boundary Method implemented in the flow solver.

A key flow diagnostic is the location of stagnation points, which provides a basis for a quantitative comparison between REEF3D and DNS reference solutions. The upstream stagnation point on the cube front face is marked A while the other one positioned farther from the front face is labeled F (see Figure 6.13, last row). The one that exists downstream is marked D . The location of stagnation points is reported in Table 6.6. Again, the results of the reference DNS solution [127] are accurately replicated. In this case, the mesh is conformal with the channel but non-conformal for the cube. In line with remarks in Section 4.3, this demonstrates that IBM is an accurate alternative to boundary-fitted meshes.

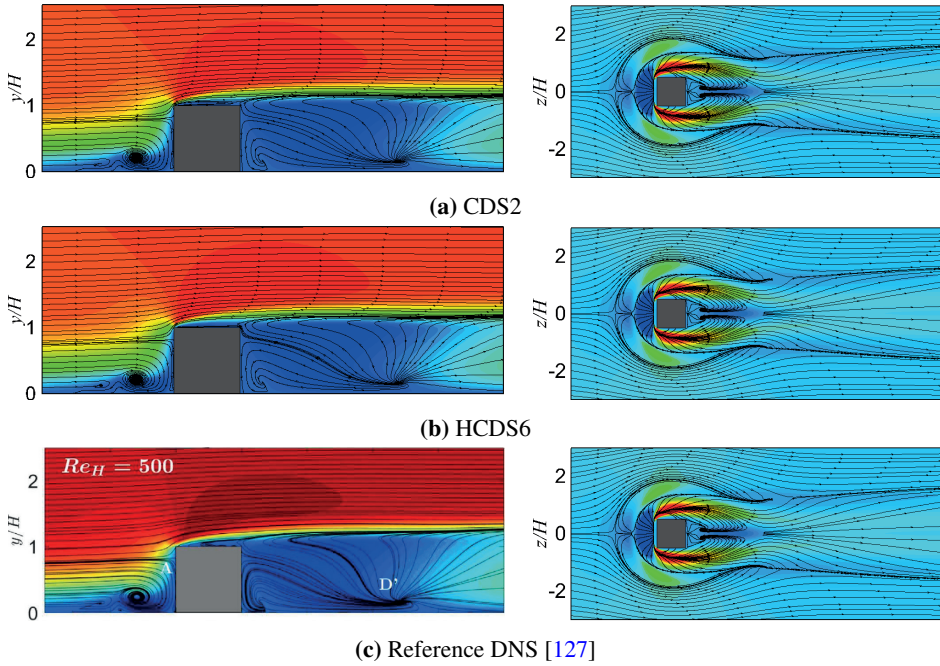


Figure 6.13: Time-averaged streamwise velocity contours with mean flow streamline around a wall-attached cube at $Re_H = 500$. Left: $x - y$ plane, right: $x - z$ plane. The color scale for \bar{u} spans from $-0.1U_\infty$ in dark blue to $1.1U_\infty$ in dark red for the left column and $0.2U_\infty$ in dark red for the right column.

Solver	Method	y_A	x_D	y_D	x_F
Incompact3d [127]		0.82	3.48	0.17	-1.6
REEF3D (CDS2)	Enhanced direct forcing IBM approach	0.82	3.48	0.16	-1.5
REEF3D (HCDS6)		0.82	3.48	0.17	-1.5
REEF3D (CDS2)	Local directional ghost cell approach	0.82	3.48	0.16	-1.5
REEF3D (HCDS6)		0.82	3.48	0.17	-1.5

Table 6.6: Positions of stagnation points for the mean flow around the wall-attached cube immersed in a laminar boundary layer.

6.2.2 Steady Non-axisymmetric Flow Past a Sphere

The flow of a viscous fluid past a stationary sphere can trigger instabilities with three-dimensional flow patterns, despite the body symmetry. However, unlike two-dimensional flows, such three-dimensional patterns introduce a level of complexity that is characterized by wake formation and vortical interactions. Despite its apparent simplicity, this scenario represents a canonical problem in the

family of immersed bluff body flows with numerous applications. This benchmark is extensively documented in scientific literature [128–130]. An enhanced direct forcing IBM and local directional ghost cell approaches implemented in the REEF3D framework are used to simulate the flow at $Re_D = 250$ (based on the free stream velocity U_∞ and the sphere diameter D) in a steady laminar regime. A large computational domain of $[-10D, 10D]$ is considered in all three spatial directions. The sphere center is positioned at a distance $8D$ from the inlet. A uniform grid spacing of $0.02D$ is generated within a rectangular refinement zone of $[4D \times 2D \times 2D]$ surrounding the sphere. To limit the mesh size, the cells are stretched with a growth ratio of 1.25 between the refined zone and the domain external boundaries, where the maximum cell size is $0.2D$. A Dirichlet boundary condition $u/U_\infty = 1, v = 0$ and $w = 0$ is applied at the inlet, and an outflow condition is imposed at the outlet boundary. A symmetry boundary condition is adopted for lateral directions, while a no-slip boundary condition is enforced on the sphere. To assess the performance of the numerical method, the drag (C_D) and lift (C_L) coefficients are compared with experimental data by Johnson and Patel [129]:

$$C_D = \frac{F_x}{\frac{1}{2}\rho U_\infty^2 \frac{\pi D^2}{4}} \quad (6.7)$$

$$C_L = \frac{F_y}{\frac{1}{2}\rho U_\infty^2 \frac{\pi D^2}{4}} \quad (6.8)$$

In Table 6.7, the results for drag and lift coefficients using both the standard second-order central differential scheme (CDS2) and the pseudo sixth-order central scheme (HCDS6) are presented. In the case of axisymmetric flow, the lift coefficient is naturally zero. Compared to the experimental data, the current approach can accurately compute steady drag and lift coefficients.

$Re_D = 250$	Method	C_D	C_L
Johnson and Patel [129]		0.7	0.062
REEF3D (CDS2)	Enhanced direct forcing IBM approach	0.7	0.054
REEF3D (HCDS6)		0.7	0.062
REEF3D (CDS2)	Local directional ghost cell approach	0.69	0.055
REEF3D (HCDS6)		0.68	0.059

Table 6.7: Drag and lift coefficients for a flow past a sphere at $Re_D = 250$.

For a qualitative comparison of this non-axisymmetric flow, the streamlines of

projected streamwise velocity in the $x - z$ and $y - z$ planes are shown in Figure 6.14. Although the flow is steady state, it is non-axisymmetric at $Re_D = 250$ with a plane of symmetry. The present IBM correctly replicates the streamlines center compared to Johnson and Patel [129]. The length of the recirculation bubble and the location of the vortex center are well reproduced. In order to accurately capture the wake structure, it is crucial to predict the precise location of the boundary layer separation. This becomes particularly challenging when dealing with smooth curved geometries like a sphere. Despite utilizing an isotropic and non-body conformal mesh, the IBM method was able to correctly predict this phenomenon. This capability holds significance in the context of building applications, especially when simulating the flow around moving objects such as occupants, which may exhibit similar flow characteristics.

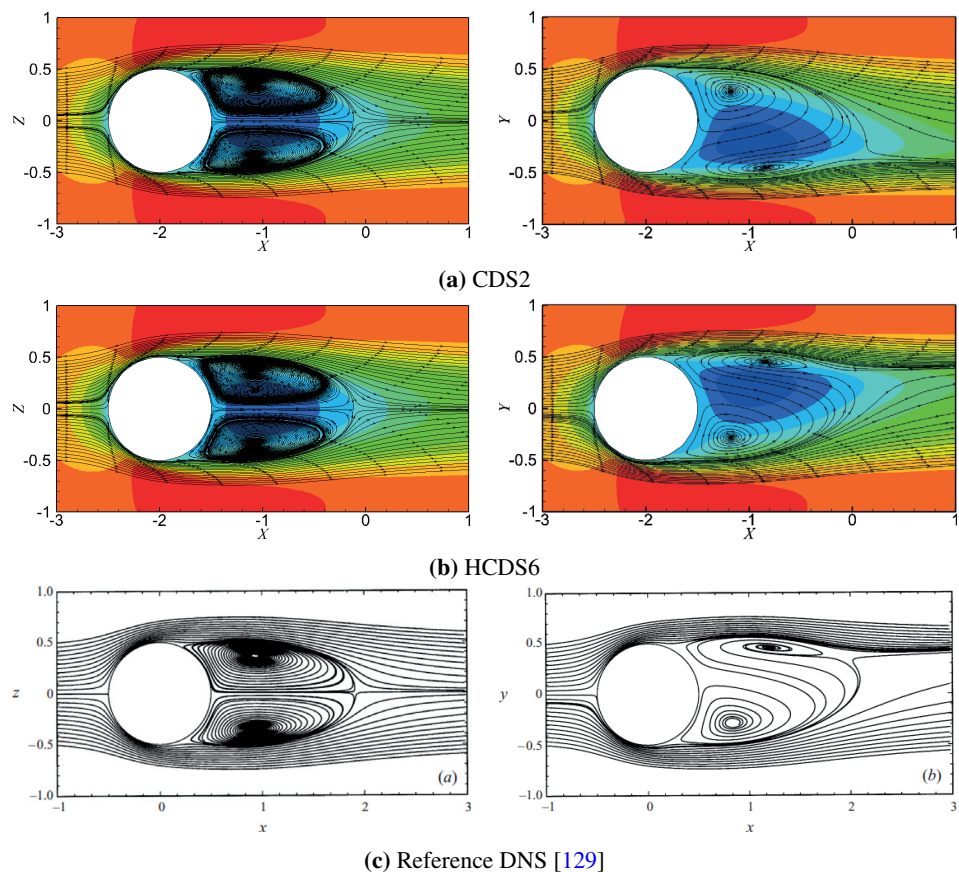


Figure 6.14: Streamlines of projected streamwise velocity for a flow past a sphere at $Re_D = 250$.

LES of the Contaminant Breach in Isolation Rooms with a Sliding Door

In the concluding test case, the potential of the framework outlined in Chapter 4 and its implementation within the REEF3D solver for indoor airflow applications are investigated.

7.1 Isolation Rooms with a Sliding Door

Containment failure due to the airflows induced by a door movement is a critical concern in environments requiring strict isolation measures, such as hospital isolation rooms. The door motion initiates complex airflow patterns that can lead to the escape of potentially contaminated air. This can be particularly vital in the presence of airborne pathogens, as it increases the risk of spreading infectious agents to adjacent spaces. Traditional hinged doors, commonly found in healthcare facilities, are known to exacerbate this issue. Sliding doors, on the other hand, have shown promise in mitigating containment failure by minimizing the airflows generated during operation. Understanding these airflow dynamics is necessary for designing effective containment strategies to ensure the safety of both patients and healthcare personnel. Although quantitative measurements such as tracer gas techniques offer valuable data on airflow leakage, they may provide limited insight into the detailed turbulent flow structures that are mainly developed within the doorway. Moreover, these experiments can be complex and

costly in terms of instrumentation setup and data collection. Alternatively, the CFD modeling using the LES approach overcomes the challenges associated with experimental measurements. Detailed visualization of airflow patterns by eliminating the need for full-scale mock-ups and specialized instrumentation can be provided by CFD simulations. However, the accuracy and reliability of airflow predictions during sliding door operations depends on the chosen numerical method

The flow induced by a sliding door was extensively studied by Saarinen et al. [95], employing both laboratory experiments and LES using ANSYS CFX 15.0. Their findings highlighted the inadequacy of URANS in accurately predicting this particular flow. The same setup as Saarinen et al. [95] is adopted here, maintaining consistency with their test cases and utilizing their solution as a reference. The experimental setup involves two identical isothermal rooms without ventilation, namely the isolation room and the anteroom, interconnected by a sliding door situated in the middle of a partition wall. The dimensions of each room are $3.0 \times 4.7 \times 4.0 m^3$ ($H \times W \times D$), as shown in Figure 7.1. The smallest width and height of the doorway are 1.1 and 2.06 m, respectively, with a frame thickness of 0.1 m. The door is 1.22 m wide, 2.125 m high, and has a thickness of 0.055 m.

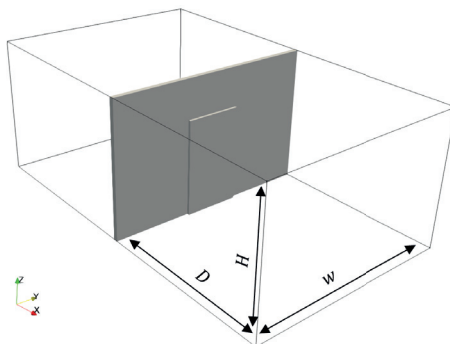


Figure 7.1: The geometry of the isolation room and anteroom connected via a sliding door.

The sequence of door operation involves two movement phases separated by a waiting period. First, the door slides open for a duration of three seconds, covering a distance of 1.2 m linearly towards the negative y direction. The door is held fully open for nine seconds. Finally, it starts closing and reaches the initial position after five seconds. The simulation is continued for a period of ten seconds to monitor the gradual airflow dissipation.

Similar to Saarinen et al. [95], the WALE SGS model is adopted in this simulation. To limit the mesh size, the computational grid is refined uniformly

within a volume of $[x = 0.4\text{ m} \times y = 1.5\text{ m} \times z = 2.2\text{ m}]$ surrounding the doorway where the unsteady vortical structures are generated. A smooth transition is performed away from the refined zone up to the domain boundaries with a growth ratio of 1.15. To study grid independence, four different grid resolutions of $\Delta x = \Delta y = \Delta Z = 0.0025, 0.005, 0.00625,$ and 0.01 m are adopted in the refined volume for the ultrafine, fine, intermediate, and coarse grid, respectively. A no-slip boundary condition is applied to the room walls, including the separating wall and sliding door. Zero velocity components are initialized everywhere within two rooms. Consequently, each room serves as a large reservoir, and the airflow patterns are solely driven by the door motion. A constant time step of 4 ms is chosen to resolve temporal variation while ensuring the numerical stability of the simulation by maintaining the CFL below one.

7.1.1 Vortical Structures

To visualize the rotational motion and shear flow generated by the sliding door, the vertical component of vorticity derived from the lateral gradients of velocity components $(\nabla \times u)_z$ is shown in Figure 7.2. The vorticity field is depicted when the door has fully opened and is extracted on a plane 1 m above the floor. The opening of the door generates a wake with flow instabilities. The LES performed by Saarinen et al. [95] using a fine grid is shown in Figure 7.2(h) and is in line with flow visualization during their experiments. REEF3D accurately reproduces all number of vortices generated within the doorway on both intermediate and fine mesh resolutions, particularly when the new spatial discretization scheme (HCDS6) is employed. It should be noted that a direct comparison of accuracy with the LES of Saarinen et al. [95] is not feasible, given their omission of information regarding mesh size near the door in their refined 15.6 M nodes mesh. Nonetheless, the coarse mesh used in this study maintains an equivalent grid size of 0.01 m in proximity to the door, akin to the 10.7 M nodes mesh employed by Saarinen et al. [95].

On the coarse mesh resolution, the limitations of the bounded second-order central difference scheme in ANSYS Fluent and the CDS2 in REEF3D are evident in their inability to accurately represent main flow structures. In contrast, the HCDS6 scheme demonstrates a better capability to capture the main features of these structures despite the presence of significant aliasing errors visible in the form of waves. This is attributed to the coarse mesh used, particularly compared to the door width. Additionally, it is noteworthy that the HCDS6 scheme, without artificial numerical dissipation, contributes to the observed aliasing errors.

With further mesh refinement to a cell size of 0.00625 m in the refined zone (intermediate mesh), the performance of the CDS2 scheme exhibits significant

improvement. It now demonstrates enhanced capability in capturing vortices within the doorway, compared to the coarse grid. Despite this improvement, some residual aliasing errors are still noticeable in the solution. Conversely, when employing the HCDS6 scheme on the intermediate mesh, aliasing errors are considerably reduced, resulting in a smoother visualization of the interaction of vortices. Although the solution of Saarinen et al. [95] reveals improved capture of vortices on a fine mesh (Figure 7.2(h)), the solution remains somewhat inaccurate. Some details are still smeared when compared with the HCDS6 solution (Figure 7.2(d)). Even with further improvements in the CDS2 solution on our fine mesh, which are achieved by reducing aliasing errors and refining the vortical structure shape, it remains incapable of accurately reproducing the correct position of rotational structures.

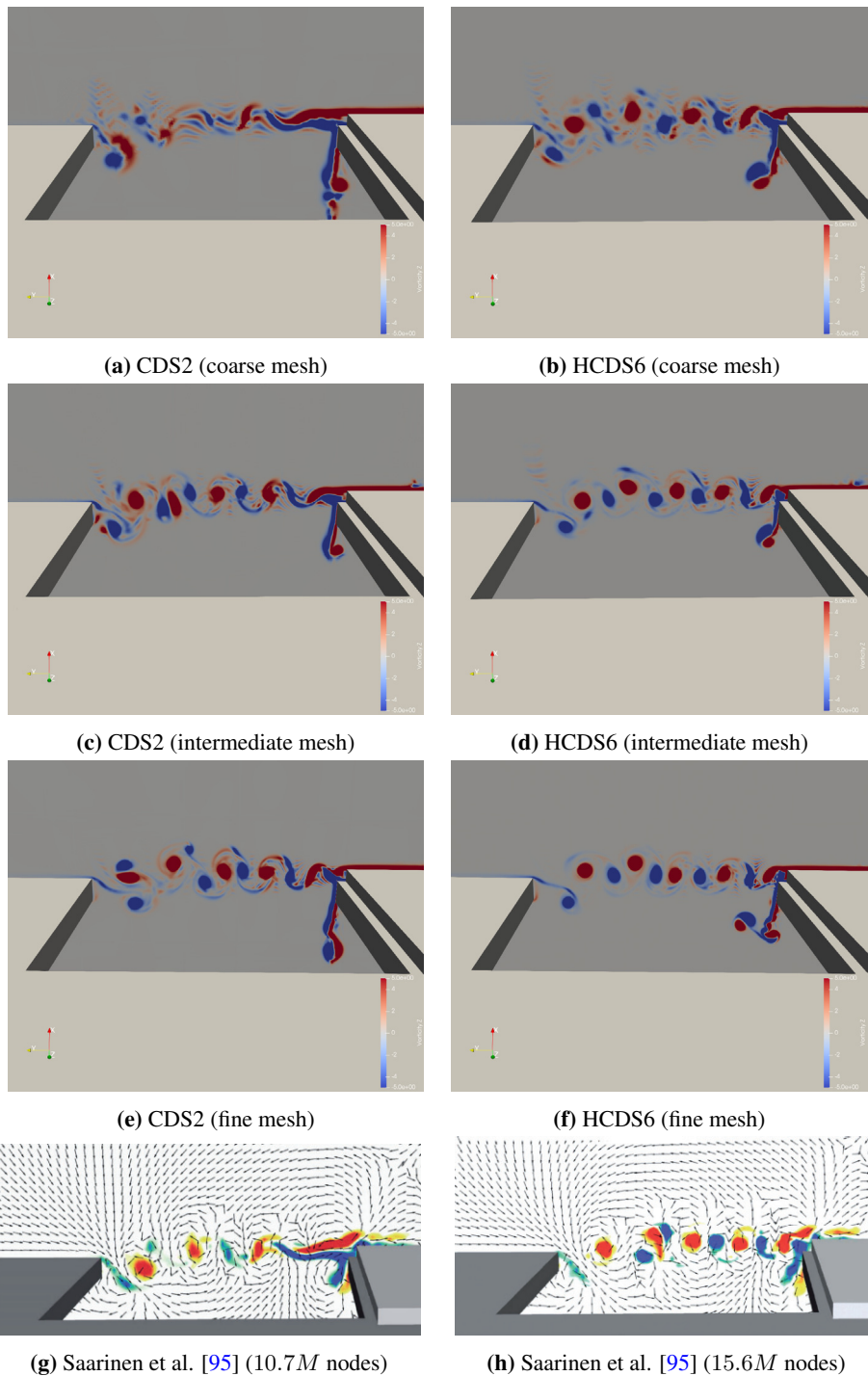


Figure 7.2: Contours of the vertical component of vorticity ($\nabla \times u)_z$ at the end of door opening stage.

7.1.2 Air Volume Migration

The flow dynamics induced by door motion in the proximity of the doorway can be examined in detail using tracer gas. Moreover, the effect of cross-doorway airflow behavior on airborne particles and infectious droplet nuclei leading to possible containment failure can easily be characterized by dosing gases into the isolation room and anteroom. Similar to Saarinen et al. [95], the tracer gas is modeled as a passive scalar concentration with a kinematic diffusivity of $1e - 5 m^2/s$ [131] in REEF3D. The turbulent Schmidt number (S_{c_t}) is set at a value of 0.9 to treat turbulent diffusive flux. The volume of air passing through the doorway from the isolation room to the anteroom as a function of time during the door cycle can be calculated using a gaseous contaminant dosed in the isolation room:

$$\Delta V(t)_{\text{isolation room} \rightarrow \text{anteroom}} = \frac{\Delta m(t)}{C_{\text{isolation room}}(t_0)} \quad (7.1)$$

The migrated mass of the gaseous contaminant (Δm) is obtained by integrating the tracer mass concentration (C) over the volume of anteroom:

$$\Delta m(t)_{\text{isolation room} \rightarrow \text{anteroom}} = \iiint_V^{\text{anteroom}} C(x, y, z, t) dV \quad (7.2)$$

Time evolution of Air Volume Migration (AVM) quantifies how rapidly the air volume in the isolation room is escaping to the anteroom at different phases of the door cycle. The amount of air volume migrated from the isolation room to the anteroom over time is plotted in Figure 7.3 for the different grid sizes.

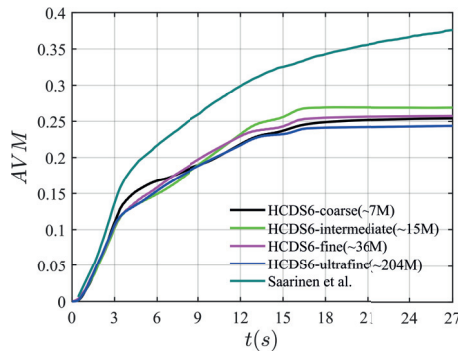


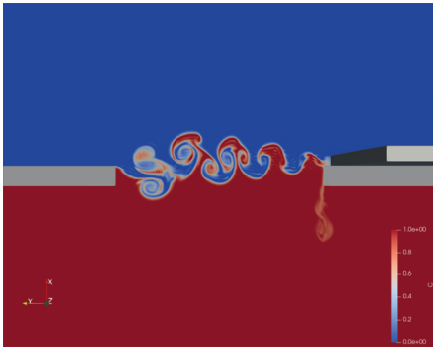
Figure 7.3: Time evolution of the AVM during the sliding door operation cycle.

The flow instabilities near the doorway trigger the migration flow rate in the

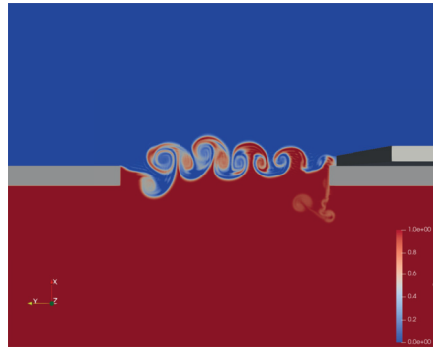
initial stage of the door opening. The intense volume of air passing through the doorway from the isolation room to the anteroom at the beginning can also be attributed to the piston effect induced by the moving door sliding within the anteroom. Consequently, the AVM increases quickly from 0 to 3 seconds when the door opens. The solution for the HCDS6 is identical during this opening phase for the four meshes. During the waiting period, when the sliding door is held open, a gradual increase in the migrated air volume is predicted due to the diffusion of turbulent vortices induced by the opening door motion. Consequently, the AVM continues to increase for the 9 seconds during which the door is held open (until $t = 12\text{ s}$). The rate of AVM increase gradually diminishes over the subsequent 5 seconds as the door begins to close (until $t = 17\text{ s}$). Once the door is fully closed, the AVM remains constant. It is worth noting that the AVM evaluated by Saarinen et al. [95] is very similar during the opening phase. However, after this phase, their predicted value is significantly higher than in our simulations. Surprisingly, their AVM keeps increasing when the door is closed after $t = 17\text{ s}$ while it should remain constant as predicted by the present LES. It questions the conservation properties of scalar quantities in their numerical method, including IBM.

7.1.3 Passive Scalar Concentration

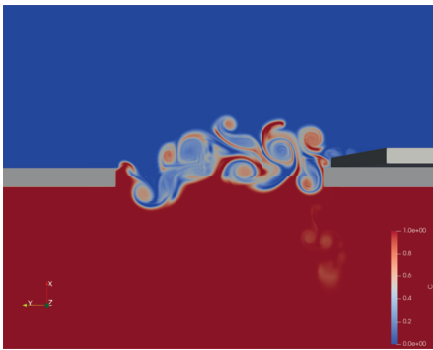
In order to visualize the transient structures arising from the dynamic operation of the sliding door, Figure 7.4 presents contours of passive scalar concentration on a plane situated 1 m above the floor. These contours depict specific time intervals – namely, immediately after the door has fully opened ($t = 3\text{ s}$), during the initial stages of closure ($t = 12\text{ s}$), and after the door has completely closed ($t = 17\text{ s}$). It is evident that the precision of the spatial discretization scheme to treat the convective term plays a key role in achieving an accurate solution. The HCDS6 scheme exhibits superior resolution of flow structures, leading to notable distinctions in flow patterns when compared to the CDS2 scheme over an extended duration. This highlights the advantage of employing an orthogonal grid, enabling the derivation of numerical schemes with enhanced accuracy, which is particularly beneficial for modeling transitional airflows within building environments.



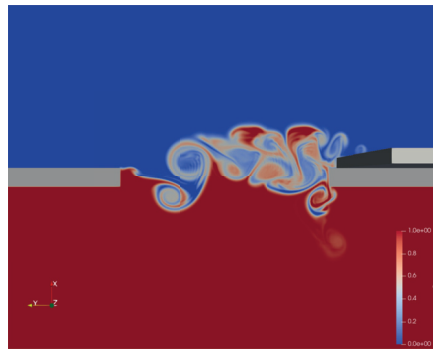
(a) CDS2 ($t = 3s$)



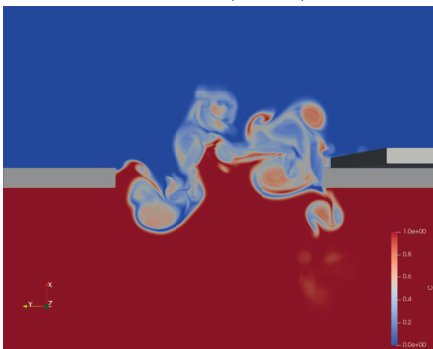
(b) HCDS6 ($t = 3s$)



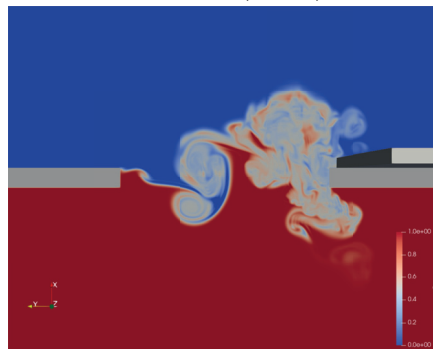
(c) CDS2 ($t = 6s$)



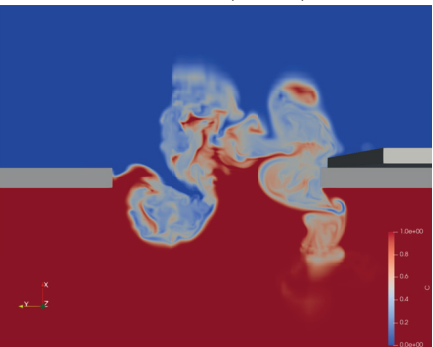
(d) HCDS6 ($t = 6s$)



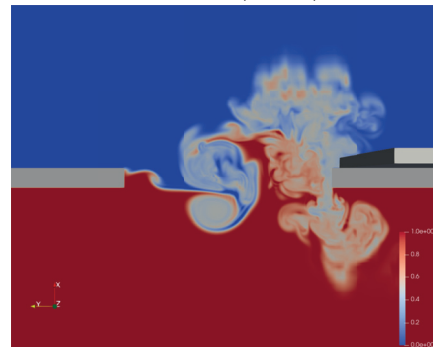
(e) CDS2 ($t = 9s$)



(f) HCDS6 ($t = 9s$)



(g) CDS2 ($t = 12s$)



(h) HCDS6 ($t = 12s$)

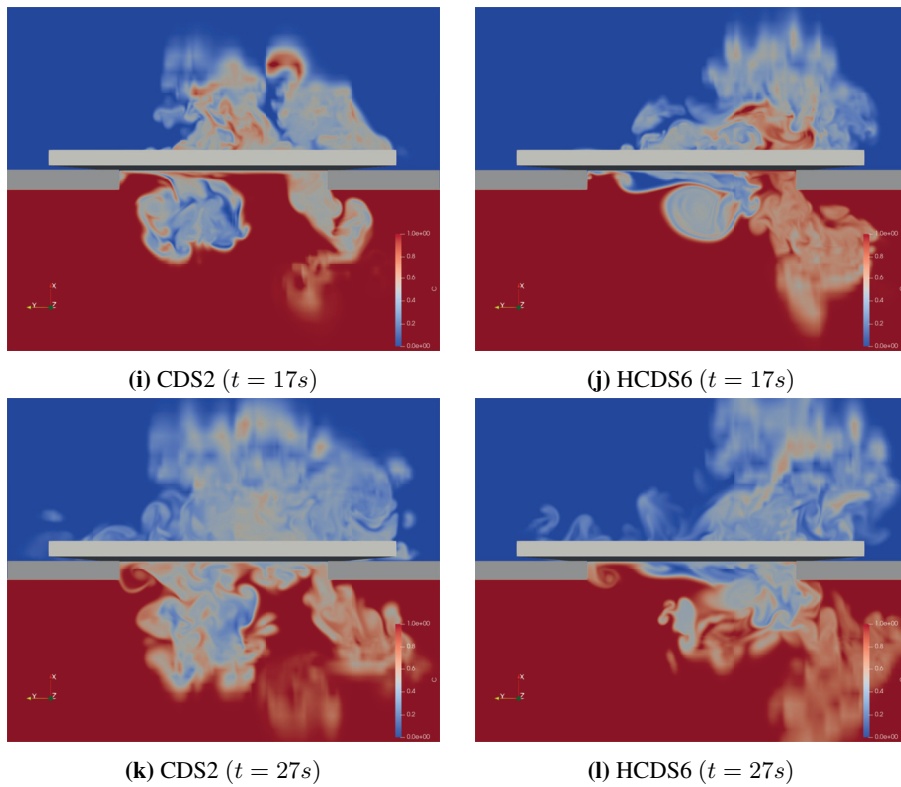


Figure 7.4: Contours of the passive scalar concentration at six different door opening stages using CDS2 (left) and HCDS6 (right).

Conclusions and Outlook

In the first part of the thesis, a comparative assessment between LES and RANS was conducted, focusing on two critical ventilation benchmarks: the cavity flow and density-driven flow through a doorway. In the case of the cavity flow, LES proved to be more universal than RANS in the sense that the same turbulence model can be used across transitional and fully turbulent flow regimes. In the case of density-driven flow through a doorway, the choice of turbulence model had minimal impact on the time-averaged flow. Nevertheless, LES revealed several unsteady flow phenomena that are not captured by the RANS approach, such as interfacial mixing between warm and cold airstreams.

A main conclusion from the literature review and the analysis of the doorway case highlighted that a very regular mesh is needed to guarantee stability and accuracy and minimize artificial diffusion. This conclusion led to the second and main part of the thesis. Given this strong constraint on the mesh, the Ph.D. thesis explored the potential of LES on orthogonal grids as a viable alternative to conventional flow solvers like Fluent or OpenFOAM. The thesis discussed the advantages and drawbacks leveraged by orthogonal grids where the geometrical complexity is addressed using the IBM.

8.1 Main Achievements

The main achievements of this study can be summarized as follows:

- An Optimized Numerical Framework for Indoor Airflow Simulations: In conclusion, a numerical framework based on the REEF3D solver optimized

for orthogonal non-conformal grids has been successfully implemented for accurate and efficient indoor airflow simulations. The precise adaptation of the REEF3D solver has not only demonstrated its flexibility but has also highlighted the need for tailored approaches in the context of CFD.

- **Advantages of Orthogonal Grids and Spatial Discretization:** The opportunity to extend the numerical stencil and implement high-order non-dissipative spatial discretization schemes offered by orthogonal grids can enhance numerical accuracy by minimizing truncation errors. The advantages inherent in these grids have not only enhanced our understanding of discretization accuracy but have also positioned them as a valuable alternative to conventional central schemes, particularly in the context of high-resolution explicit LES. The optimization of spatial discretization on orthogonal grids emerged as a pivotal achievement in this study. A new low-dispersion central scheme for the convective term was developed to perform explicit LES on staggered grids. The evaluation of the new finite difference scheme on both uniform and non-uniform staggered grids indicated that the proposed scheme is more accurate than the standard second-order scheme and has a compact numerical stencil compared to existing fourth-order kinetic energy-conserving schemes. In a grid-convergence analysis for the advection of an isentropic vortex, the RMS of the vortex velocity using the HCDS6 scheme was reduced by two orders of magnitude compared to the standard second-order central scheme. For the Taylor-Green vortex flow, vortical structures were visualized and compared with a DNS reference solution. Here, these structures were better captured by the HCDS6 than by the standard second-order scheme. The under-resolved turbulent channel flow benchmark was a challenging case for investigating the stability and accuracy of the scheme on a non-uniform grid. Simulations showed that the HCDS6 remains stable even if the simulations are getting highly under-resolved. The flow statistics were comparable to the standard second-order scheme, strictly conserving discrete kinetic energy. It proved that, even though the HCDS6 does not strictly conserve the discrete kinetic energy, it does not affect the numerical stability and flow statistics. The new scheme is thus an alternative to the existing central scheme for incompressible flow simulation on a staggered grid. It can facilitate the use of staggered grids in combination with complex geometries modeled using IBM.
- **Transitional Flows and Validation of Immersed Boundary Method:** A noteworthy contribution lies in the ability of the proposed framework to adeptly capture transitional flows, even under coarser mesh resolutions.

This resilience speaks for the efficiency of the employed enhanced direct forcing and ghost cell IBM, validated through simulations depicting detached flows around a sphere and a wall-attached cube at $Re_D = 250$ and $Re_H = 500$, respectively.

- **Moving Objects Simulation and Practical Applications:** Despite the extensive studies on building ventilation and airflow patterns during the pandemic, many have relied on steady-state assumptions, neglecting dynamic events like door movements. The simulation of moving objects, exemplified by the sliding door test case, has showcased the practical applicability of the enhanced direct forcing Immersed Boundary Method. Its elegant treatment of dynamic scenarios using a fixed mesh, without resorting to complex re-meshing techniques, positions it as a promising tool for real-world applications, especially in scenarios involving varying airflow dynamics.

8.2 Future Work and Perspectives

As we conclude this chapter, it is imperative to delineate promising avenues for future research.

- While the presented test cases serve to showcase the applicability of the framework within REEF3D for indoor airflow scenarios, additional test cases could provide deeper insights into its capabilities. Exploring scenarios involving thermal plumes, for instance, should be investigated, given their key role in indoor airflow dynamics [132]. One test case of a human thermal plume has been successfully validated by Choi et al. [93], using structured grids and IBM.
- The resolution of the mesh was limited along the walls to maintain the feasibility of explicit time integration, thereby avoiding the need for semi-implicit methods. Future research should explore and assess the implementation of fully implicit time integration. In scenarios featuring airflow inlets, considerations for mesh refinement near these inlets, where the velocity magnitude is high, may be necessary. This is particularly relevant in cases such as a cavity flow with a slot inlet, where severe time step conditions based on the CFL criterion must be observed [13]. By employing an orthogonal mesh refined in the wall-normal direction, the high-velocity air entering through the slot will cross well-refined cells, thereby posing challenges to the time step due to the strict CFL condition. Adopting fully implicit time integration becomes a viable solution to release this constraint.

- An essential consideration is the computational time, which is an aspect that is not explicitly addressed and compared with general-purpose solvers in this study. The focus remains on showcasing that the proposed approach achieves comparable accuracy with fewer grid points than conventional flow solvers. The intricate nature of comparing computational times across different flow solvers necessitates dedicated benchmarks that offer a comprehensive description of simulation setups and parameters – an undertaking that is reserved for future endeavors.
- This study did not investigate cases with wall functions to assess the performance of wall-modeled LES. The test cases investigated in this thesis have a moderate Reynolds number. Wall functions are thus imperative in order to extend the application for higher Reynolds numbers. The implementation and in-depth investigation of wall functions emerge as a crucial next step, offering an opportunity to delve into the intricacies of boundary layer interactions within the proposed framework. This exploration is anticipated to further refine the understanding of airflow dynamics, especially in indoor environments. The RANS-LES, in combination with IBM and wall functions, is also a valuable topic of investigation, as it would significantly reduce the mesh size requirement for boundary layers and, consequently, computational costs.
- The sliding door case shows that aliasing errors may occur in highly under-resolved simulations with a pure central scheme (which is expected). In future work, the scheme could be complemented by a controlled amount of artificial numerical dissipation to address this phenomenon. As the numerical stencil has seven points in each spatial direction, it is indeed possible to tailor a high-order dissipation term (sometimes called hyperdiffusion term) that will only be active on the smallest resolved scales of the mesh, in line with the concept of explicit LES. An example of such a hyper-dissipative term is the fifth-order scheme with a sixth-order spatial derivative of velocity in the flow solver PENCIL [133]. Such a hyperdiffusion term cannot be easily implemented in a general-purpose flow solver.

Declaration of Generative AI and AI-assisted Technologies in the Writing Process

During the preparation of this work, the author used OpenAI's ChatGPT to enhance the readability and fluency of the text. This AI-assisted technology was employed solely to improve the language and clarity of the manuscript. After using ChatGPT, the author carefully reviewed and edited the content as needed and takes full responsibility for the entirety of the content in this publication.

Bibliography

- [1] Peter V Nielsen. “Fifty years of CFD for room air distribution”. In: *Building and Environment* 91 (2015), pp. 78–90.
- [2] Bert Blocken. “LES over RANS in building simulation for outdoor and indoor applications: A foregone conclusion?” In: *Building Simulation*. Vol. 11. 5. Springer. 2018, pp. 821–870.
- [3] Hans Bihs, Arun Kamath, Mayilvahanan Alagan Chella, Ankit Aggarwal and Øivind A Arntsen. “A new level set numerical wave tank with improved density interpolation for complex wave hydrodynamics”. In: *Computers & Fluids* 140 (2016), pp. 191–208.
- [4] Qingyan Chen. “Ventilation performance prediction for buildings: A method overview and recent applications”. In: *Building and Environment* 44.4 (2009), pp. 848–858.
- [5] Liangzhu Leon Wang and Qingyan Chen. “Evaluation of some assumptions used in multizone airflow network models”. In: *Building and Environment* 43.10 (2008), pp. 1671–1677.
- [6] Ahmed Chérif Megri and Fariborz Haghghat. “Zonal modeling for simulating indoor environment of buildings: Review, recent developments, and applications”. In: *Hvac&R Research* 13.6 (2007), pp. 887–905.
- [7] EJ Teshome and F F. Haghghat. “Zonal models for indoor air flow-A critical review”. In: *International Journal of Ventilation* 3.2 (2004), pp. 119–129.

- [8] Wangda Zuo and Qingyan Chen. “Fast and informative flow simulations in a building by using fast fluid dynamics model on graphics processing unit”. In: *Building and Environment* 45.3 (2010), pp. 747–757.
- [9] Jiri Blazek. *Computational fluid dynamics: principles and applications*. Butterworth-Heinemann, 2015.
- [10] MV Pham, FDKS Plourde and KS Doan. “Direct and large-eddy simulations of a pure thermal plume”. In: *Physics of Fluids* 19.12 (2007).
- [11] Peter V Nielsen. “Berechnung der Luftbewegung in einem zwangsbelüfteten Raum”. In: *GI-Gesundheits Ingenieur* (1973), p. 299.
- [12] Peter V Nielsen. “Flow in air conditioned rooms: Model experiments and numerical solution of the flow equations”. PhD thesis. Denmark: Technical University of Denmark, 1974.
- [13] Peter V Nielsen, A Restivo and JH Whitelaw. “The velocity characteristics of ventilated rooms”. In: *Journal of Fluids Engineering* 100.3 (1978), pp. 291–298.
- [14] Peter V Nielsen, A Restivo and JH Whitelaw. “Buoyancy-affected flows in ventilated rooms”. In: *Numerical Heat Transfer* 2.1 (1979), pp. 115–127.
- [15] AD Gosman, PV Nielsen, A Restivo and JH Whitelaw. “The flow properties of rooms with small ventilation openings”. In: *Journal of Fluids Engineering* 102.3 (1980), pp. 316–323.
- [16] Shuzo Murakami and Shinsuke Kato. “Numerical and experimental study on room airflow—3-D predictions using the $k - \varepsilon$ turbulence model”. In: *Building and Environment* 24.1 (1989), pp. 85–97.
- [17] HB Awbi. “Application of computational fluid dynamics in room ventilation”. In: *Building and environment* 24.1 (1989), pp. 73–84.
- [18] PJ Jones and GE Whittle. “Computational fluid dynamics for building air flow prediction—current status and capabilities”. In: *Building and Environment* 27.3 (1992), pp. 321–338.
- [19] Mathieu Barbason and Sigrid Reiter. “About the choice of a turbulence model in building physics simulations”. In: *7th Conference on Indoor Air Quality, Ventilation and Energy Conservation in buildings (IAQVEC 2010)*. 2010.
- [20] Zhiqiang John Zhai, Zhao Zhang, Wei Zhang and Qingyan Yan Chen. “Evaluation of various turbulence models in predicting airflow and turbulence in enclosed environments by CFD: Part 1—Summary of prevalent turbulence models”. In: *Hvac&R Research* 13.6 (2007), pp. 853–870.

-
- [21] Twan van Hooff, Bert Blocken and GJF Van Heijst. “On the suitability of steady RANS CFD for forced mixing ventilation at transitional slot Reynolds numbers”. In: *Indoor Air* 23.3 (2013), pp. 236–249.
- [22] Miao Wang and Qingyan Chen. “Assessment of various turbulence models for transitional flows in an enclosed environment (RP-1271)”. In: *Hvac&R Research* 15.6 (2009), pp. 1099–1119.
- [23] Dan Nørtoft Sørensen and Peter Vilhelm Nielsen. “Quality control of computational fluid dynamics in indoor environments.” In: *Indoor Air* 13.1 (2003), pp. 2–17.
- [24] Y Sakamoto and Y Matsuo. “Numerical predictions of three-dimensional flow in a ventilated room using turbulence models”. In: *Applied Mathematical Modelling* 4.1 (1980), pp. 67–72.
- [25] K Hibi, S Murakami and A Mochida. “Prediction of room air flow by means of large eddy simulation”. In: *Summaries of Technical Papers of Annual Meeting, Architectural Institute of Japan*. 1985.
- [26] S Murakami, A Mochida and K Hibi. “3-D numerical simulation of room convection by means of large eddy simulation”. In: *Proceedings of Technical Display for NBS/CBT Building Technology Symposium, Room Convection and Indoor Air Quality Simulation Modelling, NBS Administration Building, Gaithersburg, MD, USA*. 1986.
- [27] Peter V Nielsen. “The selection of turbulence models for prediction of room airflow”. In: *ASHRAE Transactions* 104 (1998), pp. 1119–1127.
- [28] Qingyan Chen and Jelena Srebric. *How to Verify, Validate, and Report Indoors Environment Modeling CFD Analyses*. ASHRAE, 2001.
- [29] Dan Nørtoft Sørensen and Peter Vilhelm Nielsen. “Guest editorial: CFD in indoor air”. In: *Indoor Air* 13.1 (2003), p. 1.
- [30] Zhao Zhang, Wei Zhang, Zhiqiang John Zhai and Qingyan Yan Chen. “Evaluation of various turbulence models in predicting airflow and turbulence in enclosed environments by CFD: Part 2—Comparison with experimental data from literature”. In: *Hvac&R Research* 13.6 (2007), pp. 871–886.
- [31] Twan van Hooff, Bert Blocken and Yoshihide Tominaga. “On the accuracy of CFD simulations of cross-ventilation flows for a generic isolated building: Comparison of RANS, LES and experiments”. In: *Building and Environment* 114 (2017), pp. 148–165.

- [32] Ariane Frère, Koen Hillewaert, Philippe Chatelain and Grégoire Winckelmans. “High Reynolds number airfoil: from wall-resolved to wall-modeled LES”. In: *Flow, Turbulence and Combustion* 101 (2018), pp. 457–476.
- [33] Elyas Larkermani, Vegard Mikkelsen Bjerkeli and Laurent Georges. “Comparing the performance of RANS turbulence models between different cavity flow benchmarks”. In: *Proceedings ROOMVENT CONFERENCE. 16TH 2022.(ROOMVENT 2022)(2 PARTS) Item#: 065443 Held 16-19 September 2022, Xi’an, China*. EDP Sciences. 2022.
- [34] Peter V Nielsen. “Specification of a two-dimensional test case.” In: *International Energy Agency (IEA), Energy Conservation in Buildings and in Community Systems. Annex 20: Air Flow Pattern Within Buildings. No. 1.45. Internal Report, ISSN 0902-7513 R9040* (1990).
- [35] N Vogl and U Renz. “Simulation of simple test cases”. In: *International Energy Agency (IEA), Energy Conservation in Buildings and in Community Systems. Annex 20: Air Flow Pattern Within Buildings. No. 1.46*. (1991). URL: <https://www.cfd-benchmarks.com>.
- [36] Qingyan Chen. “Comparison of different $k-\varepsilon$ models for indoor air flow computations”. In: *Numerical Heat Transfer, Part B Fundamentals* 28.3 (1995), pp. 353–369.
- [37] Q Chen. “Prediction of room air motion by Reynolds-stress models”. In: *Building and Environment* 31.3 (1996), pp. 233–244.
- [38] Lars Peter Kølgaard Voigt. “Navier-Stokes simulations of airflow in rooms and around a human body”. PhD thesis. Denmark: Technical University of Denmark, 2001.
- [39] L. Rong and P. V. Nielsen. *Simulation with Different Turbulence Models in an Annex 20 Room Benchmark Test Using Ansys CFX 11.0*. DCE Technical reports 46. Department of Civil Engineering, Aalborg University, 2008.
- [40] D Blay. “Confined turbulent mixed convection in the presence of horizontal buoyant wall jet”. In: *HTD Vol. 213, Fundamentals of Mixed Convection* (1992).
- [41] Twan van Hooff, Bert Blocken, Thijs Defraeye, Jan Carmeliet and GJF Van Heijst. “PIV measurements of a plane wall jet in a confined space at transitional slot Reynolds numbers”. In: *Experiments in Fluids* 53 (2012), pp. 499–517.

- [42] Bert Blocken. “Computational Fluid Dynamics for urban physics: Importance, scales, possibilities, limitations and ten tips and tricks towards accurate and reliable simulations”. In: *Building and Environment* 91 (2015), pp. 219–245.
- [43] Javad Taghinia, Md Mizanur Rahman, Timo Siikonen and Ramesh K Agarwal. “One-equation sub-grid scale model with variable eddy-viscosity coefficient”. In: *Computers & Fluids* 107 (2015), pp. 155–164.
- [44] MA Zasimova, NG Ivanov and D Markov. “Numerical modeling of air distribution in a test room with 2D sidewall jet. II. LES-computations for the room with finite width,” in: *St. Petersburg Polytechnical State University Journal. Physics and Mathematics* 13.3 (2020), pp. 65–79.
- [45] Twan van Hooff, Bert Blocken, P Gousseau and GJF van Heijst. “Counter-gradient diffusion in a slot-ventilated enclosure assessed by LES and RANS”. In: *Computers & Fluids* 96 (2014), pp. 63–75.
- [46] T. Van Hooff, B. Blocken and G.J.F. Van Heijst. *Mixing ventilation flow in an enclosure driven by a transitional wall jet*. URL: https://www.kbwiki.ercoftac.org/w/index.php/Abstr:UFR_4-20.
- [47] Simon Bjuri, Elyas Larkermani and Laurent Georges. “Influence of the Inlet Boundary Conditions on the LES Performance for the Cavity Flow Benchmark”. In: *Proceedings ROOMVENT CONFERENCE*. Stockholm, Sweden, Apr. 2024.
- [48] Stephen B Pope. “Ten questions concerning the large-eddy simulation of turbulent flows”. In: *New Journal of Physics* 6.1 (2004), p. 35.
- [49] Elyas Larkermani, Guangyu Cao and Laurent Georges. “Characterization of the density-driven counter-flow through a doorway using Large Eddy Simulation”. In: *Building and Environment* 221 (2022), p. 109319.
- [50] Farzad Bazdidi-Tehrani, Shahin Masoumi-Verki and Payam Gholamalipour. “Impact of opening shape on airflow and pollutant dispersion in a wind-driven cross-ventilated model building: Large eddy simulation”. In: *Sustainable Cities and Society* 61 (2020), p. 102196.
- [51] David W Etheridge and Mats Sandberg. *Building ventilation: theory and measurement*. Vol. 50. John Wiley & Sons Chichester, UK, 1996.
- [52] F Allard and Y Utsumi. “Airflow through large openings”. In: *Energy and Buildings* 18.2 (1992), pp. 133–145.
- [53] DJ Wilson and DE Kiel. “Gravity driven counterflow through an open door in a sealed room”. In: *Building and Environment* 25.4 (1990), pp. 379–388.

- [54] Joanna Polak. “Experimental study of the airflow distribution in a room with heating equipment”. MA thesis. NTNU, 2015.
- [55] L Georges, G Cao and HM Mathisen. “Further Investigation of the Convective Heat Transfer between Rooms through Open Doorways”. In: *the 12th REHVA World Congress*. Vol. 5. 2016.
- [56] Adrien Lefauve, JL Partridge and PF Linden. “Regime transitions and energetics of sustained stratified shear flows”. In: *Journal of Fluid Mechanics* 875 (2019), pp. 657–698.
- [57] Gopal Robert Yalla. “Numerical discretization effects in large eddy simulation of turbulence”. PhD thesis. University of Texas at Austin, 2022.
- [58] AG Kravchenko and Parviz Moin. “On the effect of numerical errors in large eddy simulations of turbulent flows”. In: *Journal of Computational Physics* 131.2 (1997), pp. 310–322.
- [59] Sandip Ghosal. “An analysis of numerical errors in large-eddy simulations of turbulence”. In: *Journal of Computational Physics* 125.1 (1996), pp. 187–206.
- [60] John W Glendening and Tracy Haack. “Influence of advection differencing error upon large-eddy simulation accuracy”. In: *Boundary-Layer Meteorology* 98 (2001), pp. 127–153.
- [61] Fotini Katopodes Chow and Parviz Moin. “A further study of numerical errors in large-eddy simulations”. In: *Journal of Computational Physics* 184.2 (2003), pp. 366–380.
- [62] Jessica Gullbrand and Fotini Katopodes Chow. “The effect of numerical errors and turbulence models in large-eddy simulations of channel flow, with and without explicit filtering”. In: *Journal of Fluid Mechanics* 495 (2003), pp. 323–341.
- [63] Claudio Canuto, M Yousuff Hussaini, Alfio Quarteroni and Thomas A Zang. *Spectral methods: fundamentals in single domains*. Springer Science & Business Media, 2007.
- [64] Santhanam Nagarajan, Sanjiva K Lele and Joel H Ferziger. “A robust high-order compact method for large eddy simulation”. In: *Journal of Computational Physics* 191.2 (2003), pp. 392–419.
- [65] Sylvain Laizet and Eric Lamballais. “High-order compact schemes for incompressible flows: A simple and efficient method with quasi-spectral accuracy”. In: *Journal of Computational Physics* 228.16 (2009), pp. 5989–6015.

-
- [66] Omar A Mahfoze and Sylvain Laizet. “Non-explicit large eddy simulations of turbulent channel flows from $Re_\tau = 180$ up to $Re_\tau = 5,200$ ”. In: *Computers & Fluids* 228 (2021), p. 105019.
- [67] Rajat Mittal and Gianluca Iaccarino. “Immersed Boundary Methods”. In: *Annual Review of Fluid Mechanics* 37 (2005), pp. 239–261.
- [68] Francis H Harlow. “MAC numerical calculation of time-dependent viscous incompressible flow of fluid with free surface”. In: *Physics of Fluids* 8 (1965), p. 12.
- [69] FE Ham, FS Lien and AB Strong. “A fully conservative second-order finite difference scheme for incompressible flow on nonuniform grids”. In: *Journal of Computational Physics* 177.1 (2002), pp. 117–133.
- [70] P Moin and R Verzicco. “On the suitability of second-order accurate discretizations for turbulent flow simulations”. In: *European Journal of Mechanics-B/Fluids* 55 (2016), pp. 242–245.
- [71] P Orlandi. “A numerical method for direct simulation of turbulence in complex geometries”. In: *Annual Research Briefs, 1989* (1990), pp. 215–229.
- [72] Matthieu Duponcheel, Paolo Orlandi and Grégoire Winckelmans. “Time-reversibility of the Euler equations as a benchmark for energy conserving schemes”. In: *Journal of Computational Physics* 227.19 (2008), pp. 8736–8752.
- [73] Eugenia Kálnay de Rivas. “On the use of nonuniform grids in finite-difference equations”. In: *Journal of Computational Physics* 10.2 (1972), pp. 202–210.
- [74] Zhenfu Tian, Xian Liang and Peixiang Yu. “A higher order compact finite difference algorithm for solving the incompressible Navier–Stokes equations”. In: *International Journal for Numerical Methods in Engineering* 88.6 (2011), pp. 511–532.
- [75] Youhei Morinishi. “Conservative properties of finite difference schemes for incompressible flow”. In: *Center for Turbulence Research Annual Research Briefs: 1995* (1995).
- [76] Yohei Morinishi, Thomas S Lund, Oleg V Vasilyev and Parviz Moin. “Fully conservative higher order finite difference schemes for incompressible flow”. In: *Journal of Computational Physics* 143.1 (1998), pp. 90–124.

- [77] RWCP Verstappen and AEP Veldman. “Spectro-consistent discretization of Navier-Stokes: a challenge to RANS and LES”. In: *Floating, Flowing, Flying: Pieter J. Zandbergen’s Life as Innovator, Inspirator and Instigator in Numerical Fluid Dynamics* (1998), pp. 163–179.
- [78] Oleg V Vasilyev. “High order finite difference schemes on non-uniform meshes with good conservation properties”. In: *Journal of Computational Physics* 157.2 (2000), pp. 746–761.
- [79] RWCP Verstappen and AEP Veldman. “Symmetry-preserving discretization of turbulent flow”. In: *Journal of Computational Physics* 187.1 (2003), pp. 343–368.
- [80] RWCP Verstappen and AEP1488542 Veldman. “Direct numerical simulation of turbulence at lower costs”. In: *Journal of Engineering Mathematics* 32 (1997), pp. 143–159.
- [81] AEP Veldman and K Rinzema. “Playing with nonuniform grids”. In: *Journal of engineering mathematics* 26.1 (1992), pp. 119–130.
- [82] RWCP Verstappen and AEP Veldman. “Numerical simulation of a turbulent flow in a channel with surface mounted cubes”. In: *Applied Scientific Research* 59 (1997), pp. 395–408.
- [83] Bingqian Chen, Sumei Liu, Junjie Liu, Nan Jiang and Qingyan Chen. “A new wall function for indoor airflow with buoyancy effect”. In: *Building and Environment* 202 (2021), p. 108029.
- [84] Franck Nicoud and Frédéric Ducros. “Subgrid-scale stress modelling based on the square of the velocity gradient tensor”. In: *Flow, Turbulence and Combustion* 62.3 (1999), pp. 183–200.
- [85] Laurent Bricteux, Matthieu Duponcheel and Grégoire Winckelmans. “A multiscale subgrid model for both free vortex flows and wall-bounded flows”. In: *Physics of Fluids* 21.10 (2009).
- [86] Hervé Jeanmart and Grégoire Winckelmans. “Investigation of eddy-viscosity models modified using discrete filters: A simplified “regularized variational multiscale model” and an “enhanced field model””. In: *Physics of Fluids* 19.5 (2007).
- [87] Joel H Ferziger, Milovan Perić and Robert L Street. *Computational Methods for Fluid Dynamics*. Springer, 2019.

-
- [88] Ed MJ Komen, Edo MA Frederix, THJ Coppen, Valerio D'Alessandro and JGM Kuerten. "Analysis of the numerical dissipation rate of different Runge–Kutta and velocity interpolation methods in an unstructured collocated finite volume method in OpenFOAM®". In: *Computer Physics Communications* 253 (2020), p. 107145.
- [89] Tobias Kempe and Andreas Hantsch. "Large-eddy simulation of indoor air flow using an efficient finite-volume method". In: *Building and Environment* 115 (2017), pp. 291–305.
- [90] Nina Morozova, FX Trias, R Capdevila, Carlos David Pérez-Segarra and A Oliva. "On the feasibility of affordable high-fidelity CFD simulations for indoor environment design and control". In: *Building and Environment* 184 (2020), p. 107144.
- [91] Shaolin Mao and Ismail B Celik. "Modeling of indoor airflow and dispersion of aerosols using immersed boundary and random flow generation methods". In: *Computers & Fluids* 39.8 (2010), pp. 1275–1283.
- [92] Ji Choi and JR Edwards. "Large eddy simulation and zonal modeling of human-induced contaminant transport." In: *Indoor Air* 18.3 (2008), pp. 233–249.
- [93] J-I Choi and Jack R Edwards. "Large-eddy simulation of human-induced contaminant transport in room compartments". In: *Indoor Air* 22.1 (2012), pp. 77–87.
- [94] Rainald Löhner, Harbir Antil, Ashok Srinivasan, Sergio Idelsohn and Eugenio Oñate. "High-fidelity simulation of pathogen propagation, transmission and mitigation in the built environment". In: *Archives of Computational Methods in Engineering* 28 (2021), pp. 4237–4262.
- [95] Pekka Saarinen, Petri Kalliomäki, Hannu Koskela and Julian W Tang. "Large-eddy simulation of the containment failure in isolation rooms with a sliding door—An experimental and modelling study". In: *Building Simulation*. Vol. 11. Springer. 2018, pp. 585–596.
- [96] Petter A Berthelsen and Odd M Faltinsen. "A local directional ghost cell approach for incompressible viscous flow problems with irregular boundaries". In: *Journal of Computational Physics* 227.9 (2008), pp. 4354–4397.
- [97] Chi-Wang Shu and Stanley Osher. "Efficient implementation of essentially non-oscillatory shock-capturing schemes". In: *Journal of Computational Physics* 77.2 (1988), pp. 439–471.

- [98] E Weinan and Jian-Guo Liu. “Projection method I: convergence and numerical boundary layers”. In: *SIAM Journal on Numerical Analysis* (1995), pp. 1017–1057.
- [99] John Kim and Parviz Moin. “Application of a fractional-step method to incompressible Navier-Stokes equations”. In: *Journal of Computational Physics* 59.2 (1985), pp. 308–323.
- [100] Robert D Falgout and Ulrike Meier Yang. “hypr: A library of high performance preconditioners”. In: *International Conference on Computational Science*. Springer. 2002, pp. 632–641.
- [101] Yu-Heng Tseng and Joel H Ferziger. “A ghost-cell immersed boundary method for flow in complex geometry”. In: *Journal of Computational Physics* 192.2 (2003), pp. 593–623.
- [102] Liang Yang. “One-fluid formulation for fluid–structure interaction with free surface”. In: *Computer Methods in Applied Mechanics and Engineering* 332 (2018), pp. 102–135.
- [103] SW Armfield. “Finite difference solutions of the Navier-Stokes equations on staggered and non-staggered grids”. In: *Computers & Fluids* 20.1 (1991), pp. 1–17.
- [104] AW Vreman and Johannes GM Kuerten. “Comparison of direct numerical simulation databases of turbulent channel flow at $Re_\tau = 180$ ”. In: *Physics of Fluids* 26.1 (2014).
- [105] Ping He. “A high order finite difference solver for massively parallel simulations of stably stratified turbulent channel flows”. In: *Computers & Fluids* 127 (2016), pp. 161–173.
- [106] Sanjiva K Lele. “Compact finite difference schemes with spectral-like resolution”. In: *Journal of Computational Physics* 103.1 (1992), pp. 16–42.
- [107] Alexandre Joel Chorin. “Numerical solution of the Navier-Stokes equations”. In: *Mathematics of Computation* 22.104 (1968), pp. 745–762.
- [108] Henk A Van der Vorst. “Bi-CGSTAB: A fast and smoothly converging variant of Bi-CG for the solution of nonsymmetric linear systems”. In: *SIAM Journal on Scientific and Statistical Computing* 13.2 (1992), pp. 631–644.
- [109] Robert D Falgout, Jim E Jones and Ulrike Meier Yang. “Conceptual interfaces in hypr”. In: *Future Generation Computer Systems* 22.1-2 (2006), pp. 239–251.

-
- [110] Hung Le and Parviz Moin. “An improvement of fractional-step methods for the incompressible Navier-Stokes equations”. In: *Journal of Computational Physics* 89.1 (1990), p. 253.
- [111] Athony Leonard. “Energy cascade in large-eddy simulations of turbulent fluid flows”. In: *Advances in Geophysics*. Vol. 18. Elsevier, 1975, pp. 237–248.
- [112] F Piscaglia, A Montorfano, Angelo Onorati and F Brusiani. “Boundary conditions and sgs models for les of wall-bounded separated flows: An application to engine-like geometries”. In: *Oil & Gas Science and Technology–Revue d’IFP Energies nouvelles* 69.1 (2014), pp. 11–27.
- [113] ACY Yuen, GH Yeoh, Victoria Timchenko, SCP Cheung and T Chen. “Study of three LES subgrid-scale turbulence models for predictions of heat and mass transfer in large-scale compartment fires”. In: *Numerical Heat Transfer, Part A: Applications* 69.11 (2016), pp. 1223–1241.
- [114] Farzad Bazdidi-Tehrani, Shahin Masoumi-Verki, Payam Gholamalipour and Mohsen Kiamansouri. “Large eddy simulation of pollutant dispersion in a naturally cross-ventilated model building: Comparison between sub-grid scale models”. In: *Building Simulation*. Vol. 12. Springer. 2019, pp. 921–941.
- [115] Nitish Arya and Ashoke De. “Effect of grid sensitivity on the performance of wall adapting SGS models for LES of swirling and separating–reattaching flows”. In: *Computers & Mathematics with Applications* 78.6 (2019), pp. 2035–2051.
- [116] Twan van Hooff, Peter V Nielsen and Yuguo Li. “Computational fluid dynamics predictions of non-isothermal ventilation flow—How can the user factor be minimized?” In: *Indoor Air* 28.6 (2018), pp. 866–880.
- [117] Patrick J Roache. “Verification of codes and calculations”. In: *AIAA Journal* 36.5 (1998), pp. 696–702.
- [118] Laurent Bricteux, Stéphanie Zeoli and Nicolas Bourgeois. “Validation and scalability of an open source parallel flow solver”. In: *Concurrency and Computation: Practice and Experience* 29.21 (2017), e4330.
- [119] Corentin Carton de Wiart, Koen Hillewaert, Matthieu Duponcheel and Grégoire Winckelmans. “Assessment of a discontinuous Galerkin method for the simulation of vortical flows at high Reynolds number”. In: *International Journal for Numerical Methods in Fluids* 74.7 (2014), pp. 469–493.

- [120] Charles Hirsch, Koen Hillewaert, Ralf Hartmann, Vincent Couaillier, Jean-Francois Boussuge, Frederic Chalot, Sergey Bosniakov and Werner Haase. *TILDA: towards industrial LES/DNS in aeronautics*. Springer, 2021.
- [121] John Kim, Parviz Moin and Robert Moser. “Turbulence statistics in fully developed channel flow at low Reynolds number”. In: *Journal of Fluid Mechanics* 177 (1987), pp. 133–166.
- [122] Robert D Moser, John Kim and Nagi N Mansour. “Direct numerical simulation of turbulent channel flow up to $Re_\tau = 590$ ”. In: *Physics of Fluids* 11.4 (1999), pp. 943–945.
- [123] O Thiry, G Winckelmans and M Duponcheel. “The Dynamic Smagorinsky Model in Pseudo-Spectral LES of Decaying Homogeneous Isotropic Turbulence at Very High”. In: *Direct and Large-Eddy Simulation XI*. Springer, 2019, pp. 123–128.
- [124] Hiroyuki Abe, Robert Anthony Antonia and Hiroshi Kawamura. “Correlation between small-scale velocity and scalar fluctuations in a turbulent channel flow”. In: *Journal of Fluid Mechanics* 627 (2009), pp. 1–32.
- [125] Qiang Lin, Yasuyuki Ishida, Hideyuki Tanaka, Akashi Mochida, Qingshan Yang and Yukio Tamura. “Large eddy simulations of strong wind mechanisms at pedestrian level around square-section buildings with same aspect ratios and different sizes”. In: *Building and Environment* 243 (2023), p. 110680.
- [126] Md Faiaz Khaled and Aly Mousaad Aly. “Assessing aerodynamic loads on low-rise buildings considering Reynolds number and turbulence effects: a review”. In: *Advances in Aerodynamics* 4.1 (2022), p. 24.
- [127] Carlos Diaz-Daniel, Sylvain Laizet and J Christos Vassilicos. “Direct numerical simulations of a wall-attached cube immersed in laminar and turbulent boundary layers”. In: *International Journal of Heat and Fluid Flow* 68 (2017), pp. 269–280.
- [128] Paul Ploumhans, GS Winckelmans, John K Salmon, Anthony Leonard and MS Warren. “Vortex methods for direct numerical simulation of three-dimensional bluff body flows: application to the sphere at $Re = 300, 500, \text{ and } 1000$ ”. In: *Journal of Computational Physics* 178.2 (2002), pp. 427–463.
- [129] TA Johnson and VC Patel. “Flow past a sphere up to a Reynolds number of 300”. In: *Journal of Fluid Mechanics* 378 (1999), pp. 19–70.

- [130] Jung-Il Choi, Roshan C Oberoi, Jack R Edwards and Jacky A Rosati. “An immersed boundary method for complex incompressible flows”. In: *Journal of Computational Physics* 224.2 (2007), pp. 757–784.
- [131] Rui Ning Zhuang, Xiangdong Li and Jiyuan Tu. “Should different gaseous contaminants be treated differently in CFD indoor simulations?” In: *WIT Transactions on Ecology and the Environment* 183 (2014), pp. 353–362.
- [132] Shiyi Sun, Jing Li and Jie Han. “How human thermal plume influences near-human transport of respiratory droplets and airborne particles: a review”. In: *Environmental Chemistry Letters* 19 (2021), pp. 1971–1982.
- [133] Nils Erland L Haugen and Axel Brandenburg. “Inertial range scaling in numerical turbulence with hyperviscosity”. In: *Physical Review E* 70.2 (2004), p. 026405.

Appendix

A.1 Paper I

Characterization of the density-driven counter-flow through a doorway using Large Eddy Simulation

Elyas Larkermani, Guangyu Cao, Laurent Georges

Building and Environment 221 (2022), p. 109319.



Contents lists available at ScienceDirect

Building and Environment

journal homepage: www.elsevier.com/locate/buildenv

Characterization of the density-driven counter-flow through a doorway using Large Eddy Simulation

Elyas Larkermanni^{*}, Guangyu Cao, Laurent Georges

Norwegian University of Science and Technology, Department of Energy and Process Engineering, Kolbjørn Hejes v 1B, NO-7491, Trondheim, Norway

ARTICLE INFO

Keywords:

Natural convection
Large vertical opening
Discharge coefficient
Large eddy simulation

ABSTRACT

The density-driven bidirectional flow through an open doorway is of prime importance for ventilation and heat distribution between rooms in buildings. Although this flow has been extensively studied in the past, some important flow characteristics, such as unsteady flow phenomena, have not been documented in detail. Therefore, a high-resolution Large Eddy Simulation (LES) of the bulk flow through a doorway is performed. This LES can also serve as a reference solution to compare the accuracy of simpler evaluation methods, from the standard theoretical model calibrated using a discharge coefficient (C_d) to CFD solving the Reynolds-Averaged Navier-Stokes (RANS) equations. Based on LES results, the bidirectional flow can generate turbulent mixing in the middle of the doorway. However, the effects remain limited to the close vicinity of the neutral plane. The bidirectional airstream in the doorway further develops into two non-isothermal jets that entrain a fraction of the airflow. Furthermore, the two jets create large unsteady flow structures when they expand in the adjoining rooms. The results show that unsteady RANS is a good alternative to the resource-intensive LES if the analysis of turbulent jets is not of interest. The standard theoretical model demonstrates that two-dimensional contraction is the dominant effect driving the C_d value, while the viscous effects have a minor influence. Unlike previous studies, LES results show that viscous effects tend to increase the C_d as they moderate the contraction effect. This paper also provides guidelines for the laboratory measurement of C_d and its use in building performance simulation tools.

1. Introduction

Natural convection in confined spaces has received considerable interest due to its prominent role in ventilation, air conditioning and indoor air contaminants transmission. In most situations, heat and mass are convected through an opening located within an internal partition wall between two enclosures by an intrinsically three-dimensional and transient flow field. The characteristics of such a complicated flow are of great importance to many applications and practical research fields. Specifically, airflow through large vertical openings could significantly contribute to the thermal behavior of buildings and the air circulation patterns in a room [1]. The influence of airflow is also determinant in transmitting airborne diseases, such as COVID-19. For instance, the airflow through large openings could be vital in hospital operating theatres where the passage of airborne diseases to clean rooms increases the risk of infection [2–6]. Hence correct estimation of doorway flow rates and flow patterns is essential from the airborne contaminant control point of view.

1.1. Flow regimes

Several mechanisms, such as pressure and density differences, occupant movement, and door motion, may drive the airflow through a large vertical opening [7]. A combination of different mechanisms along with many physical parameters makes it complex to derive a general solution for a counter-flow passing through an opening. However, it is important to distinguish between the *boundary layer flow* and *bulk flow* regimes. In the boundary layer flow regime, the air temperature inside an interconnected multizone enclosure is almost equal everywhere, while the temperature difference between the air and the walls generates boundary layers that drive the flow along the walls of the room. In this case, no significant difference in hydrostatic pressure arises between two adjoining rooms. In the bulk flow regime, the temperature difference between the room air and its walls is limited, which corresponds to the isothermality factor close to unity. In this regime, the air temperature difference between interconnected rooms leads to a difference in hydrostatic pressure that drives the flow through the door opening. A

^{*} Corresponding author. Kolbjørn Hejes v 1B, NO-7491, Trondheim, Norway.
E-mail address: elyas.larkermanni@ntnu.no (E. Larkermanni).

<https://doi.org/10.1016/j.buildenv.2022.109319>

Received 3 March 2022; Received in revised form 14 June 2022; Accepted 15 June 2022

Available online 20 June 2022

0360-1323/© 2022 The Authors. Published by Elsevier Ltd. This is an open access article under the CC BY license (<http://creativecommons.org/licenses/by/4.0/>).

previous study by Allard et al., IEA EBC Annex 20 [8], demonstrated that the bulk flow regime is dominant in buildings.

The transition from the boundary layer to the bulk flow regime was examined in the experimental studies of Scott et al. [9] and Neymark et al. [10]. This transition between both flow regimes was explained by the blockage effect when the aperture size in the partition wall starts to be small. Georges et al. [11] conducted Computational Fluid Dynamics (CFD) simulations of a bidirectional flow through a doorway using the Reynolds-Averaged Navier-Stokes (RANS) approach. Unlike the previous works of Scott et al. [9] and Neymark et al. [10] that neglect thermal radiation between walls, Georges et al. [11] showed that, in addition to the aperture size, the thermal radiation strongly influences the isothermality factor and thus the flow regime.

1.2. Standard theoretical model

In Building Performance Simulation (BPS) tools like TRNSYS or IDA ICE [12], the volume of air in each thermal zone is isothermal. Airflow networks, such as COMIS [13] or CONTAM [14], are used to compute the airflows between the interconnected zones [15]. The standard (or conventional) model assumes a bulk flow to compute airflow rates through large vertical openings in airflow networks. It considers two isothermal reservoirs at different temperatures and a one-dimensional inviscid steady-state flow. These assumptions lead to a simple model based on the Bernoulli equation, defined here as the standard theoretical model [8].

The resulting maximum theoretical flow is then corrected using the discharge coefficient (C_d) to match the actual airflow in the doorway. The C_d can be calibrated on the actual mass ($C_{d,M}$) or the heat flow ($C_{d,Q}$). Allard and Utsumi [16] mentioned that this phenomenological coefficient includes the effect of local flow contraction caused by the vertical opening (i.e., a two-dimensional effect). They investigated various approaches to determine the C_d , which may be expressed as a function of opening height or the air temperature difference between the interconnected rooms. They demonstrated the difficulty of determining the C_d and pointed out that various definitions for this coefficient have been introduced in the literature. They concluded that the definition of C_d is still ambiguous and requires more precise simulation or experimental measurements. Heiselberg et al. [17] argued that the different values of C_d for door openings reported in previous studies might be attributed to simple and unrealistic assumptions. The uniform air temperature distribution inside the enclosures and the one-dimensional flow field at the opening are clear examples of these assumptions.

1.3. Knowledge gap

The bulk flow through a doorway has been investigated extensively, for instance, in IEA EBC Annex 20 [8]. However, several characteristics of the flow have not been studied in detail.

Assuming an inviscid flow, the velocity profile shows a sharp

gradient at the level of the neutral plane (NP), see Fig. 1(a). With viscous flow, two related phenomena shown in Fig. 1(b) can occur in the vicinity of the NP:

- The two airstreams going in opposite directions create a shear layer. In a recent study by Lefaive et al. [18], two reservoirs filled with a fluid of different densities were connected by a long channel. They demonstrated that a sustained stratified shear flow could generate large unsteady flow structures.
- Wilson and Kiel [19] reported some interfacial mixing between the two airstreams in opposite directions. Interfacial mixing causes a fraction of the warm airflow initially flowing towards the opening to be brought back into the warm zone, entrained by the cold airstream. This re-entrainment effect also takes place for the cold airflow and leads to an exchange of momentum between the two counter-flowing streams passing through a large vertical opening. According to these authors, the resulting velocity and temperature profiles are smoother at the level of the NP compared to inviscid flow, as shown in Fig. 1(a). Consequently, the mass and heat flow exchanged through the doorway could be reduced compared to the inviscid flow (i.e., the assumption used in the standard model).

Detached shear layers are formed at the edges of the doorway. According to the literature review, the transition of these detached shear layers into a three-dimensional turbulent flow has not been investigated in earlier studies. The two airstreams in the opposite direction develop non-isothermal jets in the adjoining rooms, which is a phenomenon that has scarcely been documented in the literature. Finally, most existing studies report on the velocity field, and a few of them analyzed the temperature field within the doorway in detail. However, the temperature field directly impacts the convective heat transfer between interconnected rooms. The main objective of this paper is to characterize flow separation at the opening edge, interfacial mixing between counter-flowing streams and turbulent flow development.

1.4. Need for high-resolution CFD

To answer this question, the bulk flow passing through a doorway between a warm and a cold room can be investigated using laboratory measurements or CFD. Several previous studies have measured the airflow characteristics between two chambers at different temperatures separated by a partition wall, e.g. Refs. [8,20,21]. They typically relied on intrusive flow measurements using low-velocity anemometers. These measurements are demanding since they should be done at many locations within the aperture of the doorway and inside both rooms due to the three-dimensional nature of the airflow field. As it will be shown in the paper, measuring the airflow only along a vertical line in the middle of the doorway leads to rough simplifications. Consequently, the airflow should be measured in the entire doorway, which is demanding. Moreover, anemometers have a lower accuracy for air velocity magnitudes

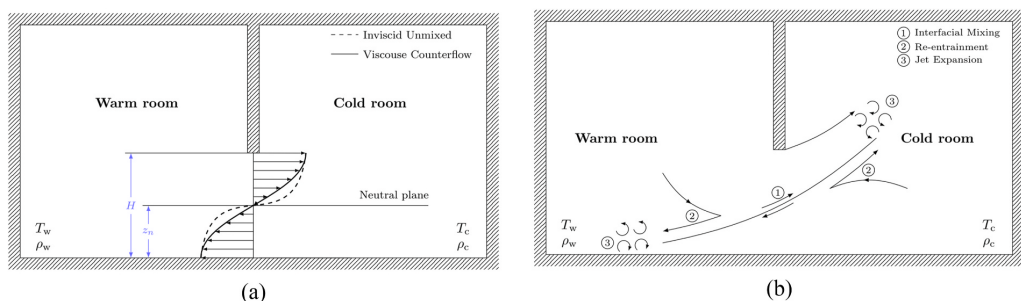


Fig. 1. Streamwise velocity profiles (left) and re-entrainment by cross-stream interfacial mixing (right) for the bidirectional flow in a doorway.

below 0.1 m/s, which are typically found in the middle of the doorway. Non-intrusive measurement methods such as Particle Image Velocimetry (PIV) are also demanding as the flow needs to be visualized over several meters, the typical door height (H) being 2 m. However, a common methodology for investigating airflows in buildings uses non-dimensional analysis and water on reduced-scale models [9,22]. This makes the use of PIV easier. However, the effect of thermal radiation would not be addressed using water [10,22,23], and the flow regime would most likely not be a density-driven bulk flow. Finally, tracer gases or smoke visualization can be used [5], but they do not measure physical quantities, like velocity, locally in the doorway. In conclusion, laboratory measurements are possible but challenging to investigate the physical phenomena introduced in Section 1.3.

Several studies have investigated the bulk flow through large vertical openings using CFD. However, these studies are not appropriate to address the physical phenomena explained in Section 1.3. Firstly, these studies did not aim to capture these complex unsteady flow phenomena. As an example, Favarolo and Manz [24] used the LVEL k- ϵ turbulence model [25] in the FloVENT commercial CFD software. They analyzed the impact of different parameters, such as the temperature difference between indoor and outdoor air and the location of large openings on the C_d . Secondly, these studies were conducted using unsteady RANS turbulence modeling. It has not been proven that the RANS approach is appropriate to capture the instabilities of the shear flows for this particular case.

Large Eddy Simulation (LES) has the potential to provide more reliable and detailed information about the natural ventilation in buildings on a sufficiently fine grid resolution [26–30]. The large-scale structures of indoor airflows containing most of the energy are explicitly resolved using LES, while small scales that tend to be more isotropic and universal are filtered out. LES is more appropriate than RANS to capture the flow instabilities this paper seeks to characterize. LES of the flow through a doorway has been performed in the past but on relatively coarse meshes compared to the computational power that is currently available, see, e.g. Ref. [31]. A previous study by Saarinen et al. [5] investigated the flow through a doorway using LES with a high resolution, but they considered the transient regime when the door between both rooms is suddenly opened, and an occupant moves through the door.

1.5. Research questions

Consequently, high-resolution LES of the bulk flow passing through the doorway in a steady-state regime is performed using the Wall-Adapting Local Eddy-viscosity (WALE) subgrid scale model in ANSYS Fluent. The geometry and boundary conditions are developed to approximate a single laboratory experiment with significant temperature stratification in the warm and cold rooms, the baseline case. Measurements and CFD results are compared for this test case.

As explained in Section 1.3, the main research question is to characterize flow separation at the opening edge, interfacial mixing between counter-flowing streams and turbulent flow development (Q1). However, with this reference solution (i.e., high-resolution LES), complementary research questions can also be addressed:

- Viscous effects can be distinguished from two- and three-dimensional effects by comparing Euler (i.e., inviscid solution) to RANS and LES solutions (Q2).
- The ability of the RANS method to capture the bulk flow can be investigated by comparing it to the reference LES solution (Q3).
- The influence of temperature stratification in both rooms can be investigated by comparing the LES solutions of the baseline case with temperature stratified rooms with the second case of two isothermal interconnected rooms at different temperatures (Q4).
- As BPS software typically assumes isothermal rooms, the error created by neglecting stratification can be discussed (Q5).

- The influence of the measurement setup on the evaluation of C_d can be clarified. For instance, the mass and heat flow can be measured in the entire doorway plane or along a single vertical line in the middle of the doorway to reduce the number of measurement points (Q6).

2. The standard theoretical model of bulk flow

The air temperature difference (ΔT) between warm and cold zones in an interconnected multizone enclosure and the aperture geometry are the only physical parameters needed to define the bulk flow regime. In this case, the room air temperature is assumed to be in thermal equilibrium with the wall temperature. The air temperature difference between both sides of the opening leads to different air densities and, consequently, different hydrostatic pressure fields. Due to the conservation of mass, hydrostatic pressure fields on both sides of the opening are equal at the NP located near the middle of the doorway, see Fig. 1(a). The difference in hydrostatic pressure above and below the NP generates two counter-flowing streams of warm and cold air. The standard model equations are derived for two interconnected isothermal reservoirs in Section 2.1, while the difference compared to thermally stratified rooms is explained qualitatively (i.e., without the model equations).

2.1. Airflow between two interconnected isothermal rooms

Assuming inviscid and steady flow, the problem can be solved by applying the Bernoulli equation between two points along a streamline passing from one semi-infinite reservoir to another. With a one-dimensional flow field assumption, the Bernoulli equation can be written in the following way along a horizontal streamline that connects a point located in the warm room to a point close to the opening but in the cold room:

$$p_w(z) + \rho_w g z = p_D(z) + \rho_w g z + \rho_w \frac{u_D(z)^2}{2} \quad (1)$$

where subscripts W and C indicate the warm and cold rooms, respectively, while subscript D refers to the level of the doorway. z denotes the vertical distance from the floor. The pressure of the flow entering the receiving room (p_D) is assumed to be equal to the hydrostatic pressure in that room, i.e. $p_D(z) = p_C(z)$. As both rooms are isothermal with negligible velocity, the integration of the hydrostatic equation along z enables the static pressures p_w and p_C to be related to the floor pressure for the warm and cold rooms, respectively:

$$p_w(z) = p_w(0) - \rho_w g z \quad (2)$$

$$p_C(z) = p_C(0) - \rho_C g z \quad (3)$$

Substituting expressions (2) and (3) in Equation (1) gives the vertical profile of the horizontal velocity through the door opening from the warm room to the cold room:

$$u_{wC}(z) = \sqrt{\frac{2}{\rho_w} (p_w(0) - p_C(0) - (\rho_w - \rho_C) g z)} \quad (4)$$

The level of the NP (z_N) can be computed directly by imposing $u_{wC}(z_N) = 0$:

$$z_N = \frac{p_w(0) - p_C(0)}{(\rho_w - \rho_C) g} \quad (5)$$

Using the definition of the NP in Equation (4) removes the need to evaluate the pressure difference between the rooms at the floor level. The theoretical velocity profile above the NP from the warm room to the cold one is then defined as:

$$u_{wC}(z) = \sqrt{\frac{2g(\rho_C - \rho_w)}{\rho_w} (z - z_N)} \quad z \geq z_N \quad (6)$$

By following the same procedure along a streamline connecting a particle moving from the cold to the warm room, one obtains:

$$u_{cW}(z) = \sqrt{\frac{2g(\rho_c - \rho_w)}{\rho_c}}(z_N - z) \quad z \leq z_N \quad (7)$$

A schematic representation of these two velocity profiles for bi-directional flow along the doorway is depicted in Fig. 1(a).

The corresponding maximum theoretical mass flow rate per unit width above and below the NP is given by:

$$\dot{m}_{wC}(z) = \int_{z_N}^H \rho_w u_{wC}(z) dz = \frac{2}{3} \rho_w \sqrt{\frac{2g(\rho_c - \rho_w)}{\rho_w}} (H - z_N)^{3/2} \quad (8)$$

$$\dot{m}_{cW}(z) = \int_0^{z_N} \rho_c u_{cW}(z) dz = \frac{2}{3} \rho_c \sqrt{\frac{2g(\rho_c - \rho_w)}{\rho_c}} z_N^{3/2} \quad (9)$$

The sum of these two mass flow rates must respect the conservation of mass. In other words, the mass flow entering the sealing room must equal the mass flow leaving the room ($\dot{m}_{wC}(z) = \dot{m}_{cW}(z) = \dot{m}_{\max}(z)$). This mathematical constraint enables the neutral layer location to be expressed as a function of air densities:

$$z_N = \frac{H}{\left(1 + \left(\frac{\rho_c}{\rho_w}\right)^{1/3}\right)} \quad (10)$$

indicating warm airstream above the NP is thicker than the cold airstream below the NP as $\rho_w < \rho_c$.

In reality, the flow is neither inviscid nor one-dimensional. The airflow has contraction and viscous effects. Therefore, the actual mass flow rate is obtained by applying a correction factor, the discharge coefficient ($C_{d,M}$), to the maximum theoretical mass flow rates from Equations (8) and (9):

$$\dot{m}_{\text{actual}} = C_{d,M} \dot{m}_{\max} \quad (11)$$

For sharp-edged openings, $C_{d,M}$ is about 0.6 [19].

A convective heat transfer between two interconnected zones is generated by the density-driven airflow. Assuming a constant specific heat capacity (c_p), the theoretical net heat flow rate convected per unit width is given by:

$$\begin{aligned} \dot{Q}_{\max} &= \int_{z_N}^H \rho_w u_{wC}(z) c_p (T_W - T_{\text{ref}}) dz - \int_0^{z_N} \rho_c u_{cW}(z) c_p (T_C - T_{\text{ref}}) dz = \int_{z_N}^H \rho_w u_{wC}(z) c_p T_W dz - \int_0^{z_N} \rho_c u_{cW}(z) c_p T_C dz = c_p (T_W \dot{m}_{wC}(z) - T_C \dot{m}_{cW}(z)) \\ &= \dot{m}_{\max} c_p (T_W - T_C) \end{aligned} \quad (12)$$

where T_{ref} is the reference temperature that can be eliminated due to the conservation of mass. With a uniform room air temperature, the actual heat flow rate is a fraction of the theoretical net heat flow rate:

$$\dot{Q}_{\text{actual}} = \dot{m}_{\text{actual}} c_p (T_W - T_C) = C_{d,M} \dot{m}_{\max} c_p (T_W - T_C) = C_{d,M} \dot{Q}_{\max} = C_{d,Q} \dot{Q}_{\max} \quad (13)$$

According to the standard theory, this proves that the same C_d (i.e., $C_{d,M} = C_{d,Q}$) can be used for both mass and heat flow rates when both rooms are isothermal.

2.2. Airflow between two interconnected stratified rooms

In Section 2.1, the air temperature was assumed to be uniform in both rooms. However, in reality, the air temperature is often not isothermal within a room, an important effect being the vertical

temperature stratification. This stratification impacts the vertical profile of hydrostatic pressure and thus the location of the NP [7]. Moreover, unlike isothermal rooms, the velocity profiles are no longer parabolic in the aperture.

In most applications, the vertical air temperature distribution can be assumed to be linear [32–34]. The equations of the standard models in Section 2.1 can be extended for a case with linear vertical temperature stratification [7]. In this case, the most important conclusion is the prediction of a same discharge coefficient for the mass and heat flows by the standard theoretical model, as for the isothermal rooms.

3. Methodology

3.1. Experimental setup

The experiment has been conducted by Paul Minard [35] in a full-scale climate chamber. The environmental chamber consists of two rooms connected by an open doorway of height 1.9 m and width 0.83 m located in the middle of the vertical partition wall. The dimensions of the warm and cold rooms are $2.65 \times 2.3 \times 3.8 \text{ m}^3$ and $3.9 \times 7.8 \times 6.9 \text{ m}^3$ ($H \times W \times D$), respectively. The partition wall has a thickness of 0.1 m. Both rooms are equipped with a mechanical ventilation system that is turned off during the experiment. Two electric panel heaters were installed in the warm room far away from the door while the cold room was not heated. Ten omnidirectional anemometers TSI 8475 (with accuracy $\pm 3\% \pm 0.005 \text{ m/s}$) and PT-100 sensors (with accuracy $\pm 0.1^\circ\text{C}$) were mounted on a vertical bar located in the middle of the doorway to measure air velocity and temperature. The sensors were uniformly distributed along z from the floor to the top of the door. The surface of all PT-100 sensors is coated with aluminum to limit the effect of thermal radiation. The temperature stratification inside the warm and cold rooms was measured with five PT-100 sensors mounted on a vertical pole, 2 m away from the opening. When radiators were turned on, it took several hours before steady-state conditions were reached. Then, data were recorded every 20 s during a period of 10 min. More details about the procedure and probe locations can be found in Refs. [11,35].

3.2. Computational domain

Measurements showed significant temperature stratification in both

rooms, especially in the heated room. It is challenging to reproduce the same stratification in CFD. It would require detailed measurements of the surface temperature for both rooms and the heat emitters. Fortunately, measurements revealed that the airflow was in the bulk flow regime. Consequently, the computational domain was defined to enforce this bulk flow regime rather than to reproduce the exact geometry of the laboratory. In this respect, the rooms were defined considerably larger than the doorway size (Fig. 2). In addition, the measured temperature stratification is imposed as initial conditions within both reservoirs. At the start of the simulation, when both reservoirs are put in contact, a transient flow is established through the doorway until it reaches a pseudo steady-state. The same procedure was followed in the experimental setup of Lefauve et al. [18]. As both rooms are large, the convective heat transfer through the doorway does not have time to significantly influence the temperature of both reservoirs during the period of physical time computed by the CFD. The partition wall has the

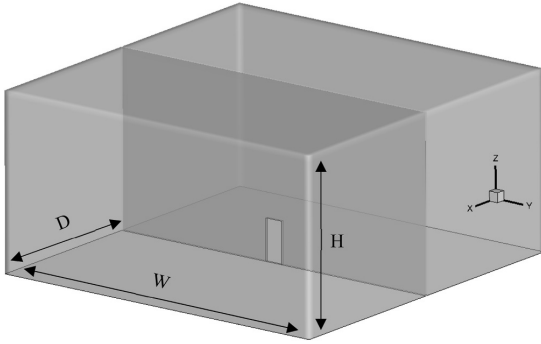


Fig. 2. Three-dimensional multizone enclosure configuration ($H \times W \times D = 8 \times 16 \times 8 \text{ m}^3$).

same thickness as the laboratory experiments.

3.3. Governing equations

Applying an implicit filtering operator and considering the Boussinesq approximation in the body force term, the filtered incompressible Navier-Stokes equations solved by the LES can be expressed as:

$$\frac{\partial \bar{u}_i}{\partial x_i} = 0 \tag{14}$$

$$\frac{\partial \bar{u}_i}{\partial t} + \frac{\partial \bar{u}_i \bar{u}_j}{\partial x_j} = -\frac{1}{\rho_{ref}} \frac{\partial \bar{p}}{\partial x_i} + \frac{\partial}{\partial x_j} [2\nu \bar{S}_{ij}] - \frac{\partial \tau_{ij}}{\partial x_j} + g_i [1 - \beta(\bar{T} - T_{ref})] \tag{15}$$

$$\frac{\partial \bar{T}}{\partial t} + \frac{\partial \bar{u}_j \bar{T}}{\partial x_j} = \frac{\partial}{\partial x_j} \left[\alpha \frac{\partial \bar{T}}{\partial x_j} \right] - \frac{\partial \tau_{jT}}{\partial x_j} \tag{16}$$

where the bar represents the implicit grid filtering, x_i denotes the i^{th} spatial coordinate direction, \bar{u}_i represents the filtered velocity field in the x_i direction, t the time, \bar{p} the modified filtered pressure, and \bar{T} the filtered temperature. The last term in Equation (15) is the buoyancy term where $\beta = 1/T_{ref}$ is the thermal expansion coefficient of the air modeled as an ideal gas and g_i the gravitational acceleration. The parameters ν and α indicate the kinematic viscosity and thermal diffusivity, respectively. They are assumed constant (i.e., independent of the air temperature) and taken for the air at T_{ref} . The subgrid scale (SGS) stress tensor and the scalar SGS thermal flux vector are included, respectively, in the momentum and energy equations above via the unresolved terms $\tau_{ij} = \bar{u}_i \bar{u}_j - \bar{u}_i \bar{u}_j$ and $\tau_{jT} = \bar{u}_j \bar{T} - \bar{u}_j \bar{T}$.

3.4. SGS modeling in LES

The closure of the Navier-Stokes equations can be achieved by utilizing the WALE turbulence model to calculate the SGS kinematic viscosity, ν_{SGS} , based on the invariants of the velocity gradient tensor:

$$\tau_{ij} = \bar{u}_i \bar{u}_j - \bar{u}_i \bar{u}_j = -2\nu_{SGS} \bar{S}_{ij} + \frac{2}{3} k_{SGS} \delta_{ij} \tag{17}$$

$$\nu_{SGS} = \bar{\Delta}^2 C_w^2 \frac{(\bar{S}_{ij}^* \bar{S}_{ij}^*)^{3/2}}{(\bar{S}_{ij} \bar{S}_{ij})^{5/2} + (\bar{S}_{ij}^* \bar{S}_{ij}^*)^{5/4}} \tag{18}$$

$$\bar{S}_{ij}^* = \frac{1}{2} (\bar{s}_{ij}^2 + \bar{s}_{ii}^2) - \frac{1}{3} \bar{s}_{kk}^2 \delta_{ij} \tag{19}$$

$$\bar{s}_{ij}^2 = \bar{s}_{ik} \bar{s}_{kj} = \frac{\partial \bar{u}_i}{\partial x_k} \frac{\partial \bar{u}_k}{\partial x_j} \tag{20}$$

where C_w is the model coefficient, here taken at a constant value of 0.325 [36], and the effective filter width is computed using the local cell volume, $\bar{\Delta} = \sqrt[3]{V_c}$. k_{SGS} and \bar{S}_{ij} are the SGS kinetic energy and resolved scale strain rate tensor:

$$\bar{S}_{ij} = \frac{1}{2} \left(\frac{\partial \bar{u}_i}{\partial x_j} + \frac{\partial \bar{u}_j}{\partial x_i} \right) \tag{21}$$

By analogy to the SGS stress tensor modeling, the scalar SGS thermal flux vector, τ_{jT} , can be approximated by the following expression [37]:

$$\tau_{jT} = \bar{u}_j \bar{T} - \bar{u}_j \bar{T} = -\frac{\nu_{SGS}}{Pr_{SGS}} \frac{\partial \bar{T}}{\partial x_j} \tag{22}$$

where Pr_{SGS} denotes the SGS Prandtl number and is fixed at 0.85. The WALE SGS model has been selected for the following reasons. The WALE turbulence model is able to reproduce the near-wall behavior correctly. Thus, unlike the Smagorinsky SGS model, which requires a wall-damping function, the WALE eddy viscosity model recovers the proper y^3 near-wall scaling for the turbulent eddy viscosity [38]. The model also generates zero turbulent viscosity in the case of pure shear. Therefore, it is expected to capture the transitional flow from laminar to turbulent [38,39]. On top of that, the formulation of the WALE SGS model depends on both the strain and the rotation rate of the small turbulent structures, making WALE model a more reliable SGS model than the dynamic Smagorinsky model to predict the interfacial mixing layer accurately [38,40,41].

To investigate the influence of turbulence modeling, unsteady RANS is also employed here using the most common turbulence model for ventilation flow prediction, i.e., the RNG k- ϵ model [42]. The governing equations for this method would be the Reynolds-averaged incompressible Navier-Stokes equations.

3.5. Grid

A structured grid with 127,316,480 hexahedral cells is generated for the interconnected rooms. A refined uniform grid has been defined in the vicinity of the doorway. The finest elements have a dimension of 0.6 cm to properly resolve interfacial mixing, re-entrainment, and other unsteady flow phenomena. For the sake of the conciseness, the design of the grid and the resulting LES resolution are discussed in Appendix. The aperture area on the y-z plane is covered by 44800 cells and extruded in the x-direction by 20 cells. A smooth transition between cells of different sizes is performed. The maximum growth ratio of 1.03 is adopted for top corners far enough from the doorway and 1.008 is used inside a domain of 1.5 m around the doorway. The computational grid is shown in Fig. 3.

3.6. Boundary conditions and initialization

In order to keep the temperature inside the reservoirs constant in time during the simulations, all walls including the partition wall, are assumed to be adiabatic. Slip boundary conditions are applied to each wall. This explains why no near-wall grid refinement is necessary, as no boundary layer is generated.

The bidirectional airflow through the aperture is simulated for the stratified interconnected rooms (i.e., the baseline case) and also for two isothermal rooms at different temperatures. For the baseline case, the temperature stratification measured in Paul Minard's experiments [35] is used as the initial temperature. This one-dimensional vertical air temperature profile is applied to the computational domain using User Defined Function (UDF) hooked in ANSYS Fluent. For the test case with isothermal reservoirs, no experimental data is available. Hence, the measured air temperature from the stratified case averaged along the vertical direction (z) is taken as the initial condition for the temperature. This leads to a temperature difference of 1.68 °C ($\Delta T = 1.68^\circ\text{C}$). The reference temperature (T_{ref}) is the arithmetic average of the room air

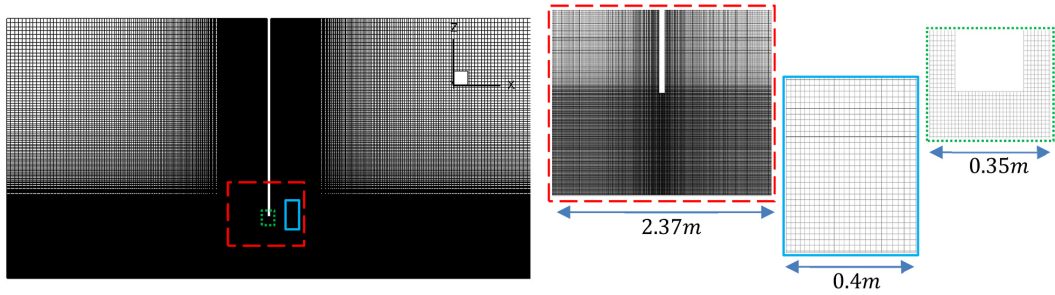


Fig. 3. Computational grid.

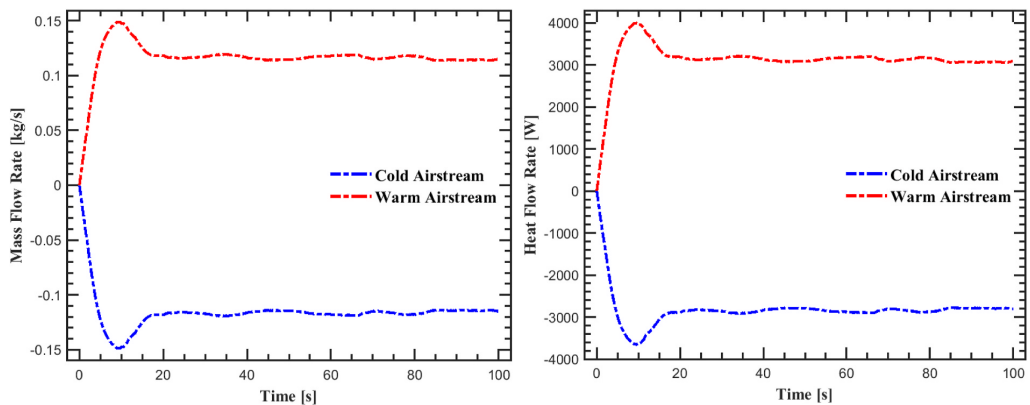


Fig. 4. Time histories of mass (left) and heat (right) flow rates for the stratified baseline case.

temperatures taken at the level of the NP in the middle of the warm and cold zones. Despite preliminary tests showing that initializing the simulation with URANS before switching to LES could partly reduce the initialization time, both enclosures are initialized with zero velocity for simplicity and to ensure that the initialization procedure does not impact the final results. As a result, each room acts as a large reservoir, and the flow through the door is only driven by the differences of hydrostatic pressure in both reservoirs.

During the first phase of the simulation, the bidirectional airflow passing through the doorway is strongly transient. A pseudo-stationary regime is reached after about 60 s of physical time. Then, the airflow is fully established throughout the enclosure, and the transition to turbulent flow is settled. This can be clearly seen from the time histories of heat and mass flow rates for each airstream shown in Fig. 4. In this pseudo-steady state regime ($t > 60$ s), data are collected during 40 s to reach full-converged time-averaged statistics. During this period, the volume-averaged air temperature of both reservoirs remains almost constant.

3.7. Solver settings

The nonlinear governing equations are discretized using the second-order cell-centered finite volume method (FVM) implemented in the ANSYS Fluent commercial CFD package. The *Semi-Implicit Method for Pressure Linked Equations* (SIMPLE) algorithm is employed for pressure-velocity coupling. The time derivatives are advanced in time using the *Second Order Implicit* scheme. In the LES, a constant time step of $\Delta t = 0.01$ s is applied to keep the Courant number below 1.0 to achieve high temporal accuracy. For the LES, the *Central Differencing* scheme is adopted for the treatment of the convective terms of the governing

equations, while a *Second Order Upwind* scheme is used for the RANS and Euler simulations. The pressure interpolation is provided by the *Body Force Weighted* scheme, recommended by the ANSYS Fluent User's Guide.

ANSYS Fluent is capable of running on distributed processors and uses the public domain Open MPI implementation of the standard Message Passing Interface (MPI) to conduct inter-processor communication. The present LES simulations were performed on the resources provided by UNINETT Sigma2, the National Infrastructure for High Performance Computing and Data Storage in Norway. The simulations are performed on a 15-node cluster equipped with multiple 32-core Intel Xeon processors leading to a total of 480 cores and a minimum of 160 GB of RAM.

4. Results

4.1. Description of the flow

The analysis of results starts with a general description of the flow. The instantaneous velocity magnitude field on the opening plane and midplane computed using LES is shown in Fig. 5. The time-averaged temperature field is reported in Fig. 6(a) and (b). As expected, a bidirectional flow is generated. Warm air flows from the warm room (on the left) to the cold room (on the right) in the higher part of the doorway, while the cold air flows in the opposite direction in the lower part of the doorway. Both airstreams flowing in opposite directions (i.e., bidirectional flow) generate a shear layer. The shear layer in the middle of the doorway is inclined by 39° upwards compared to the horizontal plane. This clearly indicates that the airflow through the doorway is not horizontal, as assumed by the standard theory. Moreover, both airstreams

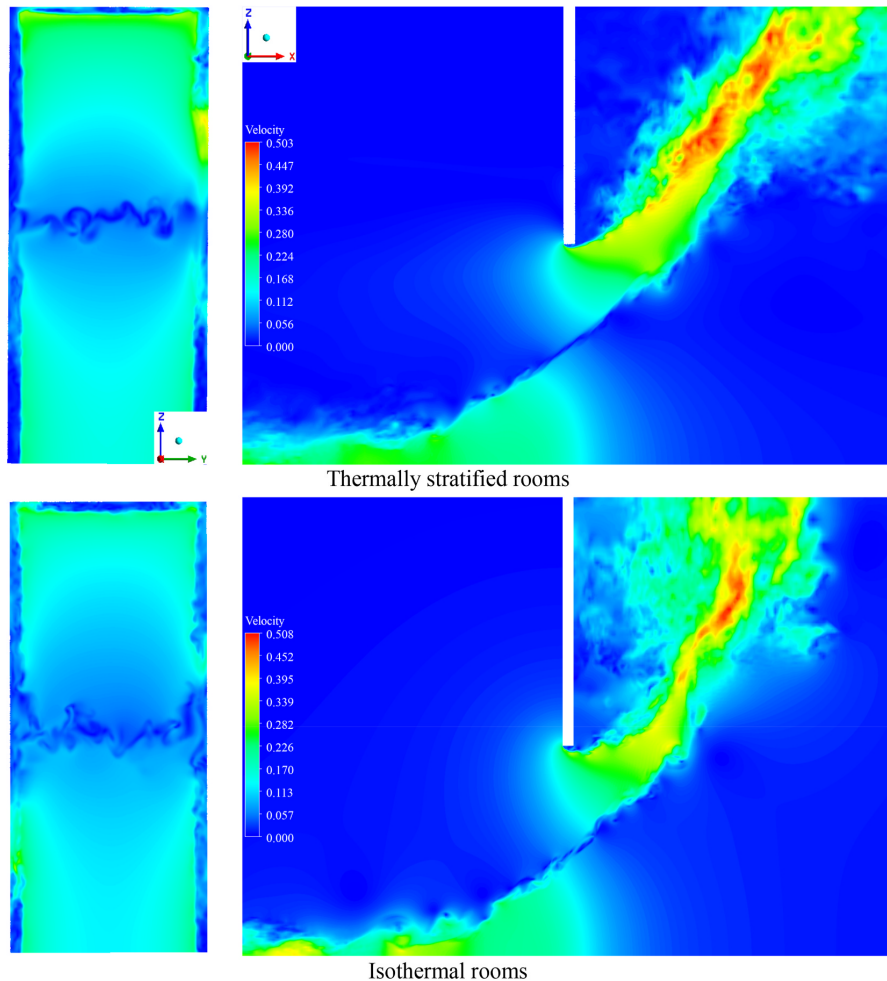


Fig. 5. Instantaneous velocity magnitude in the doorway y-z plane (left) and on an x-z plane at the middle of the door (right).

undergo a contraction when they expand in the opposite room. This contraction, known as the *vena contracta* effect, decreases the mass flow through the doorway compared to the standard theory and partly explains the need to introduce a discharge coefficient. The warm airstream develops into a warm jet that expands upwards in the cold zone, while the cold airstream develops as an attached cold jet along the floor in the warm zone. The velocity magnitude is zero near the middle of the doorway at the location of the NP.

This general description of the bidirectional airflow passing through the doorway can be deduced from all the CFD models used in this study (meaning LES, RANS and Euler), as shown in Fig. 6. Euler simulation is the only exception since inviscid flow does not generate a shear layer between the opposite airflows. Nevertheless, it is worth mentioning that the Euler equations are discretized spatially using a second-order upwind scheme that introduces some amount of artificial numerical dissipation (even though this is limited). This is enough to smooth sharp spatial gradients or generate spurious unsteadiness in the flow.

4.2. Characterization of the re-entrainment

The re-entrainment is a result of interfacial mixing between counter-

flowing streams. However, re-entrainment focuses more on the airstreams that develop into turbulent jets in the opposite rooms. Turbulent jets generate entrainment, and it should be investigated how much of the air in the opposite airstream is diverted from the doorway by this phenomenon. The streamlines in Fig. 6 show that the warm rising jet modifies the airflow direction of the cold air approaching the doorway. This effect is less pronounced for the cold jet expanding in the warm zone. Compared to RANS and Euler, re-entrainment computed by the LES deviates the airflow on a more extensive zone (highlighted by a dashed rectangle in Fig. 6), especially for the thermally stratified rooms. This shows that the re-entrainment is more important using LES and can be under-estimated using RANS.

4.3. Characterization of the shear layer mixing

The time-averaged streamwise velocity and air temperature along a vertical line in the middle of the doorway are depicted in Fig. 7. The transition between the temperature of the warm airstream and the cold airstream indicates the thickness of the shear layer. In addition, the shear layer thickness can also be assessed by the time-averaged temperature field on the midplane in Fig. 6. Analyzing the flow near the NP

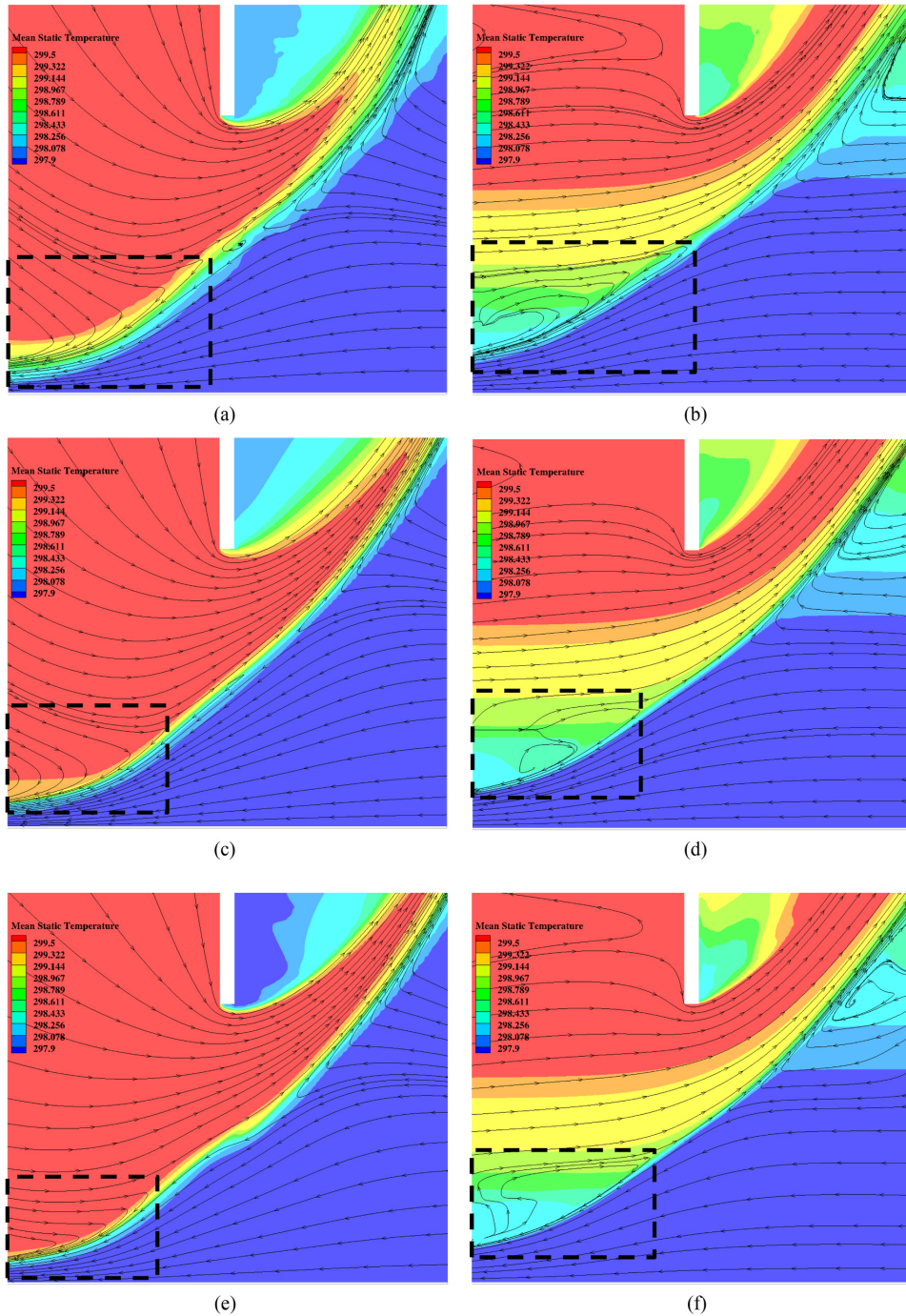


Fig. 6. Mean temperature with streamlines on the vertical plane ($y = 0$) obtained from LES (top), RANS (middle) and Euler (bottom) in isothermal rooms (left) and thermally stratified rooms (right). A dashed black box highlights a region where the re-entrainment of warm airstream occurs.

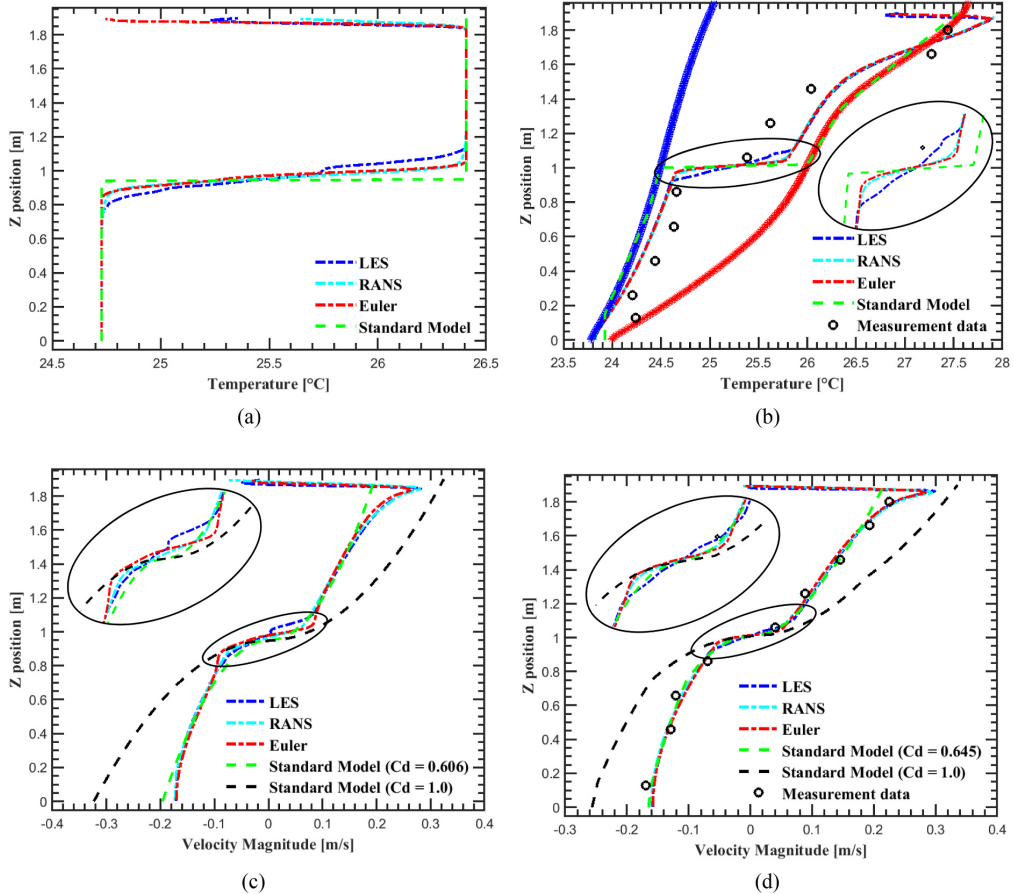


Fig. 7. Time-averaged temperature (a,b) and streamwise velocity (c,d) profiles along a vertical line in the middle of the doorway in isothermal rooms (left) and thermally stratified rooms (right). The thick blue and red lines in the thermally stratified case (b) indicate the vertical profiles of measured air temperature in the cold and warm zones, respectively. (For interpretation of the references to colour in this figure legend, the reader is referred to the Web version of this article.)

in Fig. 6 and 7 shows limited differences between the LES, RANS and Euler solutions for the baseline case with thermally stratified interconnected rooms, suggesting that the shear layer generates no intense interfacial mixing. In the isothermal interconnected rooms, the Euler and RANS are almost equal. However, the shear layer generated by the LES for this case is slightly thicker and can be explained by the mixing generated by the unsteady flow structures shown in Fig. 5. In conclusion, unsteady flow structures do not systematically develop in the middle of the doorway. If they develop, these structures and the resulting mixing remain limited in the vicinity of the NP.

4.4. Unsteady flow structures

A well-resolved LES can capture unsteady flow structures and turbulent mixing precisely. The instantaneous velocity field in Fig. 5 revealed that the flow develops several unsteady flow structures that could not be captured using unsteady RANS. The main observations are:

- The warm and cold jets become turbulent when they expand in the cold and warm rooms, respectively.

- Unsteady flow structures are generated in the shear layer near the NP between two isothermal rooms, while these structures are not visible when both rooms are thermally stratified.
- The NP is not a straight horizontal line and fluctuates in the vertical direction. These fluctuations are more pronounced in the isothermal rooms than in the thermally stratified rooms. To the authors' best knowledge, these time variations of the NP have not been reported in the literature.
- The airflow is detached at the edges of the doorway, from the horizontal head jamb but also from the vertical side jambs. The LES shows that these detached flows are unsteady, especially in isothermal rooms.

Fig. 8 depicts turbulent kinetic energy (k) contours computed using unsteady RANS and LES on the vertical midplane. While RANS does not predict any level of turbulence between counter-flowing streams along the interfacial mixing layer, the LES provides a region of lower k near the NP in the middle of the doorway, followed by a higher magnitude of k when the non-isothermal jets expand in the adjoining rooms. This can be attributed to unsteady flow structures generated in the shear layer and turbulent mixing where jet expansion occurs. LES of both isothermal and thermally stratified cases predict higher k where the detached shear

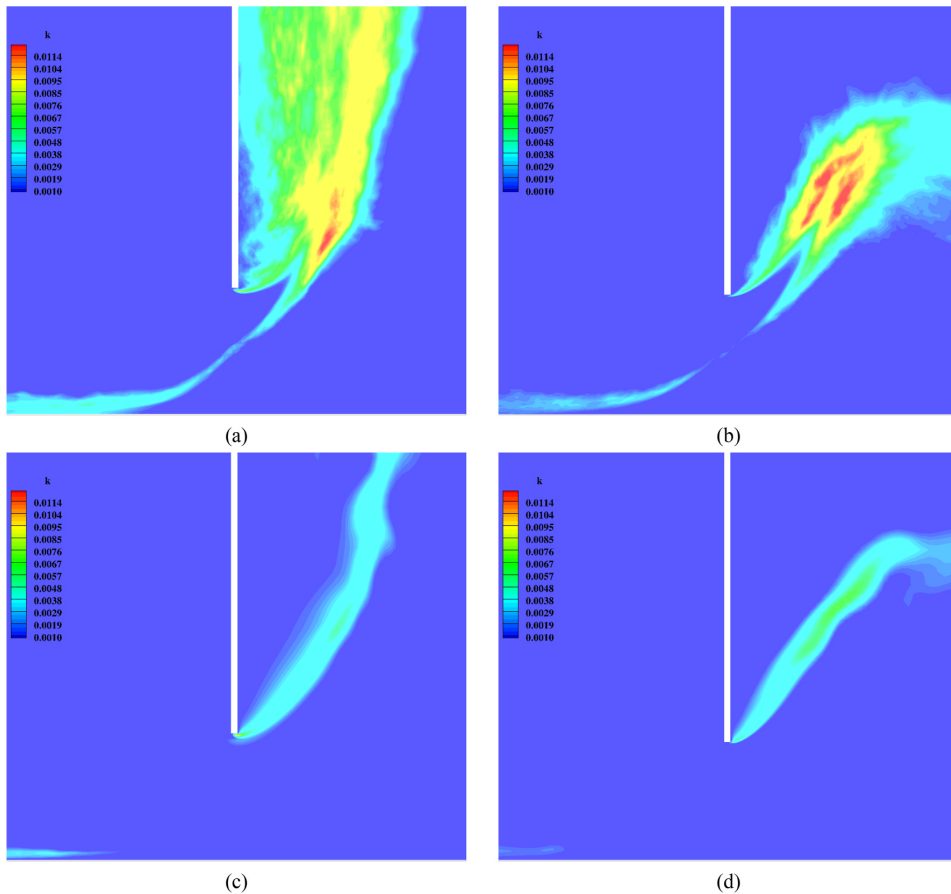


Fig. 8. Contours of turbulent kinetic energy (k) on the vertical plane ($y = 0$) obtained from LES (top) and RANS (bottom) in isothermal rooms (left) and thermally stratified rooms (right).

layer and interfacial mixing layer merge. Compared to thermally stratified rooms, the warm jet spreads in a broader area in the cold room for the isothermal case, in line with the jet expansion observed in Fig. 5, which is more extensive along the vertical partition wall. This indicates that the warm jet cannot develop up to the ceiling in the thermally stratified cold room as the temperature difference between the warm jet and cold zone disappears progressively with height.

4.5. Comparison with experiments and with the standard model

Time-averaged experimental results are reported along a vertical line in the middle of the doorway in Fig. 7(b) and (d). The time-averaged streamwise velocity in Fig. 7(d) computed using LES, RANS, and Euler shows excellent agreement with laboratory measurements with an average deviation of less than 10%. However, the measured temperature in Fig. 7(b) is only qualitatively similar to the LES, RANS and Euler results. This means that the time-averaged temperature above the NP moves progressively from the temperature of the cold zone to the temperature of the warm zone over a same distance (from the NP at about 0.9 m–1.6 m above the floor). Quantitatively, the measured and CFD simulated temperatures show a significant deviation up to 0.5°C. A plausible reason is the influence of longwave thermal radiation from the laboratory walls that could impact the sensor (PT-100) measurements. The mean radiant temperature observed by the PT100 probes is between

the wall temperature of the cold and warm rooms. It could explain that the air temperature measurements in the lower and upper part of the doorway are not strictly equal to the temperature of the cold and warm rooms, respectively. Another reason for this deviation could be the approximation of the laboratory by two large reservoirs in the CFD geometry.

In conclusion, the comparison with the experimental measurements shows reasonably good agreement with CFD results. However, on the one hand, the number of measurement points is limited, and on the other hand, the temperature field shows only similar behavior. Nevertheless, they tend to demonstrate that the same physics is investigated in both experimental and CFD conditions.

For a discharge coefficient based on the mass flow ($C_{d,M}$) computed using the LES, the standard model gives a velocity profile close to measurements, except on the top part of the doorway, where the standard model underpredicts the velocity magnitude because it neglects important 2D effects (Fig. 7(d)). The temperature profile predicted by the standard theory is defined by the one-dimensional and inviscid flow assumptions meaning that the air temperature below the NP within the doorway is equal to the temperature of the cold room, while above the NP, it is equal to the warm room temperature. In other words, the temperature transition in the standard model between the warm and cold airstreams is discontinuous. This discontinuity is located at the level of the NP that can be obtained using Equation (10). For the isothermal

rooms, the transition computed by the CFD is smoother even though limited in the close vicinity of the NP. For the stratified rooms, as mentioned in the previous section, the transition happens over a considerable vertical distance from about 0.9 m to 1.6 m above the floor. In conclusion, unlike the time-averaged velocity magnitude, the time-averaged temperature from the standard theory deviates from reality over a large fraction of the doorway.

4.6. Bulk quantities and C_d

The mass (\dot{m}) and heat flows (\dot{Q}) are analyzed either only using data along a vertical line in the middle of the doorway (like in the laboratory experiments) or using data in the entire doorway plane. The measurement setup along a vertical line in the middle of the doorway is also relevant as it is done in several studies, such as in the laboratory measurements considered in our paper [35]. It should be checked if limiting the measurement points to a single vertical line strongly impacts the bulk quantities and the C_d . Two discharge coefficients, $C_{d,M}$ and $C_{d,Q}$, are evaluated using \dot{m} or \dot{Q} , respectively. Based on the conclusions from the previous section and the values of C_d in Table 1, the following conclusions can be derived. The case using CFD data over the entire doorway plane is analyzed first as this is a consistent evaluation of the mass and heat flows:

- The discharge coefficient evaluated by the Euler model is similar to the LES and RANS values. A maximum deviation of up to 10% can be found. It means that the largest part of the C_d value can be explained by the difference between Euler and the standard theoretical model, namely the two-dimensional contraction effects.
- For the thermally stratified rooms where the interfacial mixing is limited, the difference of C_d between Euler, RANS and LES is minimal (e.g., from 0.494 to 0.509 for the $C_{d,M}$). The difference between the $C_{d,M}$ and $C_{d,Q}$ is evaluated in the last column of Table 1. This value is similar for the Euler, RANS and LES, the $C_{d,Q}$ being about 8% lower than the $C_{d,M}$.
- For the isothermal rooms where the interfacial mixing is not negligible, the difference of C_d between Euler, RANS and LES is more considerable and up to 10%. The difference between $C_{d,M}$ and $C_{d,Q}$ is

different between the Euler, RANS and LES: the $C_{d,Q}$ is 3.4% lower for Euler to 6.8% lower for the LES.

- The difference between RANS and LES is practically very small (maximum 5%).

The discharge coefficient computed using the data along a vertical line in the middle of the doorway is also reported in Table 1. In this case, the contraction effects due to the finite width (W) of the door along the vertical side jambs are neglected. Then, the resulting C_d is systematically overestimated. In addition, the difference between the $C_{d,M}$ and $C_{d,Q}$ looks more pronounced than using data over the entire door opening. This is a spurious effect that can be explained by Equation (12). According to the theory, the reference temperature (T_{ref}) can be removed from the equation because the mass is conserved. However, in reality, the flow is three-dimensional and the \dot{m}_{WC} is not strictly equal to \dot{m}_{CW} when they are evaluated along a single vertical line. Consequently, the heat flow is still dependent on the definition of T_{ref} , which is not appropriate.

5. Discussions

Based on the analysis of the results, the research questions from Q1 to Q6 defined in the introduction section can be answered:

- Q1: The unsteady flow structures and turbulent mixing have been characterized in Section 4.
- Q2: Based on the analysis of the discharge coefficient in Section 4.6, the C_d value can be mainly explained by the two-dimensional effects, while introducing viscous effects with the RANS and LES generate a maximum change of 10%. According to Wilson and Kiel [19], the re-entrainment effect should lead to lower mass flow rates and thus C_d . However, Table 1 reveals that the C_d using Euler simulations is lower than CFD simulations including viscous effects, like RANS and LES. This result is not intuitive, but a reasonable physical explanation can be given. As previously mentioned, the flow contraction is the dominant factor driving the C_d value. Fig. 9 shows the time-averaged velocity magnitude on a plane perpendicular to the warm jet near the maximum of flow contraction. One can see that the Euler simulation leads to a more concentrated jet than RANS. As the blockage from

Table 1

Discharge coefficients obtained based on the mass ($C_{d,M}$) and heat flow rate ($C_{d,Q}$) for isothermal and thermally stratified rooms: values computed with data over the entire doorway are indicated by an empty rectangle, while values computed using data along a vertical line in the middle of the doorway are represented by a divided rectangle.

		$C_{d,M} = \frac{\dot{m}_{actual}}{\dot{m}_{max}}, C_{d,Q} = \frac{\dot{Q}_{actual}}{\dot{Q}_{max}}$		Center Line	Doorway Plane	$C_{d,M}$	$C_{d,Q}$	$E\% = \frac{ C_{d,M} - C_{d,Q} }{C_{d,M}}$
				←→	▢			
Thermally stratified rooms	\dot{m}_{max} and \dot{Q}_{max} based on measured room temperature	LES	▢	▢	0.626	0.680	8.6	
			▢	▢	0.509	0.464	8.8	
		RANS	▢	▢	0.636	0.626	1.5	
			▢	▢	0.509	0.468	8	
		Euler	▢	▢	0.621	0.635	2.2	
			▢	▢	0.494	0.457	7.5	
	Measurement	▢	▢	0.645	0.663	2.79		
Isothermal rooms	\dot{m}_{max} and \dot{Q}_{max} based on the averaged room temperature	LES	▢	▢	0.606	0.558	7.9	
			▢	▢	0.543	0.506	6.8	
		RANS	▢	▢	0.619	0.699	12.92	
			▢	▢	0.519	0.492	5.2	
		Euler	▢	▢	0.595	0.536	9.91	
		▢	▢	0.495	0.478	3.4		

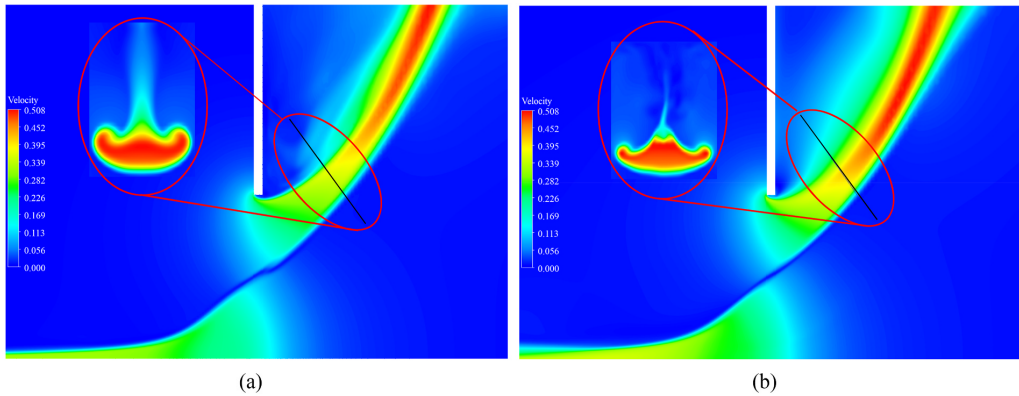


Fig. 9. Time-averaged velocity magnitude from RANS (left) and Euler (right) taken on a plane perpendicular to the jet near the maximum of flow contraction.

this contraction is more important in the Euler simulation, the C_d is lower.

- Q3: The RANS simulation using the RNG k-ε model gives similar results to LES. The interfacial mixing in the middle of the doorway can be underestimated by RANS simulations. However, this mixing in LES remains in the close vicinity of the NP. More importantly, RANS is not able to capture the transition of the airstreams into unsteady turbulent jets when they expand in the opposite rooms, as shown by the contours of turbulent kinetic energy in Fig. 8.
- Q4: The temperature stratification has a significant effect on the temperature distribution within the doorway due to two-dimensional effects (see Section 4.5). The transition between the temperature of the cold room below the NP and the temperature of the warm room above the NP takes place over a large part of the doorway (from 0.9 to 1.6 m). This leads to a significant deviation compared to the temperature field used in the standard theory. In addition, unsteady flow structures are less pronounced in the stratified room case than in the isothermal case. Both cases have been simulated using the exact same CFD setup. The explanation for this last phenomenon should be investigated in further research work.
- Q5: In BPS, the temperature in each room is assumed to be isothermal [43]. The mass and heat fluxes exchanged by a bidirectional airflow in the doorway are computed using the standard model corrected by a discharge coefficient, as described in Section 2.1. If the air temperature simulated by BPS in each room is precisely equal to the measured air temperature averaged along the vertical direction (z), the data in Table 2 shows that there are large discrepancies

between the resulting $C_{d,M}$ and $C_{d,Q}$ if the rooms are not isothermal in reality (up to 46%). The $C_{d,M}$ is only slightly affected when the stratification in both rooms is neglected in the standard model. However, the largest influence is on the $C_{d,Q}$ which increases significantly. Since the convective heat flux is the product of the velocity and the temperature, If the estimate of the velocity is reasonable, the temperature advected on the upper and lower parts of the doorway is respectively lower and higher in the case of isothermal reservoirs than when taking the vertical stratification into account. The maximum theoretical heat flow (\dot{Q}_{max}) is thus lower when the two rooms are assumed to be isothermal compared to the stratified rooms, leading to a higher $C_{d,Q}$. In BPS, a single C_d is typically defined to tune the mass and heat flow to the real values. If the room is stratified, the C_d should, in reality, be different for the mass and heat flows to match the reality.

- Q6: Evaluating the discharge coefficient based on measurements along a vertical line in the middle of the doorway leads to significant errors (see Section 4.6). It overestimates the $C_{d,M}$ as the contraction effects along the vertical side jambs are neglected. Mass imbalance along the vertical line makes the evaluation of the heat flow dependent on the T_{ref} , which is not reliable.

The CFD setup has been defined to reproduce the flow measurements in a climate chamber. However, the limited number of measurement points does not constitute a full experimental validation of the CFD results. Therefore, detailed laboratory measurements or additional LES should be performed in future work.

Table 2

Discharge coefficients obtained based on the mass ($C_{d,M}$) and heat flow rate ($C_{d,Q}$) for BPS analysis: values computed with data over the entire doorway are indicated by an empty rectangle, while values computed using data along a vertical line in the middle of the doorway are represented by a divided rectangle.

	$C_{d,M} = \frac{\dot{m}_{actual}}{\dot{m}_{max}}, C_{d,Q} = \frac{\dot{Q}_{actual}}{\dot{Q}_{max}}$	Center Line \longleftrightarrow	Doorway Plane \longleftrightarrow	$C_{d,M}$	$C_{d,Q}$	$E\% = \frac{ C_{d,M} - C_{d,Q} }{C_{d,M}}$
Thermally stratified rooms	\dot{m}_{max} and \dot{Q}_{max} based on the averaged room temperature (for BPS analysis)	LES		0.578	1.009	74.6
		RANS		0.471	0.689	46.28
				0.588	0.929	57.99
		Euler		0.469	0.694	47.97
				0.573	0.943	64.57
		Measurement		0.457	0.679	48.57
				0.595	1.016	70.76

6. Conclusions

The airflow passing through an open doorway in the steady-state bulk flow regime was simulated using a high-resolution Large Eddy Simulation (LES), which enabled the capture of unsteady flow phenomena. In addition, this LES can serve as a reference solution for simplified methods, like Reynolds-Averaged Navier-Stokes (RANS) approaches or the standard theoretical model. The conclusions can be summarized as follows:

- The main objective of this study was to characterize the bidirectional unsteady flow phenomena. Firstly, the LES revealed that the bidirectional flow can generate a turbulent mixing region near the neutral plane (NP). However, results found that this effect remains located in the close vicinity of the NP so that its influence is limited. LES also showed that the instantaneous NP is not a horizontal line but rather fluctuating in the vertical direction. Secondly, the LES confirmed that the re-entrainment from the two non-isothermal jets expanding from the doorway deflects a fraction of the flow that would otherwise have moved towards the doorway. Finally, LES showed that the non-isothermal jets develop large unsteady flow structures when they expand in the opposite room.
- Results suggest that the RANS approach reproduces most of the flow characteristics from LES, except for the large unsteady flow structures generated by the jet expansion far away from the door. If this effect is not important in the application, RANS simulations are a good alternative to the time-consuming LES for this flow.
- The discharge coefficient (C_d) is mainly driven by two-dimensional contraction effects. Comparing Euler simulation to RANS simulation or LES revealed that viscous effects have a lower influence on the C_d than these contraction effects. Unlike previous results from the literature, the results from this study found that the viscous effects tend to increase the C_d as they decrease the flow contraction. This effect dominates over the mixing effects that tend to decrease the C_d .

The results also enabled guidelines to be derived for the evaluation and use of the C_d with the standard theoretical model:

Appendix A

A.1. Design of the grid

Preliminary analysis using an unstructured mesh has shown that simulations were prone to numerical errors with a non-dissipative central scheme required for LES. Then, as the geometry is simple, a structured mesh is used to keep the solution stable with a pure central scheme (recommended for LES). A no-slip boundary condition on the partition would need a wall-normal grid refinement ($y^+ < 1$) so that, consequently, using a structured mesh, an anisotropic mesh would be generated in the middle of the doorway (with the smallest grid size in the direction of the flow in the doorway and the largest grid size perpendicular to the flow direction). To solve the mixing layer, it is better to limit the mesh anisotropy. This is also better for the definition of the mesh size in the WALE model (i.e., $\sqrt[3]{\bar{V}}$). In addition, the flow is by definition driven by the difference in hydrostatic pressure in both rooms connected by the open door. Therefore, a no-slip condition on the partition wall is expected to have a limited influence on the flow in the doorway.

A.2. Grid size and LES resolution

The grid convergence analysis is not straightforward for LES since, upon further refinement of the LES grid, finer and finer scales are resolved until the LES converges to the DNS. Moreover, the computational cost of a finer grid can be restrictive [41]. However, there are specific criteria to estimate the resolution of a LES [44], such as; the ratio between modeled turbulent viscosity and laminar viscosity, i.e., $\langle \nu_t \rangle / \nu$, the ratio between modeled and total shear stress, the ratio between modeled and total turbulent kinetic energy, and the ratio of integral length scale to cell size.

In this study, the LES resolution is evaluated using three different approaches;

- The C_d should not be evaluated only based on measurement along a vertical line in the middle of the doorway, as two-dimensional effects from the vertical side jambs of the doorway would be neglected. In addition, the discharge coefficient for the heat flow ($C_{d,Q}$) is inconsistent using measurements along a vertical line.
- In building performance simulation (BPS), rooms are typically modeled as isothermal reservoirs. If, in reality, the rooms are thermally stratified, a same C_d cannot be used in BPS to calibrate both the mass flow and the heat flow. Two separate discharge coefficients, i.e., $C_{d,Q}$ and $C_{d,M}$, should be defined for the BPS to compute the right mass and heat exchanges through the doorway.

CRedit authorship contribution statement

Elyas Larkermanni: Writing – review & editing, Writing – original draft, Visualization, Validation, Software, Resources, Methodology, Investigation, Formal analysis, Data curation, Conceptualization. **Guangyu Cao:** Writing – review & editing, Visualization, Validation, Methodology, Conceptualization. **Laurent Georges:** Writing – review & editing, Writing – original draft, Validation, Supervision, Project administration, Methodology, Investigation, Conceptualization.

Declaration of competing interest

The authors declare that they have no known competing financial interests or personal relationships that could have appeared to influence the work reported in this paper.

Data availability

Data will be made available on request.

Acknowledgments

The authors would like to acknowledge Iman Bayat, affiliated with the Ferdowsi University of Mashhad, for his comments and suggestions that greatly improved the manuscript. The authors also would like to thank the editor and anonymous reviewers for the valuable comments.

- a) The resolution of the shear layer between both the warm and cold airstreams is compared to the literature.
- b) The turbulent kinetic energy ratio is evaluated in the computational domain to check if the LES is sufficiently resolved or not.
- c) The results of LES for the isothermal case, including discharge coefficient (C_d), temperature and velocity profiles, are compared on a coarse, medium and fine grid containing 31,825,152 cells, 63,203,392 cells and 127,316,480 cells, respectively.

a) The resolution of the shear layer between both the warm and cold airstreams

It is important to capture the flow physics of the shear layer between the counter-flowing airstreams correctly as it directly influences two main phenomena analyzed in our study, meaning the mixing between both airstreams and the flow re-entrainment. It is tricky to assess the resolution of this shear layer using the analysis of the kinetic energy spectrum due to the lack of homogeneous directions in the flow field. Therefore, the resolution can be discussed by comparing the mesh size with other LES of shear layers found in the literature. The maximum time-averaged velocity difference through the shear layer (ΔU) computed using the isothermal case is about 0.4 m/s . The analysis of the velocity profile through the shear layer gives a momentum thickness (θ) and a vorticity thickness (δ) of 0.05 m and 0.18 m , respectively. These values correspond to a Reynolds number based on momentum thickness (Re_θ) of about 1400 and a Reynolds number based on vorticity thickness (Re_δ) of 4800. Close to the doorway, the mesh is almost isotropic with a size (h) of 0.6 cm .

Firstly, Balaras et al. [45] performed LES of a temporally evolving mixing layer from an initial Re_θ of 900 until a Re_θ of 3400. They performed a sensitivity analysis on the domain and grid size to be able to reproduce the flow statistics of DNS data. This study is thus a good reference for comparison. They show that they can reproduce the velocity statistics with a mesh size of 0.85θ , 0.43θ and 0.85θ in streamwise, spanwise and normal directions, respectively. The mesh size in our LES is significantly smaller than these values. Secondly, Pham et al. [46] analyzed the temporal evolution of a stratified shear layer using LES. They investigated the case of a fine LES for an initial Re_δ of 5000. They use a mesh of 0.12δ , 0.12δ and 0.03δ in the streamwise, spanwise and normal directions, respectively. This grid resolution is comparable to our mesh. For instance, their mesh size in the normal direction corresponds to 0.54 cm . Based on these two studies, it can be concluded that the mesh size in our simulation is appropriate to capture the shear layer using LES.

b) The turbulent kinetic energy ratio

Pope [47] recommends the turbulent kinetic energy ratio ($M(x, t)$) as a simple indicator of turbulence resolution. It is defined as the ratio of the unresolved turbulent kinetic energy to the total turbulent kinetic energy:

$$M(x, t) \equiv \frac{k_r(x, t)}{K(x, t) + k_r(x, t)} \tag{23}$$

where $K(x, t)$ and $k_r(x, t)$ indicate the turbulent kinetic energy of the resolved and residual motions, respectively. Smaller values of M correspond to more turbulent motions resolved on the mesh. The limit of $M = 0$ corresponds to DNS while $M = 1$ is representative for a RANS. Based on his suggestion, the turbulence is well resolved by the LES if $M < 0.2$.

Since the turbulent kinetic energy ratio (M) is smaller than 0.09 for LES of thermally stratified rooms, the grid employed for LES is fine enough to simulate the turbulent structures precisely.

c) Comparison of LES results on three different grid resolutions

A grid-sensitivity analysis is conducted for the LES for the case of two isothermal interconnected rooms at different temperatures. The coarse, medium and fine grid contain 31,825,152 cells, 63,203,392 cells and 127,316,480 cells, respectively. The mean streamwise velocity and temperature profiles for three different meshes are plotted along a vertical line in the middle of the doorway in Fig. 10. All three grids provide almost the same profiles, while the fine grid indicates a slight departure from the results of the coarse and medium grids between $0.95 < z < 1.1$. The maximum difference between the coarse and the fine grid in this area goes up to 0.053 m/s and 0.49°C for velocity and temperature, respectively. The shear layer thickness is roughly the same for the three grid resolutions.

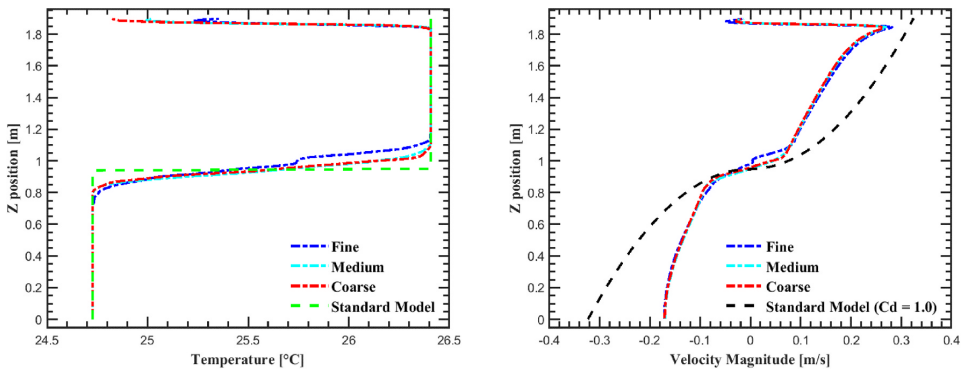


Fig. 10. Time-averaged temperature and streamwise velocity profiles along a vertical line in the middle of the doorway in isothermal rooms on three different grids using LES.

The discharge coefficients, $C_{d,M}$ and $C_{d,Q}$ based on mass (\dot{m}) and heat flows (\dot{Q}) are obtained for the coarse, medium and fine mesh. The data are reported in Table 3.

Table 3

Discharge coefficients obtained based on the mass ($C_{d,M}$) and heat flow rate ($C_{d,Q}$) from LES on three different grids.

		Doorway Plane 		$C_{d,M}$	$C_{d,Q}$
$C_{d,M} = \frac{\dot{m}_{\text{actual}}}{\dot{m}_{\text{max}}}, C_{d,Q} = \frac{\dot{Q}_{\text{actual}}}{\dot{Q}_{\text{max}}}$					
Isothermal rooms	\dot{m}_{max} and \dot{Q}_{max} based on the averaged room temperature	Coarse Grid		0.511	0.486
		Medium Grid		0.510	0.484
		Fine Grid		0.543	0.506

While the previous two arguments showed that the fine grid was refined enough, the sensitivity analysis on the C_d shows that a coarser grid would not be able to capture the physics properly. The C_d is relatively constant between the coarse and medium meshes but increases significantly for the fine grid.

References

- [1] F. Bazdidi-Tehrani, S. Masoumi-Verki, P. Gholamalipour, Impact of opening shape on airflow and pollutant dispersion in a wind-driven cross-ventilated model building: large eddy simulation, *Sustain. Cities Soc.* 61 (2020), 102196.
- [2] P. Kalliomäki, P. Saarinen, J.W. Tang, H. Koskela, Airflow patterns through single hinged and sliding doors in hospital isolation rooms—Effect of ventilation, flow differential and passage, *Build. Environ.* 107 (2016) 154–168.
- [3] A. Bediako-Bowan, K. Mølbak, J. Kurtzhals, E. Owusu, S. Debrah, M. Newman, Risk factors for surgical site infections in abdominal surgeries in Ghana: emphasis on the impact of operating rooms door openings, *Epidemiol. Infect.* 148 (2020).
- [4] B. Ljungqvist, B. Reinmüller, J. Gustén, L. Gustén, J. Nordenadler, Contamination risks due to door openings in operating rooms, in: 41 St R 3-Nordic Symposium, 2010, p. 148.
- [5] P.E. Saarinen, P. Kalliomäki, J.W. Tang, H. Koskela, Large eddy simulation of air escape through a hospital isolation room single hinged doorway—validation by using tracer gases and simulated smoke videos, *PLoS One* 10 (7) (2015), e0130667.
- [6] X. Shao, K. Hashimoto, L. Fang, A.K. Melikov, K.G. Naydenov, C. Rasmussen, Experimental study of airborne particle transmission through the doorway of a cleanroom due to the movement of a person, *Build. Environ.* 183 (2020), 107205.
- [7] D.W. Etheridge, M. Sandberg, *Building Ventilation: Theory and Measurement*, John Wiley & Sons, Chichester, UK, 1996.
- [8] F. Allard, D. Bienfait, F. Haghighat, G. Liebecc, K. Maas, R. Pelletret, L. Vandaele, *Airflow through Large Openings in Buildings, Annex 20: Air Flow Patterns within Buildings*, 1992.
- [9] D. Scott, R. Anderson, R. Figliola, Blockage of natural convection boundary layer flow in a multizone enclosure, *Int. J. Heat Fluid Flow* 9 (2) (1988) 208–214.
- [10] J. Neymark, C.R. Boardman III, A. Kirkpatrick, R. Anderson, High Rayleigh number natural convection in partially divided air and water filled enclosures, *Int. J. Heat Mass Tran.* 32 (9) (1989) 1671–1679.
- [11] L. Georges, G. Cao, H.M. Mathisen, Further investigation of the convective heat transfer between rooms through open doorways, in: The 12th REHVA World Congress, vol. 5, Aalborg University, Department of Civil Engineering., Aalborg, 2016.
- [12] E.S. AB, *IDA Indoor climate and energy*. <http://www.equ.se/en/ida-ice/>, 2013. (Accessed 24 December 2015).
- [13] A. Haas, A. Weber, V. Dorer, W. Keilholz, R. Pelletret, COMIS v3.1 simulation environment for multizone air flow and pollutant transport modelling, *Energy Build.* 34 (9) (2002) 873–882.
- [14] M.J. Alonso, W.S. Dols, H. Mathisen, Using Co-simulation between EnergyPlus and CONTAM to evaluate recirculation-based, demand-controlled ventilation strategies in an office building, *Build. Environ.* (2021), 108737.
- [15] Q. Chen, Ventilation performance prediction for buildings: a method overview and recent applications, *Build. Environ.* 44 (4) (2009) 848–858.
- [16] F. Allard, Y. Utsumi, Airflow through large openings, *Energy Build.* 18 (2) (1992) 133–145.
- [17] P.K. Heiselberg, L. Jepsen, A. Hyldgaard, P.V. Nielsen, M. Perino, Short-Term Airing by Single-Sided Natural Ventilation: Part 1: Measurement of Transient Air Flow Rates, Short-Term Airing by Single-Sided Natural Ventilation, Tsinghua University, 2003, pp. 117–124.
- [18] A. Lefaue, J. Partridge, P. Linden, Regime transitions and energetics of sustained stratified shear flows, *J. Fluid Mech.* 875 (2019) 657–698.
- [19] D. Wilson, D. Kiel, Gravity driven counterflow through an open door in a sealed room, *Build. Environ.* 25 (4) (1990) 379–388.
- [20] W. Brown, K. Solvason, Natural convection through rectangular openings in partitions—1: vertical partitions, *Int. J. Heat Mass Tran.* 5 (9) (1962) 859–868.
- [21] W. Brown, Natural convection through rectangular openings in partitions—2: horizontal partitions, *Int. J. Heat Mass Tran.* 5 (9) (1962) 869–881.
- [22] M. Nansteel, R. Greif, An investigation of natural convection in enclosures with two- and three-dimensional partitions, *Int. J. Heat Mass Tran.* 27 (4) (1984) 561–571.
- [23] M. Nansteel, R. Greif, *Natural Convection in Undivided and Partially Divided Rectangular Enclosures*, 1981.
- [24] P. Favaro, H. Manz, Temperature-driven single-sided ventilation through a large rectangular opening, *Build. Environ.* 40 (5) (2005) 689–699.
- [25] D. Agonafer, L. Gan-Li, D.B. Spalding, The LEVEL turbulence model for conjugate heat transfer at low Reynolds numbers, *Application of CAE/CAD Electronic Systems, ASME* 18 (1996) 23–26.
- [26] W. Zhang, Q. Chen, Large eddy simulation of indoor airflow with a filtered dynamic subgrid scale model, *Int. J. Heat Mass Tran.* 43 (17) (2000) 3219–3231.
- [27] Y. Jiang, Q. Chen, Study of particle dispersion in buildings with large eddy simulation, *Proceedings of Indoor Air 2* (2002).
- [28] N. Ivanov, M. Zsimova, Large eddy simulation of airflow in a room with a sidewall jet: comparison with benchmark test data for occupied zone, in: *Proc. of Roomvent & Ventilation 2018: Excellent Indoor Climate and High Performing Ventilation*, 2018, pp. 319–324.
- [29] B. Blocken, LES over RANS in Building Simulation for Outdoor and Indoor Applications: a Foregone Conclusion?, *Building Simulation, Springer*, 2018, pp. 821–870.
- [30] Z. Zhang, W. Zhang, Z.J. Zhai, Q.Y. Chen, Evaluation of various turbulence models in predicting airflow and turbulence in enclosed environments by CFD: Part 2—comparison with experimental data from literature, *HVAC R Res.* 13 (6) (2007) 871–886.
- [31] W.K. Chow, G. Zou, Correlation equations on fire-induced air flow rates through doorway derived by large eddy simulation, *Build. Environ.* 40 (7) (2005) 897–906.
- [32] J.D. Balcomb, *Heat Distribution by Natural Convection, Intersol Eighty Five, Elsevier* 1986, pp. 277–281.
- [33] D.D. Weber, *Similitude Modeling of Natural Convection Heat Transfer through an Aperture in Passive Solar Heated Buildings*, 1981.
- [34] R. Pelletret, H. Khodr, E. de Sophia Antipolis, A New Model to Compute Air Distribution, *Building Simulation, 1989*, pp. 291–296.
- [35] P. Minard, Experimental Study of the Temperature and Velocity Distribution through a Doorway between a Warm and a Cold Room, Norwegian University of Science and Technology, 2015.
- [36] F. Nicoud, F. Ducros, Subgrid-scale stress modelling based on the square of the velocity gradient tensor, *Flow, Turbul. Combust.* 62 (3) (1999) 183–200.
- [37] A. Leonard, Energy cascade in large-eddy simulations of turbulent fluid flows, *Adv. Geophys.* 18 (A) (1974) 237–248.
- [38] F. Piscaglia, A. Montorfano, A. Onorati, F. Brusiani, Boundary conditions and sgs models for les of wall-bounded separated flows: an application to engine-like geometries, *Oil Gas Sci. Technol. Revue d'IFP Energies nouvelles* 69 (1) (2014) 11–27.
- [39] A. Yuen, G. Yeoh, V. Timchenko, S. Cheung, T. Chen, Study of three LES subgrid-scale turbulence models for predictions of heat and mass transfer in large-scale

- compartment fires, *Numer. Heat Tran., Part A: Applications* 69 (11) (2016) 1223–1241.
- [40] F. Bazdidi-Tehrani, S. Masoumi-Verki, P. Gholamalipour, M. Kiamansouri, Large Eddy Simulation of Pollutant Dispersion in a Naturally Cross-Ventilated Model Building: Comparison between Sub-grid Scale Models, *Building Simulation*, Springer, 2019, pp. 921–941.
- [41] N. Arya, A. De, Effect of grid sensitivity on the performance of wall adapting SGS models for LES of swirling and separating-reattaching flows, *Comput. Math. Appl.* 78 (6) (2019) 2035–2051.
- [42] V. Yakhot, S.A. Orszag, Renormalization group analysis of turbulence. I. Basic theory, *J. Sci. Comput.* 1 (1) (1986) 3–51.
- [43] J.L. Hensen, R. Lamberts, *Building Performance Simulation for Design and Operation*, Routledge, 2012.
- [44] L. Davidson, *Fluid Mechanics, Turbulent Flow and Turbulence Modeling*, Chalmers University of Technology, Goteborg, Sweden, 2018. Nov 2011.
- [45] E. Balaras, U. Piomelli, J.M. Wallace, Self-similar states in turbulent mixing layers, *J. Fluid Mech.* 446 (2001) 1–24.
- [46] H.T. Pham, S. Sarkar, Large eddy simulations of a stratified shear layer, *J. Fluid Eng.* 136 (6) (2014).
- [47] S.B. Pope, Ten questions concerning the large-eddy simulation of turbulent flows, *New J. Phys.* 6 (1) (2004) 35.

A.2 Paper II

Development of an Accurate Central Finite-Difference Scheme with a Compact Stencil for the Simulation of Unsteady Incompressible Flows on Staggered Orthogonal Grids

Elyas Larkermanni, Hans Bihs, Grégoire Winckelmans, Matthieu Duponcheel,
Tobias Martin, Bernhard Müller, Laurent Georges



Contents lists available at ScienceDirect

Computer Methods in Applied Mechanics and Engineering

journal homepage: www.elsevier.com/locate/cma

Development of an accurate central finite-difference scheme with a compact stencil for the simulation of unsteady incompressible flows on staggered orthogonal grids

Elyas Larkermani^{a,*}, Hans Bihs^b, Grégoire Winckelmans^c, Matthieu Duponcheel^c, Tobias Martin^b, Bernhard Müller^a, Laurent Georges^a

^a Department of Energy and Process Engineering (EPT), Norwegian University of Science and Technology (NTNU), Trondheim, Norway

^b Department of Civil and Environmental Engineering, Norwegian University of Science and Technology (NTNU), Trondheim, Norway

^c Institute of Mechanics, Materials, and Civil Engineering (iMMC), Université Catholique de Louvain (UCLouvain), Louvain-la-Neuve, Belgium

ARTICLE INFO

Keywords:

Finite difference method
Large Eddy Simulation
Incompressible flow
Staggered grid

ABSTRACT

In scale-resolving simulations such as Large Eddy Simulations (LES), the spatial discretization scheme of the convective term plays a crucial role in avoiding interference between the numerical errors and the subgrid-scale model. Accurate schemes lead to lower truncation errors and better predictions of turbulent flows without the need for an excessively refined grid. To this end, a new second-order finite-difference scheme (HCDS6) has been developed for incompressible flows and orthogonal staggered grids. Compared to the standard second-order scheme, the new scheme has significantly lower dispersion errors. Compared to existing high-order schemes, the numerical stencil of HCDS6 is more compact, which makes it easier to implement, especially considering boundary conditions around complex geometries using Immersed Boundary Methods (IBM). The HCDS6 scheme conserves the discrete momentum with limited production or dissipation of discrete kinetic energy, which guarantees its numerical stability. Its performance is evaluated using an open-source CFD package called REEF3D. Three benchmarks demonstrate the key properties and performance of the scheme: the convection of an isentropic vortex, the Taylor-Green vortex flow, and turbulent channel flow. Its relatively low dispersion errors, combined with ease of implementation, make the HCDS6 scheme a promising candidate for efficient scale-resolving simulations of turbulent flows.

1. Introduction

This research aims to construct an accurate finite-difference scheme for incompressible unsteady turbulent flow simulations such as Large Eddy Simulations (LES) or Direct Numerical Simulations (DNS). More specifically, the paper focuses on the convective term of the momentum equation. It considers orthogonal non-uniform grids where complex geometries can be considered using Immersed Boundary Methods (IBM) [1]. In this context, as many different numerical methods can be applied, the introduction will first define the specific framework of our study.

Previous studies [2-7] have demonstrated the significant influence of numerical errors on the prediction accuracy of LES.

* Corresponding author

E-mail address: elyas.larkermani@ntnu.no (E. Larkermani).

<https://doi.org/10.1016/j.cma.2024.117117>

Received 6 March 2024; Received in revised form 1 June 2024; Accepted 1 June 2024

Available online 14 June 2024

0045-7825/© 2024 The Author(s). Published by Elsevier B.V. This is an open access article under the CC BY license (<http://creativecommons.org/licenses/by/4.0/>).

Significant kinetic energy at high wavenumbers in LES requires a numerical scheme that performs well in this range. Although spectral methods are known for their uniform accuracy at all wavenumbers, they do have inherent limitations concerning geometry and boundary conditions, which makes them less applicable in practical cases involving irregular or complex geometries [8]. Furthermore, aliasing errors are important when using spectral methods. Unless explicitly removed using filtering techniques, these errors can lead to a degradation of the solution and negatively impact the accuracy of the simulation [9]. Finite difference, finite volume and finite element methods have lower aliasing errors due to the damping at high wavenumbers [9]. They are often preferred in practical LES applications due to their computational efficiency and flexibility for boundary conditions [10]. For these numerical methods, the conservation of the discrete kinetic energy is an important property for the spatial discretization of the convective term of the momentum equation. Turbulence is characterized by kinetic energy transfer between the different turbulent flow scales. Therefore, the numerical scheme should not interfere in this process through artificial numerical dissipation. In explicit LES, the kinetic energy dissipation at smaller flow scales should be left to the subgrid-scale (SGS) model. Central schemes are known to be non-dissipative, but generally, they do not conserve the discrete kinetic energy. In practice, this may affect the numerical stability of under-resolved simulations, such as LES. Only a subset of central schemes has been tailored to enforce the discrete kinetic energy conservation (assuming negligible time integration errors), which guarantees numerical stability [11,12].

Collocated grids placing all the flow variables (i.e., the velocity and pressure fields) at the same points leads to the checkerboard problem (i.e., spurious pressure oscillations). This effect can be avoided by using stabilization or special interpolation techniques [13]. Although popular and widely used in LES, these techniques introduce some numerical dissipation [14]. Alternatively, the staggered grid arrangement does not suffer from the checkerboard problem by placing flow variables at different locations. This arrangement is challenging to apply for complex grids, such as unstructured grids. However, the complexity is acceptable for orthogonal non-uniform grids, as discussed in this paper. Finally, it is also worth mentioning that Laizet and Lamballais [10] managed to introduce a high-order compact scheme for incompressible flow on orthogonal grids by using a semi-staggered arrangement (meaning that all the velocity components are located at the same point, except for pressure).

The remainder of the paper discusses central finite differences on staggered orthogonal grids, with a special focus on the conservation of the discrete kinetic energy by the convective term. Existing schemes in this category will be discussed to introduce the originality of the new scheme proposed in the paper.

- One remarkable example is the second-order central finite-difference scheme developed by Harlow and Welch for staggered meshes [15]. It has proved to be well-suited for DNS and LES of turbulent flow [16-19]. This scheme conserves not only the discrete mass and momentum but also the discrete kinetic energy on a uniform grid. Vasilyev [11] analyzed the conservation properties of finite differences on non-uniform staggered grids. In finite differences, the convective term can be discretized into three different forms: the divergence, advective and skew-symmetric forms. Vasilyev demonstrated that his second-order discretization cannot simultaneously conserve the discrete momentum and kinetic energy on a non-uniform mesh (called “commutation error” in [11]). In the divergence form, the scheme conserves discrete momentum on a non-uniform grid, while the conservation of discrete kinetic energy is limited to a uniform grid. In contrast, in the skew-symmetric form, the scheme exhibits the opposite behavior. Verstappen et al. [12] introduced a second-order finite volume scheme on non-uniform staggered grids. As it is a finite volume method, it inherently conserves the discrete momentum, but it also manages to conserve the discrete kinetic energy.
- In these schemes for non-uniform grids, the coefficients of the numerical stencil are not adapted locally as a function of the local grid-stretching to conserve the skew-symmetry property of the discretization operator. By preserving the skew-symmetry property of the operator, the discrete kinetic energy is conserved. As the coefficients are not adapted to the local grid-stretching, it leads to a local truncation error that is first order. Nevertheless, studies by Rivas (referenced by Eq. (1) in her article [20]) and Manteufel and White [21] have demonstrated that these schemes can achieve second-order accuracy on non-uniform grids.
- Although widely used for simplicity and efficiency, the second-order central scheme has large dispersion errors. Higher-order numerical schemes overcome the impact of truncation errors, thereby providing more accurate approximations and improving the fidelity of the resolved scales [22]. Morinishi et al. [23] introduced high-order finite differences (i.e., fourth-order and higher) on staggered orthogonal grids that conserve the discrete momentum and kinetic energy on uniform meshes. Vasilyev extended these schemes to non-uniform grids [11]. Similar conclusions apply to the fourth-order schemes as observed in the second-order central schemes. Among the three forms of the fourth-order finite difference schemes introduced by Vasilyev, none can simultaneously conserve both discrete momentum and kinetic energy. However, the fourth-order finite volume scheme by Verstappen et al. [12] proves to achieve this conservation. The main challenge with these two schemes is that the numerical stencil is not compact due to the use of high-order interpolations. From second- to fourth-order accuracy, these numerical stencils are not only increased from three to seven points along lines for the three spatial directions but also expanded from two to four points in the perpendicular directions to each line. These schemes are thus more complex to implement, and they make the treatment of boundary conditions more complicated, particularly when dealing with complex geometries in practical engineering applications using IBM.

The paper, therefore, introduces a new second-order numerical scheme on staggered grids with lower dispersion errors than the conventional second-order schemes of Vasilyev [11] and Verstappen et al. [12]. The new scheme involves seven points in each spatial direction, but unlike the existing fourth-order schemes on staggered grids, the numerical stencil remains compact. This simplifies the implementation and the treatment of boundary conditions. Although the scheme is formally second-order accurate, it is six-order accurate for linear advection problems, providing relatively low dispersion errors. Finally, the strict conservation of the discrete kinetic energy has to be sacrificed to enable this improvement. Still, the numerical tests introduced in the paper prove that this has a

limited impact on results for LES. The key properties of the new scheme are evaluated using three benchmarks: the convection of an isentropic vortex, the three-dimensional Taylor-Green vortex flow, and the turbulent channel flow simulation.

The paper is organized as follows. In Section 2, the discrete equations for the incompressible Navier-Stokes equations and the new scheme are introduced. Section 3 analyzes the performance of the new scheme against the three flow benchmarks. Section 4 concludes the paper by summarizing the findings and outlining future research directions.

2. Numerical method

2.1. Governing equations

The incompressible Navier-Stokes equations are presented in Eq. (1) and translate the mass conservation and Newton’s second law:

$$\begin{aligned} \frac{\partial u_m}{\partial x_m} &= 0 \\ \frac{\partial u_m}{\partial t} + \frac{\partial}{\partial x_n} (u_n u_m) &= -\frac{1}{\rho} \frac{\partial p}{\partial x_m} + \nu \frac{\partial^2 u_m}{\partial x_n^2} \end{aligned} \tag{1}$$

where x_m denotes the m^{th} spatial coordinate direction in the physical space, u_m represents the velocity field in the x_m direction. Here, the Einstein summation convention is used, where repeated indices imply summation. Parameter t is the time, p is the pressure, ν is the kinematic viscosity and ρ is the density. They are assumed to be constant – i.e., independent of the temperature.

2.2. Spatial discretization

A schematic representation of a two-dimensional fully staggered grid arrangement where the velocity components are located at the cell surfaces while the pressure and other scalar quantities are stored in the cell center [13] is illustrated in Fig. 1. Here, i and j are mesh indices in the x_1 and x_2 directions, respectively.

In our work, the discretization operation is performed in computational space to preserve symmetries of the underlying operator. The derivatives in physical space are calculated using the local Jacobian, which can be determined numerically using the same stencil and corresponding weights as the finite differencing operator in the computational space with a uniform grid [11]. In a one-dimensional case, this gives:

$$\frac{\delta \phi}{\delta x} = \frac{1}{J} \frac{\delta \phi}{\delta \zeta} = \frac{1}{J} \frac{\phi_{i+1} - \phi_{i-1}}{2\Delta} \tag{2}$$

In the above definition, ζ denotes the spatial coordinate in the computational domain, and ϕ represents a discrete variable in three spatial coordinate directions. J is the Jacobian of the transformation $x \rightarrow \zeta$ that can be defined numerically as:

$$J = \frac{\delta x}{\delta \zeta} = \frac{x_{i+1} - x_{i-1}}{2\Delta} \tag{3}$$

where Δ is the uniform grid spacing in the computational domain.

Using the notation of Morinishi et al. [23], the finite difference operator $(\delta_n / \delta_n \zeta_1)$ with respect to ζ_1 and the interpolation operator $(\bar{\phi}^{n\zeta_1})$ in the ζ_1 direction in computational space with a stencil n acting on the field ϕ are respectively defined as:

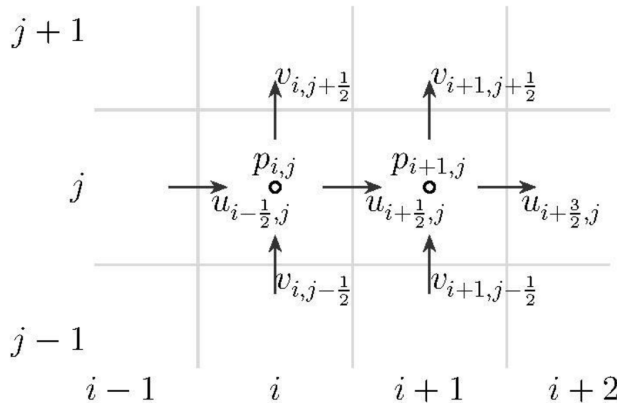


Fig. 1. Staggered arrangement of variables in two dimensions.

$$\begin{aligned} \frac{\delta_n \phi}{\delta_n \zeta_1} \Big|_{\zeta_1, \zeta_2, \zeta_3} &= \frac{\phi(\zeta_1 + n\Delta_1/2, \zeta_2, \zeta_3) - \phi(\zeta_1 - n\Delta_1/2, \zeta_2, \zeta_3)}{n\Delta_1} \\ \overline{\phi}^{\zeta_1} \Big|_{\zeta_1, \zeta_2, \zeta_3} &= \frac{\phi(\zeta_1 + n\Delta_1/2, \zeta_2, \zeta_3) + \phi(\zeta_1 - n\Delta_1/2, \zeta_2, \zeta_3)}{2} \end{aligned} \tag{4}$$

These two operators can be extended to the other spatial directions. Following these operators, the standard second-order scheme of Vasilyev for the non-linear convective term in Eq. (1) on a non-uniform staggered grid is defined as:

$$\begin{aligned} (\text{Div.})_m &= \frac{\delta(u_n u_m)}{\delta \zeta_n} = \frac{\delta_1}{\delta_1 \zeta_n} \{ \overline{u}_n^{1\zeta_m} \overline{u}_m^{1\zeta_n} \} \\ (\text{Adv.})_m &= u_n \frac{\delta(u_m)}{\delta \zeta_n} = \frac{1}{J_n} \left[\overline{u}_n^{1\zeta_m} \frac{\delta_1 u_m}{\delta_1 \zeta_n} \right] \\ (\text{Skew.})_m &= \frac{1}{2}(\text{Div.})_m + \frac{1}{2}(\text{Adv.})_m \end{aligned} \tag{5}$$

This scheme in divergence form, here termed CDS2, conserves the discrete momentum on a non-uniform mesh, while the discrete kinetic energy is conserved only on a uniform mesh. The new scheme (HCDS6) also employs the divergence form for the convective term, using an original hybrid formulation for its discretization. It uses a symmetric, seven-point stencil where the convection velocity is interpolated with a second-order accurate interpolation operator, whereas the convective fluxes are discretized using a high-order central interpolation scheme:

$$\frac{\delta(u_n u_m)}{\delta x_n} = \frac{\delta_1}{\delta_1 x_n} \{ \overline{u}_n^{1x_m} (\alpha_1 \overline{u}_m^{1x_n} + \alpha_3 \overline{u}_m^{3x_n} + \alpha_5 \overline{u}_m^{5x_n}) \} \tag{6}$$

with α_1 , α_3 , and α_5 being the constant scheme coefficients, not adapted according to the local grid-stretching. The coefficients $\alpha_1 = 37/30$, $\alpha_3 = -8/30$, and $\alpha_5 = 1/30$ are chosen such that Eq. (6) corresponds to the standard sixth-order central difference approximation for a constant convection velocity (see Section 2.3). For $\alpha_1 = 1$, $\alpha_3 = 0$, and $\alpha_5 = 0$, the method is degraded to the standard second-order central differential scheme of Vasilyev (CDS2). The HCDS6 is thus tailored to reduce dispersion errors compared to the CDS2. However, the conservation of the discrete kinetic energy had to be sacrificed for this purpose. The HCDS6 conserves the discrete

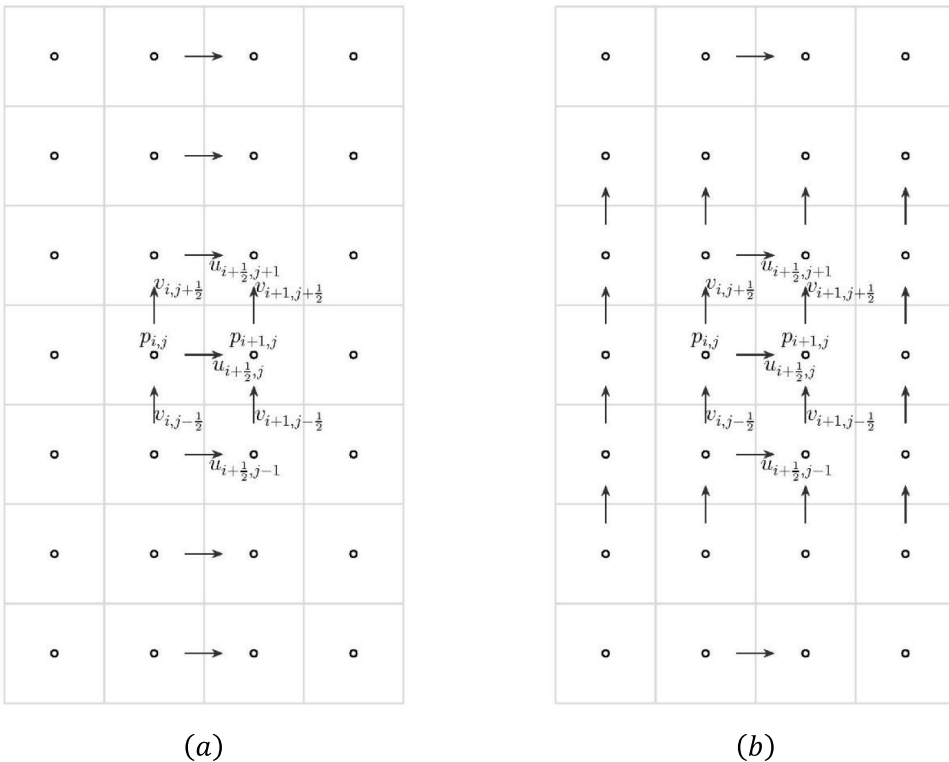


Fig. 2. Comparison of the numerical stencil for HCDS6 (a) and CDS4 (b) for $m = 1$ and $n = 2$.

momentum on non-uniform grids; however, it does not conserve the discrete kinetic energy, even in the case of uniform grids. However, results will show that this effect remains limited as the stencil weights are not adapted according to the local grid-stretching.

It can be observed that the new HCDS6 and CDS2 schemes are more compact than the fourth-order finite-difference schemes of Vasilyev [11] – for example, in divergence form (CDS4):

$$\frac{\delta(u_n u_m)}{\delta x_n} = \frac{9}{8} \frac{\delta_1}{\delta_1 x_n} \left\{ \left(\frac{9}{8} \bar{u}_n^{1x_m} - \frac{1}{8} \bar{u}_n^{3x_m} \right) \bar{u}_m^{1x_n} \right\} - \frac{1}{8} \frac{\delta_3}{\delta_3 x_n} \left\{ \left(\frac{9}{8} \bar{u}_n^{1x_m} - \frac{1}{8} \bar{u}_n^{3x_m} \right) \bar{u}_m^{3x_n} \right\} \quad (7)$$

The term compact stencil should not be confused with compact finite difference schemes [24]. A compact stencil here means that the spatial extension of the points involved in the numerical stencil remains localized in a limited volume. Like the HCDS6, the CDS4 has a seven-point stencil in each spatial direction. However, in contrast to the HCDS6, the CDS4 computes the convection velocity using a fourth-order interpolation. As a result, CDS4 has a stencil that involves four points in the directions perpendicular to each spatial direction, making the stencil not compact, see Fig. 2.

Using the definition of the finite difference and the interpolation operators in Eq. (4) at the mesh indexes i, j , and k , the new central scheme (HCDS6) for the convective terms on staggered grids can be rewritten for the momentum equation in the direction x_1 . To simplify the notation, u_1 and u_2 are simplified to u and v , and x_1 and x_2 to x and y , respectively:

$$\begin{aligned} \frac{\delta(uu)}{\delta x} \Big|_{i+1/2,j,k} &= \frac{\frac{u_{i+1/2,j,k} + u_{i+3/2,j,k}}{2} \left(\alpha_1 \frac{u_{i+1/2,j,k} + u_{i+3/2,j,k}}{2} + \alpha_3 \frac{u_{i-1/2,j,k} + u_{i+5/2,j,k}}{2} + \alpha_5 \frac{u_{i-3/2,j,k} + u_{i+7/2,j,k}}{2} \right)}{x_{i+1} - x_i} \\ &- \frac{\frac{u_{i-1/2,j,k} + u_{i+1/2,j,k}}{2} \left(\alpha_1 \frac{u_{i-1/2,j,k} + u_{i+1/2,j,k}}{2} + \alpha_3 \frac{u_{i-3/2,j,k} + u_{i+3/2,j,k}}{2} + \alpha_5 \frac{u_{i-5/2,j,k} + u_{i+5/2,j,k}}{2} \right)}{x_{i+1} - x_i} \\ \frac{\delta(vu)}{\delta y} \Big|_{i+1/2,j,k} &= \frac{\frac{v_{i,j+1/2,k} + v_{i,j+3/2,k}}{2} \left(\alpha_1 \frac{u_{i+1/2,j,k} + u_{i+1/2,j+1,k}}{2} + \alpha_3 \frac{u_{i+1/2,j-1,k} + u_{i+1/2,j+2,k}}{2} + \alpha_5 \frac{u_{i+1/2,j-2,k} + u_{i+1/2,j+3,k}}{2} \right)}{y_{j+1/2} - y_{j-1/2}} \\ &- \frac{\frac{v_{i,j-1/2,k} + v_{i,j-3/2,k}}{2} \left(\alpha_1 \frac{u_{i+1/2,j-1,k} + u_{i+1/2,j,k}}{2} + \alpha_3 \frac{u_{i+1/2,j-2,k} + u_{i+1/2,j+1,k}}{2} + \alpha_5 \frac{u_{i+1/2,j-3,k} + u_{i+1/2,j+2,k}}{2} \right)}{y_{j+1/2} - y_{j-1/2}} \end{aligned} \quad (8)$$

Compared to the CDS2, the HCDS6 scheme does not significantly increase the computational time to evaluate the momentum equation in the inner part of the computational domain. However, the situation is different near the boundaries, as the numerical stencil of HCDS6 has seven points in each spatial direction. Firstly, this means that three layers of ghost points need to be created for Dirichlet and Neumann boundary conditions. Secondly, in parallel computation, three layers of points must be exchanged between partitions considering a multi-block domain decomposition. This increases the amount of data to be exchanged between processors, in contrast to the CDS2, which only requires the communication of one layer of points. The spatial discretization of the continuity equation is the same for the CDS2 and HCDS6 schemes. The computational time related to solving the continuity equation is thus identical for both schemes, for instance, to solve the Poisson equation in the context of a projection method (see Section 2.4).

2.3. Linear advection problem

Consider the 1D linear advection equation of the form:

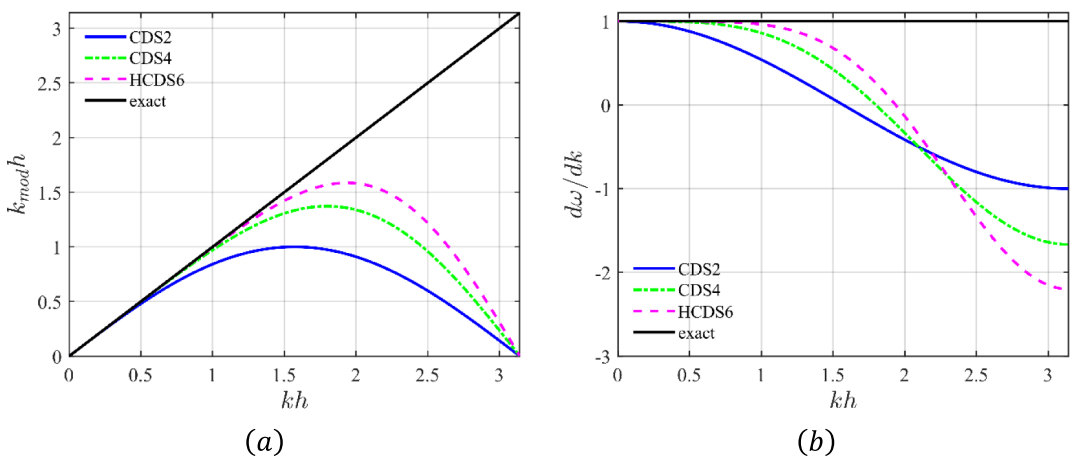


Fig. 3. Non-dimensional modified wavenumber (a) and group velocity (b) for $a = 1$ with CDS2, CDS4, and HCDS6.

$$\frac{\partial u}{\partial t} + a \frac{\partial u}{\partial x} = 0 \quad (9)$$

where a is the constant advection velocity on the spatial domain $x \in [0, 2\pi]$ with periodic boundary conditions. Using the new central difference scheme (HCDS6) defined in Eq. (6) to discretize the convective term on a uniform mesh ($\Delta x = h$), the semi-discretized one-dimensional linear advection equation is obtained:

$$\frac{\partial u_i}{\partial t} + \left[a \frac{\delta_1}{\delta_1 x_i} \left(\frac{37}{30} \bar{u}_i^{1x_i} - \frac{8}{30} \bar{u}_i^{3x_i} + \frac{1}{30} \bar{u}_i^{5x_i} \right) \right]_{x_i, y_j, z_k} = 0 \quad (10)$$

$$\frac{\partial u_i}{\partial t} + \frac{a}{2h} \left(\frac{1}{30} u_{i+3} - \frac{3}{10} u_{i+2} + \frac{3}{2} u_{i+1} - \frac{3}{2} u_{i-1} + \frac{3}{10} u_{i-2} - \frac{1}{30} u_{i-3} \right) = 0 \quad (11)$$

This spatial discretization is six-order accurate, which explains why the new scheme has been given the acronym HCDS6. The modified wavenumber analysis can be performed. The details of the mathematical developments are given in the Appendix. Fig. 3(a) shows that the non-dimensional modified wavenumber ($k_{mod}h$) of the CDS2 and HCDS6 schemes almost follow the exact wavenumber up to about $\xi = kh = 0.4$ and 1.2 , respectively. The non-dimensional modified wavenumber for CDS2 decreases from the maximum at $\xi = \pi/2$ to zero at $\xi = \pi$, while the $k_{mod}h$ for HCDS6 stays near the exact solution even at $\xi = \pi/2$, where $k_{mod}h = 1.47$.

The group velocity ($d\omega/dk$) is the velocity at which groups of waves and also energy are transported. Fig. 3(b) indicates that HCDS6 computes the group velocity more correctly than CDS2. For $\xi \geq \pi/2$, groups of waves and energy are transported in the wrong direction with CDS2, whilst they are transported in the right direction with HCDS6. For $\xi = \pi$, $d\omega/dk = -a$ for CDS2, and $d\omega/dk = -2.2a$ for HCDS6. Remember that the exact group velocity is a .

As HCDS6 better represents the phase velocity and group velocity at higher wavenumbers than CDS2, fewer points per wavelength are required for HCDS6 than for CDS2. This can significantly reduce the number of grid points in three dimensions to reach the same accuracy. It is worth noting that, for a linear advection problem, the performance of HCDS6 is superior to the fourth-order accurate scheme of Vasilyev [11] (CDS4). The analysis of the phase speed anisotropy is given in the Appendix.

2.4. REEF3D solver package

REEF3D is an open-source CFD software package that focuses on CFD in hydrodynamics, environmental, and marine engineering. In REEF3D, physical models, numerical methods and solvers are implemented as a collection of C++ classes and objects. The object-oriented design of REEF3D makes the code extendable and easy to customize. Users can modify existing solvers or create new ones by subclassing and extending the existing classes. REEF3D uses a ghost-cell immersed-boundary method to deal with complex geometry on an orthogonal grid [25]. The ghost-cell method belongs to the general category of IBM, which can potentially treat arbitrary immersed bodies on orthogonal meshes [26]. In REEF3D, the incompressible Navier-Stokes equations are solved in parallel using domain decomposition. Partitions communicate with their neighbors using ghost cells and the Message Passing Interface (MPI) [27]. The current simulations were performed on the FRAM cluster provided by UNINETT Sigma2, which is the National Infrastructure for High-Performance Computing and Data Storage in Norway. It is a distributed memory system that consists of 1,004 dual-socket and two quad-socket nodes, interconnected with a high-bandwidth, low-latency Infiniband network. The interconnect network is organized in an island topology, with 9,216 cores in each island. Each standard compute node has two 16-core Intel Broadwell chips (2.1 GHz) and 64 GiB memory. In addition, eight larger memory nodes with 512 GiB RAM are available, catering to computational tasks that demand substantial memory resources for more complex simulations and data-intensive processing. The total number of compute cores is 32,256.

In REEF3D, the pressure velocity coupling is ensured by using the projection method proposed by Chorin [28]. Here, the computation of velocity and pressure is decoupled and performed in three steps. During the first step, the method proceeds by neglecting the incompressibility constraint to compute an intermediate velocity field u^* using Eq. (12):

$$\frac{u_m^* - u_m^k}{\Delta t} + \frac{\delta}{\delta x_n} (u_n^k u_m^k) = -\frac{1}{\rho} \frac{\delta p^k}{\delta x_m} + \frac{\delta}{\delta x_n} \left[v \left(\frac{\delta u_m^k}{\delta x_n} + \frac{\delta u_n^k}{\delta x_m} \right) \right] \quad (12)$$

where u_m^k is the velocity at k^{th} time step. Note that the resulting intermediate velocity u_m^* does not satisfy the continuity equation (Eq. (1)). To enforce continuity, the intermediate velocity is projected onto the space of incompressible divergence-free vector fields to obtain u_m^{k+1} :

$$\frac{u_m^{k+1} - u_m^*}{\Delta t} = \frac{1}{\rho} \frac{\delta_1 (p^{k+1} - p^k)}{\delta_1 x_m} \quad (13)$$

This is done by solving a Poisson equation for the pressure field, using the divergence of the intermediate velocity field and enforcing $\delta_1 u_m^{k+1} / \delta_1 x_m = 0$. The fully parallelized Bi-Conjugate Gradients Stabilized (BiCGStab) algorithm [29] solves the resulting Poisson pressure equation by using geometric multigrid preconditioning provided by the high-performance solver library, HYPRE [30].

$$\frac{\delta_1}{\delta_1 x_m} \left(\frac{1}{\rho} \frac{\delta_1 (p^{k+1} - p^k)}{\delta_1 x_m} \right) = - \frac{1}{\Delta t} \frac{\delta_1 u_m^e}{\delta_1 x_m} \tag{14}$$

The result is a pressure field that enforces the incompressibility constraint on the velocity field. Finally, the new velocity field u_m^{k+1} at time step $k + 1$ is obtained by subtracting the gradient of the pressure field scaled by $\Delta t/\rho$ from intermediate velocity (Eq. (13)). This results in a velocity field that satisfies both the momentum and continuity equations. It is noteworthy that Eq. (13) is strictly the same for CDS2 and HCDS6.

By default, the governing equations are advanced in time using a fully explicit third-order Total Variation Diminishing (TVD) Runge-Kutta scheme [31]. At each Runge-Kutta stage, Chorin’s projection method is applied so that all the substep velocity fields are divergence-free, and the Poisson equation is solved three times per time step [32].

For the viscous terms, the second-order central difference scheme is adopted (i.e., the same for CDS2 and HCDS6):

$$\frac{\delta}{\delta x_n} \left[\frac{\delta u_m}{\delta x_n} \right] \Big|_{i,j,k} = \frac{\delta_1}{\delta_1 x_n} \left\{ \frac{\delta_1 u_m}{\delta_1 x_n} \right\} \Big|_{i,j,k} \tag{15}$$

3. Validation tests

This section describes three benchmark tests that were carried out in the REEF3D flow solver [27] to demonstrate the properties and performance of the present numerical method, including the convection of an isentropic vortex, the three-dimensional Taylor-Green vortex flow, and turbulent channel flow simulations.

3.1. Convection of an isentropic vortex

In order to test the performance of the HCDS6 scheme concerning its dissipation and dispersion properties, the convection of a two-dimensional isentropic vortex is considered using incompressible Euler equations. The vortex is convected by a uniform flow in the positive x direction. The initial solution is represented by the velocity components in the x and y directions:

$$\begin{pmatrix} u \\ v \end{pmatrix} = \begin{pmatrix} u_\infty \\ 0 \end{pmatrix} + u_A e^{(1-(r/b)^2)/2} \begin{pmatrix} (y - y_0)/b \\ -(x - x_0)/b \end{pmatrix} \tag{16}$$

with $r^2 = (x - x_0)^2 + (y - y_0)^2$ being the distance from the vortex center (x_0, y_0) . The circumferential velocity induced by the vortex reaches its maximum value (u_A) at $r = b$. The vortex is translated with a mean-flow velocity in the x direction within a two-dimensional periodic domain. To minimize the impact of the boundary conditions and geometry on the results, a large computational domain $[-25L, 25L]^2$ is considered. Here $L = \sqrt{\ln 2} b$ is a representative length scale of the vortex where $e^{-(r/b)^2} = 1/2$ at $r = L$.

A strong vortex with $u_A/u_\infty = 0.8$ is convected from the initial location at $(x_0, y_0) = (-18.75L, 0)$ to the final position $(x, y) = (18.75L, 0)$ for a time period of $u_\infty t/L = 37.5$ on a uniform Cartesian grid. The Courant number is selected to be extremely small ($CFL = 1.152e - 3$) on the finest grid so that the effect of time discretization error is negligible.

3.1.1. Verification and consistency

The Root-Mean-Square (RMS) error between the numerical and analytical solutions as a function of the grid resolution for the CDS2

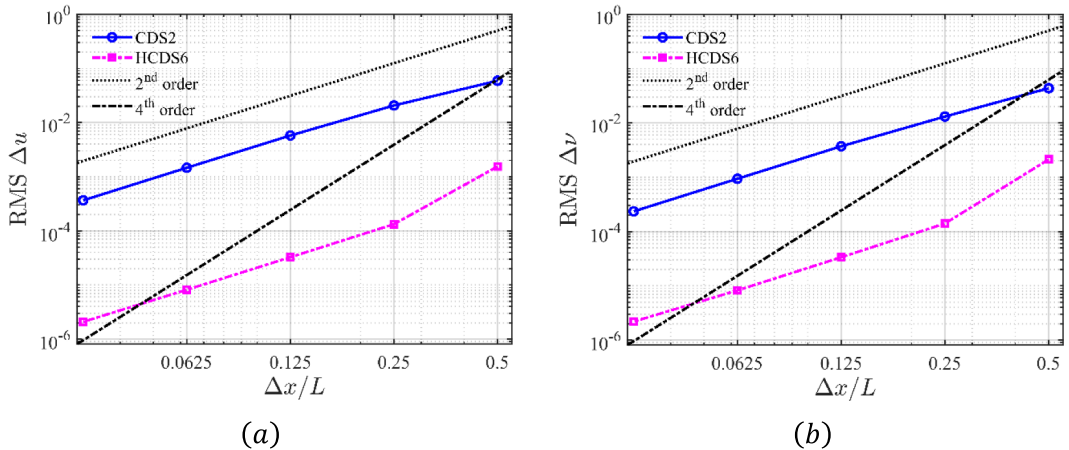


Fig. 4. Convection of strong isentropic vortex on a uniform grid: grid dependence of the root-mean-square value of difference with the analytical solution at the time $u_\infty t/L = 37.5$. (a): velocity component u , (b): velocity component v .

and HCDS6 schemes is shown in Fig. 4.

This shows that the HCDS6 scheme is indeed second-order accurate. For cell sizes smaller than $L/4$, the discretization error of second-order starts to dominate the global error. However, the error is reduced by approximately two orders of magnitude for the HCDS6, compared to the standard CDS2.

3.1.2. Shape and position of the vortex

The local resolution of the vortex on two different grid sizes ($\Delta x = L/2, L/4$) is shown in Fig. 5. Here, the y velocity component along the midline at $y = 0$ is compared with the analytical solution. For CDS2, the vortex has clearly lost its shape on a coarse grid ($\Delta x = L/2$), whilst it is better preserved by the lower dispersion error of the HCDS6. A close agreement with the analytical curve is achieved. As the mesh is further refined, the vortex shape is improved significantly by the CDS2 scheme, whilst the improvement for HCDS6 is minor as the solution was already accurate on the coarser mesh. The vortex center drifted upward using the CDS2 scheme due to the dispersion error, as indicated by a smaller difference between the numerical and analytical solution for the positive peak than for the negative one. In other words, the vortex consists of a collection of waves with different wavenumbers that are propagated at different velocities. Using the CDS2 scheme, the waves with low wavenumbers are propagated at the correct speed, whilst those with higher wavenumbers travel at the wrong speed. Consequently, those that are not propagated correctly are lagging and oscillating as a result of

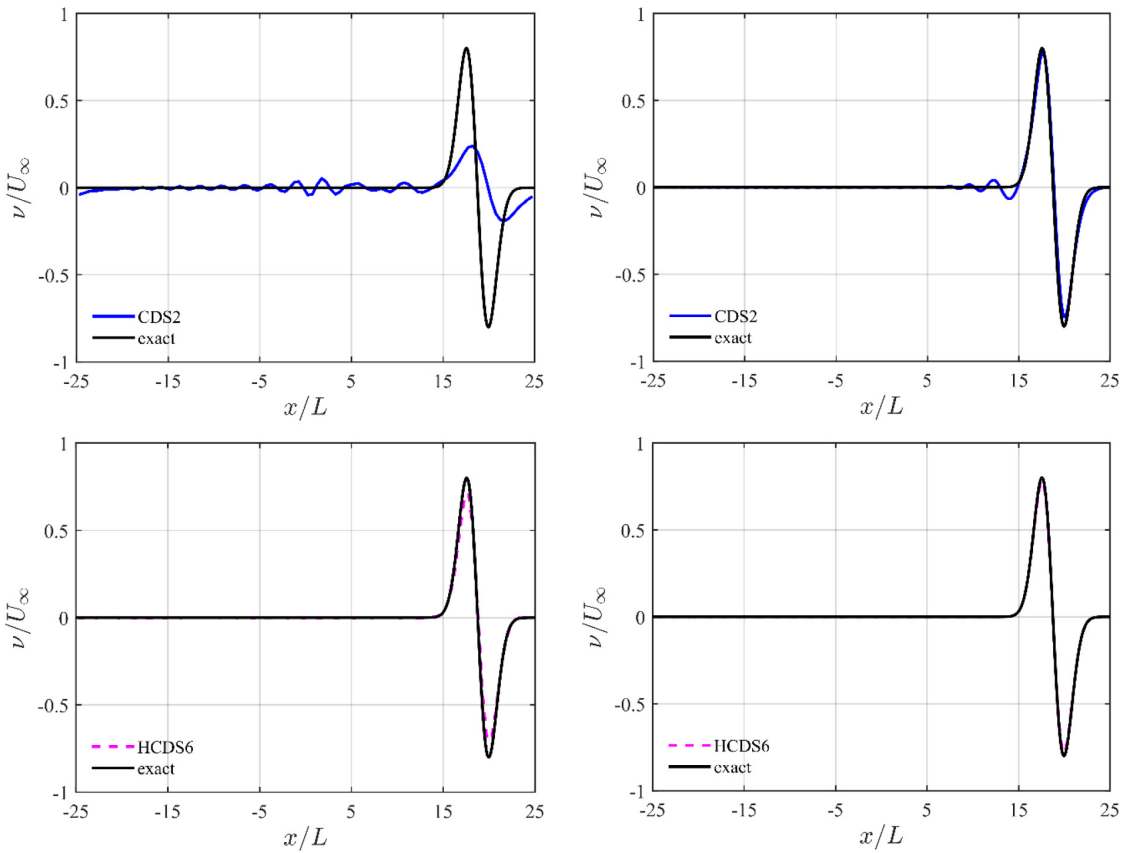


Fig. 5. y velocity component along the midline at $y = 0$. Left: coarse grid ($\Delta x = L/2$), right: fine grid ($\Delta x = L/4$).

Table 1

Comparison of the execution time of the CDS2 and HCDS6 for the convection of an isentropic vortex.

Δx	n_t	$t_{\text{CDS2}}[\text{s}]$	r_{CDS2}	$t_{\text{HCDS6}}[\text{s}]$	r_{HCDS6}	$t_{\text{HCDS6}}/t_{\text{CDS2}}$
$L/2$	1.88e6	2.98e4	-	2.96e4	-	0.99
$L/4$	1.88e6	7.19e4	2.41	7.35e4	2.48	1.02
$L/8$	1.88e6	2.01e5	2.80	2.08e5	2.83	1.03
$L/16$	1.88e6	2.73e5	1.36	2.78e5	1.34	1.02
$L/32$	1.88e6	8.07e5	2.95	8.72e5	3.13	1.08

the dispersion error. In addition, the amplitude of low wavenumbers is carried correctly. In contrast, the amplitude carried by the higher wavenumbers appears as oscillation and reduces the vortex peak amplitude. The HCDS6 outperforms the CDS2 in maintaining the shape and position of the vortex.

The computational time of both numerical schemes (t_{CDS2}, t_{HCDS6}) is shown in Table 1. The required wall-clock time to convect the vortex from the initial position to the final position with a time step of $\Delta t = 2e - 5s$ is almost identical ($t_{HCDS6} / t_{CDS2} \approx 1$) for both CDS2 and HCDS6. It should be noted that the additional computational time to evaluate this test case using the HCDS6 scheme compared to the CDS2 scheme is small. A main reason is related to the resolution of the Poisson equation for the pressure. It takes most of the CPU time per time step, while the spatial discretization of this equation is identical for both the CDS2 and HCDS6 schemes.

The ratio of the wall-clock time of each numerical scheme to the time required by the same scheme on the next coarser grid is defined by r when the grid is refined consecutively. This ratio is almost similar for both CDS2 and HCDS6 and about 6 percent higher for HCDS6 on the finest grid. This ratio shows a significant reduction when the grid is refined from $\Delta x = L/8$ to $\Delta x = L/16$ due to an increase in the number of processors.

3.2. 3D Taylor-Green vortex flow

The Taylor-Green vortex flow is a well-defined, transient, three-dimensional flow that is generated by the interaction of two counter-rotating vortices in a periodic cubic domain. This classic benchmark problem is typically used to validate numerical methods for scale-resolving simulations [33]. Interactions between different scales of motion in the fluid are driven by the non-linear advection term in the Navier-Stokes equations. These interactions create smaller-scale vortices through vortex stretching, filamentation, and reconnection. These features are responsible for transferring energy from large-scale motion to smaller scales through the energy cascade.

The counter-rotating vortices are initialized in a checkerboard arrangement from an analytical periodic vortex field where a sinusoidal velocity field with a uniform vorticity distribution in the x-y plane is specified:

$$\begin{aligned} \frac{u}{U} &= \sin\left(\frac{x}{L}\right) \cos\left(\frac{y}{L}\right) \cos\left(\frac{z}{L}\right) \\ \frac{v}{U} &= -\cos\left(\frac{x}{L}\right) \sin\left(\frac{y}{L}\right) \cos\left(\frac{z}{L}\right) \\ \frac{w}{U} &= 0 \end{aligned} \tag{17}$$

where L and U are the characteristic length and velocity scales of the problem, respectively. The Reynolds number of the flow is defined as $Re = UL/\nu$ and is equal to 1,600. A periodic cubic domain with a periodicity length of $L_x = L_y = L_z = 2\pi L$ is considered. A uniform grid is adopted with a same resolution in all three directions as $h = 2\pi L/N$, where N is the number of grid cells in one direction. The baseline and refined grid resolutions are 256^3 and 512^3 , respectively. The characteristic convective time ($t_c = L/U$) is defined as the time required for a fluid particle to traverse the characteristic length scale of the flow (L) at the characteristic velocity scale (U). A non-dimensional physical time step of $\Delta t^* = \Delta t/t_c = 0.001$ is adopted for the baseline grid to capture the temporal scales adequately. The physical time step size is halved for the refined grid. The Courant number is set such that $CFL \leq 0.1$ for each grid resolution to minimize the temporal error. The simulations are performed for a time period of $t/t_c = 10$.

Different diagnostics are introduced to evaluate the performance of the HCDS6 for the Taylor-Green vortex flow simulation. A common diagnostic is the temporal evolution of the total kinetic energy averaged over the control volume (V):

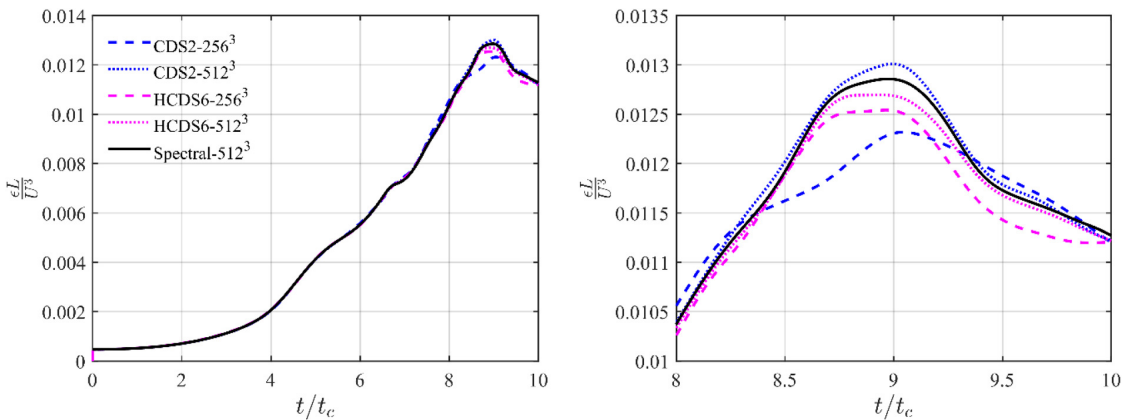


Fig. 6. Temporal evolution of the dissipation rate based on kinetic energy.

$$E_k = \frac{1}{V} \int_V \frac{u_i u_i}{2} dV \tag{18}$$

As the kinetic energy is not expected to vary much between the different scenarios investigated here, the time derivative of the total kinetic energy, defined as kinetic energy dissipation (ϵ), is a more sensitive characteristic than the total kinetic energy:

$$\epsilon = -\frac{dE_k}{dt} \tag{19}$$

A numerical scheme with significant artificial dissipation would fail to reproduce the time evolution of kinetic energy dissipation, making the scheme inappropriate for DNS or explicit LES.

3.2.1. Verification and consistency

The evolution of the total volume-averaged kinetic energy was analyzed for two different grid resolutions with 256^3 and 512^3 cells, respectively, and compared with the reference solution from a direct numerical simulation computed using a pseudo-spectral code [34]. Even at the coarsest resolution, the solution from both the CDS2 and the HCDS6 exhibited good agreement with the reference pseudo-spectral solution. However, the temporal evolution of the kinetic energy did not demonstrate sufficient sensitivity to discriminate between the performance of the two central schemes. Therefore, the temporal development of the total kinetic energy dissipation rate is considered as a more discriminating metric.

3.2.2. Evolution of the dissipation

Fig. 6 depicts the evolution of the kinetic energy-based dissipation rate using two grid resolutions compared to the reference DNS solution [34]. This is characterized by an initial rapid increase in dissipation rate associated with the formation and stretching of the initial vortices, followed by a gradual decay. As these vortices interact and break down, they transfer energy to smaller scales, thereby increasing the dissipation rate. However, as the flow evolves and the vortices continue to break down, the dissipation rate eventually reaches a steady-state value, which indicates that the energy injection and dissipation are balanced.

To assess the performance of the numerical scheme, a comparison between the CDS2 and HCDS6 on a low-resolution grid (256^3) and a refined grid (512^3) is carried out. At around $t/t_c \approx 4$, the dissipation rate increases rapidly when the transition from simple initial vortices to small-scale anisotropic turbulence occurs. This increase reaches the dissipation peak at around $t/t_c \approx 9$. For the highest under-resolution computation with 256^3 grid cells, the HCDS6 scheme deviates from the pseudo-spectral results around $t/t_c \approx 8.6$ and underpredicts the dissipation peak up to $t/t_c = 10$. The standard CDS2 scheme overestimates the dissipation rate too early at around $t/t_c \approx 7.9$ up to $t/t_c \approx 8.35$ when a significant deviation from the reference data is predicted. From $t/t_c \approx 9$, the dissipation rate gradually decreases until it intersects the pseudo-spectral line at around $t/t_c \approx 9.4$. From now on, the dissipation rate is slightly overestimated up to around $t/t_c = 10$. As the grid is refined, the numerical dissipation rate converges to the reference solution.

3.2.3. Vortical structures

Regular counter-rotating vortices stretch and twist as the flow evolves, generating smaller and more complex vortical structures.

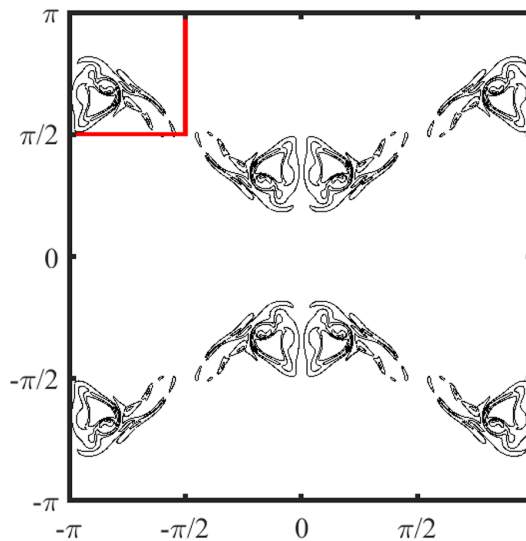


Fig. 7. Instantaneous vorticity norm from the pseudo-spectral scheme on the periodic plane ($y=0$) at $t/t_c = 9$.

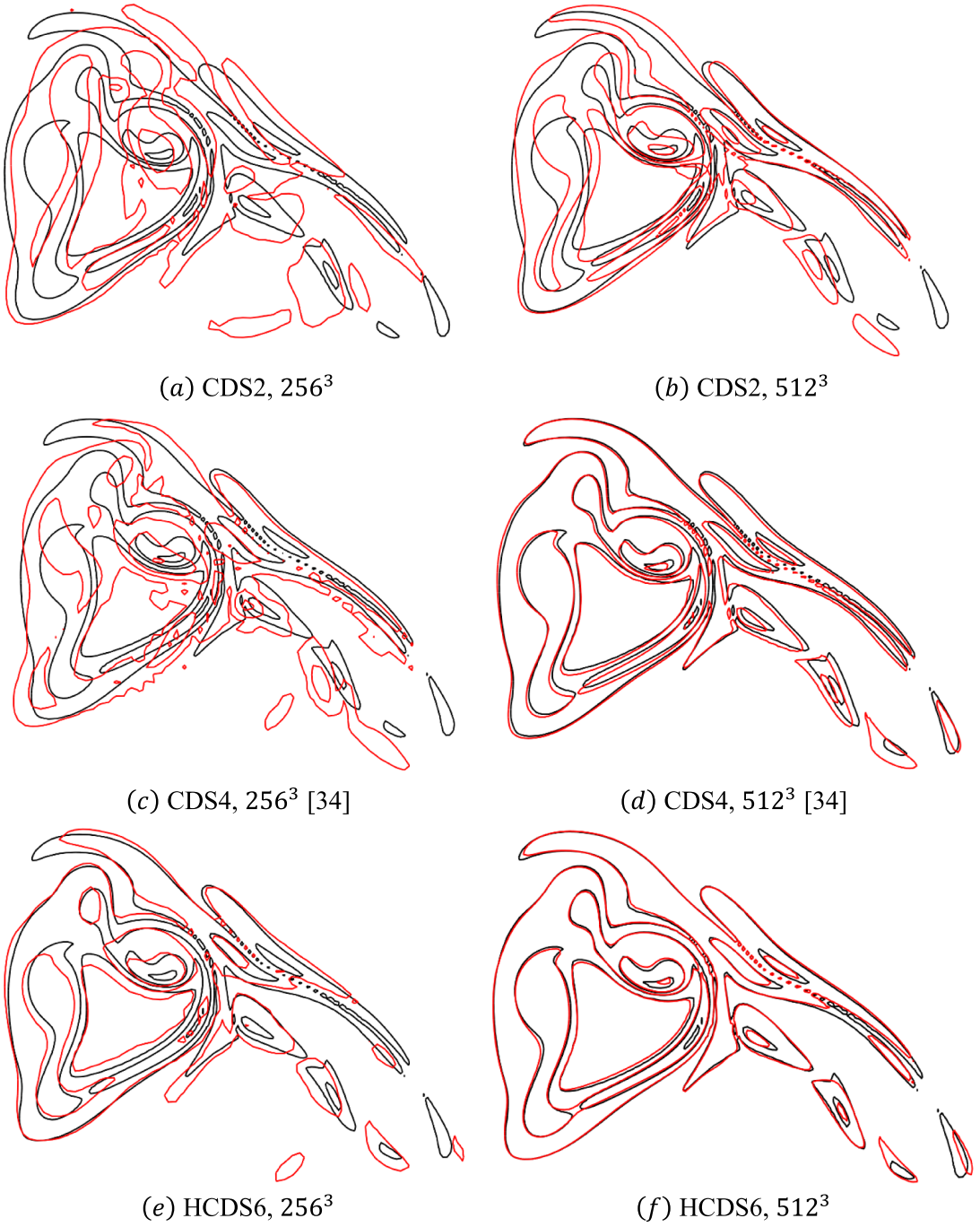


Fig. 8. Iso-contours of the vorticity norm on the periodic plane ($y = 0$) at $t/t_c = 9$. Spectral solution in black and finite-difference in red. Left: coarse grid (256^3), right: fine grid (512^3).

These structures continue to interact with each other, which creates the most intricate vortices close to the dissipation peak at $t / t_c \approx 9$. A comparison of the instantaneous vorticity field is therefore performed to analyze the accuracy and reliability of the numerical scheme to transport complex vortical structures. It is sufficient to visualize vortical structures on only a limited portion (1 / 16) of the periodic plane, as the remaining portions will be identical due to different symmetries of the flow [33], as illustrated in Fig. 7.

The vorticity iso-contours for $\omega \in [1, 5, 10, 20, 30]$ on a subset of the periodic plane ($y = 0$) at $t / t_c = 9$ obtained by CDS2 and HCDS6 schemes are superposed with those from the pseudo-spectral scheme as a reference solution [34] in Fig. 8. For this specific flow diagnostic, the performance of the fourth-order discrete kinetic energy conserving scheme (CDS4) proposed by Vasilyev [11] and provided by M. Duponcheel [34] is also shown. The results are presented for two different grid resolutions of 256^3 and 512^3 in the left and right columns, respectively. On the coarse grid, the position of the large vortical structures is somewhat captured by the CDS2 and CDS4 schemes, while the smaller vortices are diffused and contaminated by numerical noise. The HCDS6 scheme can capture the vortical structures better, although small details of the solution are smeared. The shape of the vortex structure improves and overlaps with the reference spectral solution as the grid is refined using all three schemes. However, the CDS2 scheme still struggles to predict the correct position of vortical structures even on the fine grid.

3.3. Simulation of turbulent channel flows

Numerical simulations of turbulent channel flow are performed to assess the performance of the new HCDS6 scheme. This is an insightful flow benchmark. Firstly, the flow is bounded with a no-slip boundary condition, which generates turbulence. Additionally, previous test cases in this paper were performed on a uniform mesh while, for the channel flow, a grid-stretching is applied in the wall-normal direction. Finally, the under-resolved channel flow is very sensitive to spurious production and dissipation of the discrete kinetic energy. Uncontrolled numerical dissipation strongly impacts the flow statistics, and significant spurious discrete kinetic energy production can lead to numerical instability.

In this benchmark, a fully developed turbulent flow is created between two infinite parallel plates separated by a distance 2δ . A constant adverse pressure gradient is applied to the flow in the streamwise direction to drive the flow through the channel. The no-slip condition is set for the top and bottom walls. Periodic boundary conditions are applied in the streamwise and spanwise directions to approximate infinite homogenous directions. The periodic domain sizes are selected so that the two-point correlations in the streamwise and spanwise directions would be essentially zero at maximum separation (half the domain size). A uniform grid is adopted in the periodic directions, whilst the grid is stretched in the direction normal to the wall in order to properly resolve the boundary layers. This grid-stretching is based on a hyperbolic tangent function:

$$y_j = -\frac{\tanh\left(\gamma\left(1 - \frac{2j}{N_y}\right)\right)}{\tanh\gamma} \quad j = 0, 1, \dots, N_y \tag{20}$$

where N_y is the number of grid points in the wall-normal direction, and γ is the stretching factor. The mesh is body-fitted, and boundary conditions are introduced using ghost points. A small time step is selected to capture temporal scales precisely and keeps the Courant number below one, guaranteeing numerical stability.

3.3.1. DNS for verification and consistency

In this section, the DNS of a turbulent channel flow at the frictional Reynolds number of $Re_\tau = 180$ is carried out to verify the consistency of the HCDS6 scheme, meaning whether the simulation results converge to the exact solution as the grid resolution is refined. These results are compared to DNS data obtained using a spectral code [35,36].

A same computational domain as that of Moser et al. [36] with $L_x = 4\pi\delta$, $L_y = 2\delta$, $L_z = 4\pi/3\delta$ is used. The grid resolution is $N_x = 256$, $N_y = 256$, $N_z = 256$, where N_x , N_y , and N_z are the number of cells in x , y and z directions, respectively. The stretching factor is equal to 1.6. The corresponding non-dimensional grid spacings in wall units are reported in Table 2.

The computational domain is initialized with a random solenoidal velocity field. The default explicit time integration scheme is not used for this specific test case. A semi-implicit time marching algorithm is rather applied with the implicit Crank Nicholson for the diffusion term and an explicit third-order Runge-Kutta method for the other terms [37]. The bulk time scale ($t^* = L_x / U_b$) is equivalent to a Flow-Through Time (FTT) of the domain, which corresponds to how long it takes for the fluid to traverse the entire computational domain at a constant mean bulk velocity (U_b). Once the flow has reached a statistical steady state condition, the flow statistics are averaged in the streamwise and spanwise homogeneous directions over a time interval of $50\delta/u_\tau$, approximately equivalent to 37 FTT, which ensures fully converged statistics.

The mean streamwise velocity profile (U^+), the total Reynolds shear stress (T_{xy}), and the square root of the second-order velocity moments normalized by the friction velocity are shown in Fig. 9 as a function of the dimensionless distance to the wall.

The HCDS6 solution is in excellent agreement with the reference DNS results. The mean total Reynolds shear stress compares

Table 2
Channel flow mesh resolution.

Re_τ	Δx^+	Δz^+	Δy^+
180	8.836	2.945	$\in [0.372 - 2.441]$

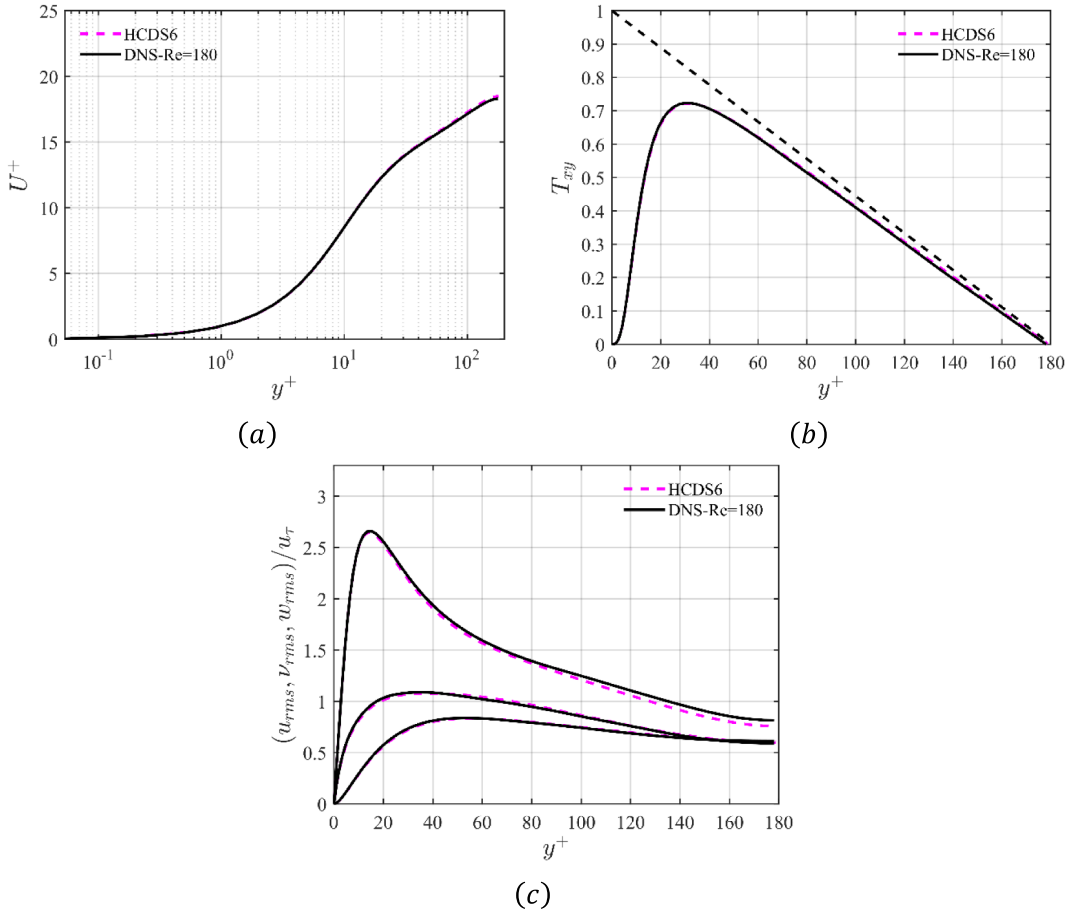


Fig. 9. Mean streamwise velocity normalized by the DNS shear velocity (a), non-dimensional mean total Reynolds shear stress (b), mean normalized square root of the second-order velocity moments (c) (u_{rms} (top), v_{rms} (middle), w_{rms} (bottom)) for the DNS of turbulent channel flow at $Re_\tau = 180$.

relatively well with the DNS data shown in the top-right graph in Fig. 9. Investigating turbulence intensities involves analyzing the individual components of the total stress tensor illustrated at the bottom of Fig. 9. The predictions for the spanwise (w_{rms}) and wall-normal (v_{rms}) turbulence-intensity components overlap with the reference DNS of Moser et al. [36]. The streamwise component (u_{rms}) exhibits only a slight deviation for y^+ above 80. All the predictions confirm the consistency of the HCDS6 scheme on non-uniform meshes.

3.3.2. TNS of the channel flow at $Re_\tau = 180, 640, 950, 2000$

In contrast to DNS, which resolves all the turbulent scales, the performance of the HCDS6 in marginally resolved simulations termed Truncated Navier-Stokes Simulations (TNS) is also investigated. In TNS, no turbulence modeling is applied. When a scheme does not conserve the discrete kinetic energy, spurious injection or dissipation of discrete kinetic energy takes place and increases as the simulation gets more under-resolved. TNS thus enables us to investigate whether the lack of discrete kinetic energy conservation affects the HCDS6 performance.

Table 3

Computational domain size and mesh densities for TNS of channel flow at $Re_\tau = 180, 640, 950, 2000$.

Re_τ	L_x	L_y	L_z	N_x	N_y	N_z	Δx^+	Δz^+	Δy^+	γ	FTT
180	$2\pi\delta$	2δ	$\pi\delta$	128	128	128	8.96	4.48	$\in [0.12 - 14.4]$	2.8	42
640	$2\pi\delta$	2δ	$\pi\delta$	128	128	128	31.2	15.6	$\in [0.43 - 29.7]$	2.8	175
950	$2\pi\delta$	2δ	$\pi\delta$	128	128	128	45.7	22.9	$\in [0.63 - 37.1]$	2.8	266
2000	$2\pi\delta$	2δ	$\pi\delta$	128	128	128	99.4	49.7	$\in [1.37 - 58.9]$	2.8	167

The same setup as DNS of turbulent channel flow is carried out at four frictional Reynolds numbers of $Re_\tau = 180, 640, 950$ and 2000 , but on a different computational domain and a coarser mesh. In addition, the grid-stretching is increased compared to the DNS and is made representative of LES applications. The computational domain size, grid resolution, and corresponding non-dimensional grid spacings for each frictional Reynolds number are provided in Table 3.

As the grid is non-uniform with significant grid stretching, the CDS2 does not conserve the discrete kinetic energy. To establish a reference solution for our tests, the skew-symmetric form of the second-order scheme of Vasilyev [11] (given in Eq. (5)) is also simulated since it strictly conserves the discrete kinetic energy on a non-uniform mesh. However, the simulation showed identical results for the divergence and skew-symmetric forms. This aligns with the findings in the channel flow tests conducted by Morinishi et al. [38]. Given that both the divergence and skew-symmetric forms yield the same results, they will not be distinguished and will be simply referred to as CDS2 in this section. It is noteworthy that adjusting the weights of the HCDS6 stencil to accommodate local grid stretching would result in unstable simulations, even at $Re_\tau = 180$.

The mean normalized streamwise velocity profiles for four frictional Reynolds numbers of $Re_\tau = 180, 640, 950, 2000$ along the channel height are shown in Fig. 10. The two discretization schemes agree well with the DNS data at $Re_\tau = 180$. For higher frictional Reynolds numbers, HCDS6 and DNS profiles almost collapse within the viscous sublayer and buffer layer with a slight underprediction in the logarithmic inertial layer. However, the buffer layer, the log layer, and the outer region are strongly affected using the CDS2 scheme, where it starts to deviate from the reference in the buffer layer at $y^+ \approx 10$. At $Re_\tau = 2000$, the grid resolution is insufficient to accurately capture the viscous sublayer, buffer layer and log layer. While HCDS6 tends to overestimate the velocity profile, it manages to capture the accurate shape across the channel height. Conversely, CDS2 struggles to predict the correct velocity profile behavior, and the deviation from DNS data notably increases, particularly in the log layer.

The non-dimensional profiles of mean total Reynolds shear stress at four frictional Reynolds numbers are depicted as a function of the distance from the wall to the center of the channel in Fig. 11. In a fully developed channel flow, the shear stresses and velocity gradients are more significant near the wall, which is indicated by a peak that decreases gradually to the channel centerline as the interaction between the mean velocity profile and the turbulent fluctuations is dampened. For all four frictional Reynolds numbers, CDS2 and HCDS6 can properly reproduce the total Reynolds shear stress of DNS. As the Reynolds number increases in a fully developed

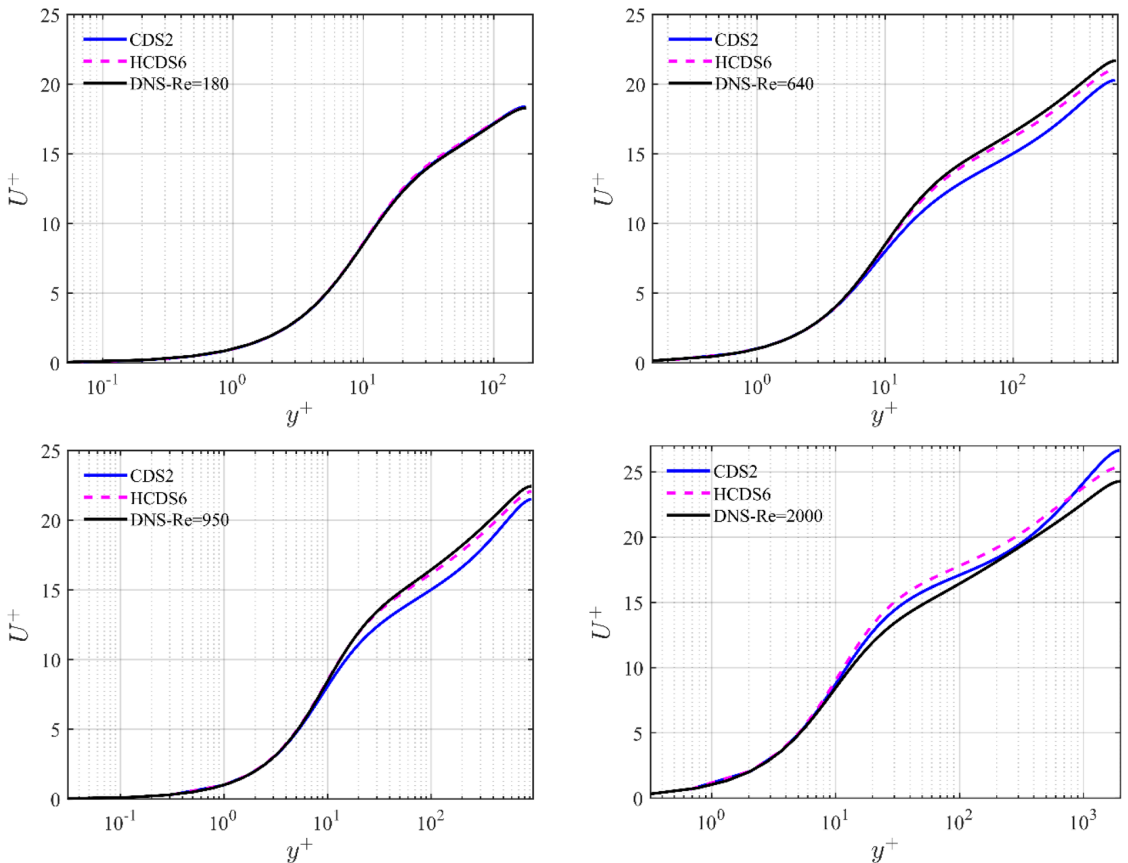


Fig. 10. Mean streamwise velocity normalized by the DNS shear velocity for the TNS of turbulent channel flow at $Re_\tau = 180, 640, 950, 2000$.

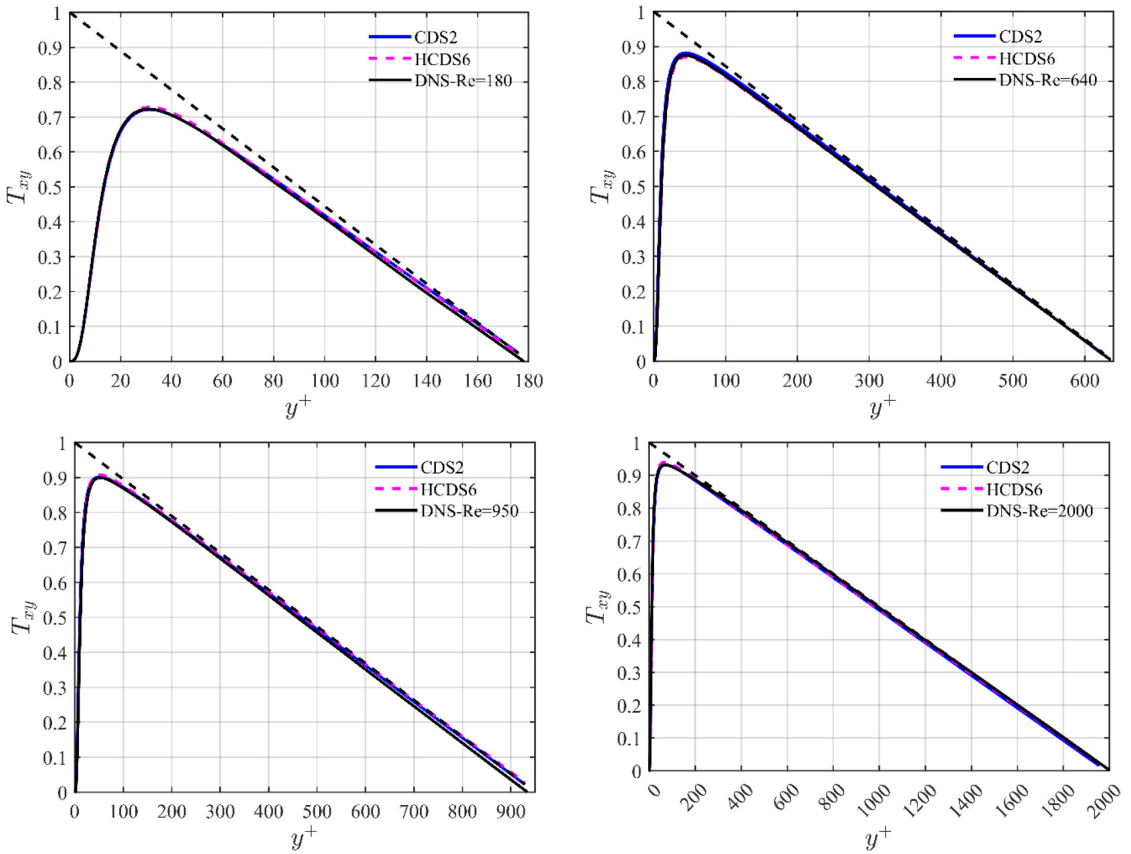


Fig. 11. Non-dimensional mean total Reynolds shear stress for the TNS of turbulent channel flow at $Re_\tau = 180, 640, 950, 2000$.

channel flow, the peak values of the non-dimensional Reynolds stress near the channel walls become more pronounced due to higher turbulence intensity. Moreover, stronger velocity gradients near the walls contribute to a steeper slope of the Reynolds stress profile in this region and promote more efficient mixing and transport of momentum across the flow cross-section. With higher Reynolds numbers, the peak location is shifted toward the wall due to the altered balance between turbulent production and dissipation.

The mean normalized velocity fluctuations of the TNS are compared to DNS data in Fig. 12. For turbulent channel flow at a low Reynolds number of $Re_\tau = 180$, CDS2 performs an excellent job of representing all three components of the total stress tensor in the near wall and core section of the flow. However, the results from HCDS6 predict a slight overprediction, particularly for u_{rms} shear stress distribution when y^+ exceeds 10. By increasing the frictional Reynolds number to $Re_\tau = 640$, all the predictions of HCDS6 for the three velocity fluctuations remain accurate across the channel height, whilst significant deviations from the DNS data are observed for the CDS2 with reduced values of u_{rms} in the buffer and log layers. Both the spanwise and wall-normal components, w_{rms} and v_{rms} , are underpredicted with the CDS2 scheme for the buffer layer and outer region in the core of the flow. The agreement of the turbulent intensity components with DNS at a higher Reynolds number of $Re_\tau = 950$ clearly shows the superiority of the HCDS6 scheme compared to the CDS2. The exception is streamwise stress, u_{rms} , that fails to capture the peak intensity in the vicinity of the wall. The deviation is more pronounced for CDS2, where the elevated prediction of the peak is followed by an underprediction away from the wall. Similarly to $Re_\tau = 640$, wall-normal velocity fluctuation shows an underprediction for wall units of approximately 20 to 210, and it is more pronounced in the outer region for y^+ above 800. Again, HCDS6 successfully reproduces the DNS profile of w_{rms} and v_{rms} . In a highly under-resolved simulation at $Re_\tau = 2000$, streamwise velocity fluctuation swings up and down around the DNS profile using the CDS2 scheme. This indicated that the CDS2 is less reliable as the under-resolution increases. The HCDS6 scheme tends to overpredict the streamwise stress across the channel. Despite this, the overall behavior of HCDS6 remains consistent when compared to the DNS solution, particularly for the other two components of velocity fluctuations.

Two dimensionless gradient-based cell Reynolds numbers evaluated using the norm of vorticity and the strain rate tensor are defined to assess the resolution level of each TNS. The cell Reynolds number based on the vorticity norm ($Re_\Delta - \omega$) and the norm of strain rate tensor ($Re_\Delta - S$) are defined as:

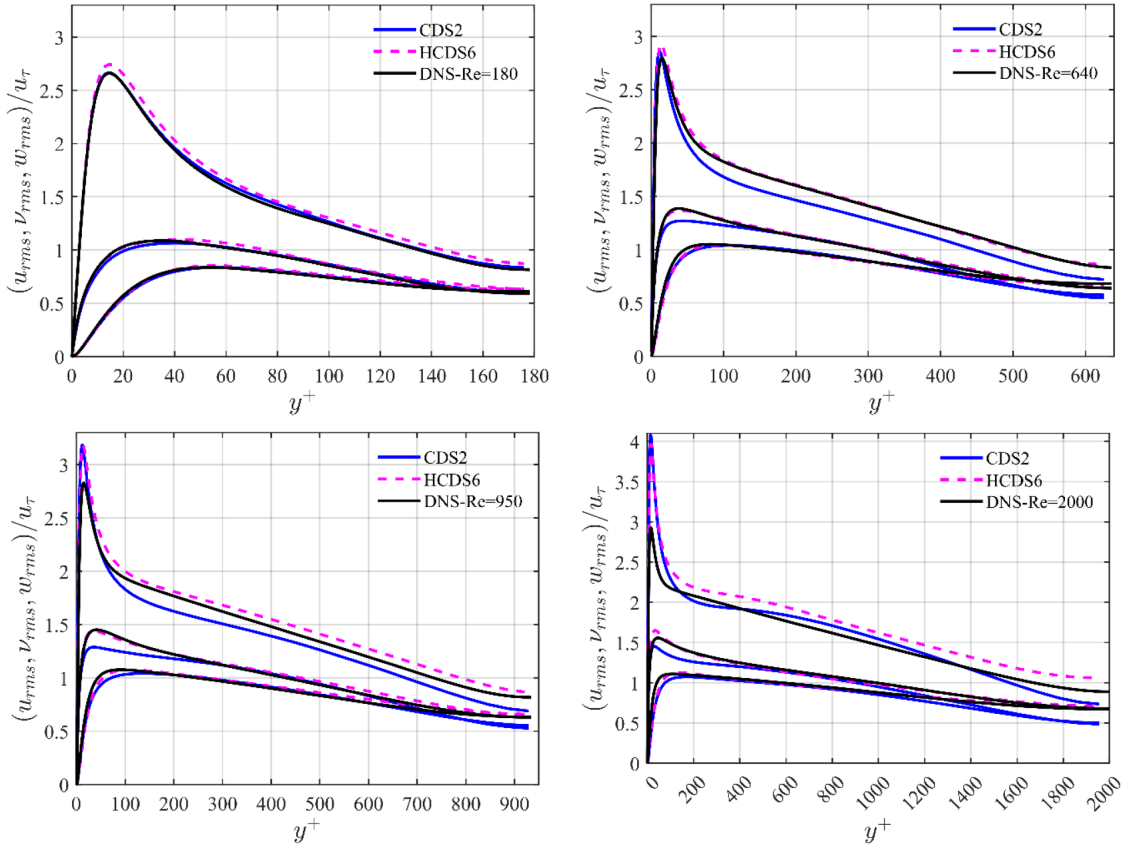


Fig. 12. Velocity fluctuations in streamwise (u_{rms} , **top**), wall-normal (v_{rms} , **middle**) and spanwise (w_{rms} , **bottom**) direction as a function of the distance to the wall (y^+) for the TNS of turbulent channel flow at $Re_\tau = 180, 640, 950, 2000$.

$$\begin{aligned}
 Re_\Delta - \omega &= \frac{\langle \omega \rangle (\sqrt[3]{\Delta x \Delta y \Delta z})^2}{\nu} \sim \left(\frac{\sqrt[3]{\Delta x \Delta y \Delta z} * u_\tau}{\nu} \right)^2 \\
 Re_\Delta - S &= \frac{\langle S \rangle (\sqrt[3]{\Delta x \Delta y \Delta z})^2}{\nu} \sim \left(\frac{\sqrt[3]{\Delta x \Delta y \Delta z} * u_\tau}{\nu} \right)^2
 \end{aligned}
 \tag{21}$$

where $\langle \omega \rangle$ represents the vorticity magnitude and $\langle S \rangle$ denotes the strain rate magnitude averaged along homogeneous directions. $\sqrt[3]{\Delta x \Delta y \Delta z}$ is the characteristic cell size based on the cell volume. Δx , Δy , and Δz are the cell dimensions in x , y , and z directions, respectively.

The profiles of the mean cell Reynolds numbers across the channel height using the HCDS6 scheme are shown in Fig. 13. As expected, the cell Reynolds numbers increase with the Re_τ . They reach a maximum value in the laminar sublayer and then decrease to a relatively flat profile towards the center of the channel. The following argument demonstrates that the TNS is well under-resolved for $Re_\tau = 2000$:

- At the wall, the vorticity is equal to the gradient of the streamwise velocity component with respect to y , leading to $Re_\Delta - \omega = (\Delta y^+)^2$. In a wall-resolved DNS or LES, the typical recommended near-wall resolution is $\Delta y^+ \sim 1$. This value is lower or close to 1 in the four TNS, as shown in Table 3. However, the cell Reynolds number exhibits a peak value in the vicinity of the wall. This peak increases by a factor of 50 from the TNS at $Re_\tau = 180$ to $Re_\tau = 2000$.
- In the center of the channel, the flow is comparable to homogeneous isotropic turbulence (HIT). Then, the value taken by the cell Reynolds number of a LES for a HIT can be considered as a reference point for our TNS. In a LES of decaying homogeneous isotropic turbulence (DHIT) at high Reynolds numbers using the Smagorinsky subgrid-scale model, the theory predicts that the model constant (C_s) should be equal to 0.027. This is equivalent to a $Re_\Delta - S$ of about 37 when evaluated on the subgrid-scale eddy viscosity. In a study by Thiry et al. [39], a LES of the DHIT is performed using the dynamic Smagorinsky model. The Taylor

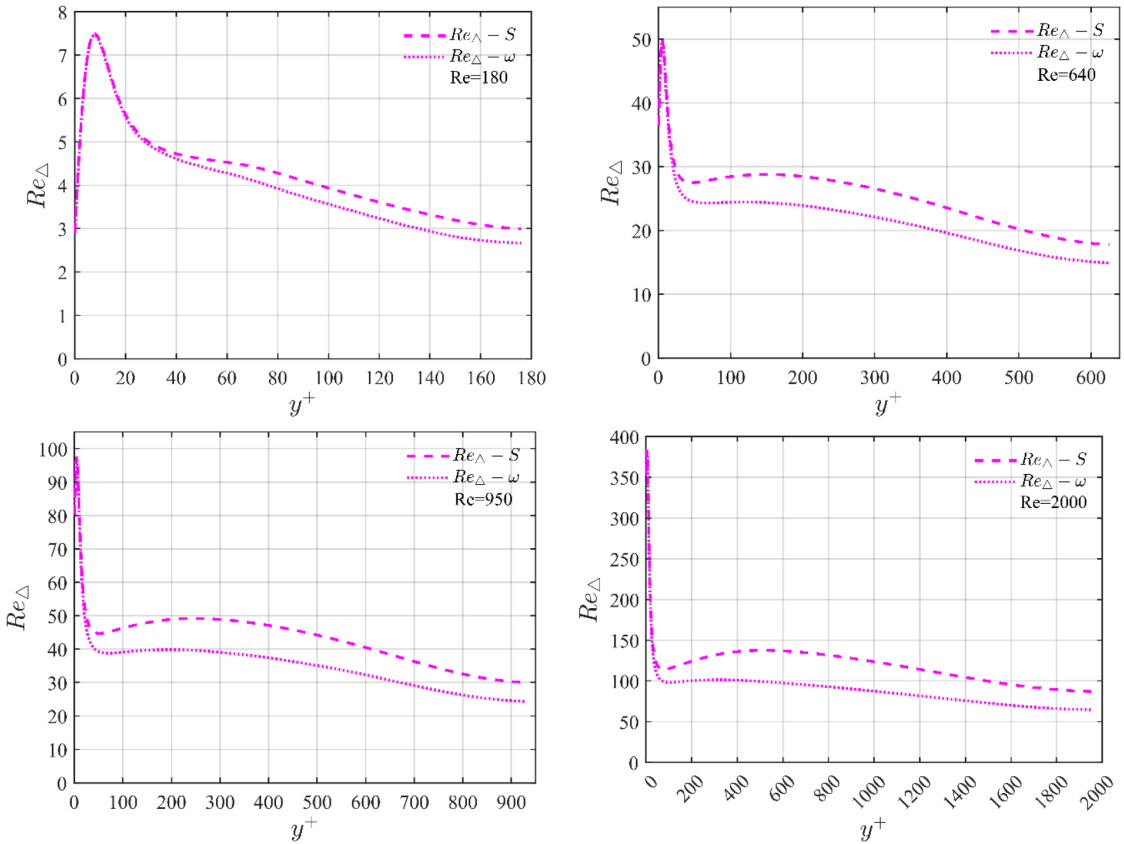


Fig. 13. Mean cell Reynolds number based on vorticity ($Re_{\Delta} - \omega$) and strain term ($Re_{\Delta} - S$) as a function of the distance to the wall (y^+) for the TNS of turbulent channel flow at $Re_{\tau} = 180, 640, 950, 2000$.

micro-scale Reynolds number was taken very large (i.e., v_{SGS}/ν converges to infinity), and the DHIT was computed on a 512^3 mesh using a pseudo-spectral method. The C_s evaluated by the dynamic procedure was then equal to 0.0115, well lower than the theoretical constant. This value corresponds to a $Re_{\Delta} - S$ of about 87 based on the subgrid-scale eddy viscosity. For the TNS at $Re_{\tau} = 2000$, the $Re_{\Delta} - S$ has a value of about 100 near the center of the channel when HCDS6 is adopted. This indicates that the level of under-resolution reached by the TNS at $Re_{\tau} = 2000$ is representative of a LES at very high Reynolds number in the center of the channel flow.

In conclusion, when a scheme does not conserve the discrete kinetic energy, the resulting spurious production or dissipation of discrete kinetic energy increases with the level of under-resolution. Even though the TNS at $Re_{\tau} = 2000$ is under-resolved near the wall and has a resolution comparable to LES at high Reynolds number in the center of the channel, the HCDS6 scheme is not affected by the non-conservation of the discrete kinetic energy. As previously shown, the flow statistics predicted by the HCDS6 are similar to the standard second-order scheme of Vasilyev in the skew-symmetric form that strictly conserves the discrete kinetic energy. It is also worth mentioning that a significant spurious injection of discrete kinetic energy would eventually make the simulation unstable. This is not the case for our simulations when the HCDS6 scheme is adopted.

4. Conclusions

A new second-order finite-difference scheme (HCDS6) was introduced to discretize the convective terms of the incompressible Navier-Stokes equations on an orthogonal non-uniform staggered grid. This scheme is expressed in divergence form and conserves the discrete mass and momentum with limited production or dissipation of discrete kinetic energy. Compared to the standard second-order scheme, the proposed scheme is more accurate. Compared to existing fourth-order kinetic energy-conserving schemes, the new scheme has a numerical stencil that is more compact, which makes its implementation and the treatment of boundary conditions easier.

The scheme performance was evaluated on viscous and inviscid flow simulations conducted on both uniform and non-uniform grids. In a grid-convergence analysis for the advection of an isentropic vortex, the RMS of the vortex velocity using the HCDS6

scheme was reduced by two orders of magnitude compared to the standard second-order central scheme. For the Taylor-Green vortex flow, iso-contours of the vorticity norm in the midplane close to the dissipation peak were compared with a DNS reference solution. Here, complex vortical structures were better captured by the HCDS6 than by the standard second-order scheme. The under-resolved turbulent channel flow benchmark was a challenging case for investigating the stability and accuracy of the scheme on a non-uniform grid. Simulations showed that the HCDS6 remained stable even if the simulations were getting highly under-resolved (by increasing the frictional Reynolds number to 2000). The flow statistics were comparable to the standard second-order scheme, which strictly conserves discrete kinetic energy. It proved that, even though the HCDS6 does not strictly conserve the discrete kinetic energy, it does not affect the numerical stability and flow statistics.

The new scheme is thus an alternative to the existing central scheme for incompressible flow on staggered meshes. It can facilitate the use of staggered grids in combination with complex geometries modeled using Immersed Boundary Methods (IBM).

CRedit authorship contribution statement

Elyas Larkermanni: Writing – review & editing, Writing – original draft, Visualization, Validation, Software, Resources, Methodology, Investigation, Formal analysis, Conceptualization. **Hans Bihs:** Supervision, Software, Methodology. **Grégoire Winckelmans:** Validation, Supervision, Methodology, Investigation, Conceptualization. **Matthieu Duponcheel:** Validation, Methodology, Investigation, Conceptualization. **Tobias Martin:** Writing – review & editing, Software, Investigation. **Bernhard Müller:** Writing – review & editing, Validation, Supervision, Methodology, Investigation. **Laurent Georges:** Writing – review & editing, Validation, Supervision, Software, Resources, Project administration, Methodology, Investigation, Formal analysis, Conceptualization.

Declaration of competing interest

The authors declare that they have no known competing financial interests or personal relationships that could have appeared to influence the work reported in this paper.

Data availability

Data will be made available on request.

Appendix

For an initial condition $u(x, 0) = e^{ikx}$, the exact solution of the linear advection equation (Eq. (9)) on the spatial domain $x \in [0, 2\pi]$ with periodic boundary conditions:

$$u(x, t) = e^{ik(x-at)} \quad (22)$$

is admitted. Here, k is the wavenumber.

The numerical solution can be expressed in terms of its Fourier series:

$$u_j(t) = \sum_k u_k(t) e^{ikx_j} \quad (23)$$

where u_k is the amplitude of the k^{th} Fourier mode.

The Fourier transform of the semi-discretized Eq. (11) is obtained by substituting $u_j(t)$ from Eq. (23):

$$\frac{\partial u_k(t)}{\partial t} e^{ikx_j} = -\frac{au_k(t)}{2h} \left(\frac{1}{30} e^{3ikh} - \frac{3}{10} e^{2ikh} + \frac{3}{2} e^{ikh} - \frac{3}{2} e^{-ikh} + \frac{3}{10} e^{-2ikh} - \frac{1}{30} e^{-3ikh} \right) e^{ikx_j} \quad (24)$$

and is simplified using Euler's formula ($e^{\pm ikh} = \cos kh \pm i \sin kh$):

$$\frac{\partial u_k(t)}{\partial t} = -\frac{ai}{h} \left(\frac{1}{30} \sin(3kh) - \frac{3}{10} \sin(2kh) + \frac{3}{2} \sin(kh) \right) u_k(t) \quad (25)$$

The solution of Eq. (25) in Fourier space can be written as:

$$u_k(t) = e^{-\frac{ait}{h} \left(\frac{1}{30} \sin(3kh) - \frac{3}{10} \sin(2kh) + \frac{3}{2} \sin(kh) \right) t} \quad (26)$$

Substituting this expression into Eq. (23), the numerical solution can be obtained in physical space:

$$u_j(t) = \sum_k e^{i \left(kx_j - \frac{ait}{h} \left(\frac{1}{30} \sin(3kh) - \frac{3}{10} \sin(2kh) + \frac{3}{2} \sin(kh) \right) \right)} \quad (27)$$

Comparing the exact and numerical solutions of the 1D linear advection equation (Eqs. (22) and (27)), the non-dimensional modified wavenumber $\tilde{k}_{mod} = k_{mod}h$ reads as a function of the non-dimensional wavenumber $\xi = kh$:

$$\tilde{k}_{mod} = \frac{1}{30} \sin(3\xi) - \frac{3}{10} \sin(2\xi) + \frac{3}{2} \sin(\xi) \tag{28}$$

The dispersion relation ($\omega = k_{mod}a$), the phase velocity (ω/k) and the group velocity ($d\omega/dk$) become:

$$\begin{aligned} \omega &= \frac{a}{h} \left(\frac{1}{30} \sin(3\xi) - \frac{3}{10} \sin(2\xi) + \frac{3}{2} \sin(\xi) \right) \\ \frac{\omega}{k} &= \frac{a}{\xi} \left(\frac{1}{30} \sin(3\xi) - \frac{3}{10} \sin(2\xi) + \frac{3}{2} \sin(\xi) \right) \\ \frac{d\omega}{dk} &= a \left(\frac{1}{10} \cos(3\xi) - \frac{3}{5} \cos(2\xi) + \frac{3}{2} \cos(\xi) \right) \end{aligned} \tag{29}$$

To ensure a comprehensive analysis, the phase speed anisotropy is evaluated following the procedure outlined by Lele [24]. Fig. 14 illustrates that the HCDS6 outperforms the CDS2 for all angles of the propagation direction (θ) and wavenumbers.

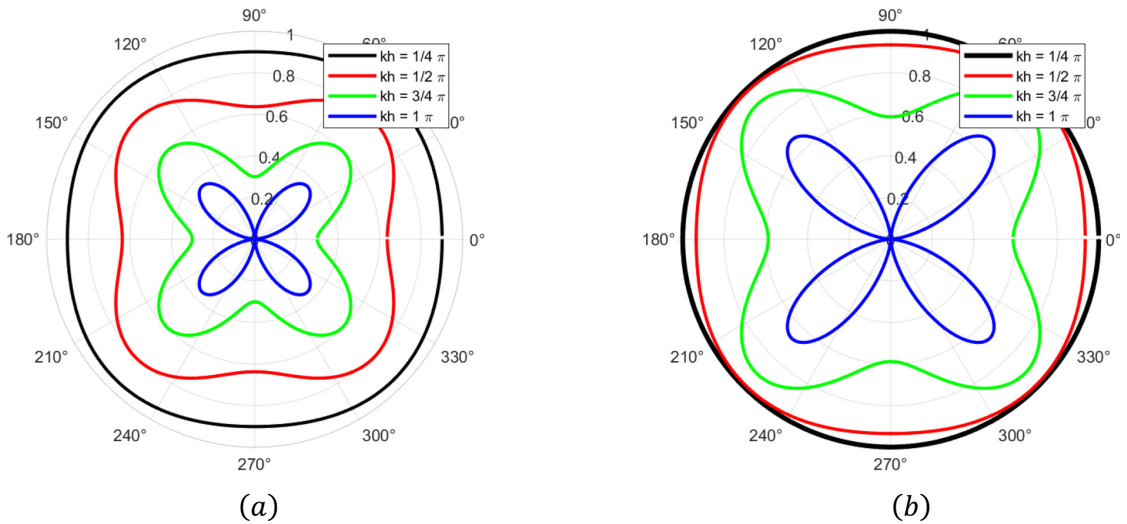


Fig. 14. Polar plot of phase speed anisotropy for the CDS2 (a) and HCDS6 (b) for different wavenumbers ($\pi/4$, $\pi/2$, $3\pi/4$) and (π).

References

[1] R. Mittal, G. Iaccarino, Immersed boundary methods, *Annu. Rev. Fluid Mech.* 37 (2005) 239–261.
 [2] Yalla, G.R., *Numerical discretization effects in large eddy simulation of turbulence*. 2022.
 [3] A. Kravchenko, P. Moin, On the effect of numerical errors in large eddy simulations of turbulent flows, *J. Comput. Phys.* 131 (2) (1997) 310–322.
 [4] S. Ghosal, An analysis of numerical errors in large-eddy simulations of turbulence, *J. Comput. Phys.* 125 (1) (1996) 187–206.
 [5] J.W. Glendening, T. Haack, Influence of advection differencing error upon large-eddy simulation accuracy, *Boundary. Layer. Meteorol.* 98 (2001) 127–153.
 [6] F.K. Chow, P. Moin, A further study of numerical errors in large-eddy simulations, *J. Comput. Phys.* 184 (2) (2003) 366–380.
 [7] J. Gullbrand, F.K. Chow, The effect of numerical errors and turbulence models in large-eddy simulations of channel flow, with and without explicit filtering, *J. Fluid. Mech.* 495 (2003) 323–341.
 [8] C. Canuto, et al., *Spectral methods: fundamentals in single domains*, Springer Science & Business Media, 2007.
 [9] S. Nagarajan, S.K. Lele, J.H. Ferziger, A robust high-order compact method for large eddy simulation, *J. Comput. Phys.* 191 (2) (2003) 392–419.
 [10] S. Laizet, E. Lamballais, High-order compact schemes for incompressible flows: A simple and efficient method with quasi-spectral accuracy, *J. Comput. Phys.* 228 (16) (2009) 5989–6015.
 [11] O.V. Vasilyev, High Order Finite Difference Schemes on Non-uniform Meshes with Good Conservation Properties, *J. Comput. Phys.* 157 (2) (2000) 746–761.
 [12] R. Verstappen, A. Veldman, Symmetry-preserving discretization of turbulent flow, *J. Comput. Phys.* 187 (1) (2003) 343–368.
 [13] S. Armfield, Finite difference solutions of the Navier-Stokes equations on staggered and non-staggered grids, *Comput. Fluids.* 20 (1) (1991) 1–17.
 [14] E.M.J. Komen, et al., Analysis of the numerical dissipation rate of different Runge-Kutta and velocity interpolation methods in an unstructured collocated finite volume method in OpenFOAM®, *Comput. Phys. Commun.* 253 (2020) 107145.
 [15] F.H. Harlow, J.E. Welch, Numerical calculation of time-dependent viscous incompressible flow of fluid with free surface, *Phys. fluids* 8 (12) (1965) 2182–2189.
 [16] F. Ham, F. Lien, A. Strong, A fully conservative second-order finite difference scheme for incompressible flow on nonuniform grids, *J. Comput. Phys.* 177 (1) (2002) 117–133.
 [17] P. Moin, R. Verzicco, On the suitability of second-order accurate discretizations for turbulent flow simulations, *Eur. J. Mech.-B/Fluids* 55 (2016) 242–245.
 [18] P. Orlandi, A numerical method for direct simulation of turbulence in complex geometries, *Ann. Res. Briefs* 1990 (1989) 215–229.

- [19] M. Duponcheel, P. Orlandi, G. Winckelmans, Time-reversibility of the Euler equations as a benchmark for energy conserving schemes, *J. Comput. Phys.* 227 (19) (2008) 8736–8752.
- [20] E. Kálmay de Rivas, On the use of nonuniform grids in finite-difference equations, *J. Comput. Phys.* 10 (2) (1972) 202–210.
- [21] T.A. Manteuffel, A.B. White, The numerical solution of second-order boundary value problems on nonuniform meshes, *Math. Comput.* 47 (1986) 511–535.
- [22] Z. Tian, X. Liang, P. Yu, A higher order compact finite difference algorithm for solving the incompressible Navier–Stokes equations, *Int. J. Numer. Methods Eng.* 88 (6) (2011) 511–532.
- [23] Y. Morinishi, et al., Fully conservative higher order finite difference schemes for incompressible flow, *J. Comput. Phys.* 143 (1) (1998) 90–124.
- [24] S.K. Lele, Compact finite difference schemes with spectral-like resolution, *J. Comput. Phys.* 103 (1) (1992) 16–42.
- [25] P.A. Berthelsen, O.M. Faltinsen, A local directional ghost cell approach for incompressible viscous flow problems with irregular boundaries, *J. Comput. Phys.* 227 (9) (2008) 4354–4397.
- [26] Y.-H. Tseng, J.H. Ferziger, A ghost-cell immersed boundary method for flow in complex geometry, *J. Comput. Phys.* 192 (2) (2003) 593–623.
- [27] H. Bihs, et al., A new level set numerical wave tank with improved density interpolation for complex wave hydrodynamics, *Comput. Fluids.* 140 (2016) 191–208.
- [28] A.J. Chorin, Numerical solution of the Navier-Stokes equations, *Math. Comput.* 22 (104) (1968) 745–762.
- [29] H.A. Van der Vorst, Bi-CGSTAB: A fast and smoothly converging variant of Bi-CG for the solution of nonsymmetric linear systems, *SIAM J. Sci. Stat. Comput.* 13 (2) (1992) 631–644.
- [30] R.D. Falgout, J.E. Jones, U.M. Yang, Conceptual interfaces in hypre, *Fut. Gener. Comput. Syst.* 22 (1-2) (2006) 239–251.
- [31] C.-W. Shu, S. Osher, Efficient implementation of essentially non-oscillatory shock-capturing schemes, *J. Comput. Phys.* 77 (2) (1988) 439–471.
- [32] E. Weinan, J.-G. Liu, Projection method I: convergence and numerical boundary layers, *SIAM. J. Numer. Anal.* (1995) 1017–1057.
- [33] L. Bricteux, S. Zeoli, N. Bourgeois, Validation and scalability of an open source parallel flow solver, *Concur. Comput.: Pract. Exp.* 29 (21) (2017) e4330.
- [34] C. Carton de Wiart, et al., Assessment of a discontinuous Galerkin method for the simulation of vortical flows at high Reynolds number, *Int. J. Numer. Methods Fluids.* 74 (7) (2014) 469–493.
- [35] J. Kim, P. Moin, R. Moser, Turbulence statistics in fully developed channel flow at low Reynolds number, *J. Fluid. Mech.* 177 (1987) 133–166.
- [36] R.D. Moser, J. Kim, N.N. Mansour, Direct numerical simulation of turbulent channel flow up to $Re \tau = 590$, *Phys. Fluids* 11 (4) (1999) 943–945.
- [37] H. Le, P. Moin, An improvement of fractional step methods for the incompressible Navier-Stokes equations, *J. Comput. Phys.* 92 (2) (1991) 369–379.
- [38] Y. Morinishi, et al., Fully Conservative Higher Order Finite Difference Schemes for Incompressible Flow, *J. Comput. Phys.* 143 (1998) 90–124.
- [39] O. Thiry, G. Winckelmans, M. Duponcheel, *The Dynamic Smagorinsky Model in Pseudo-Spectral LES of Decaying Homogeneous Isotropic Turbulence at Very High*, in *Direct and Large-Eddy Simulation XI*, Springer, 2019, pp. 123–128.

A.3 Paper III

High-Fidelity Explicit Large Eddy Simulations of Airflows Inside Buildings Using the Immersed Boundary Method and Orthogonal Grids

Elyas Larkermani, Hans Bihs, Grégoire Winckelmans, Bernhard Müller, Laurent
Georges

High-Fidelity Explicit Large Eddy Simulations of Airflows Inside Buildings Using the Immersed Boundary Method and Orthogonal Grids

Elyas Larkermani^{a*}, Hans Bihs^b, Grégoire Winckelmans^c, Bernhard Müller^a, Laurent Georges^a

^aDepartment of Energy and Process Engineering (EPT), Norwegian University of Science and Technology (NTNU), Gløshaugen campus, Trondheim, Norway

^bDepartment of Civil and Environmental Engineering, Norwegian University of Science and Technology (NTNU), Trondheim, Norway

^cInstitute of Mechanics, Materials, and Civil Engineering (iMMC), Université Catholique de Louvain (UCLouvain), Louvain-la-Neuve, Belgium

Abstract

Depending on the application, both RANS and LES can be relevant for the simulation of airflows inside buildings. Although high-resolution LES can be performed using general-purpose flow solvers such as Fluent or OpenFoam, regular grids with good orthogonality and limited skewness are required. Therefore, most existing LES for airflows inside buildings rely on structured grids. Given this constraint on the grid, the paper aims to discuss how the specific features of airflows inside buildings make orthogonal non-body conformal grids relevant for high-fidelity LES. It is shown that orthogonal grids enable the introduction of more accurate spatial discretizations than in general-purpose flow solvers for scale-resolving flow simulations. Moreover, the staggered grid arrangement can be adopted to ensure the pressure-velocity coupling without artificial numerical dissipation. Given the relatively limited Reynolds number in building applications, the Immersed Boundary Method (IBM) grants the treatment of complex geometries with orthogonal grids. In addition, moving objects can be treated by IBM with a fixed mesh without using the complex re-meshing techniques required for body-conformal grids. This feature is relevant to investigate airflows induced by different movements such as door operation or human movement. To this end, this framework is implemented by adapting an existing incompressible flow solver called REEF3D, which was initially developed for hydrodynamics applications. The main adaptation was to develop and implement a new accurate central finite difference scheme to discretize the convective term in the momentum equation compatible with explicit LES. The performance of the method is then investigated on a set of generic flow benchmarks, which are also relevant to indoor airflows, along with an assessment of the sliding door case.

Keywords: Airflow inside buildings, Immersed boundary method, High-resolution Large Eddy Simulation, Finite difference

1 Introduction

Indoor environments in buildings should be comfortable and healthy for users. Air distribution in these enclosed environments is crucial with regard to thermal comfort and indoor air quality (IAQ). For instance, ventilation airflows are strictly restricted and controlled to reduce the energy use of buildings and the resulting greenhouse gas (GHG) emissions. Nevertheless, IAQ should be guaranteed so that advanced ventilation strategies are continuously improved. In hospitals, clean rooms, and public transportation, the dispersion of contaminants and pollutants is of major importance [1, 2]. Interest in the airborne spread of viruses and contaminants has increased drastically as a result of the COVID-19 pandemic [3].

* Corresponding author.

Telephone: +47 73592036

E-mail address: elyas.larkermani@ntnu.no.

Postal address: Kolbjørn Hejes v 1B, NO-7491, Trondheim, Norway.

Many modeling and simulation approaches have been extensively used to understand the physics of airflows inside buildings or to support the design of ventilation, space heating, or cooling strategies [4]. Nevertheless, there are significant variations in terms of modeling. In building performance simulation (BPS) tools (such as IDA-ICE, EnergyPlus, and TRNSYS), the conventional room models do not compute airflows: the air velocity is not considered, and the temperature and the concentration of pollutants are assumed to be constant in each room. Only airflows between rooms or to the outdoor environment are computed by BPS tools using *ventilation network approaches* [5]. Although simple, these approaches can successfully tackle specific flow problems, such as supporting the design of natural ventilation systems. Two alternatives are used to study airflows inside rooms (or complex flow patterns between rooms): so-called *zonal models* and the *computational fluid dynamics* (CFD) approach. Zonal models are an intermediate between the conventional room model in BPS and CFD [6, 7]. The room is subdivided into a limited number of control volumes, where semi-empirical laws enable the computing of the fluxes between the volumes. Alternatively, zonal models can be considered as simplified CFD computation, such as coarse grid CFD or fast fluid dynamics (FFD) [8]. These zonal models are not computationally expensive, but neither are they universal, so they must be validated for specific applications and may fail outside them. Therefore, CFD is the only general simulation tool to analyze airflows inside buildings. CFD aims to numerically solve the governing equations of fluid dynamics – namely, the Navier-Stokes equations – on a computational grid. The complexity of this approach is strongly related to the *turbulence phenomenon*, which originates from the non-linear convective terms of the momentum equation in the Navier-Stokes governing equations. Turbulence generates flow structures with a broad spectrum of length and time scales.

Reynolds-averaged Navier-Stokes (RANS) turbulence modeling discriminates between the time-averaged flow field and modeled turbulent fluctuations. This is a prevalent turbulence modeling approach in all types of applications, including buildings. Airflows inside rooms can be computed using the RANS approach with meshes of millions of points or even less. This modeling approach can, therefore, be performed on a powerful personal computer or a small workstation. Popular models for airflows in buildings are two-equation turbulence models, e.g., the *RNG $k - \epsilon$* , low Reynolds number *$k - \epsilon$* , and *SST $k - \omega$* models. Nevertheless, a significant part of flow physics is not simulated using the RANS approach but modeled. For instance, the *RNG $k - \epsilon$* model generally performs best for building airflows, whilst the *Realizable $k - \epsilon$* model is better suited for plumes [9]. Due to these limitations, it is well known that the accuracy of RANS simulations for building applications is strongly dependent on the ability of the user [9, 10] to create a suitable mesh and also to select the right RANS turbulence model for a given application. A RANS turbulence model can thus be adopted for a given application when the model performance has been properly validated against reference solutions (i.e., benchmarks) for the same category of airflows. It is, therefore, a powerful prediction tool for applied research and industry. However, the RANS turbulence models are not universal, and some unsteady flow phenomena are intrinsically difficult or impossible to capture using the RANS modeling approach [11]. Therefore, high-fidelity CFD is valuable in building science, where most of the flow physics is captured by the computational mesh and a more limited part is modeled.

For high-fidelity CFD, three different strategies regarding turbulence modeling can then be followed. In the first approach, *direct numerical simulation* (DNS) aims to accurately simulate all lengths and time scales of the flow. DNS can thoroughly document the flow physics by capturing all scales and serves as a reference solution. It is an incomparable source of information for understanding the flow physics in fundamental research. The total cost of the DNS approach increases with Re^3 , which makes it prohibitive for high Reynolds number flows. It is the main argument against using DNS in many real-life applications – typically in aeronautics but also in building environments. Nevertheless, given the continuously increasing computational power, this should no longer be taken for granted for some building airflows. With typical smallest eddies in the order of 1 to 10 mm, DNS requires billions of points when applied to a room. However, to analyze generic airflows such as jets, bidirectional airflows through large vertical openings, plumes [12], or a fraction of the room space with specific functionalities (so-called *micro-environment*), DNS with one billion points is no longer prohibitive for research applications. In another approach, *large eddy simulation* (LES) captures the turbulent eddies that are larger than the grid size, and models those that are smaller than the mesh. It is thus an unsteady simulation, where eddies containing most of the kinetic energy of the flow are resolved. Large eddies in turbulent flows depend on the geometry, whilst smaller scales are independent of domain geometry and are more universal than large scales. This means that LES models, called subgrid scale (SGS) models, are more comprehensive than RANS turbulence models. LES can capture detached flows and flows where turbulence

mixing is dominant. In addition, it can provide a direct prediction of the turbulent intensity, and can be adopted in situations where the flow is transitional [13] or not fully developed [14]. LES has already been tested in the context of airflows inside buildings, leading to contrasting performance and results compared to RANS. However, some older LES studies resort to meshes that are too coarse [15], in the same order of magnitude as using RANS. For indoor airflows, Van Hooff et al. [16] have shown that LES outperforms RANS in evaluating cross-ventilation. The near-wall grid resolution needed is comparable to DNS for a wall-resolved LES. This is a major limitation of LES and makes it prohibitive in many building applications, such as design. *Hybrid RANS-LES*, often called *detached eddy simulation* (DES), can, therefore, solve this challenge by combining the best of RANS and LES approaches. As the near-wall grid resolution is significantly lower in the RANS approach, DES typically applies RANS near the wall and LES in the bulk of the flow (away from the wall). It is, in theory, well adapted for building airflows, but the DES performance has not been properly documented so far in this context [11].

LES can be performed using different strategies that can be categorized according to several criteria. Two main aspects are discussed here:

- (a) The first distinction can be made based on the interaction between the spatial discretization error and the SGS model. In LES, the energy cascade between the different flow length scales should be properly reproduced. The discretization scheme for the convective term can introduce artificial dissipation that interacts with the energy cascade by removing kinetic energy. In *explicit LES*, the dissipation related to the subgrid scales is almost entirely performed by the SGS model. This requires the artificial dissipation from the spatial discretization of the convective term in the momentum equation to be null or limited, typically using a central scheme. To guarantee the unconditional stability of a pure central scheme in an under-resolved simulation, the discrete kinetic energy must be conserved [17]. In *implicit LES*, the artificial dissipation of the spatial discretization scheme is tailored to act as a consistent SGS model [18].
- (b) The second distinction can be made between *body conformal* and *non-body conformal* grids [19]. Body conformal meshes follow the surface geometry of the objects exactly, and may result in complex structured or unstructured grids for complex geometries. Conversely, non-body conformal grids do not need to follow the surface geometry, so dense regular grids, such as orthogonal or cartesian grids, can be used. The presence of walls is then treated in a specific way using immersed boundary methods (IBM) [19]. Orthogonal grids with IBM make it possible to easily generate meshes for complex geometries.

Most existing LES for airflows inside buildings resort to explicit LES using body conformal grids, either structured or unstructured [13, 16]. Then, artificial dissipation should be limited, which is a main reason for using (almost fully) structured grids with good orthogonality and limited skewness. Consequently, some strong constraints on the grid quality should be followed when high-fidelity LES is performed using general-purpose flow solvers such as Fluent or OpenFOAM [11].

Given this strong constraint on the mesh, the main contribution of the paper is to show that airflows inside buildings have specific features that make non-body conformal orthogonal grids an interesting alternative to the common general-purpose flow solvers. For this purpose, the opportunities introduced by non-body conformal orthogonal grids are listed and properly discussed, such as the simpler implementation of high-accurate spatial discretization. The second contribution is to introduce some adaptations of a specific incompressible flow solver based on orthogonal grids to perform explicit LES for airflows inside buildings, including moving objects, and to investigate its performance using several relevant benchmarks.

2 LES using orthogonal grids

Airflows in buildings have specific features. The flow can be laminar, transitional, or turbulent, sometimes simultaneously in different regions of the same room. They are characterized by lower Reynolds numbers than aerodynamic applications. Generally, airflows inside buildings are less dependent on geometry details than in aerodynamic applications. Moreover, their internal flow dynamics appearing in the bulk are as important as in environmental flows – e.g., due to the buoyancy effect. These flows can be assumed to be incompressible.

Employing orthogonal grids introduces the following advantages and challenges. Some of these advantages are particularly relevant for the simulation of airflows inside buildings:

- (a) In general-purpose flow solvers, the standard second-order central scheme uses a linear reconstruction of the flow variables to the cell faces. Its numerical stencil thus resorts to five points in each spatial direction when applied on a structured mesh. Using a solver tailored for orthogonal grids, extending the numerical stencil to more points makes it easy to improve the numerical accuracy – for instance, to minimize the truncation error. In transitional flows, minimized dispersion errors can be crucial to correctly capture the advection of flow structures. It is also interesting to mention that orthogonal grids ease the application of line-iterative techniques and geometrical multigrid solvers.
- (b) Due to the anisotropy of the velocity field in boundary layers, the density of grid points can be higher using non-body conformal grids than boundary-fitted meshes for high Reynolds number flows. Several factors may counterbalance this effect. Firstly, given the low Reynolds numbers in airflows inside buildings, this effect should be less critical than in aerodynamic applications. Secondly, in many indoor applications, the geometrical complexity is localized (e.g., around occupants and air supply terminals), which means that grid refinement is possible with a non-uniform orthogonal mesh along walls for the rest of the room, see Figure 1. Typically, the shape of the room can most often be approximated by a combination of boxes. In other words, the mesh can be body conformal on most of the boundaries and non-body conformal in the limited volume where the geometry is complex. Thirdly, the evaluation of the forces on surfaces is less important in building applications than in aerodynamic applications as long as the relevant physical phenomenon for ventilation is captured (such as the location of the flow detachment). Finally, the grid resolution near the wall can be very demanding in wall-resolved LES. However, wall functions have been improved in wall-modeled LES [20-22]. This enables a significant decrease in the grid resolution near the wall, which can enable the use of non-body conformal grids at high Reynolds. For instance, wall functions that better integrate the buoyancy effect have recently been developed [23].
- (c) The prevalent eddy viscosity models in explicit LES – the Smagorinsky and the wall-adapting local eddy-viscosity (WALE) SGS models [24] – tend to be too dissipative on the large resolved scales of the flow, even when applied with the dynamic procedure [25]. Multiscale SGS models apply a spatial filtering procedure to discriminate between large and small resolved scales. In this way, the SGS dissipation is only applied on the smallest resolved scales, while leaving the largest ones untouched [26]. This ensures that the SGS model remains inactive in the laminar and transitional part of the flow. Discrete spatial filters can be adopted with both unstructured and structured meshes, but the performance of the filter can be characterized more easily on an orthogonal mesh [27].
- (d) The immersed boundary method can consider moving objects without having to re-mesh at each time step [19]. This is a clear advantage compared to a body-fitted mesh, where the procedure to analyze moving objects can be demanding. IBM enables the simulation to move objects more easily in building applications, such as moving persons and transient operation of doors and windows.
- (e) The final advantage does not necessarily need to be selected but can lead to simplifications. It is possible to use a staggered arrangement of the incompressible flow variables using an orthogonal mesh [28]. With a staggered grid, there is a strong coupling of the pressure and velocity fields such that no specific numerical treatment is needed to avoid the checkerboard problem (also called odd-even decoupling). Numerical treatment of the odd-even decoupling may introduce numerical dissipation by defining an interpolation scheme for the pressure [29], whilst staggered grids are free of them. Finally, it is possible to define a convective scheme that exactly conserves discrete kinetic energy using a staggered grid, which is beneficial for explicit LES [17, 30].

Some previous studies have already applied some of these advantages of orthogonal grids to perform LES of airflows inside buildings. However, these studies lack an extended discussion of the pros and cons of orthogonal grids, covering the five points discussed earlier (from (a) to (e)).

Kempe et al. [31] introduced a numerical scheme for LES of indoor airflows using orthogonal staggered grids and IBM for stationary objects. However, their spatial discretization scheme is a standard second-order central scheme. Therefore, they do not exploit the capacity to improve spatial discretization, as discussed in point (a). On the contrary, Morozova et al. [32] resort on a fourth-order symmetry preserving finite volume method on an orthogonal staggered mesh to perform LES of airflows inside buildings. However, the treatment of complex geometries is not discussed in their work, addressing points (b) and (d). It is worth mentioning that these two studies introduced their methods to perform high-fidelity LES at moderate computational efforts.

IBM on orthogonal grids has been previously used to simulate contaminant transport in buildings. Mao and Celik [33] used orthogonal staggered grids along with a standard second-order method for the spatial discretization to perform (U)RANS simulations. Choi and Edwards investigated contaminant transport by human movement using LES [34, 35]. They resort to a second-order low-diffusion scheme for spatial discretization on collocated orthogonal grids. It is worth noting that the IBM has also been used in unstructured flow solvers to study body movement and pollutant dispersion in buildings, as seen in works like Löhner et al. [2] and Saarinen et al. [36] using ANSYS CFX. To avoid confusion, it is important to note that orthogonal grids are not the prerequisite for implementing IBM; quite the opposite, it is IBM that facilitates the use of orthogonal grids, especially with complex geometries.

Compared to these studies, the original contribution of our work is a broader integration of the benefits offered by orthogonal grids. It introduces an innovative and accurate central finite difference scheme in conjunction with IBM on a staggered orthogonal mesh that can properly model moving objects.

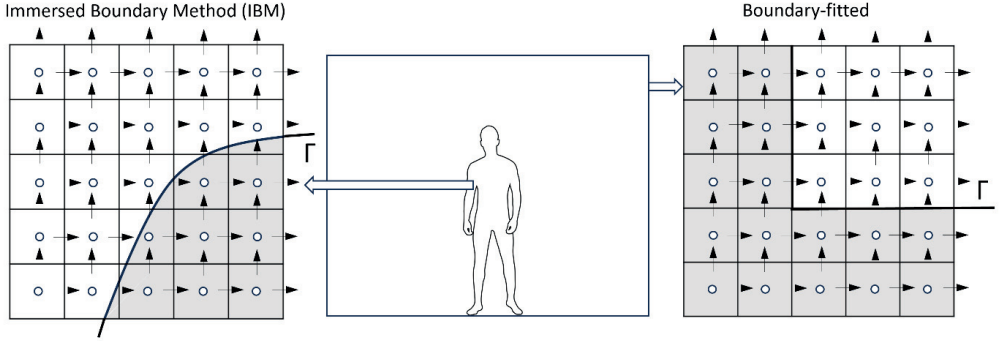


Figure 1. 2-D representation of a staggered mesh with a wall boundary Γ and two layers of ghost points in the grey zone: pressure points are indicated using circles, while velocity components are shown using arrows.

3 Numerical method

In the remainder of the article, the framework introduced in Section 2 is applied to adapt an existing incompressible flow solver with staggered orthogonal grids to high-fidelity LES for airflow inside buildings, including moving objects and accurate spatial discretization.

3.1 Governing equations

The incompressible Navier-Stokes equations for a Newtonian fluid with constant physical properties are considered. The Boussinesq approximation accounts for the change of density resulting from a temperature change. Thermal radiation between the walls is neglected. The governing equations can then be written in the following form:

$$\nabla \cdot \mathbf{u} = 0 \quad (1)$$

$$\frac{\partial \mathbf{u}}{\partial t} + \nabla \cdot (\mathbf{u}\mathbf{u}) = -\frac{\nabla(p - \rho_0 \mathbf{g} \cdot \mathbf{z})}{\rho_0} + \nabla \cdot (v(\nabla \mathbf{u} + (\nabla \mathbf{u})^T)) - \beta \mathbf{g}(T - T_{\text{ref}}) \quad (2)$$

$$\frac{\partial T}{\partial t} + \nabla \cdot (\mathbf{u}T) = \nabla \cdot (\alpha \nabla T) + Q \quad (3)$$

where $\mathbf{u} = (u, v, w)$ is the velocity vector in cartesian coordinates $\mathbf{x} = (x, y, z)$. p represents the pressure field, T is the temperature, ρ_0 the reference density. Here, parameters v and α are the kinematic viscosity and the thermal diffusivity, respectively. The last term in Equation (2) is the buoyancy term, where $\beta = 1/T_{\text{ref}}$ is the thermal expansion coefficient of the air modeled as an ideal gas and \mathbf{g} the gravitational acceleration. The second term on the right-hand side of Equation (3) (Q) is the heat source.

3.2 Flow solver adaptation

REEF3D [37] is an open-source parallel flow solver that was developed for hydrodynamics applications. From the start, the focus of REEF3D was to solve complex free surface dynamics through two-phase flow interface capturing. The architecture of REEF3D makes it a relevant candidate according to the framework introduced in Section 2. Firstly, the grid is orthogonal, with a one-dimensional grid stretching in each spatial direction. As shown in Figure 1, a staggered arrangement of the flow variables is adopted. Secondly, the baseline numerical stencil for the convective term involves seven points in each spatial direction, which enables the development of high-resolution schemes. The baseline scheme in REEF3D is a weighted essentially non-oscillatory (WENO) scheme, which is a fifth-order accurate scheme for linear advection problems. However, the formulation is hybrid in the sense that the mass conservation, the pressure gradient, and diffusion terms are still discretized using second-order central finite differences. REEF3D is thus formally second-order but with reduced dispersion errors using a seven-point numerical stencil to discretize convective terms. Thirdly, the fractional step method is used to enforce the discrete continuity equation [38]. Given the second-order discretization of the velocity divergence in Equation (1) and the pressure gradient in Equation (2), it leads to the resolution of a second-order Poisson equation. The Poisson equation is solved using an efficient geometric multigrid linear solver from the HYPRE library [39]. Finally, the effect of complex geometries is integrated using IBM.

The ghost cell approach is used for fixed, rigid boundaries (i.e., solid objects). This enables a sharp representation of the immersed boundaries, which is desirable, especially at high Reynolds numbers [19]. The local directional ghost cell approach of Berthelsen and Faltinsen [40] has been implemented in order to treat sharp corners accurately. The sharp-interface methods, such as cut cells and ghost cells, encounter a major challenge with boundary motion. A cell in a solid body can become part of the fluid domain during movement. The spatial discontinuity associated with the sharp immersed boundary can lead to a temporal discontinuity for cells near the boundary. Therefore, a straightforward temporal discretization of the momentum on these cells is not possible, as flow variables in these cells do not have a valid time history [19]. Therefore, an IBM based on a continuous forcing term in the momentum equation is implemented to treat moving boundaries, employing the method of Yang [41]. The forcing term is imposed on a few grid cells on both sides of the solid boundary, providing a smooth transition between the fluid and solid phases and removing the temporal discontinuity for cells emerging into the fluid [19]. In REEF3D, the incompressible Navier-Stokes equations are solved in parallel using domain decomposition. Partitions communicate with their neighbors using ghost cells and the message passing interface (MPI) [42].

In conclusion, REEF3D already has many of the characteristics listed in Section 2. To perform explicit LES efficiently, the flow solver should be adapted. To this end, a non-dissipative spatial discretization is developed and implemented (see Section 3.3). The default temporal discretization is high-order using the third-order explicit total variation diminishing (TVD) Runge-Kutta (RK) method with a projection step at each stage. However, a common strategy for LES and DNS is to apply an explicit time integration for the convective terms and an implicit integration for the diffusion terms. The main reason for the implicit treatment of the diffusive terms is the severe time step restriction for numerical stability in regions with substantial grid refinement, typically along the walls. As the velocity is generally very small close to the wall, the time step requirement for the explicit convective term is less severe. Therefore, REEF3D has been adapted by implementing a low-dissipative semi-implicit RK scheme (see Section 3.4). On top of that, SGS models with and without spatial filters [26] are incorporated into REEF3D, providing an option to select a multiscale SGS model or a standard one. Additionally, the original purpose of REEF3D was hydrodynamic applications; it deals with air and water and, consequently, has significant density differences compared to the density differences created by air temperature in building applications. Therefore, REEF3D did not rely on the Boussinesq approximation, and this term needs to be implemented. The two major implementations are the central discretization scheme for the convective terms and the semi-implicit RK scheme. The other two modifications can be considered as minor.

3.3 Hybrid central finite difference

Following the notation of Vasilyev [30], two discrete operators are introduced, enabling the concise formulation of central finite difference schemes on a staggered mesh. They can be applied at both pressure and

velocity points. The interpolation operator in physical space with stencil n can be applied on a field ϕ in the direction x at the grid point of index (i, j, k) :

$$\bar{\phi}^{nx}|_{i,j,k} = \frac{\phi(i+n/2, j, k) + \phi(i-n/2, j, k)}{2} \quad (4)$$

The second operator is the finite difference operator of stencil n in the direction x acting on the field ϕ at the grid point of an index (i, j, k) :

$$\frac{\delta_n \phi}{\delta_n x}|_{i,j,k} = \frac{\phi(i+n/2, j, k) - \phi(i-n/2, j, k)}{x(i+n/2, j, k) - x(i-n/2, j, k)} \quad (5)$$

The extension of these two operators to the other spatial directions, y and z , is straightforward. The grid point indices (i, j, k) will be omitted for these two operators in the remainder of the text to avoid any confusion with Cartesian tensor notation. From now on, the letters i and j will exclusively be used to index the spatial directions. Using these discrete operators, the standard second-order central finite difference (CDS2) of the convective term (Conv) in direction i can be expressed in the following way:

$$\text{Conv}_i(u) = \frac{\partial}{\partial x_j}(u_j u_i) \approx \frac{\delta_1}{\delta_1 x_j}(\bar{u}_j^{1x_i} \bar{u}_i^{1x_j}) \quad (6)$$

Here, the Einstein summation convention is used on index j . Rivas [43] showed that this scheme has a first-order truncation error on a non-uniform grid, whilst it achieves second-order accuracy on a continuously stretched grid. According to Vasilyev et al. [30], this divergence form of the convective terms in the Navier–Stokes equations preserves the conservation of continuity and momentum at the discrete level using exact time-integration in the absence of viscous dissipation. However, kinetic energy conservation by convection may not be guaranteed using the divergence form on a non-uniform staggered grid due to the commutation error term. The conservation of discrete kinetic energy is important to perform explicit LES and to guarantee the numerical stability of central schemes in under-resolved simulations like LES. The numerical stencil of CDS2 only involves three points in each spatial direction. However, REEF3D allows finite difference schemes with a numerical stencil of up to seven points by spatial direction. This feature can be used to introduce a better numerical scheme than the standard CDS2.

Morinishi et al. [44] developed high-order finite differences on staggered orthogonal grids that conserve the discrete momentum and kinetic energy when the mesh is uniform. These schemes were extended by Vasilyev [30] to preserve good conservation properties on non-uniform grids. However, it was determined that the commutation error between discrete differencing and averaging operators was a key factor contributing to non-conservation on non-uniform meshes. So, his proposed schemes can combine fourth-order accuracy with the discrete conservation of either momentum or kinetic energy on non-uniform grids. Verstappen and Veldman [17] proposed a fourth-order finite volume method for non-uniform staggered meshes. Unlike the approach of Vasilyev [30], the scheme of Verstappen and Veldman [17] can simultaneously conserve the discrete momentum and kinetic energy on a non-uniform mesh. The coefficients of these schemes [17, 30, 44] are not adjusted locally based on the local grid-stretching as they are applied to the computational space rather than the physical space to preserve the symmetry of the discrete operator. Nevertheless, they are fourth-order accurate for a continuously stretched non-uniform grid.

One of the difficulties of implementing these fourth-order schemes is that their numerical stencil is not compact in the sense that they require high-order interpolation in the three spatial directions. This makes the implementation of these schemes more complex and the treatment of boundary conditions more challenging, especially for complex geometries in practical engineering problems using IBM. Our goal is thus to improve the numerical accuracy of the CDS2 scheme with a scheme that keeps the numerical stencil compact so that the implementation and the treatment of boundary conditions remain simple. To this purpose, the CDS2 is improved by discretizing the convective fluxes more accurately using a symmetric seven-point stencil [45]. In contrast, the convection velocity remains unchanged and interpolated with a second-order accurate interpolation operator as in the original CDS2:

$$\text{Conv}_i(u) = \frac{\partial}{\partial x_j}(u_j u_i) \approx \frac{\delta_1}{\delta_1 x_j}(\bar{u}_j^{1x_i}(\alpha_1 \bar{u}_i^{1x_j} + \alpha_3 \bar{u}_i^{3x_j} + \alpha_5 \bar{u}_i^{5x_j})) \quad (7)$$

with α_1 , α_3 , and α_5 being the constant scheme coefficients, which are not adapted according to the local grid-stretching. The coefficients $\alpha_1 = 37/30$, $\alpha_3 = -8/30$, and $\alpha_5 = 1/30$ are chosen so that Equation (7) corresponds to a sixth-order central difference approximation when the convection velocity is constant. Therefore, this new scheme is termed HCDS6, where the H stands for the hybrid combination. In general, the scheme remains second-order accurate; however, it has a significantly smaller truncation error than the standard second-order central scheme (CDS2). It conserves the discrete momentum on a non-uniform mesh but not the discrete kinetic energy. For $\alpha_1 = 1$, $\alpha_3 = 0$, and $\alpha_5 = 0$, the method is degraded to CDS2, and thus, the HCDS6 only extends the numerical stencil along lines in each spatial direction, keeping the stencil compact. For instance, the new method is more compact than the fourth-order finite-difference schemes of Vasilyev [30], where the convection velocity is interpolated with a fourth-order accurate interpolation operator:

$$\text{Conv}_i(u) \approx \left[\frac{9}{8} \frac{\delta_1}{\delta_1 x_j} \left\{ \left(\frac{9}{8} \bar{u}_j^{1x_i} - \frac{1}{8} \bar{u}_j^{3x_i} \right) \bar{u}_i^{1x_j} \right\} - \frac{1}{8} \frac{\delta_3}{\delta_3 x_j} \left\{ \left(\frac{9}{8} \bar{u}_j^{1x_i} - \frac{1}{8} \bar{u}_j^{3x_i} \right) \bar{u}_i^{3x_j} \right\} \right]_{i,j,k} \quad (8)$$

3.4 Semi-implicit time integration

An accurate and low-dissipation semi-implicit time integration scheme might be needed when the grid is well refined near the walls to perform wall-resolved LES. Therefore, the popular semi-implicit Runge-Kutta method by Le and Moin [46] has been implemented in REEF3D and requires modification of the code structure. In this temporal approach, every time step is advanced in three sub-steps, each of which uses the second-order-implicit Crank-Nicholson method to integrate the diagonal contribution of the diffusive term (Laplacian term), while the other terms are explicitly integrated using a second-order Adams-Bashforth method. The predictor-corrector technique, and the Poisson equation for the three steps are formulated as follows:

$$\begin{aligned} & \frac{\hat{u}_i^m - u_i^{m-1}}{\chi_m \Delta t} + \gamma_m \frac{\delta}{\delta x_j} (u_j^{m-1} u_i^{m-1}) + \kappa_m \frac{\delta}{\delta x_j} (u_j^{m-2} u_i^{m-2}) \\ & = -\frac{1}{\rho} \frac{\delta p^{m-1}}{\delta x_i} + \frac{\delta}{\delta x_j} \left[v \left(\gamma_m \frac{\delta u_j^{m-1}}{\delta x_i} + \kappa_m \frac{\delta u_j^{m-2}}{\delta x_i} \right) \right]_{i \neq j} \\ & + \theta \left(\frac{1}{2} \frac{\delta}{\delta x_j} \left[v \frac{\delta \hat{u}_i^m}{\delta x_j} \right] + \frac{1}{2} \frac{\delta}{\delta x_j} \left[v \frac{\delta u_i^{m-1}}{\delta x_j} \right] \right) + g_i [1 - \beta (T^{m-1} - T_{ref}^{m-1})] \end{aligned} \quad (9)$$

Here, the superscript m represents the sub-step number, taking values from 1 to 3. For the initial sub-step ($m = 1$), the term corresponding to $m - 2$ is disregarded. The u_i^0 and u_i^3 denote the velocities at time steps n and $n + 1$, respectively. The coefficients γ_m , κ_m and χ_m at each sub-step m are constants provided in Table 1. The coefficient θ equals 2 for $i = j$, and 1 otherwise. The second term on the right-hand side includes the non-diagonal components of the diffusive term, while the third term incorporates the diagonal components integrated using the Crank-Nicholson method.

Table 1. Coefficients for semi-implicit Runge-Kutta method.

m	χ_m	γ_m	κ_m
1	$\frac{8}{15}$	1	0
2	$\frac{2}{5}$	$\frac{25}{8}$	$-\frac{17}{8}$
3	$\frac{15}{15}$	$\frac{9}{4}$	$-\frac{5}{4}$

The resulting intermediate velocity \hat{u}_i^m does not satisfy the continuity equation (Equation (1)). To obtain the new velocity u_i^m , the intermediate velocity is projected onto the space of incompressible divergence-free vector field:

$$\frac{u_i^m - \hat{u}_i^m}{\chi_m \Delta t} = -\frac{1}{\rho} \frac{\delta (p^m - p^{m-1})}{\delta x_i} \quad (10)$$

This is done by solving a Poisson equation for the pressure field, which is derived by applying the divergence to the intermediate velocity field and enforcing $\delta u_i^m / \delta x_i = 0$:

$$\frac{\delta}{\delta x_i} \left(\frac{1}{\rho} \frac{\delta(p^m - p^{m-1})}{\delta x_i} \right) = \frac{1}{\chi_m \Delta t} \frac{\delta \hat{u}_i^m}{\delta x_i} \quad (11)$$

In REEF3D, the fully parallelized bi-conjugate gradients stabilized (BiCGStab) algorithm [47] solves the Poisson pressure equation by using geometric multigrid preconditioning provided by the high-performance solver library, HYPRE [48].

The time integration of the energy equation is done using a single step at each RK stage:

$$\frac{T^m - T^{m-1}}{\Delta t} + \gamma_m \frac{\delta}{\delta x_j} (u_j^{m-1} T^{m-1}) + \kappa_m \frac{\delta}{\delta x_j} (u_j^{m-2} T^{m-2}) = \frac{1}{2} \left(\frac{\delta}{\delta x_j} \left[\alpha \frac{\delta T^{m-1}}{\delta x_j} \right] + \frac{\delta}{\delta x_j} \left[\alpha \frac{\delta T^m}{\delta x_j} \right] \right) \quad (12)$$

A similar approach is applied for the advection of a passive scalar, such as the concentration of a gaseous pollutant. For the viscous terms and the pressure term, the second-order central differential scheme is adopted – for example:

$$\frac{\partial}{\partial x_j} \left[\frac{\partial u_i}{\partial x_j} \right] \approx \frac{\delta_1}{\delta_1 x_j} \left\{ \frac{\delta_1 u_i}{\delta_1 x_j} \right\} \quad (13)$$

4 Results

In this section, five benchmark tests conducted using the REEF3D flow solver are presented. These tests serve to showcase the capabilities and effectiveness of the current numerical approach. They include four generic benchmarks: the three-dimensional Taylor-Green vortex flow, the DNS of a wall-attached cube, the DNS of flow past a sphere, and the LES of turbulent channel flow. Finally, one benchmark that is specific for airflow inside buildings is considered with a moving object. For this purpose, the LES of the transitional flow generated by a sliding door is analyzed.

4.1 Taylor-Green vortex flow

The Taylor-Green vortex flow is a well-defined, transient, three-dimensional flow that is generated by the interaction of two counter-rotating vortices in a periodic cubic domain. The simplicity of the domain geometry and initial and boundary conditions enables us to focus on the performance of the numerical method. This classic benchmark problem is typically used to validate numerical methods for scale-resolving simulations [49] and to evaluate high-fidelity flow solvers [50, 51]. Interactions between different scales of motion in the fluid, driven by the non-linear advection term in the Navier-Stokes equations, lead to the formation of smaller-scale vortices through vortex stretching, filamentation, and reconnection. These features are responsible for transferring energy from large-scale motion to smaller scales through the energy cascade.

The counter-rotating vortices are initialized in a checkerboard arrangement from an analytical periodic vortex field where a sinusoidal velocity field with a uniform vorticity distribution in the $x - y$ plane is specified:

$$\begin{aligned} \frac{u(x, y, z, t_0)}{U} &= \sin\left(\frac{x}{L}\right) \cos\left(\frac{y}{L}\right) \cos\left(\frac{z}{L}\right) \\ \frac{v(x, y, z, t_0)}{U} &= -\cos\left(\frac{x}{L}\right) \sin\left(\frac{y}{L}\right) \cos\left(\frac{z}{L}\right) \\ \frac{w(x, y, z, t_0)}{U} &= 0 \end{aligned} \quad (14)$$

where L and U are the characteristic length and velocity scales of the problem, respectively. The Reynolds number of the flow is defined as $Re = UL/\nu$ and is equal to 1600. A periodic cubic domain with a periodicity length of $L_x = L_y = L_z = 2\pi L$ is considered. A uniform grid is adopted with the same resolution in all three directions as $h = 2\pi L/N$, where N is the number of grid cells in one direction. The baseline and refined grid resolutions are 256^3 and 512^3 , respectively. The characteristic convective time $t_c = L/U$ is defined as the time required for a fluid particle to traverse the characteristic length scale of the flow (L) at the characteristic velocity scale (U). A non-dimensional physical time step of $\Delta t^* = \Delta t/t_c = 0.001$ is adopted for the baseline grid to capture the temporal scales adequately. The physical time step size is halved for the grid refinement. The Courant number is set such that $CFL \leq 0.1$ for each grid resolution to minimize the temporal error. The simulations are performed for a time period of $t/t_c = 10$.

Different diagnostics are introduced to evaluate the performance of the adapted REEF3D solver for the Taylor-Green vortex flow simulation. A common diagnostic is the temporal evolution of the total kinetic energy averaged over the control volume (V):

$$E_k = \frac{1}{V} \int_V \frac{u_i u_i}{2} dV \quad (15)$$

As the kinetic energy is not expected to vary much between the different scenarios investigated here, the time derivative of the total kinetic energy, defined as kinetic energy dissipation (ϵ), is a more sensitive characteristic than the total kinetic energy:

$$\epsilon = -\frac{dE_k}{dt} \quad (16)$$

A numerical scheme with significant artificial dissipation would fail to reproduce the time evolution of kinetic energy dissipation, making the scheme inappropriate for DNS or explicit LES.

4.1.1 Evolution of the kinetic energy dissipation

Figure 2 depicts the evolution of the discrete kinetic energy-based dissipation rate using two grid resolutions compared to the reference DNS solution [51]. This is characterized by an initial rapid increase in dissipation rate associated with stretching of the initial vortices. As these vortices interact and break down, they transfer energy to smaller scales, thereby increasing the dissipation rate. At around $t/t_c \approx 4$, the dissipation rate increases rapidly when the transition from simple initial vortices to small-scale anisotropic turbulence occurs. This increase reaches the dissipation peak at around $t/t_c \approx 9$. As no external force exists, the dissipation decreases as the turbulence decays. However, as the flow evolves and the vortices continue to break down, the dissipation rate eventually reaches a steady-state value, which indicates that the energy injection and dissipation are balanced at the smaller scales.

To assess the performance of the numerical scheme, a comparison between CDS2 and HCDS6 on a baseline resolution grid (256^3) and a refined grid (512^3) is carried out. For the highest under-resolution computation with 256^3 grid cells, the HCDS6 scheme deviates from the reference DNS results at around $t/t_c \approx 8.6$ and underpredicts the dissipation up to $t/t_c = 10$. The standard CDS2 scheme overestimates the dissipation rate between $t/t_c \approx 7.9$ and $t/t_c \approx 8.35$. A significant underestimation is predicted from the reference data until $t/t_c \approx 9.4$. From now on, the dissipation rate is slightly overestimated up to around $t/t_c = 10$. As the grid is refined, the numerical dissipation rate evaluated using both schemes converges with the reference DNS solution.

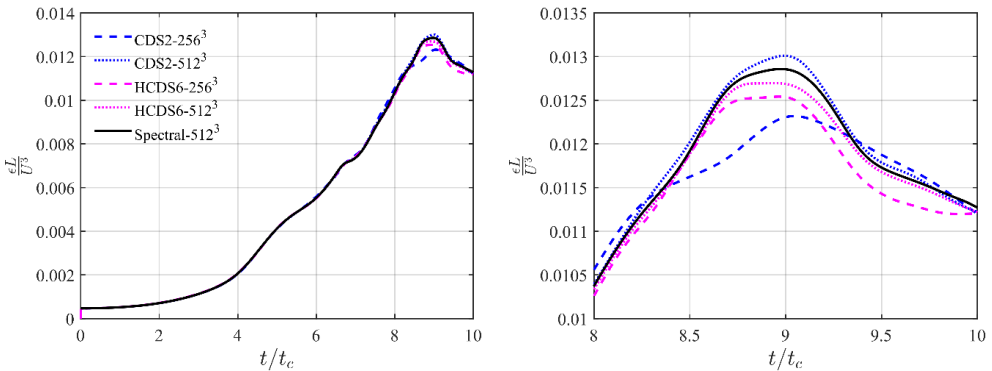


Figure 2. Temporal evolution of the dissipation rate based on kinetic energy for the Taylor-Green vortex.

4.1.2 Vortical structures

Regular counter-rotating vortices stretch and twist as the flow evolves, generating smaller and more complex vortical structures. These structures continue to interact with each other, which leads to the formation of the most intricate vortices close to the dissipation peak at $t/t_c \approx 9$. A comparison of the instantaneous vorticity

field is therefore performed to analyze the accuracy and reliability of the numerical scheme to transport complex vortical structures. It is sufficient to visualize vortical structures on only a limited portion (1/16) of the periodic plane, as the remaining portions will be identical due to different symmetries of the flow [52], as illustrated in Figure 3. It can indeed be observed in Figure 3 that the flow is very complex, yet it is not representative of a homogeneous isotropic turbulence state as it is still quite organized.

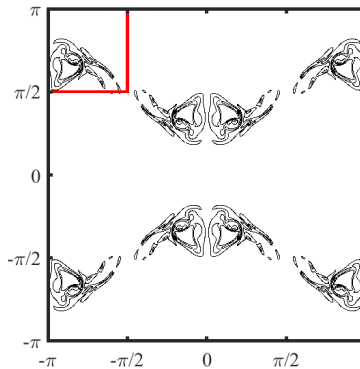
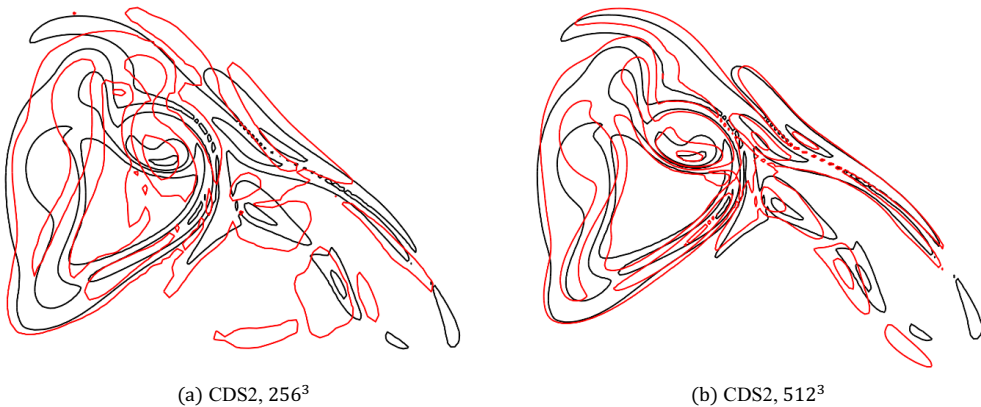


Figure 3. Instantaneous vorticity norm from the pseudo-spectral scheme on the periodic plane ($y = 0$) at $t/t_c = 9$ [51].

Five vorticity iso-contours for $\omega \in [1, 5, 10, 20, 30]$ on a subset of the periodic plane ($y = 0$) at $t/t_c = 9$ obtained by CDS2 and HCDS6 schemes are superposed with those from the reference DNS solution [51] in Figure 4. The results are presented for the two different grid resolutions of 256^3 and 512^3 in the left and right columns, respectively. On the coarser grid, the position of the large vortical structures is mostly captured by the CDS2 scheme, while the smaller vortices are diffused and contaminated by numerical noise. The HCDS6 scheme is better at capturing the vortical structures, although small details of the solution are smeared. The shape of the vortex structure improves and overlaps with the reference spectral solution as the grid is refined using both schemes. However, due to dispersion error, the CDS2 scheme still struggles to predict the correct position of vortical structures, even on the refined grid.



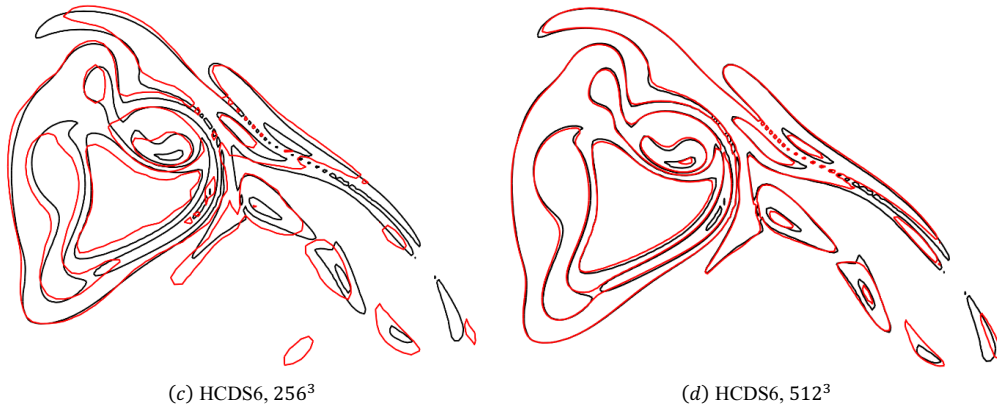


Figure 4. Iso-contours of the vorticity norm on the periodic plane ($y = 0$) at $t/t_c = 9$. Spectral solution is in black and the finite-difference is in red. Left: coarse grid (256^3), right: fine grid (512^3).

Finally, it shows that, even though the new HCDS6 scheme does not conserve the discrete kinetic energy exactly, it remains stable and non-dissipative for an under-resolved simulation. The improvement of the new scheme in terms of dispersion becomes visible by analyzing iso-contours of the vorticity norm. The solution of the second-order central scheme of OpenFOAM on the same grid resolution and using the same time step has been computed by Bricteux et al. [52]. A comparison with the vorticity iso-contours of Figure 4 clearly shows that the new second-order scheme is better at capturing the flow structures than the conventional second-order central scheme of OpenFOAM.

In line with point (a) in Section 2, this demonstrates the advantage of using the accurate spatial discretization scheme with a seven-point stencil in each spatial direction, compared to the second-order finite volume scheme (with a linear reconstruction of the flow variable) typically used in the conventional flow solvers, such as OpenFOAM and ANSYS Fluent.

4.2 Flow past a wall-attached cube

The flow around a wall-attached solid cube is a simple geometry that offers valuable insights into the interaction between a boundary layer and complex bodies immersed within it. Although the scope of this paper is about indoor airflows, the flow around square cylinders with varying aspect ratios is also an important test case in environmental applications, enabling a simulation of airflow dynamics around simplified architectural structures [53, 54]. The sharp corners of the cube challenge the performance of the IBM using the ghost cell approach. In REEF3D, the local directional ghost cell approach [38] was introduced to solve this challenge. Another approach called an enhanced direct forcing IBM implemented in the REEF3D is also adopted where the effect of solid boundaries in the Navier-Stokes equations is incorporated by introducing additional terms or forcing functions.

The wall-attached cube is a geometric solid positioned in a zero-pressure gradient boundary layer. The computational setup is identical to the one used by Diaz-Daniel et al. [55] in their DNS of wall-attached cube immersed in laminar and turbulent boundary layers. For the sake of simplicity, only the laminar case at $Re_H = 500$ is investigated here, where the inlet boundary condition is defined by the Blasius laminar boundary layer profile. The cube is located at a distance $9H$ from the inlet, where H is the cube height. The coordinate system is aligned with the front plane of the cube where the origin is located at $x = 0$. A no-slip boundary condition is applied at the bottom wall, while a homogeneous Neumann condition is imposed at the top boundary. In the spanwise direction, the periodic boundary condition is adopted to simulate an infinite array of cubes. The computational domain size and grid resolution are summarized in Table 2. Re_θ and Re_{δ^*} are based on the momentum thickness θ and the displacement thickness δ^* , respectively, for the freestream velocity U_∞ .

Table 2. Computational domain size and mesh resolution for DNS of the wall-attached cube.

Re_H	Re_θ	Re_{δ^*}	$\frac{L_x}{H} \times \frac{L_y}{H} \times \frac{L_z}{H}$	$N_x \times N_y \times N_z$	$\frac{\Delta y_{wall}}{H}$	$\frac{\Delta y_{top}}{H}$	$\frac{\Delta t U_\infty}{H}$	$\frac{T U_\infty}{H}$
--------	-------------	-----------------	---	-----------------------------	-----------------------------	----------------------------	-------------------------------	------------------------

A uniform grid with a cell size of $0.02H$ is created in a rectangular refinement area measuring $[2H \times 2H \times 2H]$ around the cube. The cells are elongated with a growth ratio of 1.2 in the wall-normal direction from the refined zone to the top boundary of the domain, ensuring that the largest cell size does not exceed $0.68H$. A smaller growth ratio of 1.05 is set in streamwise and spanwise directions from the focus zone up to the lateral boundaries of the domain, where the maximum cell size is $0.2H$ and $0.5H$ in x and z directions, respectively. The flow statistics are time-averaged over a period T following a long initial transient period until the flow is statistically steady-state.

The time-averaged streamwise velocity contours with mean flow streamlines around the wall-attached cube are illustrated in Figure 5. A deceleration region is created as the flow encounters the cube front plane. The flow accelerates gradually along the cube's leading face, with a well-behaved velocity gradient near the wall. A mild separation occurs at the leading edge, followed by a thin boundary layer along the cube top face. In the wake region behind the cube, vortices and disturbances are less pronounced than higher Reynolds numbers, resulting in a more organized flow structure. The mean-flow streamlines show a closed recirculation region in front of the cube (Figure 5, left) surrounded by a horseshoe vortex system upstream and around the wall-attached cube (Figure 5, right). The contours of time-averaged streamwise velocity show that the flow structures align remarkably well with benchmark DNS data, thereby underlining the robustness and reliability of the immersed boundary method implemented in the flow solver.

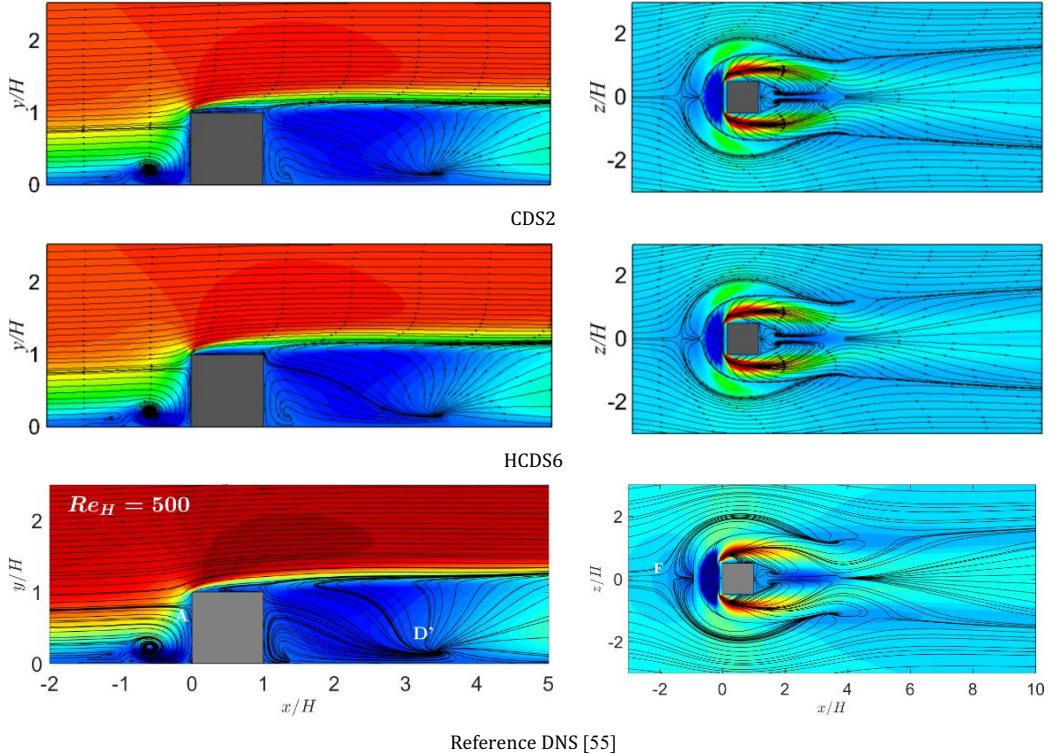


Figure 5. Time-averaged streamwise velocity contours with mean flow streamline around a wall-attached cube at $Re_H = 500$. Left: $x - y$ plane, right: $x - z$ plane. The color scale for \bar{u} spans from $-0.1U_\infty$ in dark blue to $1.1U_\infty$ in dark red for left column and $0.2U_\infty$ in dark red for right column.

A key flow diagnostic is the location of stagnation points, which provides a basis for a quantitative comparison between REEF3D and DNS reference solutions. The upstream stagnation point on the cube front face is marked A while the other one positioned farther from the front face is labeled F (see Figure 5, last row). The one that exists downstream is marked D . The location of stagnation points is reported in Table 3. Again, the results of

the reference DNS solution [55] are accurately replicated. In this case, the mesh is conformal with the channel but non-conformal for the cube. In line with point (b) in Section 2, this demonstrates that IBM is an accurate alternative to boundary-fitted meshes.

Table 3. Positions of stagnation points for the mean flow around the wall-attached cube immersed in a laminar boundary layer.

		y_A	x_D	y_D	x_F
Incompact3d [55]		0.82	3.48	0.17	-1.6
REEF3D (CDS2)	Enhanced direct forcing IBM approach	0.82	3.48	0.16	-1.5
REEF3D (HCDS6)		0.82	3.48	0.17	-1.5
REEF3D (CDS2)	Local directional ghost cell approach	0.82	3.48	0.16	-1.5
REEF3D (HCDS6)		0.82	3.48	0.17	-1.5

4.3 Steady non-axisymmetric flow past a sphere

The flow of a viscous fluid past a stationary sphere can trigger instabilities with three-dimensional flow patterns, despite the body symmetry. However, unlike two-dimensional flows, such three-dimensional patterns introduce a level of complexity that is characterized by wake formation and vortical interactions. Despite its apparent simplicity, this scenario represents a canonical problem in the family of immersed bluff body flows with numerous applications. The position of flow separation on a wall-mounted cube is mostly determined by the geometry, whereas, for a smooth surface like a sphere, it is primarily influenced by the pressure gradient and surface curvature. This benchmark is extensively documented in scientific literature [56-58].

An enhanced direct forcing IBM and local directional ghost cell approaches implemented in the REEF3D framework are used to simulate the flow at $Re_D = 250$ (based on the free stream velocity U_∞ and the sphere diameter D) in a steady laminar regime. A large computational domain of $[-10D, 10D]$ is considered in all three spatial directions. The sphere center is positioned at a distance $8D$ from the inlet. A uniform grid spacing of $0.02D$ is generated within a rectangular refinement zone of $[4D \times 2D \times 2D]$ surrounding the sphere. To limit the mesh size, the cells are stretched with a growth ratio of 1.25 between the refined zone and the domain external boundaries, where the maximum cell size is $0.2D$. A Dirichlet boundary condition $u/U_\infty = 1, v = 0$ and $w = 0$ is applied at the inlet and an outflow condition is imposed at the outlet boundary. A symmetry boundary condition is adopted for lateral directions, while a no-slip boundary condition is enforced on the sphere. To assess the performance of the numerical method, the drag (C_D) and lift (C_L) coefficients are compared with experimental data by Johnson and Patel [57]:

$$C_D = \frac{F_x}{\frac{1}{2}\rho U_\infty^2 \frac{\pi D^2}{4}} \quad (17)$$

$$C_L = \frac{F_y}{\frac{1}{2}\rho U_\infty^2 \frac{\pi D^2}{4}} \quad (18)$$

In Table 4, the results for drag and lift coefficients using both the standard second-order central differential scheme (CDS2) and the pseudo sixth-order central scheme (HCDS6) are presented. In the case of axisymmetric flow, the lift coefficient is naturally zero. Compared to the experimental data, the current approach can accurately compute steady drag and lift coefficients.

Table 4. Drag and lift coefficients for a flow past a sphere at $Re_D = 250$.

$Re_D = 250$	Method	C_D	C_L
Johnson and Patel [57]		0.7	0.062
REEF3D (CDS2)	Enhanced direct forcing IBM approach	0.7	0.054
REEF3D (HCDS6)		0.7	0.062
REEF3D (CDS2)	Local directional ghost cell approach	0.69	0.055
REEF3D (HCDS6)		0.68	0.059

For a qualitative comparison of this non-axisymmetric flow, the streamlines of projected streamwise velocity in the $(x - z)$ and $(y - z)$ planes are shown in Figure 6. Although the flow is steady state, it is non-axisymmetric at $Re_D = 250$ with a plane of symmetry. The present IBM correctly replicates the streamlines

center compared to Johnson and Patel [57]. The length of the recirculation bubble and the location of the vortex center are well reproduced. To capture the wake structure correctly, the location of the boundary layer separation must be predicted accurately, which is not trivial as the sphere geometry has a smooth curve. Even though the mesh was isotropic and non-body conformal, the IBM method was able to predict this phenomenon correctly. This is important for building applications as some moving objects, such as occupants, present similar flow characteristics.

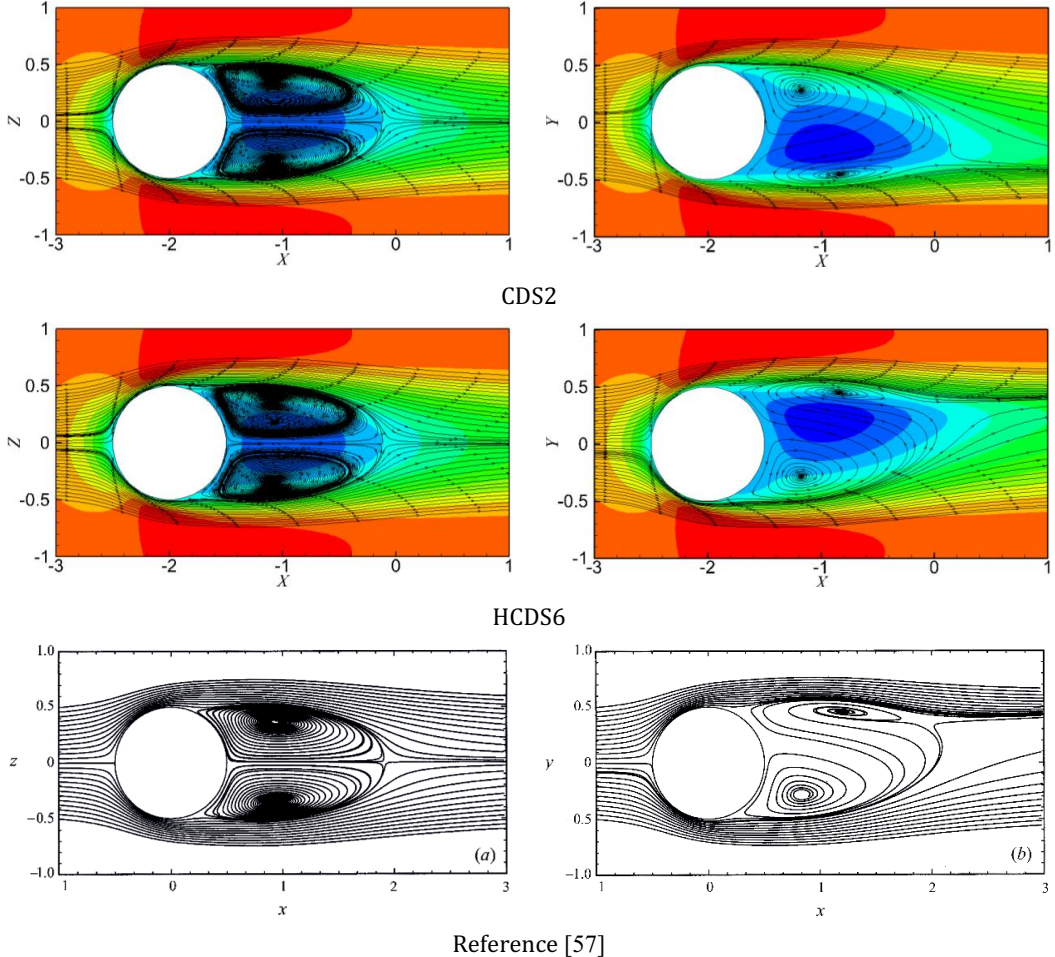


Figure 6. Streamlines of projected streamwise velocity for a flow past a sphere at $Re_D = 250$.

4.4 LES of turbulent channel flow

The performance of the flow solver was analyzed for DNS or under-resolved simulations in previous benchmarks without turbulence modeling. In this section, the interaction of the numerical method with the SGS model is investigated using the wall-resolved turbulent channel flow benchmark. This evaluation is necessary to prove that explicit LES without artificial dissipation can be properly performed. Another objective is to demonstrate that the new proposed numerical scheme remains accurate and stable on a non-uniform mesh.

The LES of a turbulent channel flow at the frictional Reynolds number of $Re_\tau = 640$ is carried out. The WALE SGS model is adopted where the SGS kinematic viscosity is based on the invariants of the velocity gradient tensor [24]. This model recovers the proper y^3 near-wall scaling for turbulent eddy viscosity. Nicoud et al. [24] have calibrated the model coefficient in the range of $0.55 \leq C_w \leq 0.6$. However, this value is not universal and depends on the numerical method and Reynolds number. In the current case, the model

coefficient value is calibrated to be $C_w = 0.46$. In this benchmark, a fully turbulent flow is developed between two infinite parallel plates separated by a distance 2δ . A constant adverse pressure gradient is applied to the flow in the streamwise direction to drive the flow through the channel. The no-slip condition is set for the top and bottom walls. Periodic boundary conditions are applied in the streamwise and spanwise directions to approximate infinite homogeneous directions. The periodic domain sizes are selected so that the two-point correlations in the streamwise and spanwise directions would be essentially zero at maximum separation (half the domain size). A uniform grid is adopted in the periodic directions, whilst the grid is stretched in the direction normal to the wall in order to properly resolve the boundary layers. This grid-stretching is based on a hyperbolic tangent function:

$$y_j = -\frac{\tanh\left(\gamma\left(1 - \frac{2j}{N_y}\right)\right)}{\tanh\gamma} \quad j = 0, 1, \dots, N_y \quad (19)$$

where N_y is the number of grid points in the wall-normal direction, and γ is the stretching factor.

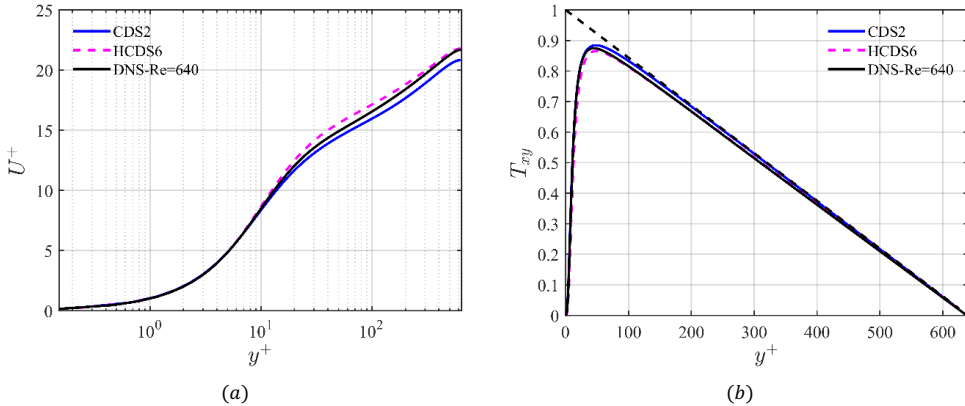
The computational domain size, grid resolution, and corresponding non-dimensional grid spacings in wall units are given in Table 5.

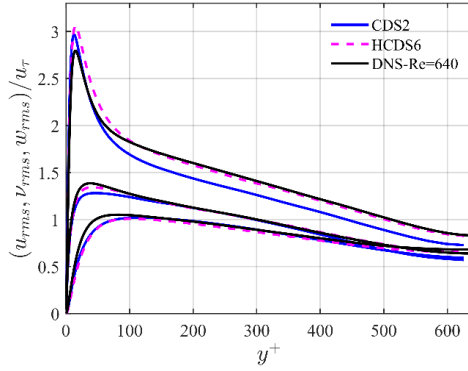
Table 5. Channel flow mesh resolution.

Re_τ	L_x	L_y	L_z	N_x	N_y	N_z	Δx^+	Δz^+	Δy^+	γ
640	$2\pi\delta$	2δ	$\pi\delta$	128	128	128	31.6	15.8	$\in [0.43 - 29.7]$	2.8

The computational domain is initialized with a random solenoidal velocity field. The bulk time scale ($t^* = L_x/U_b$) is equivalent to a flow-through time (FTT) of the domain, which corresponds to the time it takes for the fluid to traverse the entire computational domain at a constant mean bulk velocity (U_b). A small time step is selected to capture temporal scales precisely and keeps the Courant number below one, thereby guaranteeing numerical stability. Once the flow has reached a statistical steady state condition, the flow statistics are averaged in the streamwise and spanwise homogeneous directions over a time interval of $50\delta/u_\tau$ approximately equivalent to 175 FTT, thereby ensuring fully converged statistics.

The mean streamwise velocity profile (U^+), the total Reynolds shear stress (T_{xy}), and the square root of the second-order velocity moments normalized by the friction velocity are shown in Figure 7 as a function of the dimensionless distance to the wall (y^+). The HCDS6 solution is in excellent agreement with the reference DNS results of Abe et al. [59]. The mean total Reynolds shear stress using both central schemes compares relatively well with the DNS data shown in the top-right graph in Figure 7. Moreover, the predictions for the spanwise (w_{rms}) and wall-normal (v_{rms}) turbulence-intensity components overlap with the reference DNS [59]. However, the streamwise component (u_{rms}) exhibits a slight deviation for y^+ above 60 when CDS2 is employed. In conclusion, these predictions confirm the consistency of the explicit LES approach followed in the paper, where no artificial numerical dissipation competes with the dissipation of the SGS model.





(c)

Figure 7. Mean streamwise velocity normalized by the DNS shear velocity (a), non-dimensional mean total Reynolds shear stress (b), mean normalized square root of the second-order velocity moments (c) (u_{rms} (top), v_{rms} (middle), w_{rms} (bottom)) for the LES of turbulent channel flow at $Re_\tau = 640$.

4.5 LES of the contaminant breach in isolation rooms with a sliding door

In the final test case, the potential of the framework introduced in Section 2 and its implementation in the REEF3D solver for indoor airflow applications are investigated.

Containment failure due to the airflows induced by a door movement is a critical concern in environments requiring strict isolation measures, such as hospital isolation rooms. The door motion initiates complex airflow patterns that can lead to the escape of potentially contaminated air. This can be particularly vital in the presence of airborne pathogens, as it increases the risk of spreading infectious agents to adjacent spaces. Traditional hinged doors, commonly found in healthcare facilities, are known to exacerbate this issue. Sliding doors, on the other hand, have shown promise in mitigating containment failure by minimizing the airflows generated during operation. Understanding these airflow dynamics is necessary for designing effective containment strategies to ensure the safety of both patients and healthcare personnel. Although quantitative measurements such as tracer gas techniques offer valuable data on airflow leakage, they may provide limited insight into the detailed turbulent flow structures that are mainly developed within the doorway. Moreover, these experiments can be complex and costly in terms of instrumentation setup and data collection. Alternatively, the CFD modeling using the LES approach overcomes the challenges associated with experimental measurements. Detailed visualization of airflow patterns by eliminating the need for full-scale mock-ups and specialized instrumentation can be provided by CFD simulations. However, the accuracy and reliability of airflow predictions during sliding door operations depends on the chosen numerical method.

The flow induced by a sliding door has been investigated by Saarinen et al. [36] through laboratory experiments as well as LES using ANSYS CFX 15.0. They demonstrated that URANS was not able to predict this flow accurately. The same setup of their test cases is used here, and their solution is taken as a reference (both experimental and numerical). Two identical isothermal rooms (the isolation room and the anteroom) without ventilation are connected via a sliding door in the middle of a partition wall. The dimensions of each room are $3.0 \times 4.7 \times 4.0 \text{ m}^3$ ($H \times W \times D$), as shown in Figure 8. The smallest width and height of the doorway are 1.1 and 2.06 m, respectively, with a frame thickness of 0.1 m. The door is 1.22 m wide, 2.125 m high, and has a thickness of 0.055 m.

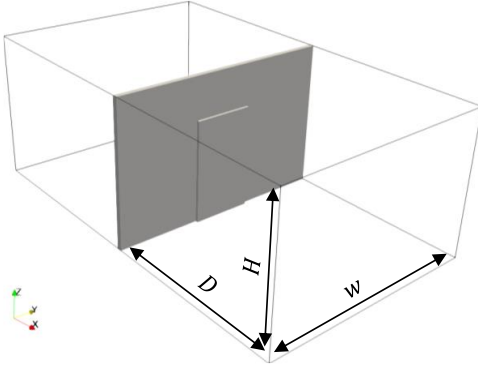


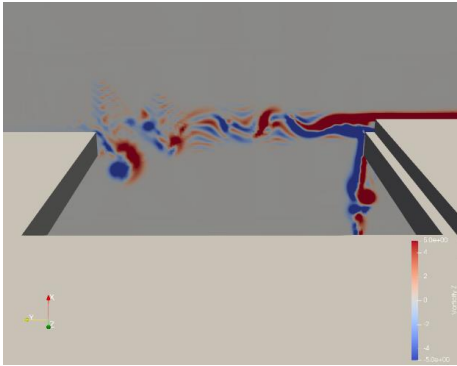
Figure 8. The geometry of the isolation room and anteroom connected via a sliding door.

The sequence of door operation involves two movement phases separated by a waiting period. First, the door slides open for a duration of three seconds, covering a distance of 1.2 m linearly towards the negative y direction. The door is held fully open for nine seconds. Finally, it starts closing and reaches the initial position at a constant velocity after five seconds. The simulation is continued for a period of ten seconds to monitor the gradual airflow dissipation. The total time for the experiment is thus 27 seconds.

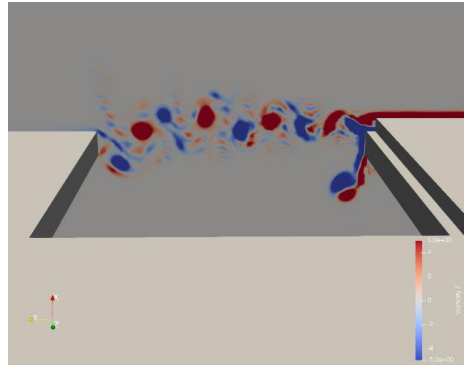
Similar to Saarinen et al. [36], the WALE SGS model is adopted in our simulation. To limit the mesh size, the computational grid is refined uniformly within a volume of $[x = 0.4\text{ m} \times y = 1.5\text{ m} \times z = 2.2\text{ m}]$ surrounding the doorway where the unsteady vortical structures are generated. A smooth transition is performed away from the refined zone up to the domain boundaries with a growth ratio of 1.15. To study grid independence, four different grid resolutions of $\Delta x = \Delta y = \Delta z = 0.0025, 0.005, 0.00625,$ and 0.01 m are adopted in the refined volume for the ultrafine, fine, intermediate, and coarse grid, respectively. A no-slip boundary condition is applied to the room walls, including the separating wall and sliding door. Zero velocity components are initialized everywhere within two rooms. Consequently, each room serves as a large reservoir, and the airflow patterns are solely driven by the door motion. A constant time step of 4 ms is chosen to resolve temporal variation while ensuring the numerical stability of the simulation by maintaining the CFL below one.

To visualize the unsteady shear flow generated by the sliding door, the vertical component of vorticity derived from the lateral gradients of velocity components $(\nabla \times \mathbf{u})_z$ is shown in Figure 9. The vorticity field is depicted when the door has fully opened and is extracted on a plane 1 m above the floor. The opening of the door generates a wake with flow instabilities. The LES performed by Saarinen et al. [36] using a fine grid is shown in Figure 9(h) and is in line with flow visualization during their experiments. REEF3D accurately reproduces all number of vortices generated within the doorway on both intermediate and fine mesh resolutions, particularly when the new spatial discretization scheme (HCDS6) is employed. It should be noted that a direct comparison of accuracy with the LES of Saarinen et al. [36] is not feasible, given their omission of information regarding mesh size near the door in their refined 15.6M nodes mesh. Nonetheless, the coarse mesh used in this study maintains an equivalent grid size of 0.01 m in proximity to the door, akin to the 10.7M nodes mesh employed by Saarinen et al. [36]. On the coarse mesh resolution, the limitations of the bounded second-order central difference scheme in ANSYS Fluent and the CDS2 in REEF3D are evident in their inability to accurately represent main flow structures. In contrast, the HCDS6 scheme demonstrates a better capability to capture the main features of these structures, despite the presence of significant aliasing errors visible in the form of waves. This is attributed to the coarse mesh used, particularly compared to the door width. Additionally, it is noteworthy that the HCDS6 scheme, without artificial numerical dissipation, contributes to the observed aliasing errors (visible in the form of small waves). With further mesh refinement to a cell size of 0.00625 m in the refined zone (intermediate mesh), the performance of the CDS2 scheme exhibits significant improvement. Compared to the coarse grid, it now demonstrates enhanced capability in capturing vortices within the doorway. Despite this improvement, some residual aliasing errors are still noticeable in the solution. Conversely, when employing the HCDS6 scheme on the intermediate mesh, aliasing errors are considerably reduced, resulting in a smoother visualization of the interaction of vortices. Although the solution of Saarinen et al. [36] reveals improved capture of vortices on a fine mesh (Figure 9(h)), the solution remains somewhat inaccurate. Some details are still smeared when compared with the HCDS6 solution (Figure 9(d)).

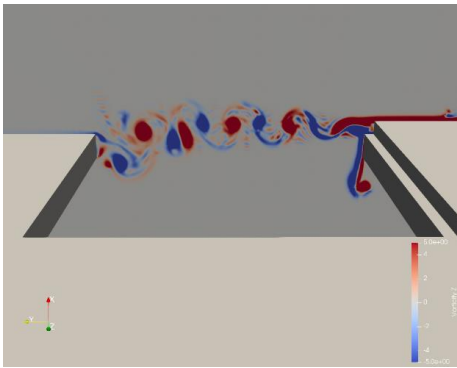
Even with further improvements in the CDS2 solution on our fine mesh, which are achieved by reducing aliasing errors and refining the vortical structure shape, it remains incapable of accurately reproducing the correct position of rotational structures.



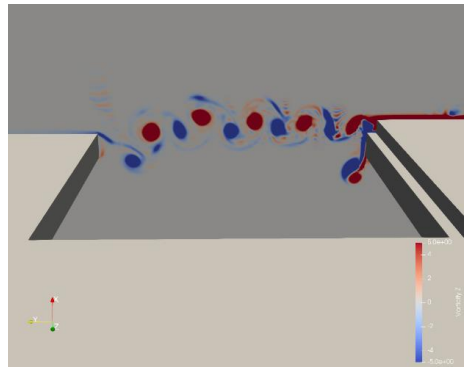
(a) CDS2 (coarse mesh)



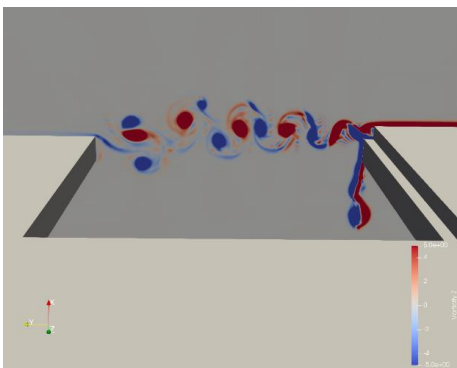
(b) HCDS6 (coarse mesh)



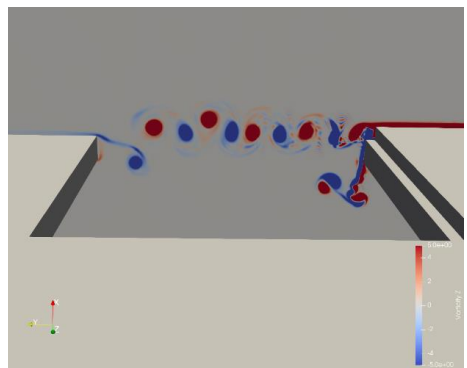
(c) CDS2 (intermediate mesh)



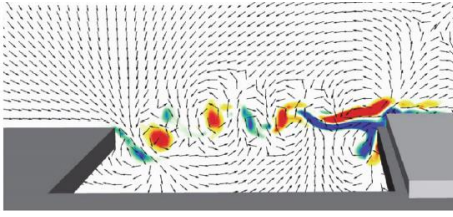
(d) HCDS6 (intermediate mesh)



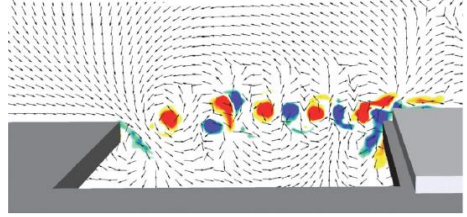
(e) CDS2 (fine mesh)



(f) HCDS6 (fine mesh)



(g) Saarinen et al. [36] (10.7M nodes)



(h) Saarinen et al. [36] (15.6M nodes)

Figure 9. Contours of the vertical component of vorticity $(\nabla \times \mathbf{u})_z$ at the end of door opening stage.

The flow dynamics induced by door motion in the proximity of the doorway can be visualized in detail using tracer gas. To compare with experiments, Saarinen et al. [36] modeled tracer gas as a passive scalar with a kinematic diffusivity of $1e-5 \text{ m}^2/\text{s}$ [60]. The turbulent Schmidt number (Sc) was set at a value of 0.9 to treat turbulent diffusive flux. The volume of air passing through the doorway from the isolation room to the anteroom as a function of time during the door cycle can be calculated using a gaseous contaminant dosed in the isolation room:

$$\Delta V(t)_{\text{isolation room} \rightarrow \text{anteroom}} = \frac{\Delta m(t)}{C_{\text{isolation room}}(t_0)} \quad (20)$$

The migrated mass of the gaseous contaminant (Δm) is obtained by integrating the tracer mass concentration (C) over the volume of anteroom:

$$\Delta m(t)_{\text{isolation room} \rightarrow \text{anteroom}} = \iiint_V^{\text{anteroom}} C(x, y, z, t) dV \quad (21)$$

Time evolution of air volume migration (AVM) quantifies how rapidly the air volume in the isolation room is escaping to the anteroom at different phases of the door cycle. The amount of air volume migrated from the isolation room to the anteroom over time is plotted in Figure 10 for the different grid sizes.

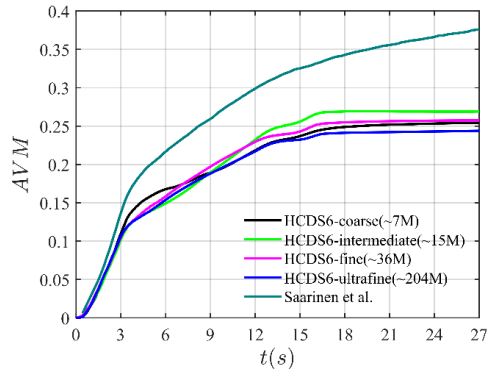
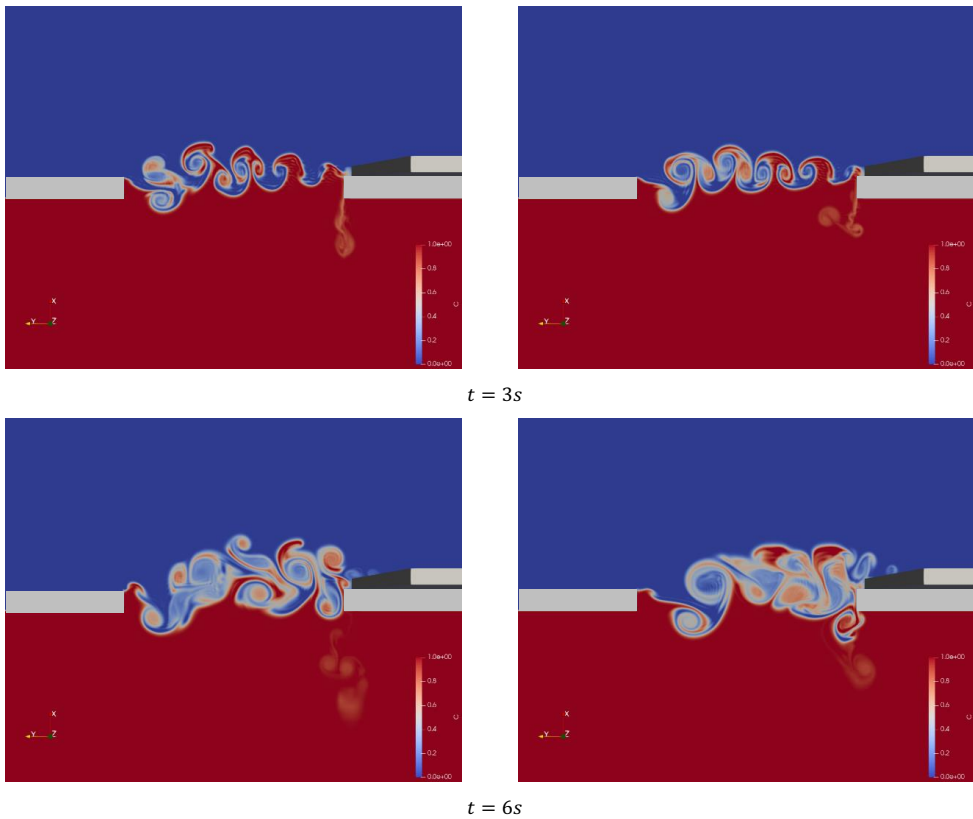


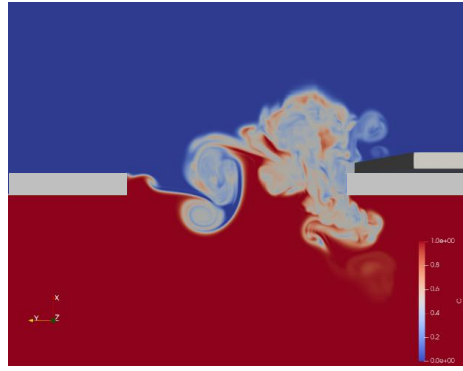
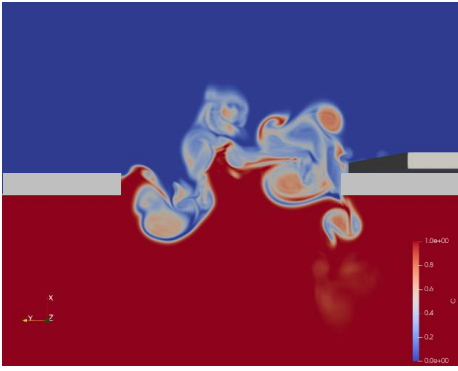
Figure 10. Time evolution of the air volume migrated during the sliding door operation cycle.

The flow instabilities near the doorway trigger the migration flow rate in the initial stage of the door opening. The intense volume of air passing through the doorway from the isolation room to the anteroom at the beginning can also be attributed to the piston effect induced by the moving door sliding within the anteroom. Consequently, the AVM increases quickly from 0 to 3 seconds when the door opens. The solution for the HCDS6 is identical during this opening phase for the four meshes. During the waiting period, when the sliding door is held open, a gradual increase in the migrated air volume is predicted due to the diffusion of turbulent vortices induced by the opening door motion. Consequently, the AVM continues to increase for the 9 seconds during which the door is held open (until $t = 12s$). The rate of AVM increase gradually diminishes over the subsequent 5 seconds as the door begins to close (until $t = 17s$). Once the door is fully closed, the AVM remains constant. It is worth noting that the AVM evaluated by Saarinen et al. [36] is very similar during the opening phase. However, after this phase, their predicted value is significantly higher than in our simulations.

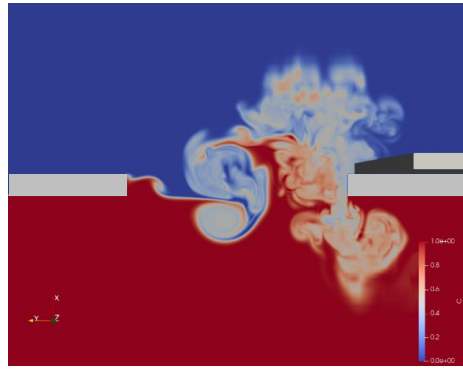
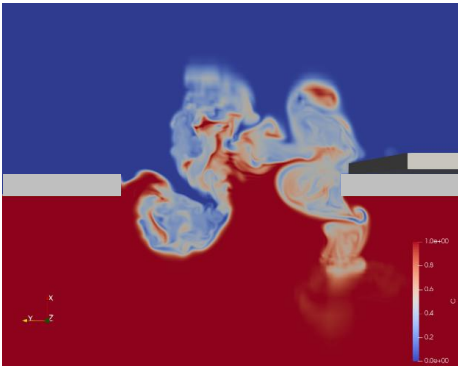
Surprisingly, their AVM keeps increasing when the door is closed after $t = 17s$ while it should remain constant as predicted by the present LES. It questions the conservation properties of scalar quantities in their numerical method including IBM.

In order to visualize the transient structures arising from the dynamic operation of the sliding door, Figure 11 presents contours of passive scalar concentration on a plane situated 1 m above the floor. These contours depict specific time intervals – namely, immediately after the door has fully opened ($t = 3s$), during the initial stages of closure ($t = 12s$), and after the door has completely closed ($t = 17s$). It is evident that the precision of the spatial discretization scheme to treat the convective term plays a key role in achieving an accurate solution. The HCDS6 scheme exhibits superior resolution of flow structures, leading to notable distinctions in flow patterns when compared to the CDS2 scheme over an extended duration. This highlights the advantage of employing an orthogonal grid, enabling the derivation of numerical schemes with enhanced accuracy, which is particularly beneficial for modeling transitional airflows within building environments.

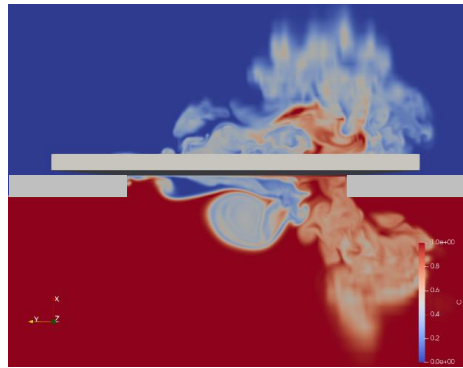
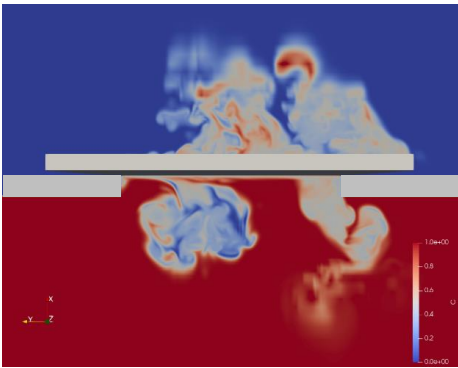




$t = 9s$



$t = 12s$



$t = 17s$

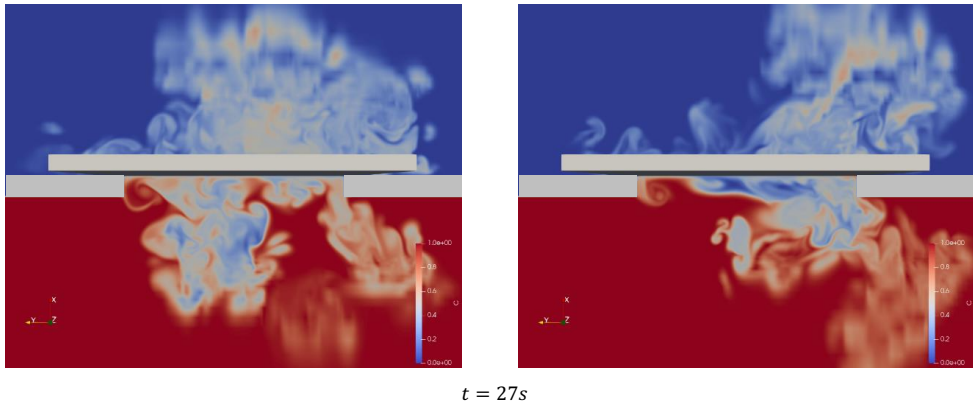


Figure 11. Contours of the passive scalar concentration at six different door opening stages using CDS2 (left) and HCDS6 (right).

5 Discussion

It is important to emphasize again that the proposed method targets indoor airflows. As recommended by Blocken [11], indoor and outdoor airflows should be clearly distinguished. The precision of capturing boundary layers becomes more crucial for outdoor airflows, which makes body conformal grids potentially more appropriate in such scenarios. The objective of this paper is not to assert the superiority of the current approach over widely-used general-purpose flow solvers such as ANSYS Fluent or OpenFOAM across all indoor airflow applications. These tools should be considered as alternatives, each with its own merits and limitations. Nevertheless, the article clearly highlights the benefits of the proposed framework, particularly in the context of high-resolution LES, transitional flows, and scenarios involving moving objects.

An essential consideration is computational time, which is an aspect that is not explicitly addressed and is not compared with general-purpose solvers in this article. The focus remains on showcasing that the proposed approach achieves comparable accuracy with fewer grid points than conventional flow solvers. The intricate nature of comparing computational times across different flow solvers necessitates dedicated benchmarks that offer a comprehensive description of simulation setups and parameters – an undertaking that is reserved for future endeavors.

Several paths can be followed for future research. While the five presented test cases serve to showcase the applicability of the framework within REEF3D for indoor airflow scenarios, additional test cases could provide deeper insights into its capabilities. Exploring scenarios involving thermal plumes, for instance, should be investigated, given their key role in indoor airflow dynamics [61]. One test case of a human thermal plume has been successfully validated by Choi et al. [34], using structured grids and IBM. Additionally, the resolution of the mesh was limited along the walls to maintain the feasibility of explicit time integration, thereby avoiding the need for semi-implicit methods. Future research should explore and assess the implementation of fully implicit time integration. In scenarios featuring airflow inlets, considerations for mesh refinement near these inlets, where the velocity magnitude is high, may be necessary. This is particularly relevant in cases such as a cavity flow with a slot inlet, where severe time step conditions must be observed based on the CFL criterion [62]. By employing an orthogonal mesh refined in the wall-normal direction, the high-velocity air entering through the slot will cross well-refined cells, thereby posing challenges to the time step due to the strict CFL condition. Adopting fully implicit time integration becomes a viable solution to release this constraint. Moreover, this study did not investigate cases with wall functions to assess the performance of wall-modeled LES. Future research should incorporate wall functions and analyze their impact on the simulation results. Finally, the sliding door case shows that aliasing errors may occur in highly under-resolved simulations with a pure central scheme (which is expected). In future work, the scheme could be complemented by a controlled amount of artificial numerical dissipation to address this phenomenon. As the numerical stencil has seven points in each spatial direction, it is indeed possible to tailor a high-order dissipation term (sometimes called hyperdiffusion term) that will only be active on the smallest resolved scales of the mesh, in line with the concept of explicit LES [63]. An example of such a hyper-dissipative term is the fifth-order scheme with a

sixth-order spatial derivative of velocity in the flow solver PENCIL [64]. Such a hyperdiffusion term cannot be easily implemented in a general-purpose flow solver.

To conclude this section, information regarding the simulation platform and hardware is given. The current simulations were performed on the FRAM cluster provided by UNINETT Sigma2, which is the National Infrastructure for High-Performance Computing and Data Storage in Norway. It is a distributed memory system that consists of 1,004 dual-socket and two quad-socket nodes, interconnected with a high-bandwidth, low-latency Infiniband network. The interconnect network is organized in an island topology, with 9,216 cores in each island. Each standard compute node has two 16-core Intel Broadwell chips (2.1 GHz) and 64 GB memory. In addition, eight larger memory nodes with 512 GB RAM are available, catering to computational tasks that demand substantial memory resources for more complex simulations and data-intensive processing. The total number of compute cores is 32,256.

6 Conclusions

The main objective of the paper was to discuss the use of solvers that are optimized for orthogonal non-conformal grids combined with the immersed boundary method (IBM) to perform high-resolution explicit LES for indoor airflows. This framework was then implemented by adapting an existing incompressible flow solver called REEF3D, which had initially been developed for hydrodynamics applications. It was shown that orthogonal grids enable the implementation of more accurate spatial discretization that outperforms the traditional second-order central scheme. This enabled the capturing of transitional flows using coarser meshes. Results showed that the immersed boundary method can capture the detached flow around an object with a smooth slope (i.e., a sphere) or sharp edges (i.e., a wall-mounted cube). The wall-resolved channel flow test case demonstrated that the numerical method was able to properly perform explicit LES. Finally, the sliding door test case demonstrated that IBM could simulate moving objects elegantly without resorting to complex re-meshing techniques. The superiority of high-accurate spatial discretization over standard second-order schemes on a same mesh is clearly shown. In further work, wall functions should be implemented to be able to address applications at higher Reynolds numbers, and the influence of these functions on the solution should be investigated.

Acknowledgments

The authors would like to acknowledge Iman Bayat for his assistance with language and proofreading during the research process.

This research did not receive any specific grant from funding agencies in the public, commercial, or not-for-profit sectors.

References

1. Tan, H., et al., *Current and potential approaches on assessing airflow and particle dispersion in healthcare facilities: a systematic review*. Environmental Science and Pollution Research, 2022. **29**(53): p. 80137-80160.
2. Löhner, R., et al., *High-fidelity simulation of pathogen propagation, transmission and mitigation in the built environment*. Archives of Computational Methods in Engineering, 2021. **28**: p. 4237-4262.
3. Lin, Y., et al., *A systematic review on COVID-19 related research in HVAC system and indoor environment*. Energy and Built Environment, 2023.
4. Chen, Q., *Ventilation performance prediction for buildings: a method overview and recent applications*. Building and Environment, 2009. **44**: p. 848-858.
5. Wang, L. and Q. Chen, *Evaluation of some assumptions used in multizone airflow network models*. Building and Environment, 2008. **43**(10): p. 1671-1677.
6. Megri, A.C. and F. Haghighat, *Zonal Modeling for Simulating Indoor Environment of Buildings: Review, Recent Developments, and Applications*. HVAC&R research, 2007. **13**(6): p. 887-905.
7. Teshome, E.J. and F. Haghighat, *Zonal Models for Indoor Air Flow: A Critical Review*. International Journal of Ventilation, 2004. **3**(2): p. 119-129.
8. Zuo, W. and Q. Chen, *Fast and informative flow simulations in a building by using fast fluid dynamics model on graphics processing unit*. Building and Environment, 2010. **45**(3): p. 747-757.

9. Zhai, Z.J., et al., *Evaluation of Various Turbulence Models in Predicting Airflow and Turbulence in Enclosed Environment by CFD: Part 1, Summary of Prevalent Turbulence Models*. HVAC&R Research, 2007. **13**(6): p. 853-870.
10. van Hooff, T., B. Blocken, and G.J.F. van Heijst, *On the suitability of steady RANS CFD for forced mixing ventilation at transitional slot Reynolds numbers*. Indoor Air, 2013. **23**: p. 236-249.
11. Blocken, B., *LES over RANS in building simulation for outdoor and indoor applications: A foregone conclusion?* Building Simulation, 2018. **11**(5): p. 821-870.
12. Pham, M.V., F. Plourde, and K.S. Doan, *Direct and large-eddy simulations of a pure thermal plume*. Physics of Fluids, 2007. **19**.
13. Wang, M. and Q. Chen, *Assessment of Various Turbulence Models for Transitional Flows in an Enclosed Environment (RP-1271)*. HVAC&R Research, 2009. **15**(6): p. 1099-1119.
14. D. N. Sørensen, P.V.N., *Quality control of computational fluid dynamics in indoor environments*. Indoor Air, 2004. **13**(1): p. 2-17.
15. Zhang, Z., et al., *Evaluation of Various Turbulence Models in Predicting Airflow and Turbulence in Enclosed Environment by CFD: Part 2, Comparison with Experimental Data from Literature*. HVAC&R Research, 2007. **13**(6): p. 871-886.
16. van Hooff, T., B. Blocken, and Y. Tominaga, *On the accuracy of CFD simulations of cross-ventilation flows for a generic isolated building: Comparison of RANS, LES and experiments*. Building and Environment, 2017. **114**: p. 148-165.
17. Verstappen, R.W.C.P. and A.E.P. Veldman, *Symmetry-preserving discretization of turbulent flow*. Journal of Computational Physics, 2003. **187**: p. 343-368.
18. Mahfoze, O.A. and S. Laizet, *Non-explicit large eddy simulations of turbulent channel flows from $Ret=180$ up to $Ret=5,200$* . Computers & Fluids, 2021. **228**: p. 105019.
19. Mittal, R. and G. Iaccarino, *Immersed Boundary Methods*. Annual Review of Fluid Mechanics, 2005. **37**(1): p. 239-261.
20. Bae, H.J., et al., *Dynamic slip wall model for large-eddy simulation*. Journal of fluid mechanics, 2019. **859**: p. 400-432.
21. Kawai, S. and J. Larsson, *Wall-modeling in large eddy simulation: Length scales, grid resolution, and accuracy*. Physics of fluids, 2012. **24**(1).
22. Lozano-Durán, A., et al., *Non-equilibrium three-dimensional boundary layers at moderate Reynolds numbers*. Journal of Fluid Mechanics, 2020. **883**: p. A20.
23. Chen, B., et al., *A new wall function for indoor airflow with buoyancy effect*. Building and Environment, 2021. **202**: p. 108029.
24. Nicoud, F. and F. Ducros, *Subgrid-scale stress modelling based on the square of the velocity gradient tensor*. Flow, turbulence and Combustion, 1999. **62**(3): p. 183-200.
25. Germano, M., et al., *A dynamic subgrid-scale eddy viscosity model*. Physics of Fluids A: Fluid Dynamics, 1991. **3**(7): p. 1760-1765.
26. Bricteux, L., M. Duponcheel, and G. Winckelmans, *A multiscale subgrid model for both free vortex flows and wall-bounded flows*. Physics of Fluids, 2009. **21**.
27. Jeanmart, H. and G. Winckelmans, *Investigation of eddy-viscosity models modified using discrete filters: A simplified “regularized variational multiscale model” and an “enhanced field model”*. Physics of Fluids, 2007. **19**(5): p. 055110.
28. Joel H. Ferziger, M.P., Robert L. Street, *Computational Methods for Fluid Dynamics*. 4 ed. 2020: Springer Cham.
29. Komen, E.M.J., et al., *Analysis of the numerical dissipation rate of different Runge–Kutta and velocity interpolation methods in an unstructured collocated finite volume method in OpenFOAM®*. Computer Physics Communications, 2020. **253**: p. 107145.
30. Vasilyev, O.V., *High Order Finite Difference Schemes on Non-uniform Meshes with Good Conservation Properties*. Journal of Computational Physics, 2000. **157**(2): p. 746-761.
31. Kempe, T. and A. Hantsch, *Large-eddy simulation of indoor air flow using an efficient finite-volume method*. Building and Environment, 2017. **115**: p. 291-305.
32. Morozova, N., et al., *On the feasibility of affordable high-fidelity CFD simulations for indoor environment design and control*. Building and Environment, 2020. **184**: p. 107144.
33. Mao, S. and I.B. Celik, *Modeling of indoor airflow and dispersion of aerosols using immersed boundary and random flow generation methods*. Computers & Fluids, 2010. **39**(8): p. 1275-1283.

34. Choi, J.-I. and J.R. Edwards, *Large-eddy simulation of human-induced contaminant transport in room compartments*. *Indoor Air*, 2012. **22**: p. 77-87.
35. Choi, J.-I. and J.R. Edwards, *Large eddy simulation and zonal modeling of human-induced contaminant transport*. *Indoor Air*, 2008. **18**: p. 233-249.
36. Saarinen, P., et al. *Large-eddy simulation of the containment failure in isolation rooms with a sliding door—An experimental and modelling study*. in *Building Simulation*. 2018. Springer.
37. Bihs, H. *REEF3D : Open-Source Hydrodynamics*. Available from: <https://reef3d.wordpress.com/>.
38. Kim, J. and P. Moin, *Application of a fractional-step method to incompressible Navier-Stokes equations*. *Journal of Computational Physics*, 1985. **59**(2): p. 308-323.
39. Falgout, R.D. and U.M. Yang. *hypre: A Library of High Performance Preconditioners*. in *Computational Science — ICCS 2002*. 2002. Berlin, Heidelberg: Springer Berlin Heidelberg.
40. Berthelsen, P.A. and O.M. Faltinsen, *A local directional ghost cell approach for incompressible viscous flow problems with irregular boundaries*. *Journal of Computational Physics*, 2008. **227**(9): p. 4354-4397.
41. Yang, L., *One-fluid formulation for fluid–structure interaction with free surface*. *Computer Methods in Applied Mechanics and Engineering*, 2018. **332**: p. 102-135.
42. Bihs, H., et al., *A new level set numerical wave tank with improved density interpolation for complex wave hydrodynamics*. *Computers & Fluids*, 2016. **140**: p. 191-208.
43. Kálnay de Rivas, E., *On the use of nonuniform grids in finite-difference equations*. *Journal of Computational Physics*, 1972. **10**(2): p. 202-210.
44. Morinishi, Y., et al., *Fully Conservative Higher Order Finite Difference Schemes for Incompressible Flow*. *Journal of Computational Physics*, 1998. **143**: p. 90-124.
45. Larkermanni, E., et al., *Development of an accurate central finite-difference scheme with a compact stencil for the simulation of unsteady incompressible flows on staggered orthogonal grids*. *Computer Methods in Applied Mechanics and Engineering*, 2024. **428**: p. 117117.
46. Le, H. and P. Moin, *An improvement of fractional step methods for the incompressible Navier-Stokes equations*. *Journal of computational physics*, 1991. **92**(2): p. 369-379.
47. Van der Vorst, H.A., *Bi-CGSTAB: A fast and smoothly converging variant of Bi-CG for the solution of nonsymmetric linear systems*. *SIAM Journal on scientific and Statistical Computing*, 1992. **13**(2): p. 631-644.
48. Falgout, R.D., J.E. Jones, and U.M. Yang, *Conceptual interfaces in hypre*. *Future Generation Computer Systems*, 2006. **22**(1-2): p. 239-251.
49. Bricteux, L., S. Zeoli, and N. Bourgeois, *Validation and scalability of an open source parallel flow solver*. *Concurrency and Computation: Practice and Experience*, 2017. **29**(21): p. e4330.
50. Hartmann, R., *Taylor-Green Vortex*, in *TILDA: Towards Industrial LES/DNS in Aeronautics: Paving the Way for Future Accurate CFD - Results of the H2020 Research Project TILDA, Funded by the European Union, 2015 -2018*, C. Hirsch, et al., Editors. 2021, Springer International Publishing: Cham. p. 373-382.
51. C. Carton de Wiart, K.H., M. Duponcheel, G. Winckelmans, *Assessment of a discontinuous Galerkin method for the simulation of vortical flows at high Reynolds number*. *Numerical Methods in Fluids*, 2013. **74**(7).
52. L. Bricteux, S.Z., N. Bourgeois, *Validation and scalability of an open source parallel flow solver*. *Concurrency and Computation: Practice and Experience*. **29**(21).
53. Lin, Q., et al., *Large eddy simulations of strong wind mechanisms at pedestrian level around square-section buildings with same aspect ratios and different sizes*. *Building and Environment*, 2023. **243**: p. 110680.
54. Khaled, M.F. and A.M. Aly, *Assessing aerodynamic loads on low-rise buildings considering Reynolds number and turbulence effects: a review*. *Advances in Aerodynamics*, 2022. **4**(1): p. 24.
55. Diaz-Daniel, C., S. Laizet, and J.C. Vassilicos, *Direct numerical simulations of a wall-attached cube immersed in laminar and turbulent boundary layers*. *International Journal of Heat and Fluid Flow*, 2017. **68**: p. 269-280.
56. Ploumhans, P., et al., *Vortex methods for direct numerical simulation of three-dimensional bluff body flows: application to the sphere at $Re= 300, 500, \text{ and } 1000$* . *Journal of Computational Physics*, 2002. **178**(2): p. 427-463.
57. Johnson, T. and V. Patel, *Flow past a sphere up to a Reynolds number of 300*. *Journal of Fluid Mechanics*, 1999. **378**: p. 19-70.

58. Choi, J.-I., et al., *An immersed boundary method for complex incompressible flows*. Journal of Computational Physics, 2007. **224**(2): p. 757-784.
59. Abe, H., R.A. Antonia, and H. Kawamura, *Correlation between small-scale velocity and scalar fluctuations in a turbulent channel flow*. Journal of Fluid Mechanics, 2009. **627**: p. 1-32.
60. Zhuang, R.N., X. Li, and J. Tu, *Should different gaseous contaminants be treated differently in CFD indoor simulations?* WIT Transactions on Ecology and the Environment, 2014. **183**: p. 353-362.
61. Sun, S., J. Li, and J. Han, *How human thermal plume influences near-human transport of respiratory droplets and airborne particles: a review*. Environmental Chemistry Letters, 2021. **19**(3): p. 1971-1982.
62. Nielsen, P.V., A. Restivo, and J.H. Whitelaw, *The Velocity Characteristics of Ventilated Rooms*. Journal of Fluids Engineering, 1978. **100**(3): p. 291-298.
63. Kritsuk, A.G., et al., *High order nonlinear filter methods for subsonic turbulence simulation with stochastic forcing*. Journal of Computational Physics, 2021. **431**: p. 110118.
64. Haugen, N.E.L. and A. Brandenburg, *Inertial range scaling in numerical turbulence with hyperviscosity*. Physical Review E, 2004. **70**(2): p. 026405.

A.4 Paper IV

Analysis of the interfacial mixing in the gravity-driven counterflow through a large vertical opening using Large Eddy Simulation

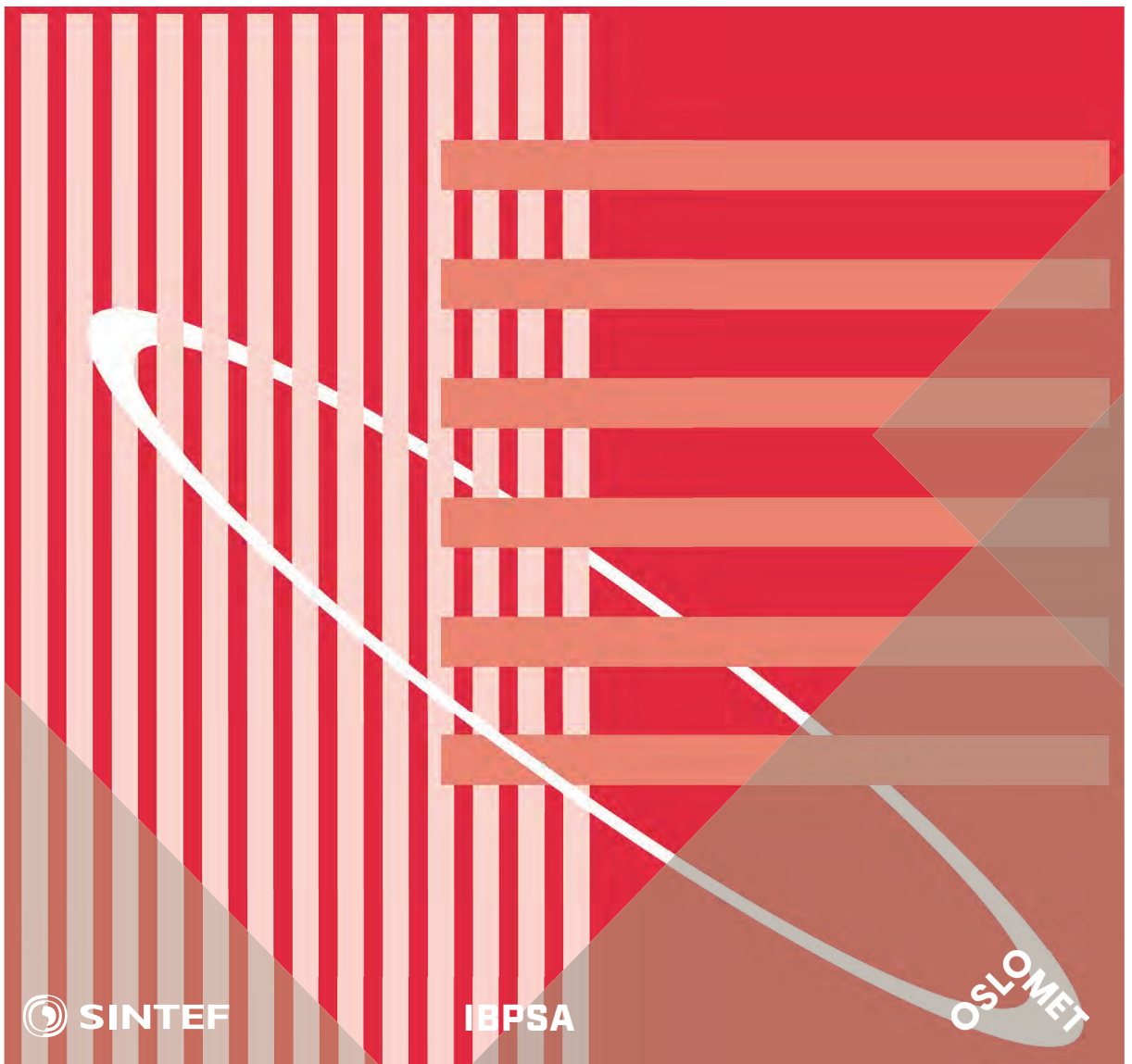
Elyas Larkermani, Laurent Georges

International Conference Organised by IBPSA-Nordic, 13th–14th October 2020, OsloMet. BuildSIM-Nordic 2020. Selected papers. SINTEF Academic Press. 2020.

International Conference Organised by
IBPSA-Nordic, 13th–14th October 2020,
OsloMet

BuildSIM-Nordic 2020

Selected papers



SINTEF Proceedings

Editors:

Laurent Georges, Matthias Haase, Vojislav Novakovic and Peter G. Schild

BuildSIM-Nordic 2020

Selected papers

International Conference Organised by IBPSA-Nordic,
13th–14th October 2020, OsloMet

SINTEF Academic Press

SINTEF Proceedings no 5

Editors:

Laurent Georges, Matthias Haase, Vojislav Novakovic and Peter G. Schild

BuildSIM-Nordic 2020

Selected papers

International Conference Organised by IBPSA-Nordic,

13th–14th October 2020, OsloMet

Keywords:

Building acoustics, Building Information Modelling (BIM), Building physics, CFD and air flow, Commissioning and control, Daylighting and lighting, Developments in simulation, Education in building performance simulation, Energy storage, Heating, Ventilation and Air Conditioning (HVAC), Human behavior in simulation, Indoor Environmental Quality (IEQ), New software developments, Optimization, Simulation at urban scale, Simulation to support regulations, Simulation vs reality, Solar energy systems, Validation, calibration and uncertainty, Weather data & Climate adaptation, Fenestration (windows & shading), Zero Energy Buildings (ZEB), Emissions and Life Cycle Analysis

Cover illustration: IBPSA-logo

ISSN 2387-4295 (online)

ISBN 978-82-536-1679-7 (pdf)



© The authors

Published by SINTEF Academic Press 2020

This is an open access publication under the CC BY-NC-ND license

(<http://creativecommons.org/licenses/by-nc-nd/4.0/>).

SINTEF Academic Press

Address: Børrestuveien 3

PO Box 124 Blindern

N-0314 OSLO

Tel: +47 40 00 51 00

www.sintef.no/community

www.sintefbok.no

SINTEF Proceedings

SINTEF Proceedings is a serial publication for peer-reviewed conference proceedings on a variety of scientific topics.

The processes of peer-reviewing of papers published in SINTEF Proceedings are administered by the conference organizers and proceedings editors. Detailed procedures will vary according to custom and practice in each scientific community.

Analysis of the interfacial mixing in the gravity-driven counterflow through a large vertical opening using Large Eddy Simulation

Elyas Larkermani^{1*}, Laurent Georges¹

¹ Department of Energy and Process Engineering, Norwegian University of Science and Technology, NTNU, Trondheim, Norway

* corresponding author: elyas.larkermani@ntnu.no

Abstract

The study of natural convection flows in multizone enclosures is a topic of great importance due to its direct influence on room air circulation patterns, distribution of indoor air contaminants, and thermal comfort inside buildings. In this research, ANSYS Fluent is used to investigate the density-driven bidirectional flow through a large vertical opening connecting two isothermal reservoirs, the so-called bulk flow regime. Many research works on the natural convection flow through a large vertical opening between two enclosures have been done. However, they paid less attention to the unsteady flow structures generated by the sophisticated bidirectional flow, especially in the middle of the doorway. Large Eddy Simulation (LES) results show the development of unsteady flow structures in the middle of the doorway, a phenomenon called “interfacial mixing”. This phenomenon has been hardly documented in the literature, only using experiments. Even though unsteady flow structures develop, they do not significantly affect bulk quantities such as the discharge coefficient (C_d).

Introduction

The behavior of natural convection in confined spaces has attracted a lot of attention originating from its application in buildings air conditioning, contaminant spread and electronic equipment cooling. The vast majority of these spaces include internal partitions that the flow can traverse partially. In most situations, the presence of internal partitions with an opening lead to an intrinsically three-dimensional and transient flow field. The characteristics of such complicated flow are of strong interest to many communities and researchers. Several parameters can have an important role in driving this flow such as temperature differences, door motion, occupant motion or wind dynamic pressure. In past investigations, Computational Fluid Dynamics (CFD) simulations of the natural convection flow through a large vertical opening between two enclosures have been performed, but mostly using RANS, and/or two-dimensional assumption, and/or what can be considered today as very coarse grids. This made the unsteady flow structures impossible to be captured by these CFD simulations. From the experimental side, several past studies reported on the flows in differently heated enclosures separated by a partition wall. While these studies analyzed the flow

inside these enclosures, the flow within the doorway itself was measured for a limited number of locations. However, the CFD standards of today enable to better investigate the unsteady nature of the bidirectional flow inside large vertical openings.

Two separate mechanisms for natural convection flow between a hot and a cold zone were investigated in the experimental study of Scott et al. [1]: the *boundary layer* regime and the *bulk density-driven* regime. The transition between both regimes was established as a function of the aperture size located in the middle of the partition wall. In another similar work, the effect of internal partitions on the convective heat transfer across an enclosure was described by Neymark et al. [2]. They developed a Nusselt-Rayleigh correlation using the aperture width and a resistance model. Georges et al. [3] conducted RANS simulations using the RNG $k - \epsilon$ model and ANSYS Fluent for two rooms with an open door in the partition wall. They proved that the thermal radiation could affect the transition between the two aforementioned regimes and opposed to previous reports claiming that the aperture size was the main driving parameter causing such transition.

Favarolo and Manz [4] employed the LVEL $k - \epsilon$ turbulence model [5] in the FLOVENT commercial CFD software to analyze the influence of different parameters such as temperature difference between indoor and outdoor air on the airflow rate through a large open window. The vertical position and the horizontal distance of the opening from the wall were diagnosed to have the greatest and minor impact on the discharge coefficient (C_d), respectively. Based on their literature review, the value of C_d varies between 0.3 and 0.8, and the origin of these large variations is not clear to the authors. Allard and Utsumi [6] mentioned that this phenomenological coefficient takes into consideration the contraction of the flow while it passes through the opening. They concluded that the definition of C_d is still ambiguous and requires more precision. Pelletret et al. [7] investigate various approaches to determine the C_d as a function of opening height or temperature difference. They also show the difficulty in determining the C_d and point out that a variety of definitions for this coefficient has been introduced in the literature. Hence, despite the significant amount of numerical and experimental studies conducted to date, no clear conclusion can be drawn from previous studies.

The standard model to evaluate the airflow in a doorway, extensively used in building performance simulation (BPS), assumes two isothermal reservoirs and a one-dimensional inviscid steady-state flow. Both assumptions lead to a simple model based on the Bernoulli equation which is defined here as the theoretical model [8]. The resulting theoretical flow is then corrected using the C_d to match the actual airflow in the doorway. Uncertainties related to this modeling framework remain unknown. In particular, the effect of the unsteady flow regime on the value of the discharge coefficient needs to be elucidated.

When both reservoirs are isothermal and the room air temperature is in thermal equilibrium with the wall temperature surrounding it, the airflow in the doorway is in the bulk flow regime. The air temperature difference (ΔT) between both zones and the aperture geometry are the only physical parameters needed to define the flow. The temperature difference between the two zones leads to different bulk air densities and, consequently, different hydrostatic pressure fields. Due to the conservation of mass, both hydrostatic pressure fields are equal at the neutral plane (NP) located near the middle of the doorway. The difference of hydrostatic pressure above and below the NP generates a counterflowing stream of warm and cold air. A schematic of the velocity profile of this bidirectional flow in the vertical centerline of the doorway is shown in Fig. 1. Assuming an inviscid flow, the velocity profile shows a sharp gradient at the level of the NP (i.e. dashed lines in Fig. 1). With a viscous flow, three related phenomena can occur. Firstly, the two airstreams going in opposite directions create a shear layer. Secondly, Wilson and Kiel [9] reported some interfacial mixing due to re-entrainment effects. According to these authors, the resulting velocity and temperature profiles show a smoother transition at the level of the neutral plane (i.e. solid line in Fig. 1). Thirdly, a similar study by Lefauve et al. [10] using two reservoirs connected by a long channel demonstrated that a sustained stratified shear flow could generate large unsteady flow structures. Consequently, the mass and heat flows exchanged through the doorway will be reduced compared to the inviscid flow (i.e., the assumption used in the standard model).

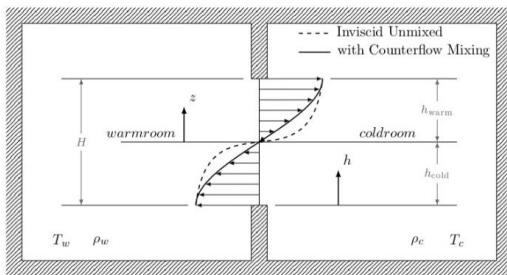


Figure 1: Inviscid and actual profiles of the streamwise velocity for the bidirectional flow in a doorway.

The present work investigates viscous effects and the resulting unsteady flow in the middle of the doorway

using Large Eddy Simulation (LES). Two large reservoirs are created by connecting two large isothermal volumes of equal size by a vertical solid partition. The single rectangular aperture located in the middle of the vertical partition enables the air to flow between the two zones. The primary objective of the present study is the interfacial mixing, meaning to characterize the mixing process (i.e. shear, re-entrainment and unsteady flow structures) and its influence on the volume airflow rate and heat transfer across the opening.

Numerical Method

Multizone enclosure description

The bidirectional airflow is generated at the aperture of height $h = 2m$ and width $w = 1m$. Each zone has the same length $L_0 = 16m$ in all spatial directions and is filled with air with constant thermodynamic properties. Figure 2 illustrates the geometry of the three-dimensional multizone enclosure.

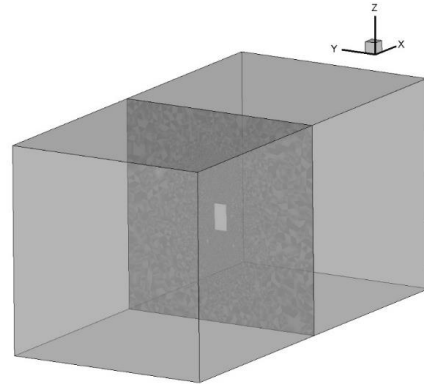


Figure 2: Three-dimensional multizone enclosure configuration.

Governing equations

After applying an implicit filtering operator and considering the Boussinesq approximation, the filtered incompressible Navier-Stokes equations can be expressed as:

$$\frac{\partial \bar{u}_i}{\partial x_i} = 0 \quad 1)$$

$$\frac{\partial \bar{u}_i}{\partial t} + \frac{\partial \bar{u}_i \bar{u}_j}{\partial x_j} = -\frac{1}{\rho} \frac{\partial \bar{p}}{\partial x_i} + \frac{\partial}{\partial x_j} [2\nu \bar{S}_{ij}] - \frac{\partial \tau_{ij}}{\partial x_j} - g_i [1 - \beta(\bar{T} - T_0)] \quad 2)$$

$$\frac{\partial \bar{T}}{\partial t} + \frac{\partial \bar{u}_j \bar{T}}{\partial x_j} = \frac{\partial}{\partial x_j} \left[\alpha \frac{\partial \bar{T}}{\partial x_j} \right] - \frac{\partial \tau_{jT}}{\partial x_j} \quad 3)$$

Where the $\bar{\Delta} = \sqrt[3]{\Delta x \Delta y \Delta z}$ was chosen as the effective filter width. x_i denotes the i^{th} coordinate direction. \bar{u}_i represents the filtered velocity field in the x_i direction, t the time, \bar{p} the modified filtered pressure, and \bar{T} the filtered temperature. The last term in Equation (2) is the buoyancy term where β is thermal expansion of the fluid and g_i the gravitational acceleration. The parameters ν , α

indicate the kinematic viscosity and thermal diffusivity, respectively. The subgrid scale (SGS) stress tensor and the scalar SGS thermal flux vector is included, respectively, in the momentum and energy equations above via the unresolved terms $\tau_{ij} = \overline{u_i u_j} - \overline{u_i} \overline{u_j}$ and $\tau_{jT} = \overline{u_j T} - \overline{u_j} \overline{T}$.

Modeling of unresolved turbulent scales

The closure of the Navier–Stokes equations can be achieved by utilizing the Wall-Adapting Local Eddy-viscosity (WALE) turbulence model for calculating the SGS kinematic viscosity, ν_{SGS} , based on the invariants of the velocity gradient tensor;

$$\tau_{ij} = \overline{u_i u_j} - \overline{u_i} \overline{u_j} = -2\nu_{SGS} \overline{S}_{ij} + \frac{2}{3} k_{SGS} \delta_{ij} \quad)4($$

$$\nu_{SGS} = \overline{\Delta}^2 C_w^2 \frac{(\overline{S}_{ij}^* \overline{S}_{ij}^*)^{3/2}}{(\overline{S}_{ij} \overline{S}_{ij})^{5/2} + (\overline{S}_{ij}^* \overline{S}_{ij}^*)^{5/4}} \quad)5($$

$$\overline{S}_{ij}^* = \frac{1}{2} (\overline{g}_{ij}^2 + \overline{g}_{ji}^2) - \frac{1}{3} \overline{g}_{kk}^2 \delta_{ij} \quad)6($$

$$\overline{g}_{ij}^2 = \overline{g}_{ik} \overline{g}_{kj} = \frac{\partial \overline{u}_i}{\partial x_k} \frac{\partial \overline{u}_k}{\partial x_j} \quad)7($$

Where C_w is the model coefficient, here taken at a constant value equal to 0.325 [11]. k_{SGS} and \overline{S}_{ij} are the SGS kinetic energy and resolved scale strain rate tensor.

$$\overline{S}_{ij} = \frac{1}{2} \left(\frac{\partial \overline{u}_i}{\partial x_j} + \frac{\partial \overline{u}_j}{\partial x_i} \right) \quad)8($$

By analogy to the SGS stress tensor modeling, the scalar SGS thermal flux vector, τ_{jT} , can be approximated by the following expression [12];

$$\tau_{jT} = \overline{u_j T} - \overline{u_j} \overline{T} = -\frac{\nu_{SGS}}{Pr_{SGS}} \frac{\partial \overline{T}}{\partial x_j} \quad)9($$

Where Pr_{SGS} denotes the SGS Prandtl number and is fixed at 0.85 in the simulations presented below. The WALE turbulence model is able to reproduce the near-wall behavior correctly. Thus, opposed to most eddy viscosity turbulence models that require wall-damping functions near the wall region, the turbulent viscosity obtained by WALE formulation approaches zero at the wall. The model also generates zero turbulent viscosity in case of a pure shear; hence it can capture the transitional flow from laminar to turbulent [13].

Computational grid and boundary conditions

To achieve high resolution using minimum number of mesh elements, the mesh has been refined in four zones with different grid sizes. The finest elements of the structured mesh concentrates predominantly in a region around the middle of the door to properly resolve 3-D interfacial mixing, re-entrainment phenomena, and other fluctuation structures. An unstructured mesh with a combination of tetrahedra and pyramid cells was employed in the other three refinement zones. A smooth transition between the cell of different sizes is performed.

In total, nearly 25 million elements have been spread all over the multizone enclosure. The computational grid is shown in Fig. 3.

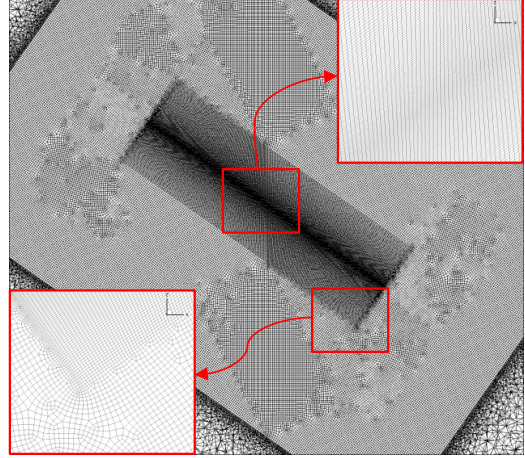


Figure 3: Computational grid.

Uniform initial temperature of $T_c = 293.15K$ and $T_H = 298.15K$ is imposed in the cold and warm reservoirs, respectively ($\Delta T = 5K$). The reference temperature (T_{ref}) is the arithmetic average of these two temperatures. The Prandtl number, $Pr = 0.73$, kinematic viscosity, $\nu = 1.538 \times 10^{-5} m^2/s$, and thermal expansion coefficient of the air, $\beta = 1/T_{ref} = 0.00335$, were applied. The enclosure is initialized with zero velocity, which would guarantee that natural convection would evolve. External walls of the enclosure are adiabatic and with a no-slip boundary condition.

During the first step of the simulation, an adaptive time step has been considered until the start-up fluctuations disappeared. Afterward, a constant time step of $\Delta t = 0.01$ is maintained to keep the Courant number value below 1.0 in order to achieve temporal accuracy and numerical stability. Note that a pseudo-stationary condition is reached after about 60 seconds when the airflow has fully established throughout the enclosure and the transition to turbulent mixing is settled. In this pseudo-steady state regime, the statistical data of time-averaged flow variables is collected for 80 seconds in order to reach full-converged statistics. During this period, the volume-averaged air temperature of both reservoirs remains almost constant.

Numerical Methodology

The non-linear governing equations are discretized using the second-order cell-centered finite volume method (FVM) implemented in the ANSYS Fluent commercial CFD package. The algorithm of Semi-Implicit Method for Pressure Linked Equations (SIMPLE) is employed for decoupling of velocity and pressure in the Navier–Stokes equations. The time derivatives are advanced in time using the Second Order Implicit scheme. The Bounded Central Differencing scheme is adopted for the treatment

of the convective term in the momentum equation. The diffusion terms are central-differenced, while the pressure interpolation is provided by the Body Force Weighted scheme.

ANSYS Fluent is capable of running on distributed processors and uses the public domain openMPI implementation of the standard message passing interface (MPI) to conduct inter-processor communication. The present LES simulation was carried out on the Idun cluster [14], containing Intel Xeon processor nodes with 40 cores and a minimum of 128GB of RAM.

Results and discussion

Interfacial Mixing

The counterflowing streams start setting up once the aperture opens and creates an opening between cold and warm zones. As expected, both warm and cold airflows are initially laminar and after a few seconds, they become turbulent. The low-density warm air descends in the heated plate side of the partition wall and is discharged into the adjacent cold zone by bending rapidly over the upper part of the opening and rise as a buoyant plume due to Archimedes force. Since the dimensions of the two reservoirs are considerable compared to the aperture area, temperature changes in each reservoir will be negligible.

Both air streams will meet at some distance from the bottom and up edges of the opening, where this interface is called the neutral plane. At the position of the neutral plane, the velocity would be zero and the pressure in both rooms are equal; hence there will be no airflow. When the flow is inviscid, there is no mixing or heat transfer between the two opposite airstreams close to and within the aperture. With viscous effects, instantaneous results provided by LES in Fig. 4 show unsteady flow structures developing in the middle of the doorway.

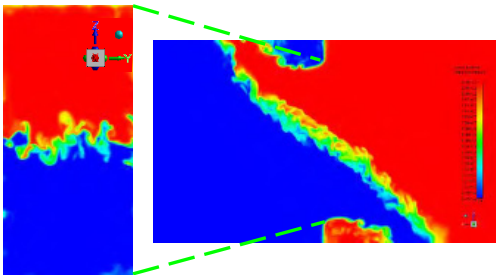


Figure 4: Instantaneous temperature in the door (left) and in a lateral view at the middle of the door in the y -direction (right).

The neutral plane (NP) is clearly visible in the left figure which shows front views of the door. This plane is not straight, and its position fluctuates slightly in space and time. To the authors' best knowledge, this effect has never been reported in the literature. The flow can also be visualized in a plane perpendicular to the door (right figure).

A snapshot of the mean temperature contours on a vertical plane in the middle of the enclosure are presented in Fig. 5. The counterflow develops from the NP with an angle of approximately 35 degrees with the horizontal. Unlike the standard theory assuming the flow to be horizontal at the doorway level, the CFD is strongly three-dimensional. Compared to inviscid flow (i.e. Euler simulation), the interfacial mixing induces a smoother transition of the temperature between both airstreams for viscous flow.

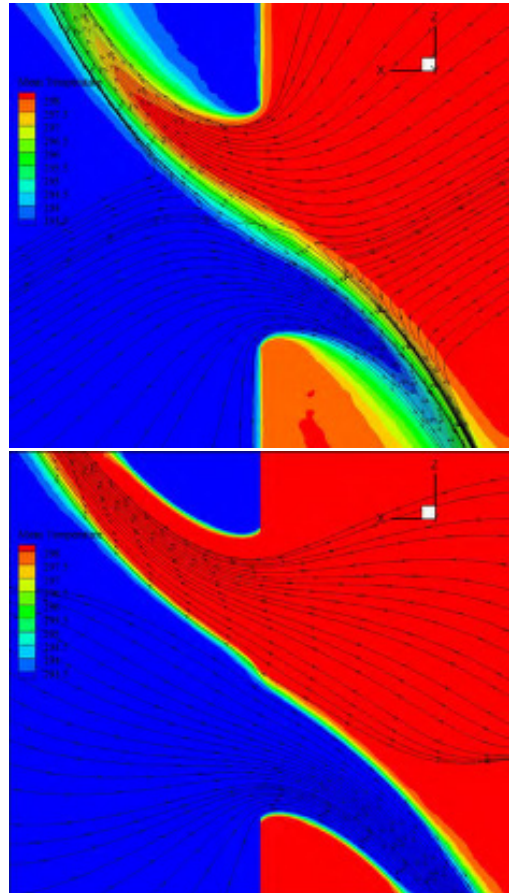


Figure 5: Mean temperature contours with streamlines, (LES above and Euler below).

The streamlines in viscous flow reveal that interfacial mixing causes a fraction of the warm airflow to be brought back into the warm zone, entrained by the cold airstream. This re-entrainment is similar for the cold airflow. However, no re-entrainment happened when the viscosity is switched off (Euler). The sharp edges of the aperture cause flow separation. At a section slightly downstream of the opening where the streamlines get almost horizontal, the maximum flow contraction takes place. In this section, the effective cross-section area for the airflow passage is minimum leading to the maximum velocity magnitude. This narrowest flow region is known as *vena contracta* and can occur when streamlines are unable to

follow sharp angles of openings. This area is shown by the streamlines passing through the aperture in Fig. 5, while it is not predicted by the theoretical model. The contraction will affect the airflow rate (or C_d) and heat exchange through the aperture.

Profiles of the time-averaged streamwise velocity and air temperature along a line in the middle of the doorway are shown in Fig. 6. The simulation results are also compared with those obtained by Euler simulation. For the theory, the velocity is scaled by a C_d calibrated by the LES (see next subsection). The first figure shows that the streamwise velocity is very similar between the LES, Euler simulation and the theory (denoted by Bernoulli) away from the middle of the door where the mixing takes place. The theory is able to successfully reproduce the streamwise velocity over a large part of the doorway. This can explain why this theory has been widely used in practice when an estimate of C_d is available. In the middle of the doorway, the Euler simulation and the theory also show similar results.

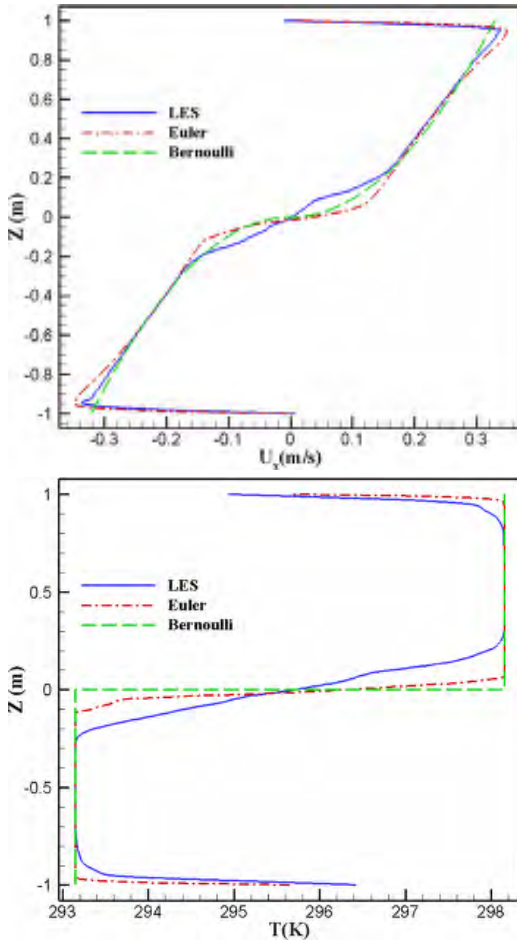


Figure 6: Time-averaged streamwise velocity and temperature profiles in the middle of the doorway.

It is only by introducing viscous effects and the resulting mixing that the velocity field shows a smoother transition. This transition zone has a length of $0.2 H$, centered on the NP.

The mean temperature profiles confirm these conclusions. The LES and Euler simulation give similar results over a large fraction of the door. In the middle of the doorway, the Euler temperature profile is close to a step function of 5K as assumed by the theory. On the contrary, the LES has a smoother transition.

Bulk Quantities

Considering the Bernoulli equation for an inviscid horizontal airflow passing through the aperture, the maximum theoretical volume flow rate (Q_{max}) can be evaluated as [9]:

$$Q_{max} = \frac{A}{3} \sqrt{g'H} \quad (10)$$

$$g' = g \frac{\Delta\rho}{\rho_e} \quad (11)$$

$$\rho_e = \rho_w \frac{(1 + (\rho_c/\rho_w)^{1/3})^3}{8} \quad (12)$$

$$Q = C_d Q_{max} \quad (13)$$

Where A and H are the aperture area and height, respectively. g' is defined as the effective acceleration of gravity. For low temperature differences until 40K the effective density, ρ_e , can be replaced with the average density [9]. The value of C_d is computed by dividing the actual volume flow rate (Q) by the maximum theoretical volume flow rate from the theory (Q_{max}). The time histories of the total volume flow rate, volume flow rate of each air stream, heat transfer, and doorway orifice coefficient are shown in Fig. 7.

The total volume flow rate of the warm and cold airflows respects the conservation of mass. In other words, the mass flow entering the sealing room must equal the mass flow leaving the room. As both reservoirs are adiabatic, energy is also conserved and the convective heat flow (Q_c) of both airstreams has the same magnitude but opposite signs.

Besides the existence of small fluctuations in Fig 4., LES and Euler approaches produce nearly the same values of each bulk quantity (i.e. volume flow rate, C_d and heat transfer). Hence it can be concluded that bulk quantities will not be affected significantly by unsteady flow structures developing along the counterflow interface.

Conclusions

The characteristics of the three-dimensional bulk flow through a large vertical opening induced by the temperature difference of two isothermal reservoirs have been extensively studied in the literature. However, factors influencing the flow (or the discharge coefficient, C_d), such as unsteady flow phenomena should still be studied. ANSYS Fluent was used to investigate this effect. LES using the WALE subgrid scale model was

adopted to predict the unsteady turbulent behaviour of the counterflowing airstreams. Results were compared to

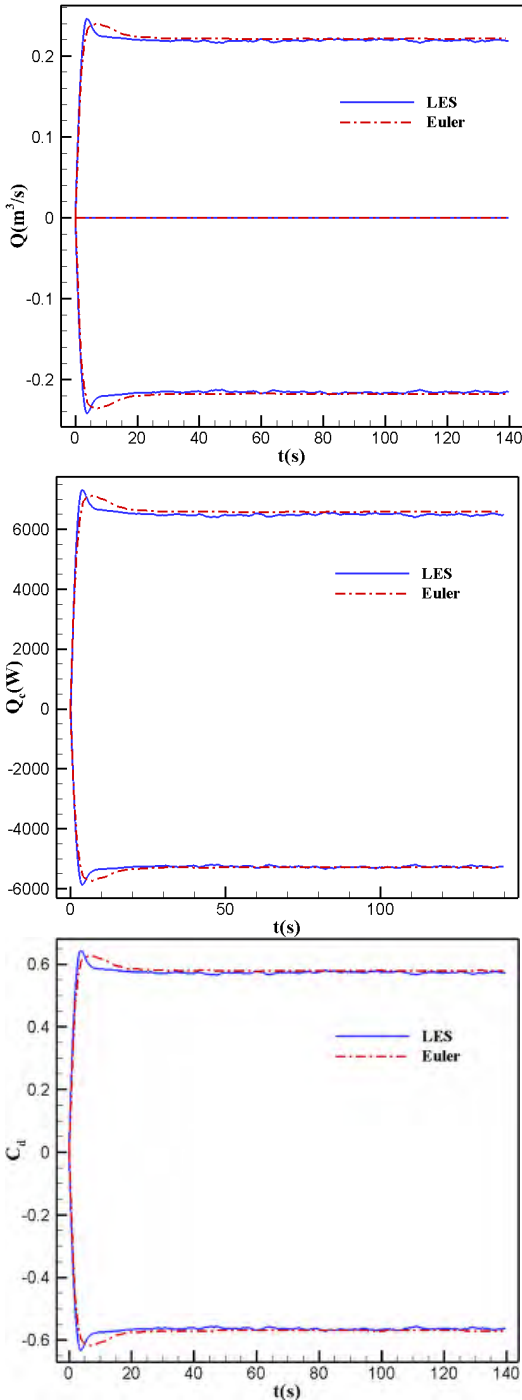


Figure 7: Time histories of mass flow rate, heat transfer, and doorway orifice coefficient.

Euler simulation. The inviscid flow showed no mixing or heat transfer between the opposite airflows close to and within the aperture. On the contrary, unsteady flow structures near the neutral plane were predicted by LES and generate interfacial mixing. Three phenomena resulted from the two counterflowing warm and cold airstreams (i.e. shear layer, re-entrainment effects and unsteady flow structures) and led to a reduction of the mass flow and heat exchange through the doorway. The theory was able to fairly reproduce the streamwise velocity and air temperature over a large fraction of the doorway. However, significant differences between viscous (i.e. LES) and inviscid flows (i.e. Euler and theoretical model) were present in the middle of the doorway ($|z| < 0.2 H$) due to mixing. Even though unsteady flow structures were present in the middle of the doorway, bulk quantities such as C_d were not affected significantly. The values of C_d calibrated by the LES and Euler simulation were very similar.

References

- [1] D. Scott, R. Anderson, and R. Figliola, "Blockage of natural convection boundary layer flow in a multizone enclosure," *International journal of heat and fluid flow*, vol. 9, no. 2, pp. 208-214, 1988.
- [2] J. Neymark, C. R. Boardman III, A. Kirkpatrick, and R. Anderson, "High Rayleigh number natural convection in partially divided air and water filled enclosures," *International Journal of Heat and Mass Transfer*, vol. 32, no. 9, pp. 1671-1679, 1989.
- [3] L. Georges, G. Cao, and H. M. Mathisen, "Further Investigation of the Convective Heat Transfer between Rooms through Open Doorways," in *the 12th REHVA World Congress: volume 5. Aalborg: Aalborg University, Department of Civil Engineering*, 2016.
- [4] P. Favaro and H. Manz, "Temperature-driven single-sided ventilation through a large rectangular opening," *Building and Environment*, vol. 40, no. 5, pp. 689-699, 2005.
- [5] D. Agonafer, L. Gan-Li, and D. B. Spalding, "The LVEL turbulence model for conjugate heat transfer at low Reynolds numbers," *Application of CAE/CAD Electronic Systems, ASME*, vol. 18, pp. 23-26, 1996.
- [6] F. Allard and Y. Utsumi, "Airflow through large openings," *Energy and Buildings*, vol. 18, no. 2, pp. 133-145, 1992.
- [7] R. Pelletret, G. Liebecq, F. Allard, J. Van der Maas, and F. Haghghat, "Modelling of large openings," in *12th AIVC Conference: Air Movement and Ventilation Control Within Buildings*, 1991.
- [8] F. Allard *et al.*, "Airflow through large openings in buildings," *Annex 20: Air flow patterns within Buildings*, 1992.
- [9] D. Wilson and D. Kiel, "Gravity driven counterflow through an open door in a sealed room," *Building and Environment*, vol. 25, no. 4, pp. 379-388, 1990.
- [10] A. Lefauve, J. Partridge, and P. Linden, "Regime transitions and energetics of sustained stratified shear

flows," *Journal of Fluid Mechanics*, vol. 875, pp. 657-698, 2019.

[11] F. Nicoud and F. Ducros, "Subgrid-scale stress modelling based on the square of the velocity gradient tensor," *Flow, turbulence and Combustion*, vol. 62, no. 3, pp. 183-200, 1999.

[12] A. Leonard, "Energy cascade in large-eddy simulations of turbulent fluid flows," *Adv. Geophys. A*, vol. 18, no. A, pp. 237-248, 1974.

[13] A. Yuen, G. Yeoh, V. Timchenko, S. Cheung, and T. Chen, "Study of three LES subgrid-scale turbulence models for predictions of heat and mass transfer in large-scale compartment fires," *Numerical Heat Transfer, Part A: Applications*, vol. 69, no. 11, pp. 1223-1241, 2016.

[14] M. Sjalander, M. Jahre, G. Tufte, and N. Reissmann, "EPIC: An energy-efficient, high-performance GPGPU computing research infrastructure," *arXiv preprint arXiv:1912.05848*, 2019.

A.5 Paper V

Comparing the performance of RANS turbulence models between different cavity flow benchmarks

Elyas Larkermani, Vegard Mikkelsen Bjerkeli, Laurent Georges

*Proceedings ROOMVENT CONFERENCE. 16TH 2022. (ROOMVENT 2022)(2
PARTS) Item#: 065443 Held 16-19 September 2022, Xi'an, China. EDP
Sciences. 2022*

Comparing the performance of RANS turbulence models between different cavity flow benchmarks

Elyas Larkermani^{1*}, Vegard Mikkelsen Bjerke¹, and Laurent Georges¹

¹Norwegian University of Science and Technology, Department of Energy and Process Engineering, Kolbjørn Hejes v 1B, NO-7491, Trondheim, Norway

Abstract. To evaluate the performance of RANS turbulence models, this study compares four different cavity flow benchmarks using the prevailing two-equation turbulence models for indoor airflows, namely the standard and RNG $k-\epsilon$ and the standard and SST $k-\omega$ models. A cavity flow consists of one air inlet and one outlet slot. The inlet slot is positioned on the upper left corner of the cavity, whereas the outlet slot is located in the lower right. This cavity flow is representative of mixing ventilation. These four cavity benchmarks differ by their geometry (i.e., the aspect ratio of the room), flow regime and whether the flow is isothermal or not. Measurements of the air velocity and temperature in these benchmarks are used to evaluate the accuracy of the RANS turbulence models. Many existing studies have investigated the airflow and heat transfer over these benchmarks. However, the numerical methods and other relevant CFD parameters are not always described in detail, reducing the transparency and reproducibility of these works. To compare the influence of the RANS turbulence model on the four cavity flows, a same CFD setup is adopted here for all benchmarks. This setup is based on the best practice in RANS, namely a steady second-order spatial discretization on a wall-resolved structured mesh and with a grid convergence analysis. The results show that $k-\epsilon$ models, particularly the standard $k-\epsilon$ model, are best suited in a fully turbulent flow regime without strong pressure gradients. On the opposite, the SST $k-\omega$ model performs best in the transitional regime while the $k-\epsilon$ models only give moderate to poor results.

1 Introduction

Accurate prediction of indoor airflows is required to design comfortable and healthy indoor environments. Designers may use indoor flow modeling to evaluate the proposed ventilation strategy and ensure that the thermal comfort and indoor air quality (IAQ) criteria are met at the design stage. However, it should deliver sufficiently accurate detail at a low financial and labor cost. The two most common approaches that have been developed to study indoor airflow are experimental measurements and computational fluid dynamics (CFD). The former approach is usually implemented on the full scale of the actual model. However, reliable and detailed information on indoor airflows can be provided at a lower cost using CFD. Substantial development in numerical schemes, turbulence models, and computational power make CFD more efficient today than 50 years ago. Although some measurement techniques are still in use and essential to validate CFD simulations, CFD can replace some of these flow measurements to reduce the costs.

The Reynolds-Averaged Navier Stokes (RANS) turbulence modeling is widely used to simulate airflows in ventilated spaces. Other approaches such as Large Eddy Simulation (LES) are more accurate for ventilation flow prediction, but their applications are quite limited due to higher computational costs.

However, three distinct physical phenomena of indoor airflows, i.e., transitional flow, turbulence anisotropy and adverse pressure gradients, are demanding for RANS modeling [1]. The performance of many RANS turbulence models may change significantly depending on the flow regime. Although a fully turbulent airflow develops in the room, a transitional airflow may still form in some regions, e.g., near supply jet or low-velocity regions. In addition, only a few RANS models can capture turbulent anisotropy present in regions of high shear. On top of that, the separation of a boundary layer due to an adverse pressure gradient is not easily predicted with high-Reynolds RANS turbulence models. Therefore, it is uncertain which RANS models are suitable depending on the airflow characteristics in the enclosure.

In two recent studies by Peng et al. [2] and van Hoff et al. [3], the accuracy of CFD simulations for indoor airflows in isothermal and non-isothermal backward facing step flow was evaluated by different teams from the ventilation research community and industry. A large spread in the results was reported during these workshops as multiple user decisions affect the final results, such as the choice of the numerical method. However, the choice of turbulence model was recognized as the parameter with the most significant impact. The results from the two studies indicate the importance of validation against benchmark test cases

* Corresponding author: elyas.larkermani@ntnu.no

with available experimental data to ensure accuracy of CFD simulations for indoor airflows. Our study evaluates the performance of RANS two-equation eddy-viscosity models in four different cavity flow benchmarks representative for mixing ventilation at both transitional and fully turbulent regimes.

2 Methodology

2.1 Description of the cavity flow benchmarks

A cavity flow represents an airflow in an empty ventilated space where an attached wall jet is discharged into the room along the ceiling. With a sufficiently high inlet velocity, the jet impinges the opposing wall and deflects into the cavity zone. The separation of the boundary layer close to the top corner of the room generates a recirculation region in the enclosure (Figure 1). The four cavity flows differ by the geometry aspect ratio, the airflow regime and thermal effects (i.e., isothermal and non-isothermal cases). The first benchmark called the IEA Annex 20 test room is isothermal. The experimental measurements were carried out by Nielsen et al. [4] using Laser Doppler Anemometry (LDA). The slot Reynolds number (Re) is 5000, indicating a fully turbulent room airflow. Since its creation, multiple attempts [5-9] have been made to reproduce the airflow pattern and velocity profile of this cavity flow using the prevailing turbulence models for indoor airflows such as $k-\epsilon$, RNG $k-\epsilon$, $k-\omega$ and $k-\omega$ SST. The dimension of the computational domain is defined in Table 1.

Benchmark 2 has a same geometry as benchmark 1 but with a different aspect ratio (Table 1). The experimental data are reported by Nielsen [10] in his Ph.D. thesis for both isothermal and non-isothermal conditions. The isothermal flow was measured with hot wire anemometry, and measurements were done only at a vertical line ($x = 2H$). The benchmark is simulated here for a Reynolds number of 7100 in isothermal mode.

In benchmark 3, a slightly different geometrical configuration compared to benchmarks 1 and 2 is adopted as the width is considerably smaller than the length and height (Table 1). So inlet and outlet openings have a smaller area than the previous ones. The flow is non-isothermal. In the experiments done by Blay et al. [11], the setup has two guard cavities to make the side walls adiabatic. The walls were made of aluminum and kept at a constant temperature using temperature-controlled water (with a precision of 0.25°C). The floor is kept at a constant temperature of 35.5°C, while the remaining three walls have a temperature equal to the inlet temperature of 15°C. A uniform velocity profile of 0.57 m/s is imposed at the inlet, leading to a Reynolds number of 684 based on the inlet height. Velocity measurements were done using Laser Doppler Velocimetry (LDV) and temperature measurements with Cr-Al thermocouples.

Benchmark 4 is a cubical cavity without buoyancy effects (Table 1). The experiment was done by van Hoff et al. [12] at two different Reynolds numbers, 1000 and 2500, representing a transitional flow. The working

fluid was water, and the velocity field was measured with a 2D PIV system.

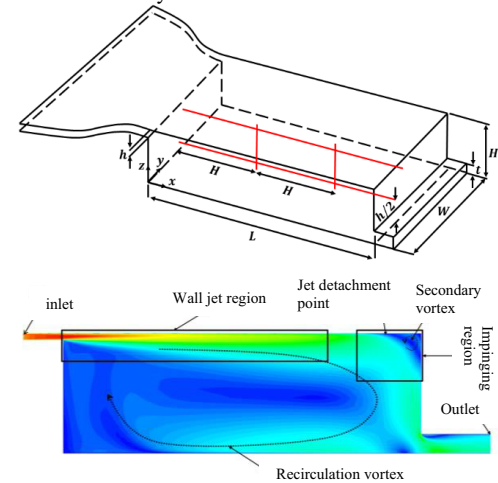


Fig. 1. IEA Annex 20 test room [4]. The measurement lines in benchmarks 1 and 2 are two vertical lines and two horizontal lines in red.

Table 1. Cavity flow benchmark description.

Benchmark	1	2	3	4
Re at inlet	5000	7100	684	1000/2500
Flow regime	Fully Turbulent	Fully Turbulent	Unknown	Transitional
Thermal effects	Isothermal	Isothermal	Non-Isothermal	Isothermal
L/H	3	3	1	1
W/H	1	4.7	0.288	1
h/H	0.056	0.056	0.0173	0.1
t/H	0.16	0.16	0.0231	0.0167
H [m]	0.0893	0.127	1.04	0.3

2.2 Governing equations and numerical setup

The airflow field in a cavity is computed using the Reynolds Averaged Navier-Stokes (RANS) equations for the mass, momentum and energy conservations where the Reynolds stresses have been modeled using an eddy viscosity:

$$\frac{\partial \bar{u}_i}{\partial x_i} = 0 \quad (1)$$

$$\frac{\partial \bar{u}_i}{\partial t} + \frac{\partial \bar{u}_i \bar{u}_j}{\partial x_j} = -\frac{1}{\rho_{ref}} \frac{\partial \bar{p}}{\partial x_i} + \frac{\partial}{\partial x_j} \left[(v + v_t) \frac{\partial \bar{u}_j}{\partial x_j} \right] + \beta g_i (\bar{T} - T_{ref}) \quad (2)$$

$$\frac{\partial \bar{T}}{\partial t} + \frac{\partial \bar{u}_j \bar{T}}{\partial x_j} = \frac{\partial}{\partial x_j} \left[(\alpha + \alpha_t) \frac{\partial \bar{T}}{\partial x_j} \right] \quad (3)$$

where the bar represents the time averaging, x_i denotes the i^{th} spatial coordinate direction, \bar{u}_i represents the time-averaged velocity field in the x_i direction, t the time, \bar{p} the time-averaged static pressure, and \bar{T} the time-averaged temperature. The effect of buoyancy forces is taken into account using the Boussinesq

approximation where $\beta = 1/T_{ref}$ is the thermal expansion coefficient of the air modeled as an ideal gas and g_i the gravitational acceleration. The parameters ν and α are the kinematic viscosity and thermal diffusivity, respectively. Turbulent kinematic viscosity and thermal diffusivity are defined with the subscript t .

After conducting a grid sensitivity analysis for each benchmark, a structured orthogonal mesh is selected based on a trade-off between accuracy and computational cost. An overview of the grid size adopted for each benchmark is provided in Table 2. All meshes have been constructed to have y^+ less than five on the walls to resolve the boundary layers. The turbulence model that showed good convergence in previous studies is selected for grid analysis. The inlet turbulent intensity is set to match the experimental value.

Table 2. Grid size based on grid sensitivity analysis.

Benchmark	1	2	3	4
Geometry	3D	3D	3D	3D
Number of cells	342000	1771000	189000	1214000
Inlet turbulent intensity	4%	5%	6%	6%
Turbulence model	Standard $k-\epsilon$	Standard $k-\epsilon$	RNG $k-\epsilon$	SST $k-\omega$

The nonlinear governing equations are discretized using a second-order cell-centered finite volume method implemented in the ANSYS Fluent commercial CFD package. The SIMPLE algorithm is employed for pressure-velocity coupling. The time derivatives are advanced in time using the “Second Order Implicit” scheme. The “Second Order Upwind” scheme is adopted for the treatment of the convective terms of the governing equations. The pressure interpolation is provided by the “Second Order” scheme. “Enhanced wall treatment” has been used as the default wall modeling option. The no-slip boundary condition is applied to all walls.

All benchmarks are run in steady-state mode. However, the averaging technique introduced by Blocken [13] is applied when fluctuations of the residuals and other physical quantities (such as the drag coefficients on the floor or ceiling) are detected. In this technique, the solution is averaged over many iterations to get a statistically independent solution. The number of iterations required is case dependent and must be investigated for each benchmark. The convergence criteria for all simulations are fulfilled when the absolute residuals drop down to 10^{-6} and the drag coefficient on the ceiling and floor walls reaches stable values.

3 Results and discussion

The performance of six turbulence models, the standard $k-\epsilon$, RNG $k-\epsilon$, realizable $k-\epsilon$, AKN low-Re $k-\epsilon$, standard $k-\omega$ and the $k-\omega$ SST, is shown for the four benchmarks in Figures 2 and 3.

3.1 Benchmarks 1 and 2

The distribution of the normalized streamwise velocity component along the cavity height at two vertical lines ($x = H$, $x = 2H$) is plotted in Figures 2(a), (b), (e) and (f). The negative velocities in the lower part of the cavity are evidence of a substantial air recirculation region inside the cavity. Figures 2(c), (d), (g) and (h) show normalized vertical velocity distribution along two horizontal lines ($z = h/2$, $z = H - h/2$) in the mid-plane. None of the turbulence models achieves a perfect fit of the experimental data. In particular, in Figure 2(c), simulation results differ remarkably from experiments. From this figure, the RNG and realizable $k-\epsilon$ turbulence models cannot correctly predict the flow direction on the cavity’s left part. In other words, solutions from these models have a different flow pattern than experiments in this part of the cavity. The most apparent differences between the turbulence models can also be found in the lower-left corner of the cavity, i.e., the left part of Figures 2(c) and (g). Turbulence models struggle to model the flow in this part of the cavity because the flow may be dominated by the transitional regime and have anisotropic behavior. Figures 2(a) and (b) also reveal a noticeable deviation between the turbulence models regarding the jet velocity along the floor and ceiling.

3.2 Benchmark 3

Profiles of normalized velocity and temperature along a vertical centerline ($x = L/2$) are depicted in Figures 2(i) and (j) as well as along a horizontal centerline ($z = H/2$) in Figures 2(k) and (l). Since simulations gave oscillatory residuals, the results were averaged over 2000 iterations for each model. According to Figures 2(i) to (l), all turbulence models predict fairly accurately the flow pattern. However, the maximum velocity for the jet along the ceiling is overestimated by two $k-\omega$ models. Moreover, all models underestimate the jet velocity along the floor and left wall under the inlet. Although the air temperature along the cavity walls is in good agreement with measurement data, it is underpredicted by all models inside the recirculation zone due to insufficient air mixing (Figures 2(j) and (l)). The realizable $k-\epsilon$ model reproduces experiment data better than other turbulence models, whereas the $k-\omega$ SST model is relatively less successful.

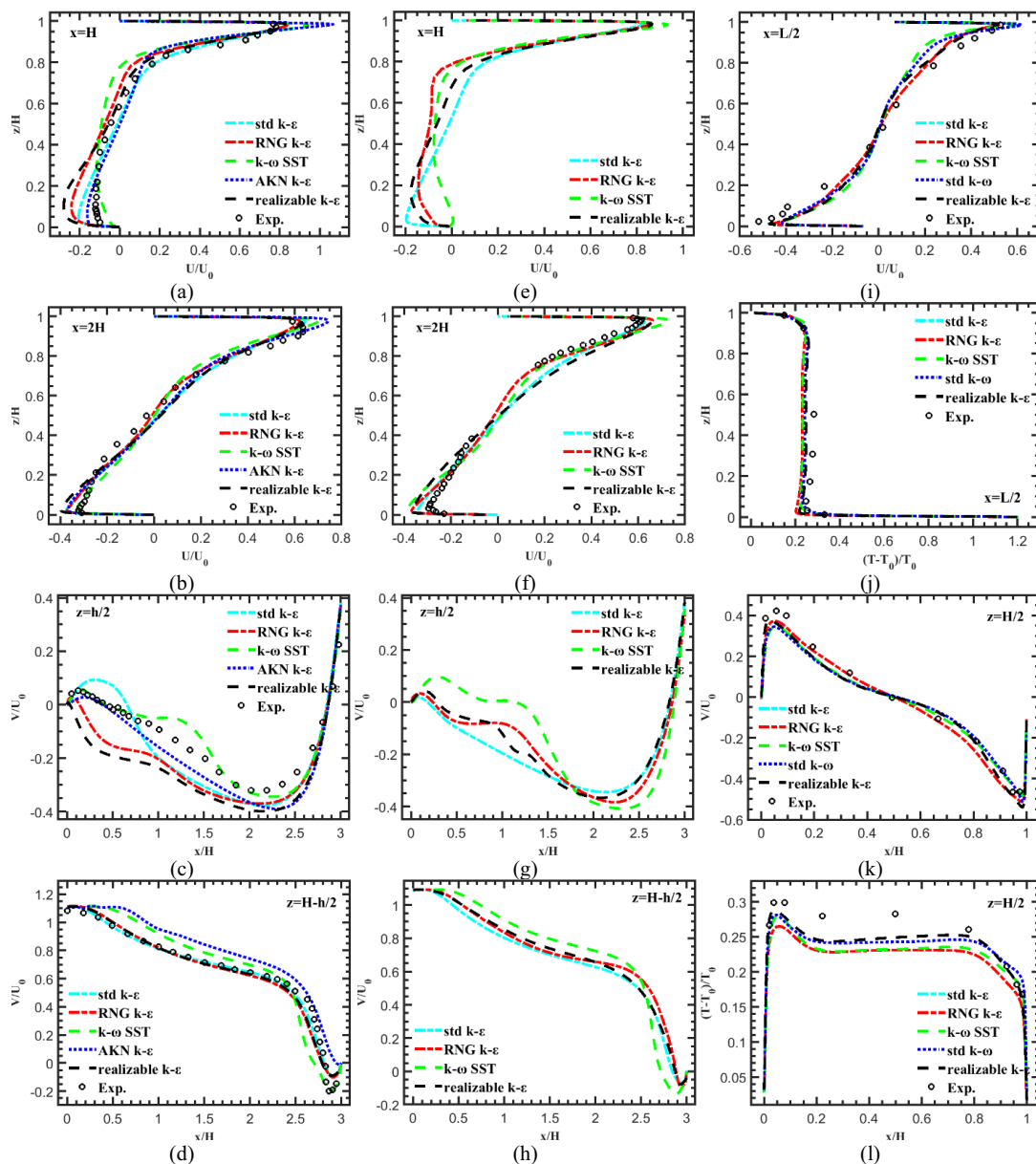


Fig. 2. Normalized velocity and temperature profiles for benchmark 1 (left column), benchmark 2 (middle column) and benchmark 3 (right column)

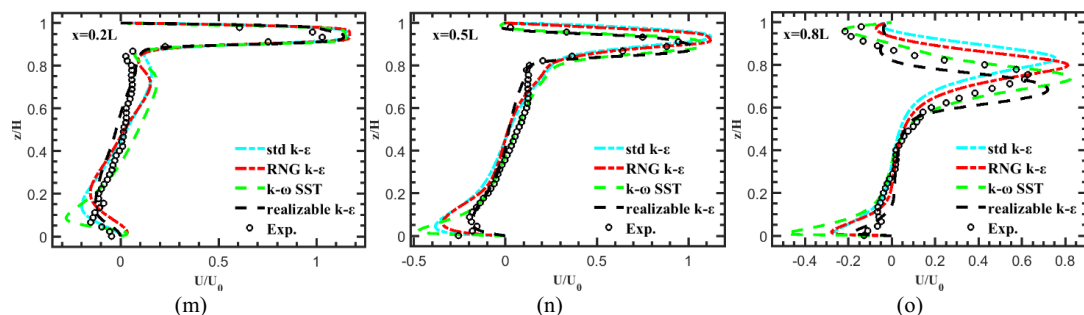


Fig. 3. Normalized velocity and temperature profiles for benchmark 4

3.3 Benchmark 4

Normalized velocity profiles from standard k- ϵ , RNG k- ϵ , realizable k- ϵ , and k- ω SST turbulence models at three vertical lines ($x = 0.2L, 0.5L, 0.8L$) are compared with the experimental results in Figures 3(m) to 3(o). Using the k- ω SST model, the location of the detachment of the jet can be predicted quite well (Figure 3(o)). The other models predict detachment further away from the inlet. Right above the floor, a large discrepancy with measurement data can be observed in the velocity profile at all three lines. However, no conclusion can be drawn due to reflections from the glass floor leading to inaccurate measurements. For all three lines, each model appears to overpredict the maximum jet velocity. The k- ω SST shows the best performance, while the standard k- ϵ has the largest deviation from experiments.

3.4 Cross comparison

It can be concluded that none of the turbulence models perform equally well for all benchmarks, so none of the models seem universal. The main conclusions are:

- Generally, a good agreement is found between CFD results and measurements that validate the use of CFD for the prediction of airflows in buildings.
- The standard k- ϵ model is the most accurate for benchmarks 1 and 2. In addition, the results obtained using the standard k- ϵ model are consistent with the literature. The standard k- ϵ model is thus a good choice when simulating indoor airflows with fully turbulent characteristics without large pressure gradients.
- The deviation from the experimental measurements in the area below the inlet in benchmarks 1 and 2 may be attributed to the anisotropy of the transitional flow present in that region because RANS eddy-viscosity models cannot be taken into account the flow anisotropy.
- All three k- ϵ models provided the best agreement with experiments in benchmark 3, whereas the k- ω SST model was clearly superior to the k- ϵ models for benchmark 4. Benchmark 4 has larger pressure gradients along the wall jet. The poor results of k- ϵ models are primarily caused by an incorrect determination of the location of jet detachment, so they should be used with caution for transitional flows. The standard k- ϵ model gave the worst results. The k- ω SST model performs better in the transitional flow regime with pressure gradients and jet impingement.

4 Conclusions

In this study, the performance of the prevalent two-equation RANS turbulence models to predict mixing ventilation was studied. The performance was compared with experimental measurements on four cavity flow benchmarks using the CFD best practice. In conclusion, none of the turbulence models performs equally well in all scenarios, confirming the importance of selecting a

suitable turbulence model for a given case, e.g., according to the flow regime. Additional benchmarks are needed to discriminate clearly the specific influence of other parameters on the CFD solution, such as the inlet boundary conditions. A similar study using the Large Eddy Simulation (LES) could also be performed to test the universality of LES to accurately predict the indoor airflow characteristics at different flow regimes.

References

1. T. van Hooff, B. Blocken, and G. Van Heijst, "On the suitability of steady RANS CFD for forced mixing ventilation at transitional slot Reynolds numbers," *Indoor Air*, **23**, no. 3, pp. 236-249, (2013).
2. L. Peng, P. V. Nielsen, X. Wang, S. Sadrizadeh, L. Liu, and Y. Li, "Possible user-dependent CFD predictions of transitional flow in building ventilation," *Building and Environment*, **99**, pp. 130-141, (2016).
3. T. van Hooff, P. V. Nielsen, and Y. Li, "Computational fluid dynamics predictions of non - isothermal ventilation flow—How can the user factor be minimized?," *Indoor Air*, **28**, no. 6, pp. 866-880, (2018).
4. P. V. Nielsen, "Specification of a two-dimensional test case:(iea)," (1990).
5. N. Vogl and U. Renz, "Energy Conservation in Buildings and in Community Systems," (1991).
6. Q. Chen, "Comparison of different k- ϵ models for indoor air flow computations," *Numerical Heat Transfer, Part B Fundamentals*, **28**, no. 3, pp. 353-369, (1995).
7. Q. Chen, "Prediction of room air motion by Reynolds-stress models," *Building and environment*, **31**, no. 3, pp. 233-244, (1996).
8. L. Voigt, "Navier-Stokes simulations of airflow in rooms and around a human body. (2001)," Technical University of Denmark.
9. L. Rong and P. V. Nielsen, "Simulation with different turbulence models in an annex 20 room benchmark test using Ansys CFX 11.0," (2008).
10. P. V. Nielsen, "Flow in air conditioned rooms: Model experiments and numerical solution of the flow equations," (1974).
11. D. Blay, "Confined turbulent mixed convection in the presence of horizontal buoyant wall jet," *HTD 213, Fundamentals of Mixed Convection*, (1992).
12. T. van Hooff, B. Blocken, T. Defraeye, J. Carmeliet, and G. Van Heijst, "PIV measurements of a plane wall jet in a confined space at transitional slot Reynolds numbers," *Experiments in Fluids*, **53**, no. 2, pp. 499-517, (2012).
13. B. Blocken, "Computational Fluid Dynamics for urban physics: Importance, scales, possibilities, limitations and ten tips and tricks towards accurate and reliable simulations," *Building and Environment*, **91**, pp. 219-245, (2015).

A.6 Paper VI

Influence of the inlet boundary conditions on the LES performance for the cavity flow benchmark

Simon Bjuri, Elyas Larkermani, Laurent Georges

Proceedings ROOMVENT CONFERENCE. Stockholm, Sweden. Apr. 2024

Influence of the inlet boundary conditions on the LES performance for the cavity flow benchmark

Simon Bjuri^{1,*}, Elyas Larkermani^{2,**}, and Laurent Georges^{2,***}

¹Department of Chemical Engineering, Norwegian University of Science and Technology, Sem Sælandsvei 4, NO- 7491, Trondheim, Norway

²Department of Energy and Process Engineering, Norwegian University of Science and Technology, Kolbjørn Hejes vei 1B, NO-7491, Trondheim, Norway

Abstract. A cavity flow consists of one air inlet and one outlet slot. The inlet slot is positioned in the upper left corner of the cavity, whereas the outlet slot is located in the lower right. This cavity flow is representative of mixing ventilation. The literature shows that the prevalent two-equation RANS turbulence models can reproduce the measured velocity field in the cavity for the transitional and fully turbulent flow regimes. However, a single turbulence model cannot perform equally well at these two flow regimes: $k-\epsilon$ models perform well for the fully turbulent regime, while the $k-\omega$ models perform best in the transitional regime. In general, this dependence on the flow regime can make the use of RANS less reliable during the ventilation design phase. By definition, LES is expected to be suited for transitional and fully turbulent flow regimes. Therefore, it is worth investigating and comparing the performance of LES and RANS on two isothermal cavity flow benchmarks, which differ by their geometry (i.e., the aspect ratio of the room) and flow regimes. Simulations are performed on structured grids using the Dynamic Smagorinsky subgrid-scale (SGS) model for LES and the standard $k-\epsilon$, standard $k-\omega$ and BSL $k-\omega$ turbulence models for RANS. In addition, the performance of DES is also investigated and compared using the Spalart-Allmaras and realizable $k-\epsilon$ DES. Results show that the LES using the Dynamic Smagorinsky is indeed able to reproduce the velocity field for both flow regimes, making the model more universal than RANS. However, results are strongly dependent on the turbulence level at the inlet. In addition, it is shown that spatial-developing synthetic turbulence at the inlet gives comparable results as a separate LES simulation, leading to simpler and less computationally expensive simulations. Regarding DES, the realizable $k-\epsilon$ DES gives fairly good results for the fully turbulent case. However, the DES has numerical stability issues when adding considerable synthetic turbulence at the inlet and suffers from the depletion of turbulent structures under the transition from RANS to LES. In conclusion, LES can be more universal to predict the ventilation performance of mixing ventilation in buildings, but it requires a good knowledge of the turbulence intensity at the air inlets, which may not be a straightforward task during design. Regarding DES, it has the potential to decrease computational costs compared to LES, but it requires further research for the cavity flow.

1 Introduction

In pursuit of improving, developing, and investigating Heating, Ventilation, and Air Conditioner (HVAC) systems, the need for accurate and robust methods to predict airflow distribution within rooms is crucial. Two main approaches exist: experimental measurement and Computational Fluid Dynamics (CFD) modelling. The CFD approach is often preferred due to its flexibility in conducting parameter sensitivity analysis and altering geometry. Especially with the continuous increase of computational power, CFD methods have become increasingly common for predicting airflow within rooms. CFD offers a variety of turbulence models to simulate the complexity of airflow, each varying in computational expense and accuracy.

Turbulence models are typically classified into three main categories: Direct Numerical Simulations (DNS), Large Eddy Simulations (LES), and Reynolds-Averaged Navier-Stokes (RANS). DNS is the most computationally demanding as it resolves all turbulence structures on the numerical mesh. LES only resolves the largest turbulent structures, modelling the effect of the smallest eddies using a subgrid-scale (SGS) model. The RANS approach solves for the time-averaged pressure and velocity fields and models the effect of the turbulent fluctuations on the time-averaged field through closure models. The Detached Eddy Simulation (DES) is a method that combines LES and RANS. In the region near the wall where a high cell count would be required to perform LES, DES employs RANS. Conversely, in the far-field region where fewer cells are required for a LES, DES utilizes LES. While DNS offers the highest accuracy, it is computationally expensive and mostly suitable for simple geometries. RANS is far less computationally expensive, but the accuracy de-

*e-mail: simon.bjuri@ntnu.no

**e-mail: elyas.larkermani@ntnu.no

***e-mail: laurent.georges@ntnu.no

depends on the specific models used, and a universal RANS model that provides high accuracy under all flow regimes does not exist, as demonstrated by Larkermanni et al. [1]. LES sits between DNS and RANS in terms of computational cost and accuracy, while DES falls between RANS and LES.

In 1978, Nielsen et al. [2] used CFD to replicate experimental data obtained by Nielsen [3] for a fully turbulent cavity flow with a Reynolds number of 5000. Numerous researchers have since explored this benchmark (see e.g., [4–7]) studying the performance of different turbulence models on this setup. Rong and Nielsen [4] tested out several RANS models on this benchmark in 2D and concluded that the standard $k-\epsilon$ model gave the best results while the SST $k-\omega$ had the worst performance. However, none of the RANS models could fully predict the flow, especially the secondary vortex by the corner. Bjuri obtained similar results [5] when running the case in 3D using RANS models. Taghinia et al. [6] and Zasimova et al. [7] also investigated LES approaches on this benchmark. Taghinia et al. used a custom-made SGS model on a mesh with 4 million cells and obtained good results. Zasimova et al. used wall-modeled LES (WMLES) with up to 48 million cells and got relatively good results except for the backflow region. Both meshes were refined close to the walls and where the inlet jet mixes with the air in the cavity. Both of these research groups used a separate LES of a periodic channel flow to recreate the turbulence at the inlet of the cavity before conducting the LES of the cavity.

Van Hooff et al. [8] created an experimental setup of transitional cavity flow with Reynolds numbers of 1000 and 2500, and compared the experimental data with several RANS turbulence models [9]. The mesh consisted of 1.3 million cells and was refined near the walls and in the area below the ceiling where the inlet jet mixes with the cavity. The conclusion was that the low-Re $k-\epsilon$ model yielded the best results. However, in studies by Bjuri [5] and Bjerkeli [10], the SST $k-\omega$ and Baseline (BSL) $k-\omega$ model performed the best. Van Hoff et al. [11] also tested out LES on this benchmark with a Reynolds number of 2500 using the dynamic Smagorinsky model with a similar mesh as in their previous study [9]. The conclusion was that the LES performed better than the RANS model for this case.

This article compares LES and DES to RANS models on the cavity flow benchmarks in fully turbulent and transitional flow regimes, as measured by Nielsen [3] and Van Hooff et al. [8], respectively. If the same turbulence model can accurately predict both test cases, it could consistently be applied to solve other cavity flows without prior knowledge of the flow regime, making the model more universal. Special care is given to the inlet boundary conditions for LES and DES. Firstly, it will be investigated how the turbulence intensity at the domain inlet will affect the results. Secondly, spatial-developing synthetic turbulence will be applied at the inlet. In previous studies, Taghinia et al. [6] and Zasimova et al. [7] conducted a separate LES of a periodic channel flow to generate the correct amount of turbulence at the inlet for the fully turbulent case. If com-

parable results can be achieved with synthetic turbulence, there would be no need for a separate LES for the inlet, leading to simpler and less computationally demanding simulations. Finally, to the author's knowledge, the performance of the DES has never been reported in the literature for these cavity flow benchmarks. DES allows for larger cells in the boundary layers than wall-resolved LES, reducing computational costs compared to LES. DES could not only shorten the computational time but also reduce the need for computational power.

2 Methodology

2.1 Governing equations

The governing equations that describe the isothermal airflow in a cavity are the incompressible Navier-Stokes equations. The different turbulence modelling approaches have different ways of solving and approximating the Navier-Stokes equations for turbulent flows. For RANS models, the Reynolds-Averaged Navier-Stokes equations (1) and (2) are being solved. The RANS equations solve for the time-averaged velocity and pressure fields \bar{u} and \bar{p} . The different RANS models have different ways of approximating the turbulent viscosity ν_t as can be further read in Fluent theory guide [12].

$$\frac{\partial \bar{u}_i}{\partial x_i} = 0 \quad (1)$$

$$\frac{\partial \bar{u}_i}{\partial t} + \frac{\partial \bar{u}_i \bar{u}_j}{\partial x_j} = -\frac{1}{\rho} \frac{\partial \bar{p}}{\partial x_i} + \frac{\partial}{\partial x_j} \left[(\nu + \nu_t) \frac{\partial \bar{u}_j}{\partial x_j} \right] \quad (2)$$

For LES, the spatial filtered Navier-Stokes equations are solved, which is identical to equations (1) and (2), except that \bar{u} and \bar{p} is the filtered velocity and pressure, and ν_t is the subgrid-scale (SGS) eddy viscosity. The main idea of LES is that the large eddies are solved on the grid, and the influence of smallest eddies is modelled through the SGS models. A common SGS model is the Dynamic Smagorinsky model, where the SGS viscosity is given by equation (3). S is the rate of strain, $\Delta = V_{cell}^{1/3}$ is the local grid size and C_s is the Smagorinsky constant. The Smagorinsky constant is determined dynamically by applying an additional test filter described by Germano et al. [13].

$$\nu_t = (C_s \Delta)^2 S \quad (3)$$

The DES Spalart-Allmaras proposed by Shur et al. [14], replaces the length scale d used for the RANS model Spalart-Allmaras with the length scale \tilde{d} which is defined in equation (4). $C_{DES} = 0.65$ is an empirical constant and Δ_{max} is the maximum edge length of the cell. This means that an LES approach is used when $C_{DES} \Delta_{max} < d$ and RANS is used otherwise.

$$\tilde{d} = \min(d, C_{DES} \Delta_{max}) \quad (4)$$

Another popular DES model is based on the realizable $k-\epsilon$ model. In this approach, the dissipation term in the transport equation of the turbulent kinetic energy is given by equation (5). l_{des} is given by equation (6). k is the turbulent kinetic energy and ϵ is the turbulent dissipation rate. This means that the transition between RANS and LES is not only dependent on the local mesh size but also by k and ϵ .

$$G_k = \frac{\rho k^{3/2}}{l_{des}} \quad (5)$$

$$l_{des} = \min(l_{rke}, l_{les}) \quad , \quad l_{rke} = \frac{k^{3/2}}{\epsilon} \quad , \quad l_{les} = C_{DES} \Delta_{max} \quad (6)$$

2.2 Description of the fully turbulent benchmark of Nielsen [3]

The geometry of the fully turbulent case is shown in Figure 1 and consists of an inlet slot with an unspecified length and a height of 0.168 m . This slot leads into a cavity measuring 9.0 m in length, 3 m in width, and 3 m in height. The outlet slot height is 0.48 m , and the length is unspecified. The Reynolds number for this setup is 5000, based on the height of the inlet slot and the inlet velocity (U_{in}). Laser-Doppler measurements were taken for both the mean velocity and the root mean square (RMS) values of the velocity at four distinct lines: $x = 3\text{ m}$, $x = 6\text{ m}$, $y = 0.084\text{ m}$, and $y = 2.916\text{ m}$. Based on the measured rms velocity, the turbulence intensity (TI) at the inlet of the cavity was estimated at about 4% by Nielsen [3].

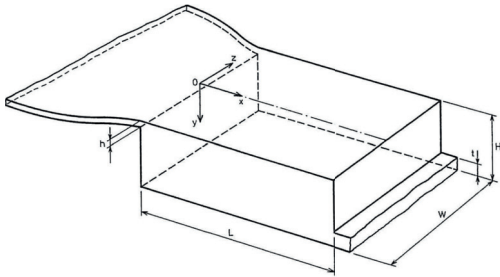


Figure 1. Geometry of fully turbulent benchmark by Nielsen, the figure is taken from [3].

For the evaluation of this benchmark using RANS, a grid sensitivity analysis was performed, resulting in the use of a mesh of 505 thousand cells. This yielded an average y^+ value of 2, which is recommended when using the enhanced wall treatment. In instances where the RANS model exhibited oscillating convergence, averages were taken over 10,000 iterations. For LES and DES, a mesh consisting of 6.8 million cells was utilized as this resolved over 80% of the turbulent kinetic energy, meeting the accuracy recommendations for LES [15]. A time sensitivity analysis determined the optimal timestep to be 0.1 seconds. To obtain averaged velocity components, the flow

was averaged over a minimum of six flow-through times (FTTs), which was sufficient to get statistical-converged first-order flow quantities. FTT is the time it takes for the air to do one circulation inside the cavity, which was calculated to be 130 seconds.

2.3 Description of the transitional benchmark of Van Hooff et al. [8]

The geometry of the transitional experimental setup by Van Hooff et al. [8] is shown in Figure 2. For the numerical studies, only the contraction at the inlet, the main cavity, and the outlet duct are included in the computational domain. The experimental data was collected at two different Reynolds numbers: 1000 and 2500, calculated based on the inlet slot height and velocity. Velocity measurements were taken at three vertical lines located at $x = 60\text{ mm}$, $x = 150\text{ mm}$, and $x = 240\text{ mm}$ away from the inlet of the cavity.

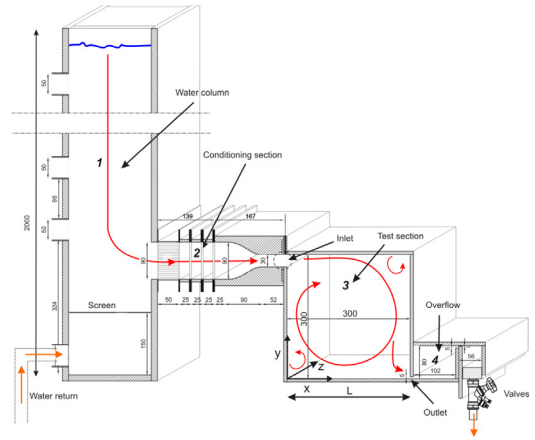


Figure 2. Experimental setup of transitional benchmark by Van Hooff et al., the figure is taken from [9].

A mesh of 1.8 million cells was used for the RANS studies, as determined by a grid sensitivity analysis. This resulted in an average y^+ value of about 1. When the RANS results exhibited oscillatory convergence, averages were taken over 10,000 iterations. For the LES and DES, a significantly finer mesh of 7.3 million cells was utilized. A sensitivity analysis led to selecting a timestep of 0.025 seconds for the case with a Reynolds number of 1000, and a timestep of 0.01 seconds for the Reynolds number of 2500. The flow was averaged over a minimum of six flow-through times (FTTs), which was sufficient to obtain converged first-order flow statistics. For the cases with Reynolds numbers of 2500 and 1000, one FTT was equivalent to 20 and 50 seconds, respectively, as determined by Van Hooff et al. [11]. At the CFD inlet, the TI was equal to 6% and 18%, respectively for the cases where the Reynolds number is 1000 and 2500. For LES, the vortex method with 180 vortices was used at the inlet in line with the setup for synthetic turbulence used by Van Hooff et al. [11].

2.4 Numerical settings

Table 1 summarises the numerical settings employed for the LES and DES. The RANS simulations utilize the same settings, except for the momentum discretization, which is performed using second-order upwind. The simulations were conducted using the Ansys Fluent 2022 R2 software.

Table 1. Numerical settings of LES and DES

Pressure-velocity coupling	SIMPLE
Pressure-velocity flux type	Rhie-Chow: distance based
Gradient discretization	Least Squares Cell Based
Pressure discretization	Second order
Momentum discretization	Bounded central differencing
Turbulence model discretization	Second order upwind
Time discretization	Second order implicit

3 Results

3.1 Fully turbulent case

The velocity profiles for the fully turbulent case resulting from the three RANS models: standard $k-\epsilon$, standard $k-\omega$ and BSL $k-\omega$ are shown for the lines $x = 3\text{ m}$, $x = 6\text{ m}$, $y = 0.084\text{ m}$ and $y = 2.919\text{ m}$ in Figure 3. H is the height of the main cavity (i.e., 3 m), and U_{in} is the average inlet velocity of the cavity. The standard $k-\omega$ model yields the best results near the floor close to the inlet, while the standard $k-\epsilon$ model predicts the best results for the horizontal line $y = 0.084\text{ m}$ and at the vertical line $x = 3\text{ m}$. The standard $k-\epsilon$ model is the RANS model giving the overall best results for the fully turbulent case.

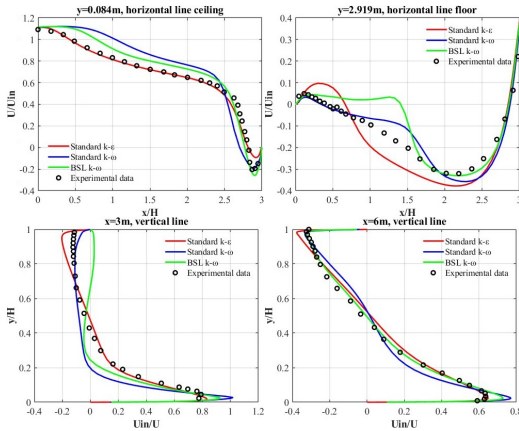


Figure 3. Velocity profiles of the standard $k-\epsilon$, standard $k-\omega$ and BSL $k-\omega$ model for the fully turbulent benchmark.

In the LES, various TI were employed at the inlet of the computational domain to reproduce meaningful turbulent structures at the inlet of the cavity, using the so-called "synthetic turbulent inflow-based spatial-developing simulation method" [16]. The TI investigated were 4%, 10%, 20%, 40% and 50%, where the vortex method was used

inserting 999 vortices at the CFD inlet. Figure 4 shows the resulting velocity profiles. It is noticeable that a TI of 4% results in insufficient turbulence structures at the inlet of the cavity, leading to an overly sharp velocity profile at the vertical line of $x = 3\text{ m}$ and near the inlet. Elevating the TI beyond 10% does not further improve the velocity profiles.

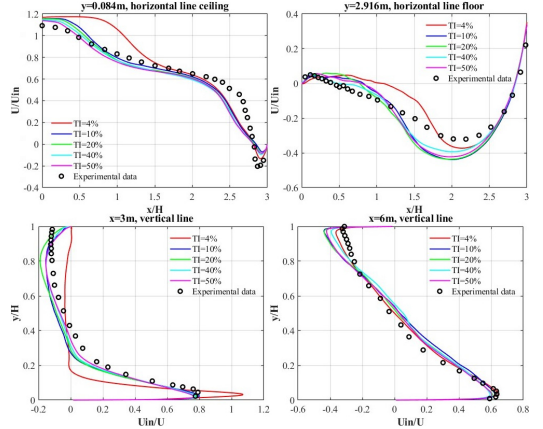


Figure 4. LES for different TI of 4%, 10%, 20%, 40% and 50% at the CFD inlet of the fully turbulent benchmark.

Figure 5 shows the resulting u_{rms} profile generated by LES for different TI at the CFD inlet. As measurements are limited near the wall, the u_{rms} profile is also compared to the DNS data of a turbulent periodic channel flow with a comparable bulk Reynolds number, meaning the DNS of Moser et al. [17] at $Re_\tau = 180$. The findings indicate that our profiles converge to the measurements as the TI at the domain inlet increases. For TI = 40% and TI = 50%, the profiles are similar with the measurements in the center of the slot and increase significantly near the wall as in the DNS profile of Moser et al [17]. This is a significant outcome as it demonstrates that the appropriate level of turbulence at the cavity inlet can be produced by using sufficient TI for the synthetic turbulence at the CFD inlet. A TI of 4% at the CFD inlet deviates significantly from the u_{rms} measured, which can explain why this velocity profile differs from the other profiles shown in Figure 4.

Figure 6 displays the contour plots of the vorticity magnitude for two scenarios with TI at the CFD inlet of 4% and 50%. This figure shows that a high TI increases the vorticity in both the inlet duct and the main cavity. Furthermore, the ceiling jet diffuses more in the scenario with a higher TI at the CFD inlet. This is consistent with the velocity profiles observed in Figure 4.

Figure 7 compares the LES velocity profiles with a TI of 50% at the CFD inlet from this study with the LES results obtained from Taghnia et al. [6] and Zasimova et al. [7]. The predicted LES velocity profiles obtained from our study are more similar to those from Zasimova et al. [7]. This encouraging outcome demonstrates that the LES from this research aligns with other LES investigations,

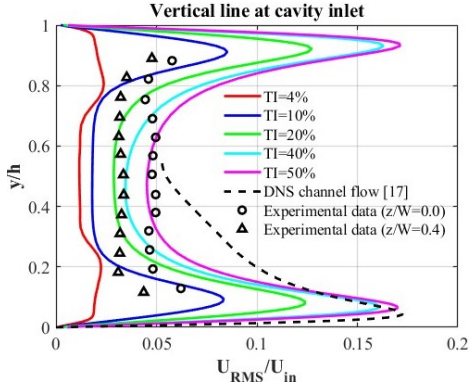


Figure 5. u_{rms} profiles at the cavity inlet of LES with various inlet TI values at the CFD inlet compared to measurement and the DNS results from Moser et al. [17] at $Re_\tau = 180$.

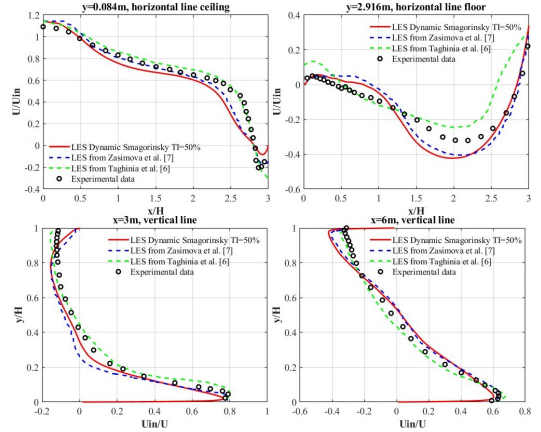


Figure 7. LES with an inlet TI of 50% at the CFD inlet compared to LES studies by Taghnia et al. [6] and Zasimova et al. [7] of the fully turbulent case.

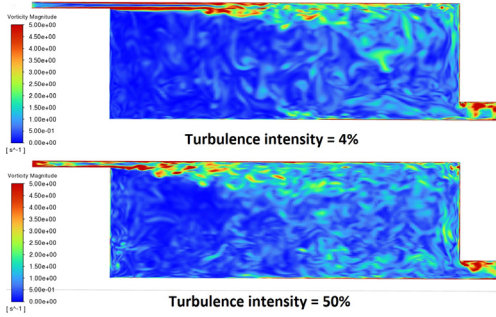


Figure 6. Instantaneous contour plots at the midplane $z = 0 m$ of the vorticity magnitude when the inlet TI is 4% and 50% for LES of the fully turbulent case.

even without utilizing a separate LES of periodic channel flow to generate the inlet boundary conditions. Consequently, the accuracy remains the same with a reduction in computational cost and complexity.

Figure 8 depicts the DES Spalart-Allmaras and DES realizable $k-\epsilon$ approaches for a turbulence intensity of 4% using the vortex method for the fully turbulent benchmark. The reason as to why DES was not implemented with a higher TI at the CFD inlet, was because it diverged for intensities exceeding 4%. This reveals a potential limitation of DES when dealing with fully turbulent flows at the inlet. The DES realizable $k-\epsilon$ model performs much better than the DES Spalart-Allmaras model, which tends to overestimate the velocity of the attached jet.

The velocity profiles of the overall best-performing RANS model, the standard $k-\epsilon$, are compared with the DES realizable $k-\epsilon$ model and the LES model with a TI of 50% in Figure 9. All of the models give relatively good predictions of the velocity field compared to the experimental data. LES and DES perform better at the line by the floor $y = 2.919 m$, while the standard $k-\epsilon$ model yields the best results at the line by the ceiling $y = 0.084 m$.

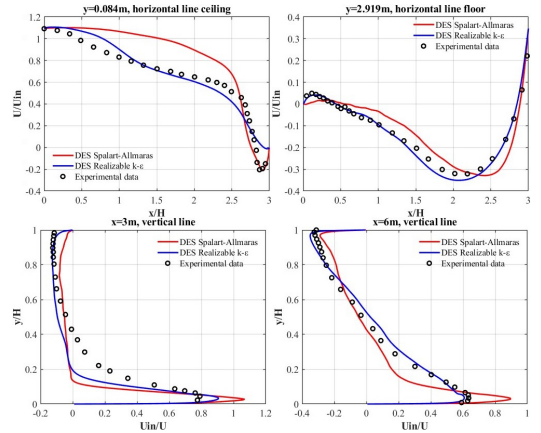


Figure 8. Velocity profiles of DES with the Spalart-Allmaras and realizable $k-\epsilon$ approach for the fully turbulent benchmark with a TI of 4%.

3.2 Transitional case $Re=1000$

The velocity profiles for the same RANS models as previously analyzed are presented at the lines $x = 60 mm$, $x = 150 mm$, and $x = 240 mm$ in Figure 10 for the transitional case with a Reynolds number of 1000. H is the height of the cavity (i.e., $300 mm$) and U_{max} is the maximum velocity from the experimental data along the line. The standard $k-\omega$ model exhibits the best performance, as the standard $k-\epsilon$ predicts the detachment too late and the BSL $k-\omega$ predicts detachment too early.

The velocity profiles of the best performing RANS model standard $k-\omega$, DES Spalart-Allmaras and the LES are shown in Figure 11. The DES anticipates an early detachment, whereas the RANS model and the LES yield comparable profiles, with the standard $k-\omega$ model marginally outperforming the LES.

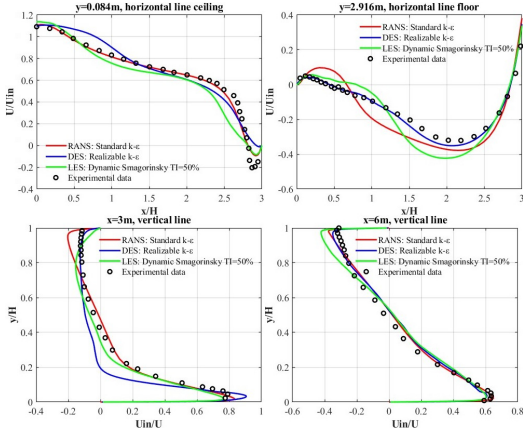


Figure 9. Velocity profiles of RANS using the standard $k-\epsilon$ model, DES and LES with a turbulence intensity of 50% at the CFD inlet of the fully turbulent benchmark.

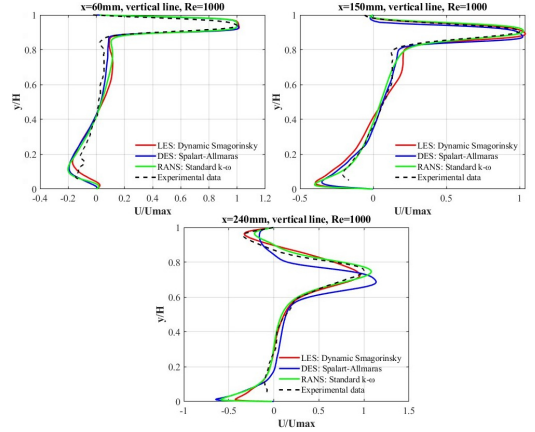


Figure 11. Velocity profiles of RANS using the standard $k-\omega$ model, DES and LES of the transitional benchmark with a Reynolds number of 1000.

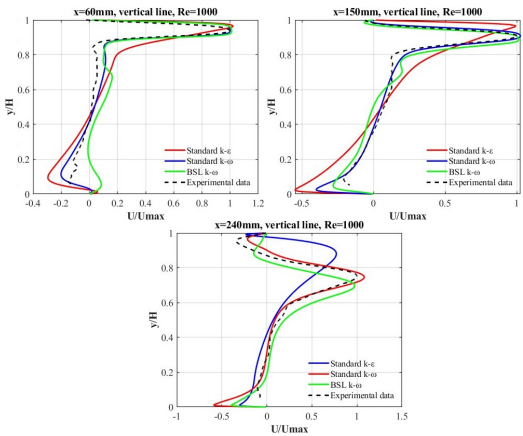


Figure 10. Velocity profiles of the various RANS models for the transitional case with a Reynolds number of 1000.

3.3 Transitional case Re=2500

The same RANS models are also employed for the transitional scenario with a Reynolds number of 2500, as illustrated in Figure 12. The BSL $k-\omega$ model delivers the best precision, whereas the standard $k-\epsilon$ predicts a detachment too late and the standard $k-\omega$ too early and both of these models underestimate the peak velocity at the jet. Upon evaluating the performance of all the RANS models against all the provided benchmarks, it becomes evident that no single RANS model outperforms the others in accurately predicting the velocity fields for all the benchmarks. This verifies the conclusion of Bjerkeli's work [10], that there does not exist one universally accurate RANS model for all the flow regimes of the cavity flow.

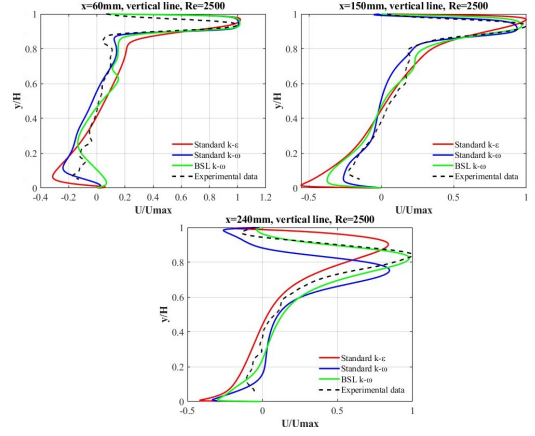


Figure 12. The velocity profiles of different RANS models on the transitional case with a Reynolds number of 2500.

Figure 13 compares the LES results from our study and from the work of Van Hooff et al. [11]. It is noticeable that the performance of the LES from our study is inferior to that of Van Hooff et al. [11]. Both LES accurately predict the detachment point, but the LES from our study underestimates the peak velocity of the jet. Despite identical numerical and LES setups, the results vary, indicating that the LES performance is dependent on the quality of the mesh.

The velocity profiles of the best performing RANS model BSL $k-\omega$, DES realizable $k-\epsilon$ and LES are presented in Figure 14. BSL $k-\omega$ model gives the best performance, while DES gives the worst. For DES, the detachment point is prematurely predicted, leading to an inaccurate velocity profile. The primary challenge with DES in the transitional case is its struggle to generate sufficient turbulent structures in the flow. This problem might stem

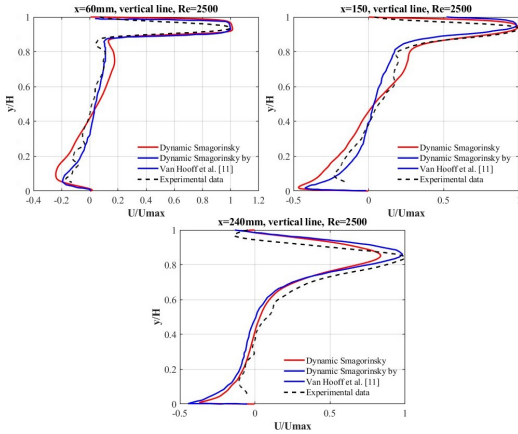


Figure 13. Comparison of velocity profiles between the LES of this work with the LES of Van Hooff et al. [11] using the Dynamic Smagorinsky model for the transitional benchmark with a Reynolds number of 2500.

from the transition from LES to RANS, which dampens the turbulence structures in the flow, causing an early detachment of the jet from the ceiling. This issue is also evident in the case with a Reynolds number of 1000. Moreover, for the fully turbulent case, DES encounters convergence problems when too much synthetic turbulence is applied at the inlet. However, the DES realizable $k-\epsilon$ model is still able to yield fairly good results for the fully turbulent case, especially close to the floor. Hence, more research is needed to obtain a definitive conclusion to determine whether DES can yield good accuracy on the turbulent cavity flows and to understand the convergence issues with the inlet synthetic turbulence.

In this scenario, the RANS model outperforms the LES. However, the challenge with RANS is the absence of a universal model that performs well for cavity flows with varying turbulent regimes and geometries. For the transitional cases the $k-\omega$ models outperform the $k-\epsilon$ models, while the opposite is the case for the fully turbulent benchmark. Therefore, LES is more versatile, and the same LES model can be used for numerous cavity flow cases with relatively good precision.

4 Conclusion

This article evaluated the performance of the LES and DES to RANS turbulence modeling using two benchmarks for turbulent cavity flow.

The first benchmark flow, by Nielsen [3], is classified as fully turbulent with a Reynolds number of 5000. The standard $k-\epsilon$ model emerges as the best-performing RANS model for this case. The turbulence intensity at the CFD inlet influences the performance of the LES. With a turbulence intensity of 10% or higher, LES results are consistent and comparable to the LES by Zasimova et al. [7] and Taghinia et al. [6]. Results also show that good accuracy can be achieved by using spatial-developing syn-

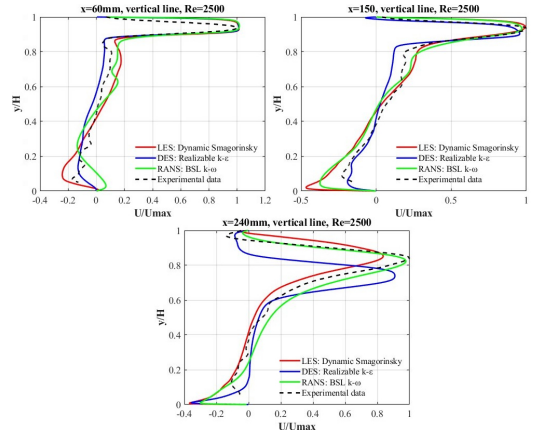


Figure 14. Velocity profiles of RANS using the BSL $k-\omega$ model, DES and LES of the transitional benchmark with a Reynolds number of 2500.

thetic turbulence at the inlet, which is less computationally demanding than conducting a separate LES of a periodic channel flow, as done in the literature. For DES, simulations cannot be converged when the turbulence intensity at the inlet exceeds 4%. However, the DES realizable $k-\epsilon$ gives fairly accurate results, leading to the best results close to the floor. The limitation of DES is visible on the wall-attached inlet jet where DES struggles with the lack of resolved turbulent structures in the transition zone between LES and RANS. In conclusion, the best RANS and LES perform well for the fully turbulent case while DES gives good results except for the wall-attached jet.

The second cavity flow benchmark investigated was created by Van Hooff et al. [8]. It involves a transitional flow with Reynolds numbers of 1000 and 2500. When the Reynolds number is 1000, the standard $k-\omega$ model is the best overall RANS model, while for a Reynolds number of 2500, the BSL $k-\omega$ model is the best RANS model. The LES also performs well for these two transitional cases. However, RANS slightly outperforms LES for the case with a Reynolds number of 2500. When comparing the LES with the study from Van Hooff et al. [6], it is clear that different results are obtained despite identical numerical setups. Regarding DES, it predicts insufficient turbulence in the flow, resulting in premature flow detachment. A possible explanation for this limitation is again related to the transition between RANS and LES.

Conclusions are in line with Larkermanni et al. [1] which states that no RANS model can simultaneously give satisfactory results for both transitional and fully turbulent flows. Our study concludes that the LES is generally more universal than RANS to compute turbulent flows inside such cavities as it does not require prior knowledge of the flow regime. However, the performance of the LES depends on the amount of synthetic turbulence at the inlet, as shown for the fully turbulent case. This quantity may be difficult to assess during a ventilation design but sensitivity analysis shows that a rough estimate could be enough.

Results also show that the spatial-developing synthetic turbulence method is simpler to provide consistent boundary conditions for LES at the cavity inlet. Regarding DES, it is a promising approach compared to LES as it enables to decrease the computational costs. Results are encouraging but, for this model to be reliable, more research is required to understand its performance on the cavity flow benchmark.

References

- [1] E. Larkermanni, V.M. Bjerkeili, L. Georges, "Comparing the performance of RANS turbulence models between different cavity flow benchmarks", The 16th ROOMVENT Conference (ROOMVENT 2022) (2022)
- [2] P.V. Nielsen, A. Restivo, J.H. Whitelaw, "The Velocity Characteristics of Ventilated Rooms", *Journal of Fluids Engineering* **100**, 291-298 (1978)
- [3] P.V. Nielsen, "Specification of a Two-Dimensional Test Case", International Energy Agency, *Energy Conservation in Buildings and Community Systems* **20**, (1990)
- [4] L. Rong ,P.V. Nielsen, "Simulation with different turbulence models in an annex 20 room benchmark test using Ansys CFX 11.0", *DCE Technical reports* **46**, (2008)
- [5] S. Bjuri, "Computational Fluid Dynamics of Airflows inside buildings: RANS-LES of the cavity flow benchmark", Master's thesis in Energi og miljø (NTNU) (2023)
- [6] J.H. Taghinia, M.M. Rahman, T. Siikonen, R.K. Agarwal, "One-equation sub-grid scale model with variable eddy-viscosity coefficient", *Computers & Fluids* **107** (2014)
- [7] M. Zasimova, N.G. Ivanov, D. Markov, "Numerical modeling of air distribution in a test room with 2D sidewall jet. II. LES-computations for the room with finite width", *St Petersburg State Polytechnical University Journal Physics and Mathematics* **13** (2020)
- [8] T. Van Hooff, B. Blocken, T. Defraeye, J. Carmeliet, G.J.F. Van Heijst, "PIV measurements of a plane wall jet in a confined space at transitional slot Reynolds numbers", *Experiments in Fluids* **53**, 499-517, (2012)
- [9] T. Van Hooff, B. Blocken, G.J.F. Van Heijst, "Mixing ventilation flow in an enclosure driven by a transitional wall jet", URL: "https://www.kbwiki.ercoftac.org/w/index.php/Abstr:UFR_4-20"
- [10] V.M. Bjerkeili, "Computational Fluid Dynamics of airflows inside buildings: a comprehensive review of the cavity flow benchmark", Master's thesis in Energi og miljø (NTNU) (2020)
- [11] T. Van Hooff, B. Blocken, P. Gousseau, G.J.F. Van Heijst, "Counter-gradient diffusion in a slot-ventilated enclosure assessed by LES and RANS", *Computers & Fluids* **96**, 63-75 (2014)
- [12] Ansys Fluent, "Ansys Fluent Theory Guide"
- [13] M. Germano, U. Piomelli, P. Moin, W.H. Cabot, "A dynamic subgrid-scale eddy viscosity model", *Physics of Fluids* **3**, 1760-1765 (1991)
- [14] M. Shur, P.R. Spalart, M. Strelets, A. Travin, "Detached-eddy simulation of an airfoil at high angle of attack", *Engineering Turbulence Modelling and Experiments* **4**, 669-678 (1999)
- [15] R.F. Pope, "Ten questions concerning the large-eddy simulation of turbulent flows", *New Journal of Physics* **6**, 35 (2004)
- [16] N.S. Dhamankar, G.A. Blaisdell, A.S. Lyrintzis, "Overview of Turbulent Inflow Boundary Conditions for Large-Eddy Simulations", *AIAA JOURNAL* **56** (2007)
- [17] R.D. Moser, J. Kim, N.N. Mansour, "Direct numerical simulation of turbulent channel flow up to $Re_\tau = 590$ ", *Physics of Fluids* **11**, 943-945 (1999)